

**THE ENERGY RELEASE IN EARTHQUAKES, and
SUBDUCTION ZONE SEISMICITY AND STRESS IN SLABS**

Thesis by

Marios Simou Vassiliou

In Partial Fulfillment of the Requirements

of the Degree of

Doctor of Philosophy

California Institute of Technology

Pasadena, California

1983

(submitted March 11, 1983)

-iii-

To my parents,

Simos G. Vassiliou

Avra S. Vassiliou

Acknowledgements

I thank my two advisors, Hiroo Kanamori and Bradford Hager, for all the assistance and support they have given me. Hiroo was my principal advisor for Part One, but helped me with Part Two as well. Brad was the principal advisor for Part Two. Both have shown great patience and enthusiasm throughout this work.

I owe a great debt as well to Tom Ahrens, with whom I worked closely on several equation-of-state projects not represented in this thesis. I consider my interaction with him to have been an important part of my scientific education.

Don Anderson has provided many helpful discussions on all phases of my work at Caltech. It was he who first pointed me in the direction of re-examining the distribution of seismicity with depth, this eventually leading to the work in Part Two.

Arthur Raefsky was one of the main agents in developing the finite element code I used in Part Two. For his help in running this program, and for the generous time commitment he made to teaching me the basics of the finite element method, I thank him. I also thank Joe Kirschvink, who saved me from having to re-invent spherical statistics. Tom Heaton provided valuable assistance and discussions on Part I. Medhat Haroun, then of EERL at Caltech, was most helpful in providing me with strong-motion data for Part I. Domenico Giardini was the source of interesting conversations about Part II, and very kindly provided me with important data of his before publication. I must thank, as well, Rob Clayton, for the use of the VAX computer, and for his assistance in that area.

Finally, I want to thank all the rest of the faculty, students, and staff of the Seismological Laboratory and the Division of Geological and Planetary Sciences, for a scholarly and research atmosphere which I believe is unmatched *anywhere*. Most of the time, it was even pleasant from a personal point of view. I will miss Caltech.

I acknowledge the support of a Beno Gutenberg Fellowship in Geophysics during my first year of study. This research was supported by the Earth Sciences Section, National Science Foundation, grants EAR77-13641 and EAR78-11973 (Part I), and grant EAR-8206528 (Part II). The research in Part II was also supported by NASA grant NSG-7610.

Abstract for Part I

Earthquake energy calculations are generally made through an empirical application of the familiar Gutenberg-Richter energy-magnitude relationships. The precise physical significance of these relationships is somewhat uncertain. We make use here of the recent increases in knowledge about the earthquake source to place energy measurements on a sounder physical basis. For a simple trapezoidal far-field displacement source-time function with a ratio x of rise time to total duration T_0 , the seismic energy E is proportional to $\frac{1}{x(1-x)^2} \frac{M_0^2}{T_0^3}$, where M_0 is seismic moment. As long as x is greater than 0.1 or so, the effect of rise time is not important. The dynamic energies thus calculated for shallow events are in reasonable agreement with the estimate $E \approx (5 \times 10^{-5}) M_0$ based on elastostatic considerations. Deep events, despite their possibly different seismological character, yield dynamic energies which are compatible with a static prediction similar to that for shallow events. Studies of strong-motion velocity traces obtained near the sources of the 1971 San Fernando, 1966 Parkfield, and 1979 Imperial Valley earthquakes suggest that even in the distance range of 1-5 km., most of the radiated energy is below 1-2 Hz. in frequency. Far field energy determinations using long period WWSSN instruments are probably not in gross error despite their bandlimited nature. The strong motion record for the intermediate depth Bucharest earthquake of 1977 also suggests little teleseismic energy outside the pass-band of a long period WWSSN instrument.

Abstract for Part II

The pattern of seismicity as a function of depth in the world, and the orientation of stress axes of deep and intermediate earthquakes, are explained using viscous fluid models of subducting slabs, with a barrier in the mantle at 670 km. 670 km is the depth of a seismic discontinuity, and also the depth below which earthquakes do not occur. The barrier in the models can be a viscosity increase of an order of magnitude or more, or a chemical discontinuity where vertical velocity is zero. Log N versus depth, where N is the number of earthquakes, shows (1) a linear decrease to about 250-300 km depth, (2) a minimum near that depth, and (3) an increase thereafter. Stress magnitude in a subducting slab versus depth, for a wide variety of models, shows the same pattern. Since there is some experimental evidence that N is proportional to $e^{k\sigma}$, where k is a constant and σ is the stress magnitude, the agreement is encouraging. In addition, the models predict down-dip compression in the slab at depths below 400 km. This has been observed in earlier studies of earthquake stress axes, and we have confirmed it via a survey of events occurring since 1977 which have been analyzed by moment tensor inversion. At intermediate depths, the models predict an approximate but not precise state of down-dip tension when the slab is dipping. The observations do not show an unambiguous state of down-dip tension at intermediate depths, but in the majority of regions the state of stress is decidedly closer to down-dip tension than it is to down-dip compression. Chemical discontinuities above 670 km, or phase transitions with an elevation of the boundary in the slab, predict, when incorporated into the models, stress peaks which are not

mirrored in the profile of seismicity versus depth. Models with an asthenosphere and mesosphere of appropriate viscosity can not only explain the state of stress observed in double Benioff zones, but also yield stress magnitude profiles consistent with observed seismicity. Models where a nonlinear rheology is used are qualitatively consistent with the linear models.

Table of Contents

Part I: The Energy Release in Earthquakes	
1. Introduction	3
2. Dynamic Energy from Source-Time Function	4
3. A Simplified Procedure for Modeling Deep Focus Events	13
4. Comparison with Static Energy Estimates	19
5. Near Source Energy Studies and the Question of Frequency Content	29
6. Energy and Magnitude	38
7. Conclusions	44
References	45
Part II: Subduction Zone Seismicity and Stress in Slabs	
1. Introduction	52
2. Observations	53
3. Calculations of Stress in Subducting Slabs	100
4. Summary and Conclusions	199
References	202
Appendix A: Mechanisms of Large Intermediate and Deep Earthquakes, 1978-1981	
	213
Appendix B: A Brief Outline of Directional Statistics	229
Appendix C: Plots of Seismicity versus Depth for the World's Subduction Zones	234

Appendix D: Spatial Stress Plots and Velocity Plots

not Included in the Text 266

PART I: THE ENERGY RELEASE IN EARTHQUAKES

Abstract

Earthquake energy calculations are generally made through an empirical application of the familiar Gutenberg-Richter energy-magnitude relationships. The precise physical significance of these relationships is somewhat uncertain. We make use here of the recent increases in knowledge about the earthquake source to place energy measurements on a sounder physical basis. For a simple trapezoidal far-field displacement source-time function with a ratio x of rise time to total duration T_0 , the seismic energy E is proportional to $\frac{1}{x(1-x)^2} \frac{M_0^2}{T_0^3}$, where M_0 is seismic moment. As long as x is greater than 0.1 or so, the effect of rise time is not important. The dynamic energies thus calculated for shallow events are in reasonable agreement with the estimate $E \approx (5 \times 10^{-5}) M_0$ based on elastostatic considerations. Deep events, despite their possibly different seismological character, yield dynamic energies which are compatible with a static prediction similar to that for shallow events. Studies of strong-motion velocity traces obtained near the sources of the 1971 San Fernando, 1966 Parkfield, and 1979 Imperial Valley earthquakes suggest that even in the distance range of 1-5 km., most of the radiated energy is below 1-2 Hz. in frequency. Far field energy determinations using long period WWSSN instruments are probably not in gross error despite their bandlimited nature. The strong motion record for the intermediate depth Bucharest earthquake of 1977 also suggests little teleseismic energy outside the pass-band of a long period WWSSN instrument.

1. Introduction

The energy released in earthquakes can be estimated in a number of ways (for a comprehensive review see Bath, 1966). We may divide the energy estimates from the variety of methods available into two broad classes: the static estimates and the dynamic estimates. Static estimates can be obtained from static values of moment and stress drop; dynamic estimates, on the other hand, are obtained from seismograms.

We review static estimates of energy in Section 4. We discuss there that with some simple assumptions, a static estimate of energy can be obtained from the formula $E = (5 \times 10^{-5}) M_0$ (Knopoff, 1958; Kanamori, 1977).

We may subdivide dynamic estimates of energy from body waves into two groups. One procedure involves the direct integration of an observed waveform at a particular station; another involves integration of an inferred displacement source-time function.

The familiar energy-magnitude relationships of Gutenberg and Richter (1942, 1956a, 1956b) fall into the first category of dynamic methods. These empirical relationships were derived on the basis of a crude approximation to the integral over a group of plane seismic waves passing by a station. The Gutenberg-Richter estimates of energy from M_s agree fairly well with the static estimates mentioned above. This might be expected, as M_s correlates quite well with $\log_{10} M_0$ (Kanamori and Anderson, 1975).

In this study, we develop dynamic energy estimates of the second kind. We apply the theory of Haskell (1964) to compute the energies of several shallow events (Section 2), using moments and source-time histories obtained in the last decade from sophisticated waveform modeling. Since there are fewer studies available on intermediate and deep focus events, we also develop a simplified modeling procedure (Section 3) to obtain moments and time functions for such events, and use these to estimate energy in the same way as for shallow earthquakes. The energy estimates we obtain are in a sense direct physical dynamic estimates, as opposed to the more empirical approach represented by the energy-magnitude relations. In Section 4, we compare dynamic and static estimates for both shallow and deep events.

Our dynamic estimates contain more high frequency information than the static ones. They are still made, however, at teleseismic distances, and they are furthermore derived from long period instruments unable to resolve displacement components of frequency greater than 1-2 Hz. It is thus possible that some critical high frequency information is missing. We address this question in Section 5., using high frequency records obtained close to seismic sources with strong-motion instruments.

Finally, in Section 6, we compare our dynamic energy estimates with estimates from the Gutenberg-Richter energy-magnitude relations, using M_S for the shallow earthquakes and *long period* body wave magnitude m_B for the deep and intermediate ones.

2. Dynamic Energy from Source Time Function

A milestone in the understanding of energy radiation from earthquakes was the paper by Haskell (1964). We essentially follow his treatment, with minor modifications, to obtain expressions for energy release in terms of parameters obtainable

from body wave modeling of earthquakes. The important parameters are the seismic moment and the duration and shape of the far field source time function. The earthquake displacement observed at far field is given by

$$u(r,t) = \left[\frac{R(\theta,\varphi)}{4\pi\rho v^3 r} \right] M_0 T(t) \quad (1)$$

where $R(\theta,\varphi)$ is a geometric factor accounting for the radiation pattern of the seismic waves; ρ, v , and r are respectively density, elastic wave velocity, and distance to the source; M_0 is the seismic moment, and $T(t)$ is the far field source time function, which is normalised to unit area. This expression assumes that we have already accounted for the effects of attenuation, instrument, receiver structure, and geometric spreading (e.g. Langston and Helmberger, 1975). In the simple case of a one dimensional rupture with a ramp function near-source dislocation history, T will generally be trapezoidal in shape (with a triangle as a special case). The trapezoid is obtained by convolving the point-source boxcar (which the near-field ramp produces at far field) with another boxcar representing source finiteness. Other shapes are certainly possible, though not always resolvable by the data. To calculate the energy associated with (1), we begin with a general form of Haskell's (1964) equations (15) and (16)

$$E = \rho v \int_{-\infty}^{\infty} \int_0^{2\pi} \int_0^{\pi} \dot{u}^2 dt r^2 \sin\theta d\theta d\varphi \quad (2)$$

Equation (2) was derived in the case of spherically symmetric radiation by Yoshiyama (1963). Rudnicki and Freund (1981) derive it for a more general radiation pattern by imposing plane wave conditions at far field. We apply equation (2) separately to P and S waves. We use (1), with $R(\theta,\varphi)$ factors appropriate (Haskell, 1964) for a

double couple source, and work the geometric integrals out analytically; adding the P and S wave energies together, we then obtain

$$E = K M_0^2 I_t \quad (3)$$

with

$$K = \left\{ \frac{1}{15\pi\rho\alpha^5} + \frac{1}{10\pi\rho\beta^5} \right\}$$

and

$$I_t = \int_{-\infty}^{\infty} \dot{T}^2(t) dt$$

where α and β are the compressional and shear wave velocities. In the earth, $\beta \approx \frac{\alpha}{\sqrt{3}}$, so that the second term in K is dominant, and the total energy is approximately equal to shear wave energy. We note that following Plancherel's theorem (Bracewell, 1978), (3) can be written as

$$E = K M_0^2 I_f \quad (4)$$

where

$$I_f = 2 \int_0^{\infty} \tilde{T}(f)^2 df$$

and $\tilde{T}(f)$ is the Fourier transform of $\dot{T}(t)$ (note that T is real).

Consider now a simple symmetric trapezoidal far field time function with a ratio of rise time to total duration represented by x (Fig. 1). In this case, the integral in (3) reduces to

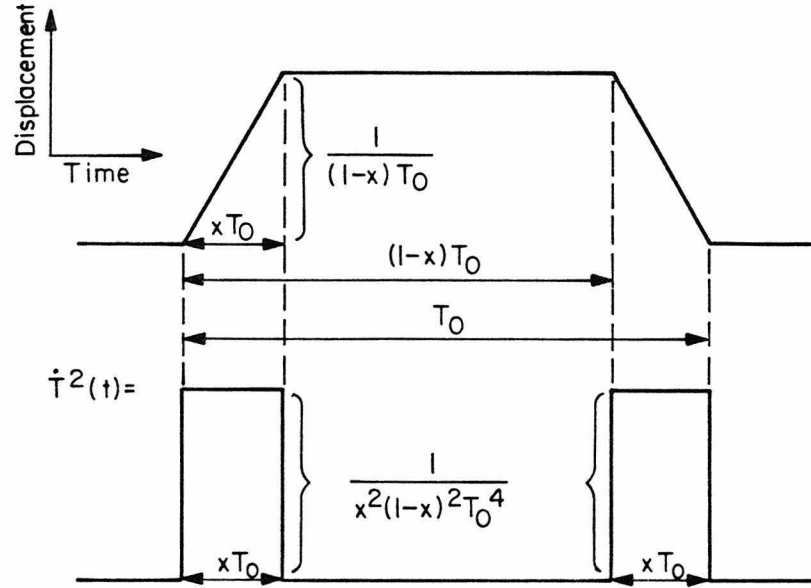
$$I_t = \frac{2}{x(1-x)^2 T_0^3} \quad (5)$$

where T_0 is total duration. Hence we have the important result that energy is proportional to the square of the moment, and inversely proportional to the cube of the duration. If one examines the function $\frac{1}{x(1-x)^2}$, one can easily see that the effect of x is not important unless x is very small; that is, trapezoidal time functions with x between ≈ 0.1 and 0.5 have roughly the same energy (Fig. 2). When functions have very short rise times, this corresponding to the presence of higher frequency components, an appreciable error in the energy can be incurred from even small errors in the rise time. Extremely short rise times are not, however, generally supported by the data, and simple but convincing scaling arguments (Kanamori, 1972; Geller, 1976) lead one to expect values of x greater than 0.1 or so. Hence we effectively have two important parameters in the energy calculation -- the total moment and the total duration. We might note here that the rather artificial presence of sharp corners in the trapezoidal time function does not have an important effect on the total energy. The corners arise from the assumption of a one dimensional rupture. A fault rupturing along its width as well as its length can be modeled by convolving the point-source far-field boxcar with two boxcars representing finiteness instead of one, this leading to a far field time function with rounded corners (e.g., Mikumo, 1971, Fig. 2). The main shape effect is still due to the rise time, and the above arguments apply.

We may use (3) to calculate the energies of some shallow events for which time functions and moments have been published. Table 1 shows the results of such calculations, which will be discussed in more detail in Section 4.

Figure 1. Trapezoidal far field displacement time function. Total duration is T_0 , rise time is αT_0 .

Trapezoidal Far-Field Time Function $T(t)$



$$I_t = \int_{-\infty}^{\infty} \dot{T}^2(t) dt$$
$$= \frac{2}{x(1-x)^2} T_0^3$$

Figure 2. Effect of trapezoid rise time on calculation of dynamic energy release (see equation 5). As long as x (rise time divided by total duration) is greater than 0.1 or so, the effect is not important.

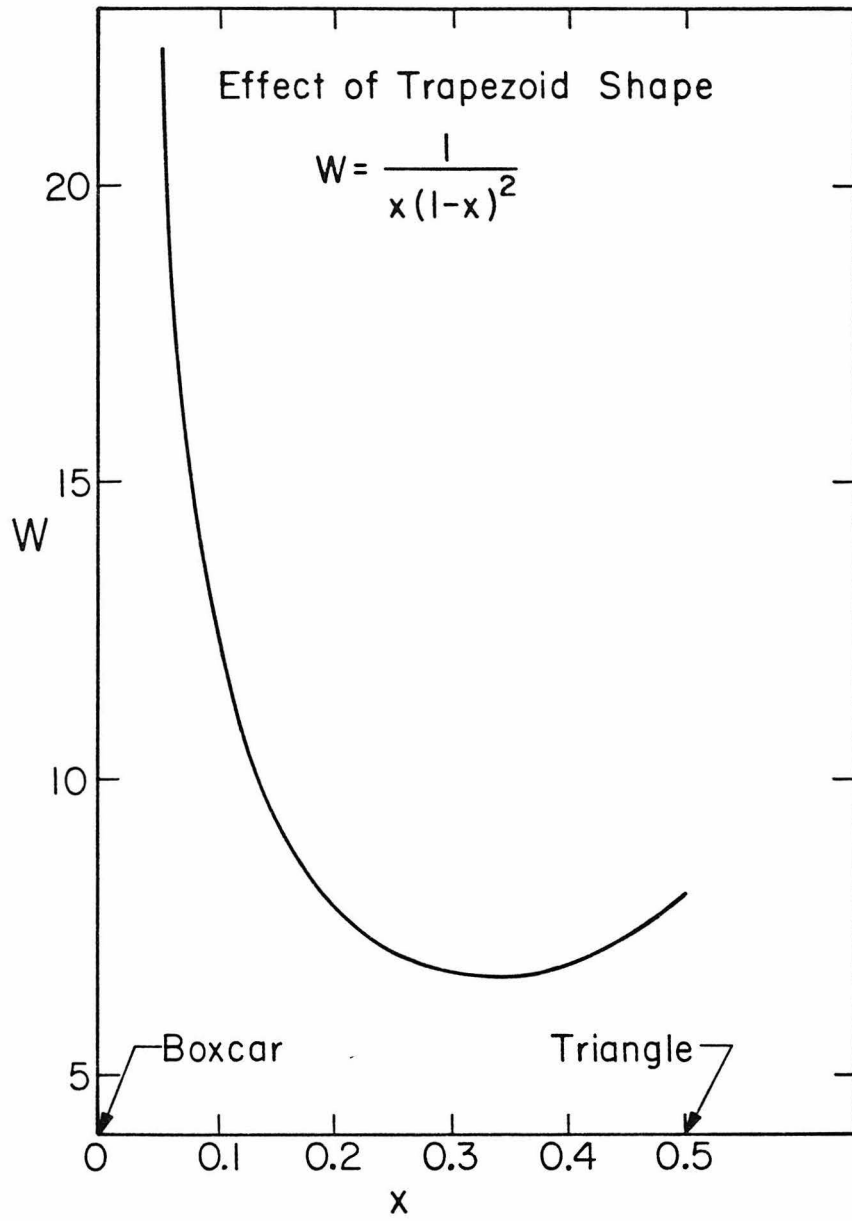


TABLE 1
ENERGY CALCULATIONS FOR SOME MODELED SHALLOW EVENTS

Event	Date	$\log M_0$ (dyne-cm)	T_0 (sec)	$\log E$ (erg)	M_s	Reference
Oroville	1975	24.8	3	19.7		Langston and Butler, 1976
Truckee	1966	24.8	3	19.7	5.9	Burdick, 1977
Friuli	5/16/76	25.5	4.5	20.5	6.5	Cipar, 1980
Friuli	9/15/76	24.7	4.0	19.2	6.0	Cipar, 1980
	9 21					
Friuli	9 '15/76	25.0	3.5	19.9	5.9	Cipar, 1981
	3 15					
Koyna	1967	25.5	6.4	20.2	6.4	Langston, 1976
El Golfo	1966	25.7	4	21.3	6.3	Ebel <i>et al.</i> , 1978
Borrego Mt.	1968	26.0	5	21.8	6.9	Burdick and Mellman, 1976
Puget Sound	1965	26.2	3	22.7		Langston and Blum, 1977
Gazli	1976	26.2	8	21.4	7.0	Hartzell, 1980
Haicheng	1975	26.5	7	22.0	7.4	Cipar, 1979
Solomon Is.	1975	27.1	10	22.7	7.7	Lay and Kanamori, 1980
Solomon Is.	7/14/71	28.1	14	24.2	7.9	Lay and Kanamori, 1980
Solomon Is.	7/26/71	28.3	16	24.4	7.9	Lay and Kanamori, 1980
	4/16/65	25.1	3.4	20.5		Liu and Kanamori, 1980
	9/4/63	25.2	2.5	21.2		Liu and Kanamori, 1980
	10/23/64	25.8	2.5	22.3		Liu and Kanamori, 1980
	9/30/71	24.9	1.6	21.0		Liu and Kanamori, 1980
	3/24/70	25.2	2.5	21.0		Liu and Kanamori, 1980
Mexico	11/29/78	27.3	15	22.6	7.8	Stewart <i>et al.</i> , 1981
Mexico	8/23/65	27.3	16	22.5	7.6	Chael and Stewart, 1982
Mexico	8/2/68	26.9	16	21.7	7.1	Chael and Stewart, 1982
Mexico	3/14/79	27.0	17	22.7	7.6	Chael and Stewart, 1982
Bermuda	3/24/78	25.5	3	21.1	6.0	Stewart and Helmberger, 1981
Gibbs	1967	26.3	17	20.5	6.5	Kanamori and Stewart, 1976
Gibbs	1974	26.7	22	20.9	6.9	Kanamori and Stewart, 1976

3. A Simplified Procedure for Modeling Deep Focus Events

Waveform modeling can be an extremely time-consuming task; the data shown in Table 1 represent a very large amount of work on the part of many investigators. To obtain a larger data base one may resort to a more simplified procedure which is still sufficiently accurate for the purposes of energy computation. The procedure we use is applicable to deep and intermediate events with comparatively simple sources. It consists essentially of estimating the duration of the time function of a simple source from the average pulse width of long period WWSSN vertical P waves (Bollinger, 1968; Chung and Kanamori, 1980), and then using the average amplitude to infer the moment. We use several stations (≥ 10), as well distributed as possible, to average out the effects of radiation pattern and directivity. When the long period P wave is a single pulse and there are no contaminating free-surface phases, this method can be quite accurate. When we applied it to the deep and intermediate events studied by Chung and Kanamori (1980), our results for moment and time function were in good agreement with theirs.

To estimate the moment and duration, we use curves of the type shown in Figs. 3 and 4 (see captions). These are obtained from synthetic seismograms which are generated by convolving source functions with an instrument response and an attenuation filter. We generally assume that the time function is a trapezoid with $x=0.2$ (as we have seen, such a trapezoid does not have a significantly different energy from that of a triangle or any trapezoid with $x \geq 0.1$), and $T^* = 0.7$ in the attenuation filter. Optimistically, this method, allowing for differences in time function shape, attenuation, etc., can give us an estimate of total duration accurate to ≈ 20 per cent, and an estimate of moment perhaps accurate to within a factor of two, given the scatter in amplitude due to receiver and other effects. The energy

Figure 3. (Adapted from Chung and Kanamori, 1980) The relation between measured pulse width W_p of direct vertical P waves on a long period WWSSN seismogram and the duration T_0 of the far field source displacement time function. The curves are obtained by convolving the time function with an instrument response and an appropriate Q filter ($T^* = 0.75$ shown here). These curves are reliable provided the P arrival is a single pulse (ie, the event is simple). In this case the event is assumed to be deep enough that the direct P wave is not contaminated by free-surface phases.

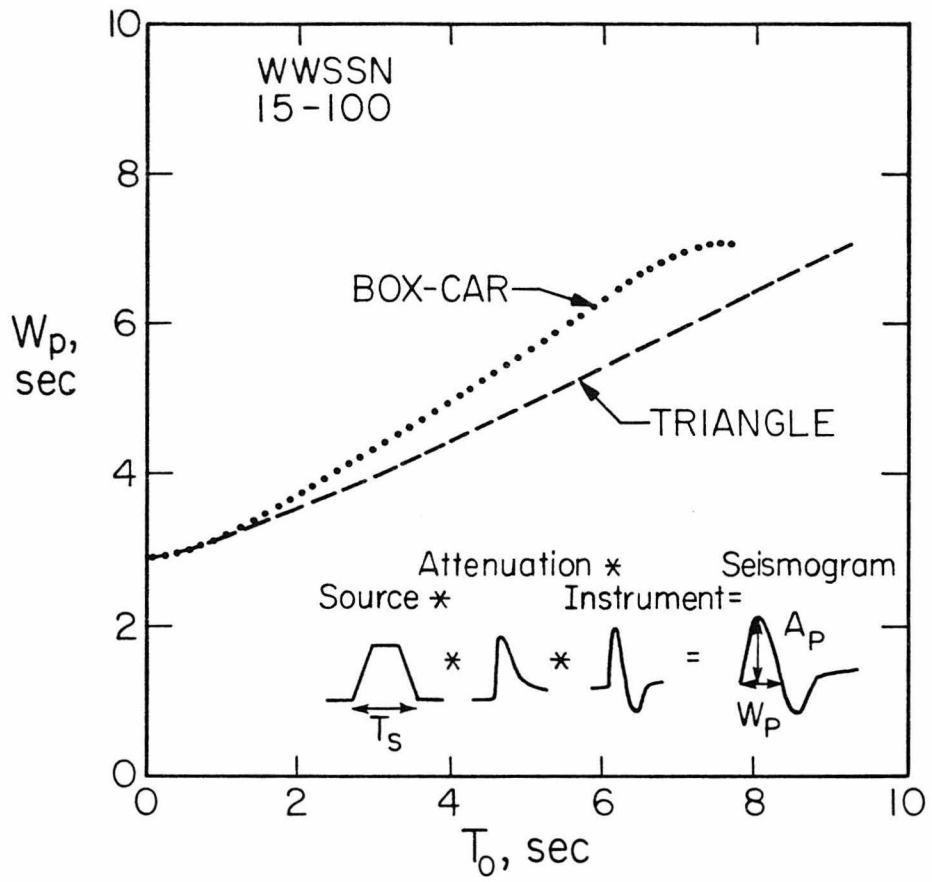


Figure 4. Examples of curves from which the moment M_0 can be determined for a simple event once the duration T_0 of the far field time function has been determined. For a source depth of 400 km., a source-station distance of 60° , and a peak instrument gain factor of 1500, a curve on this diagram shows the variation of amplitude A_p of direct P on a long period seismogram with duration of the time function if the moment of the event is 10^{25} dyn-cm. Thus for a given T_0 one can read off the expected amplitude for $M_0 = 10^{25}$ dyn-cm, and compare this with the average of amplitude measurements actually made to obtain the moment of the event (corrections are easily made to the amplitude measurement to standardise it to a distance of 60° if necessary). Since an average amplitude measurement is used, the curves drawn here are for an average value of the radiation pattern. The trapezoid function referred to in the figure has a rise time equal to $1/5$ its total duration, which is what we generally assume for events we are studying by this method. The curves drawn for the limiting cases of a boxcar and a triangle show what errors might be incurred if this assumption is unwarranted. As can be seen, these errors, as well as those due to uncertainties in attenuation, are probably quite negligible compared to errors due to scatter in amplitudes caused by receiver and other effects.

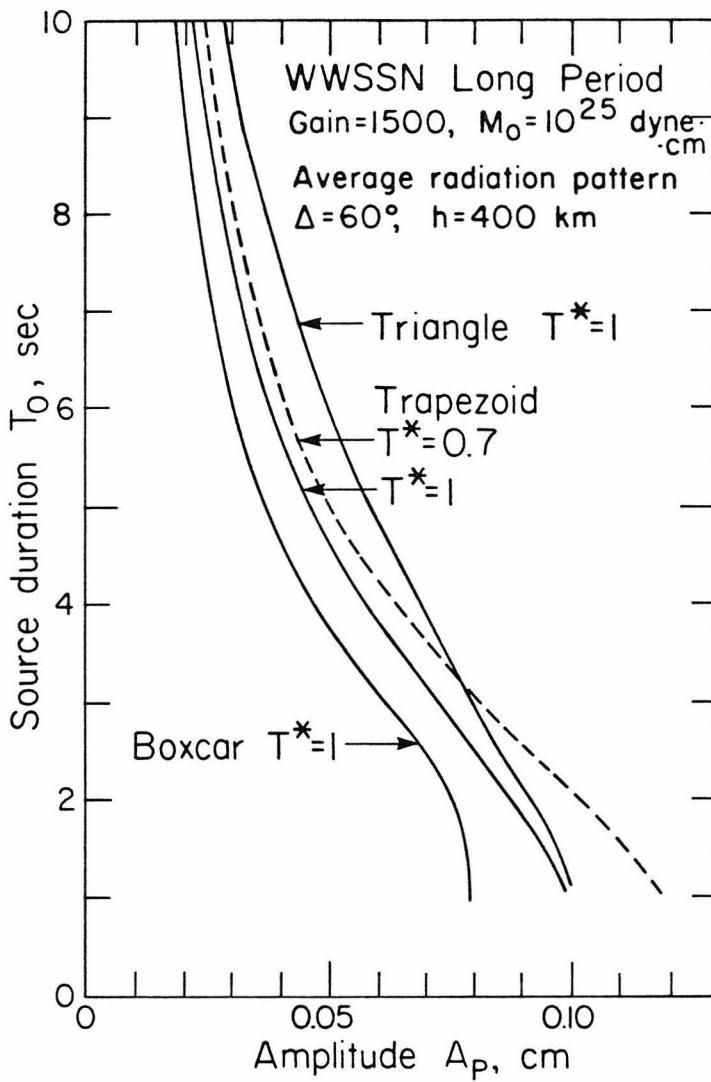


TABLE 2
ENERGIES CALCULATED FOR INTERMEDIATE AND DEEP FOCUS EVENTS STUDIED BY MEANS OF
SIMPLIFIED PROCEDURE

Origin Time					Region	Depth (km)	m_B	$\log M_0$ (dyne-cm)	T_0 (sec)	$\log E$ (erg)
M	D	Y	HMin	Sec						
03	11	68	0826	32.8	Tonga-Kermadec	112	6.2	25.9	4.6	20.7*
08	12	67	0939	44.3	Tonga-Kermadec	134	6.5	26.1	3.7	21.4*
12	08	65	1805	25.2	Tonga-Kermadec	156	6.0	25.4	3.9	20.0*
05	01	69	1905	24.5	Tonga-Kermadec	205	6.1	25.4	2.7	20.5*
03	18	65	1805	25.2	Tonga-Kermadec	219	6.0	25.6	4.7	20.1*
09	04	67	0351	58.9	Tonga-Kermadec	231	6.2	25.8	1.5	22.1*
09	26	68	1437	46.2	Tonga-Kermadec	251	6.0	25.3	2.0	20.6*
06	04	74	0414	13.8	Tonga-Kermadec	256	6.3	26.4	4.7	21.7*
02	22	75	2204	33.5	Tonga-Kermadec	333	6.6	26.5	4.6	21.9*
01	20	68	2121	31.6	Tonga-Kermadec	349	6.0	25.6	1.3	21.8*
07	21	73	0419	13.7	Tonga-Kermadec	373	6.1	25.8	2.8	21.1*
05	27	70	1205	08.3	Bonin Is.	406	6.6	27.0	5.9	22.4
11	18	65	2000	19.5	Tonga-Kermadec	424	6.2	25.6	1.75	21.1*
11	29	74	2205	23.5	Japan	429	6.5	26.6	5.1	21.6
02	03	76	1227	30.1	Tonga-Kermadec	477	6.0	25.8	2.9	20.7*
03	23	74	1428	33.0	Tonga-Kermadec	504	6.3	26.6	4.95	21.6
01	29	71	2158	03.2	Japan	515	6.6	26.8	4.45	22.2
12	28	73	0531	03.8	Tonga-Kermadec	517	6.5	26.2	2.7	21.5
10	25	73	1408	58.5	S. America	517	6.3	25.9	2.2	21.3
10	07	68	1920	20.8	Japan	518	6.7	27.3	13.0	23.4
01	28	66	0436	45.3	Tonga-Kermadec	545	5.8	25.3	1.75	20.3*
01	24	69	0233	03.4	Tonga-Kermadec	587	6.7	26.1	0.75	23.1
06	28	70	1109	51.3	Tonga-Kermadec	587	6.1	25.7	2.35	20.9
07	21	66	1830	15.3	Tonga-Kermadec	590	5.8	25.8	1.8	21.3*
02	15	67	1611	11.8	S. America	598	6.4	26.3	4.1	21.3
10	09	67	1721		Tonga-Kermadec	605	6.8	27.0	4.9	22.4
03	24	67	0900	20.0	Java	601	6.3	26.1	4.1	20.9
03	17	66	1550	33.1	Tonga-Kermadec	630	6.2	26.5	4.0	21.6*
10	01	72	2349		Philippines	632	5.8	25.0	0.7	21.0
02	10	69	2258	03.3	Tonga-Kermadec	635	6.4	25.6	5.2	21.7
12	09	65	1312	55.3	Tonga-Kermadec	649	5.7	25.7	1.8	21.2*

* Events studied by Chung and Kanamori (1980).

estimate is probably good to an order of magnitude or so. Energies calculated for deep and intermediate events studied by this method, including the events of Chung and Kanamori (1980), are listed in Table 2.

4. Comparison with Static Energy Estimates

We now examine the results of the energy calculations in the framework of an important independent method of estimating energy, based on elastostatic considerations. Consider a simple model of an earthquake where σ_0 , σ_1 , and σ_f are initial, final, and dynamic frictional stresses on the fault. We may write (Savage and Wood, 1971)

$$W = \left\{ \frac{\sigma_0 + \sigma_1}{2} - \sigma_f \right\} D S \quad (6)$$

where W is the difference between the strain energy drop and the frictional energy, D is the average dislocation, and S is the slip area. By using the stress drop $\Delta\sigma = \sigma_0 - \sigma_1$ and the seismic moment $M_0 = \mu DS$, we can rewrite (6) as

$$W = \left\{ \frac{\Delta\sigma}{2\mu} + \frac{(\sigma_1 - \sigma_f)}{\mu} \right\} M_0 \quad (7)$$

Orowan (1960) proposed a physically very reasonable model of a fault whereby motion stops when the accelerating stress decreases to a value equal to some average dynamic frictional stress, i.e. $\sigma_1 = \sigma_f$. There is thus no overshoot arising from, say, the inertia of the moving fault blocks. In Orowan's model eq. (6), which is the strain energy drop less the frictional energy represents the energy radiated as seismic waves. If Orowan's condition is satisfied, then clearly the second term in (7) vanishes, and we have simply

$$W = \frac{\Delta\sigma M_0}{2\mu} \quad (8)$$

Kanamori (1977) used this relationship to estimate the energy released in great shallow earthquakes. With $\Delta\sigma \approx 20$ to 60 bars (2 to 6×10^7 dyne/cm²), and $\mu \approx 3$ to 6×10^{11} dyne/cm²,

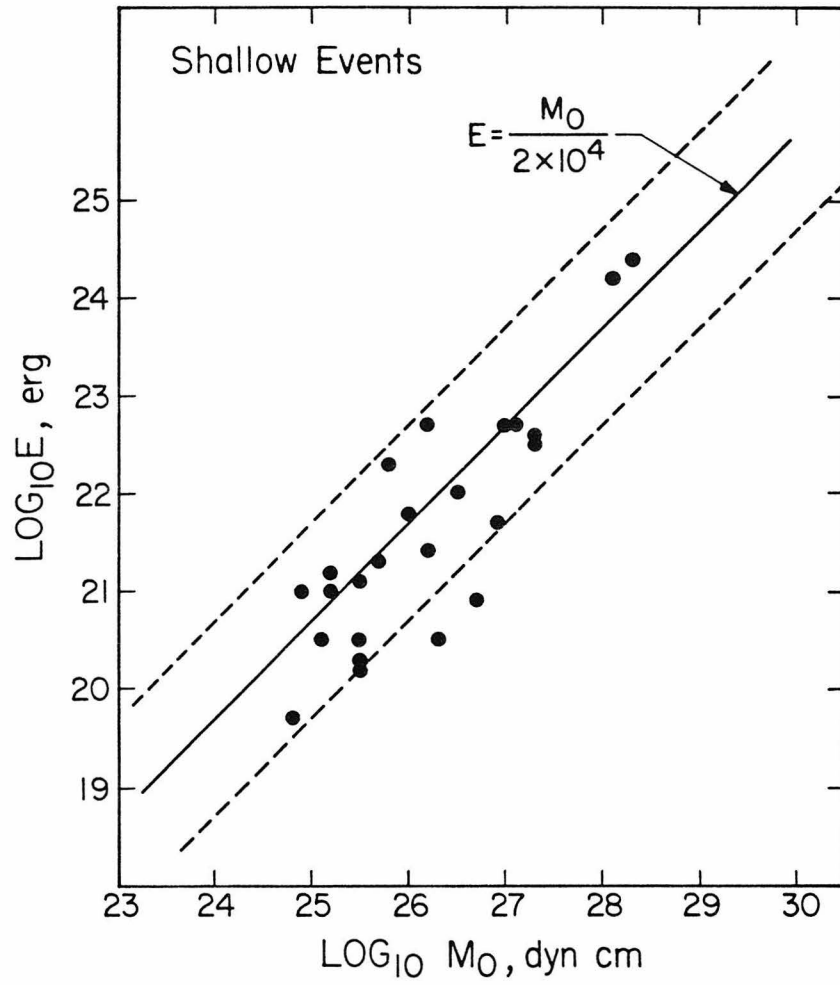
$$W_0 \approx (5 \times 10^{-5}) M_0 \quad (9)$$

where we have now adopted the subscript 0 to indicate that this is a static or essentially zero frequency estimate of energy, as opposed to the higher frequency estimates made from (3).

Fig. 5 shows a plot of energy vs. moment for the shallow events of Table 1. The line shows the energy according to (9), with parallel lines bounding an order of magnitude up or down. There is considerable scatter. Some of this scatter must be due to the errors in T_0 and M_0 . Another contributing factor, however, probably arises from the fact that (9) is derived assuming $\Delta\sigma$ is 20-60 bars, and for many events this obviously need not be true. The dynamic estimates by their very nature take into account the details of rupture for the individual events. For this reason, they can deviate considerably from the line $E = (5 \times 10^{-5}) M_0$, perhaps even more than would a crude estimate from M_s . An interesting case is that of the two Gibbs fracture zone events (Kanamori and Stewart, 1976). They lie considerably below the line. As they are known to have been especially slow events, it should not be surprising that (9) might overestimate their energy.

All in all, considering the simplicity of the model leading to the static estimate, the errors in the dynamic estimate arising from errors in M_0 and T_0 , and the independence of the two methods, the agreement between the static and dynamic energy

Figure 5. Energy calculated for some modelled shallow events (Table 1) plotted against seismic moment. The line shown corresponds to the approximate relation $E = (5 \times 10^{-5}) M_0$ (which assumes a stress drop of 20-60 bars) obtained by Kanamori (1977). The parallel lines bound an order of magnitude up or down. Considering that this simple elastostatic calculation is completely independent of the dynamic calculations made here from body waves, the agreement is encouraging (see Section 4).



determinations for shallow earthquakes is rather good. We may examine this rough equality more closely by considering some simple static stress drop scaling relations. In the case of constant stress drop, we may write the moment in terms of stress drop and fault area as (Kanamori and Anderson, 1975)

$$M_0 = \Delta\sigma S^{3/2} \quad (10)$$

Using an approximate expression $T_0 \approx \frac{\sqrt{S}}{\beta}$ for the time function duration, we obtain

$$M_0 \approx \Delta\sigma\beta^3 T_0^3 \quad (11)$$

Substituting this into (3), and using (5), we have

$$E \approx \left\{ \frac{2K}{x(1-x)^2} \right\} \Delta\sigma\beta^3 M_0 \quad (12)$$

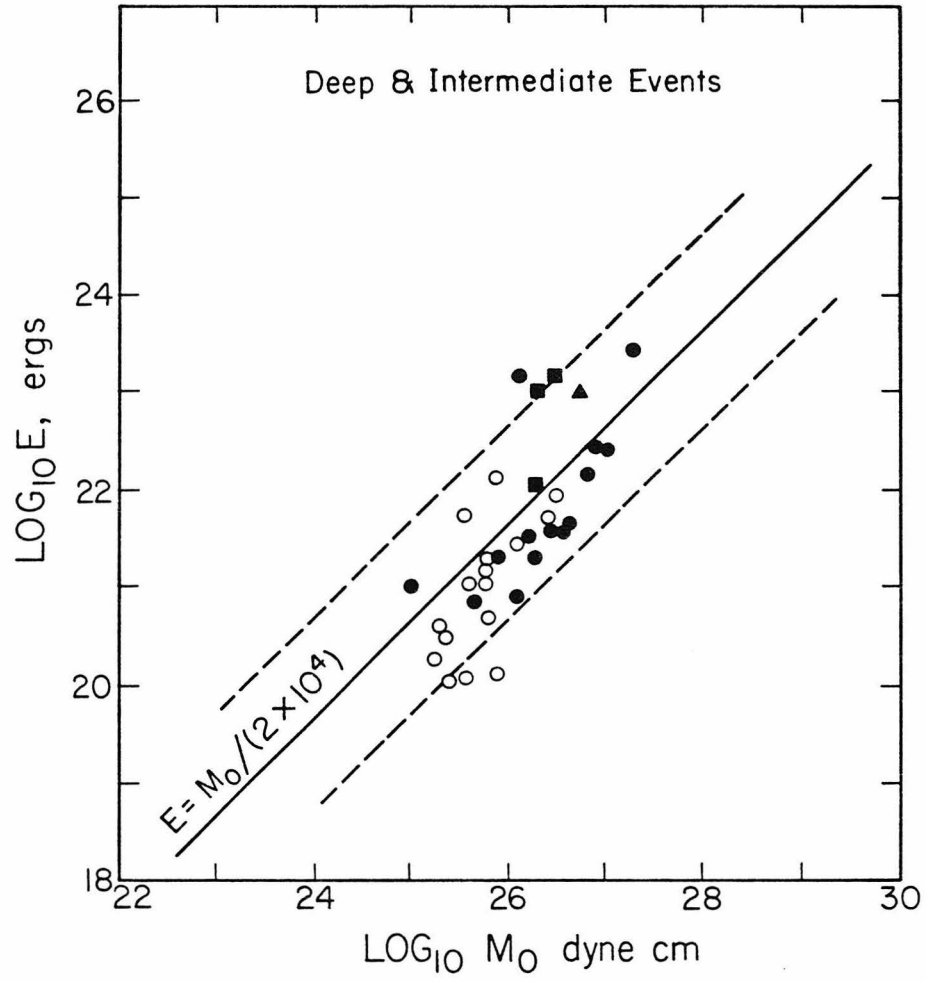
Using $x = 0.2$, $\beta = 3.4$ km/sec, $\Delta\sigma = 30$ bars, and $\rho = 2.8$ g/cc in K gives us

$$E \approx (4.6 \times 10^{-5}) M_0 \quad (13)$$

which is very close to (9).

Fig. 6 shows energy versus moment for the deep and intermediate events listed in Table 2. The lines are the same as the ones in Fig. 5. On the whole, the deep events tend to plot below the line corresponding to $W_0 = (5 \times 10^{-5}) M_0$. Of course, given that our energies are not likely to be accurate to better than an order of magnitude, this may not be significant. However, the effect is quite systematic, and contrary to what one might expect if one believed that deep events tend to have higher stress drops: the average stress drop determined by Chung and Kanamori (1980) for their deep and intermediate events is ≈ 500 bar. If $\mu \approx 6$ to 10×10^{11} dyne/cm²

Figure 6. Similar to fig. 5, but for deep and intermediate events. Circles are for events in Table 2; open circles in particular are for events also studied by Chung and Kanamori (1980), and closed ones are for the rest. Closed squares = Mikumo (1971). Closed triangle = Fukao (1970).



below 400 km, the relation $W \approx (5 \times 10^{-5})M_0$ would require $\Delta\sigma \approx 60$ to 100 bars, so if one believed the high stress drops of Chung and Kanamori (1980), one would expect at least the events they studied (we have not determined stress drop for the extra events we studied) to plot above the line.

The key to understanding this situation may lie in remembering that for (8) to hold, Orowan's condition must be met, and this need not be the case. If we assume that the condition is met, we may solve (8) for $\Delta\sigma$, and use values of moment and dynamic energy to obtain a value of stress drop which we may call 'Orowan stress drop'. This value should be equal to the actual stress drop if Orowan's condition is met; if not, it should be lower. If we calculate Orowan stress drops for the events of Chung and Kanamori (1980), we find that they are considerably lower (Fig. 7) than Chung and Kanamori's teleseismically calculated stress drops (using inferences of fault area from the source time functions). If we calculate the Orowan stress drops using energy determined from m_B (see Section 6) instead of our dynamic estimates from Section 2, the gap is even wider. The implication, then, is that either Orowan's condition is not met for these events, or the condition is met and the Chung-Kanamori stress drops are too high, by almost an order of magnitude. Since stress drop is one of the more model-dependent and poorly determined seismological quantities, this would not be too surprising.

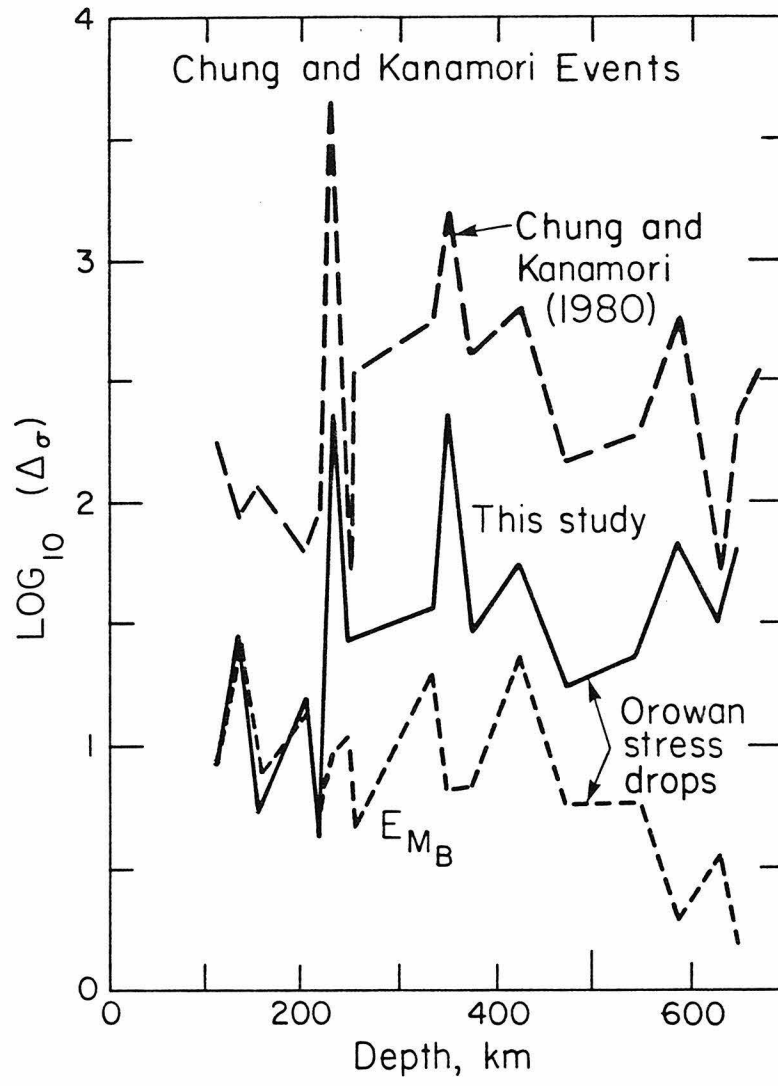
In any case, it is not difficult to see why a relationship of the form

$$E = qM_0 \tag{14}$$

can hold for deep and shallow events alike with q approximately given by 5×10^{-5} .

From (7) we see that

Figure 7. Upper dotted line = Stress drops obtained by Chung and Kanamori (1980) (using source dimensions inferred from far field time functions), plotted against depth. Lower dotted line = 'Orowan stress drops', calculated from equation (8) assuming Orowan's condition is met, and using energies obtained from m_B . Solid line = 'Orowan stress drops' calculated from equation (8) assuming Orowan's condition is met and using dynamic energies calculated in this study. The use of our energies, which are generally higher than those estimated from m_B , does not close the gap between the Orowan stress drops calculated from (8) and those obtained by Chung and Kanamori (1980). Either (1) our energies are systematically too low or (2) Chung and Kanamori's (1980) stress drops are too high or (3) Orowan's condition is not met for these deep and intermediate events.



$$q = \left\{ \frac{\Delta\sigma}{2\mu} + \frac{(\sigma_1 - \sigma_f)}{\mu} \right\} \quad (15)$$

In the case of shallow events, where Orowan's condition is likely to be met (Kanamori and Anderson, 1975), we merely have the reasonable condition, as stated before, that $\frac{\Delta\sigma}{2\mu} \approx 5 \times 10^{-5}$. For deep events, we can have a similar situation as for shallow events, or we can have a non-Orowan process with high stress drops in the first term of (15), and a negative second term.

5. Near Source Energy Studies and the Question of Frequency Content

The computations which we have carried out are based on earthquake displacement data viewed through a variety of distorting filters, such as attenuation and instrument. We address here the question of the validity of these results, given that by using a long period instrument we cannot hope to resolve displacement components of frequency greater than 1 to 2 Hz. Beyond the problem of the instrument, we must also consider the possibility that important high frequency energy is attenuated, either anelastically or through scattering, by propagation to teleseismic distances. One could make the argument that high frequencies observable only very close to the source could be responsible for a considerable portion of the total energy. We note here that we cannot simply quote the fact that teleseismic corner frequencies are relatively low for earthquakes of size similar to the ones examined here as evidence that high frequencies are unimportant. A teleseismic spectrum is not necessarily simply related to the true source spectrum at near field.

An important source of information with regard to these questions is to be found in near-source strong-motion records. By examining data obtained close (≤ 20 km.)

to the source using high frequency strong-motion instruments, we can assess the importance of the shorter period energy. From an accelerogram, one can easily obtain a velocity trace, and use that to compute the quantity

$$D(f) = \int_0^f \tilde{u}^2 df' \quad (16)$$

which is proportional to the integral of the energy spectrum to a given frequency; $\tilde{u}(f)$ is the Fourier transform of the velocity trace. The seismic wave energy obtained from a trace at a given station is given approximately by

$$E \approx 4\pi\rho\beta r^2 R(\theta, \varphi) \cdot 2D(\infty) \quad (17)$$

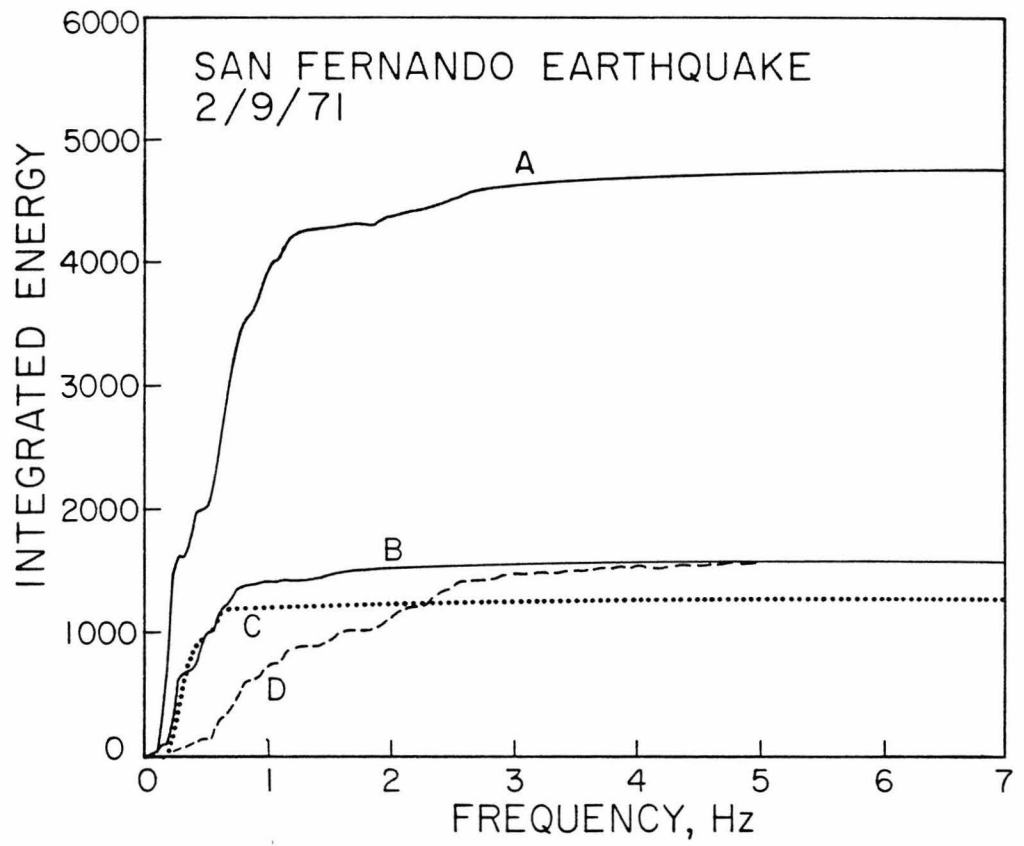
We note that (16) is not the integral of the source energy density per se, but of the trace energy density. We are thus not looking directly at the true source spectrum. There is some contamination from reflection, refraction, scattering, etc. However, if the high frequency contribution in traces obtained close to the source is not important, i.e. if D at 2 hz appears to have already reached a final value, then we can probably not be too worried that we are looking at a trace spectrum rather than a true source spectrum. That is to say, if large amounts of high frequency energy were present, we might have to be concerned that the contaminating processes we have mentioned might be the origin of it, but if such energy is not there it does not matter as much to our argument that such processes might be present. The contaminating processes we have mentioned would probably, if anything, enhance the high frequency content of the trace relative to the source, which by itself would argue that if high frequency energy is negligible in the trace, it must also be negligible in the source. Of course, this ignores attenuation; if we are close enough to the source,

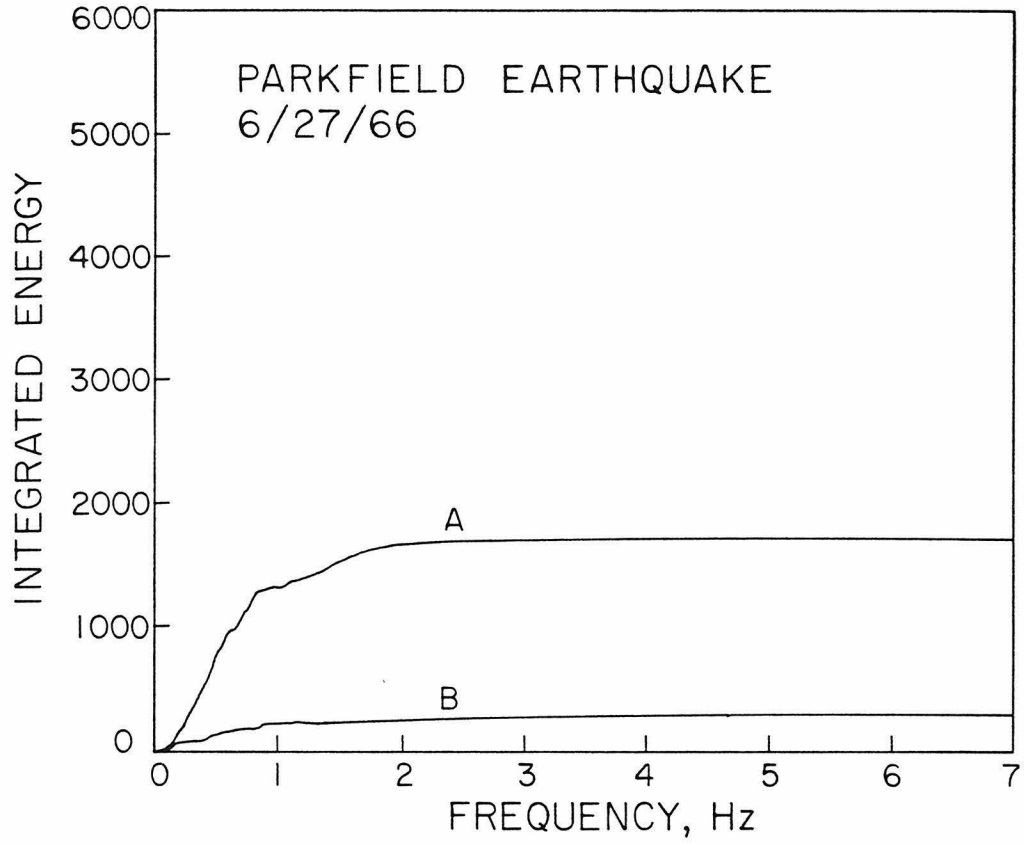
however, attenuation should not be important. We discuss this more fully below.

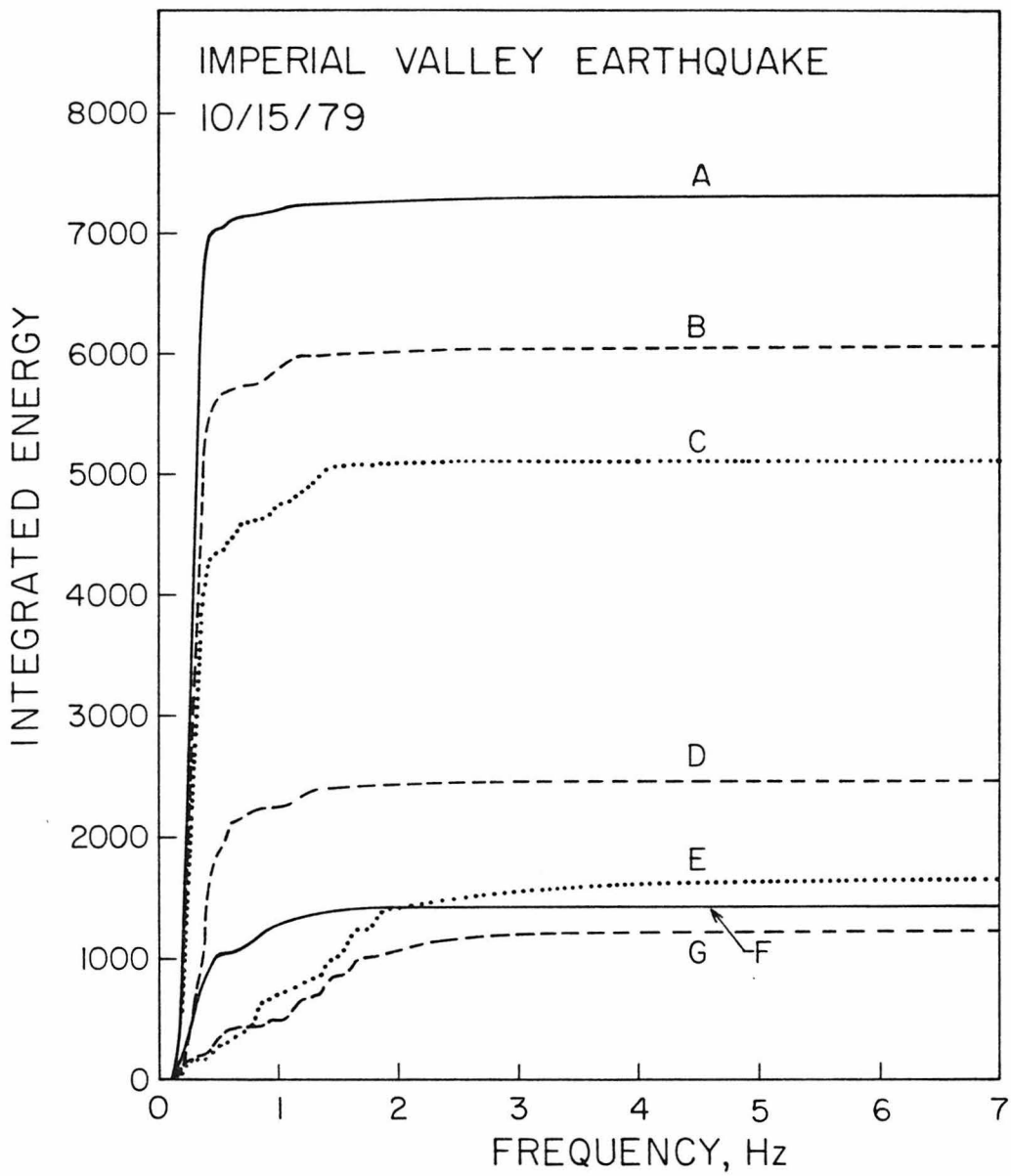
Figs. 8 a,b,c,d show $D(f)$ for several records from the 1971 San Fernando, 1966 Parkfield, 1979 Imperial Valley, and 1977 Bucharest earthquakes. Table 3 shows values of $D(10)$ and the ratios $\frac{D(1)}{D(10)}$, $\frac{D(2)}{D(10)}$ and $\frac{D(4)}{D(10)}$, where the argument is in Hz, for these and other records. We use $D(10)$ to be essentially representative of $D(\infty)$. This certainly seems justified on inspection of the figures (in addition, sampling intervals for the digital data are often such that folding frequencies themselves are not much higher than 10 Hz.). Many of the records were obtained extremely close to the source (e.g. Pacoima, less than 1km. from the nearest point on the Sierra Madre Fault (Heaton, 1982)), and in no case is any appreciable energy observable above 4 Hz. Such energy may exist in the very immediate vicinity of the source, but in that case we may raise semantic questions about which energy to consider "radiated" and which not. If this hypothetical high frequency energy is attenuated within 1 km. of the source, we cannot consider it to be radiated energy. This reasoning applies also to energy at 1 to 2 Hz. If there is important energy in this band which we cannot see even at 1 km or so from the fault (actually, with a Q of about 300 this is unlikely), then we can hardly worry about it for the purposes of computing *radiated* seismic energy.

What we have set out to do in examining the strong-motion records is to see if there was a large proportion of energy there which we were missing at teleseismic distances. It is clear from the records presented here that even very close to the source, by far the largest proportion of the energy is contained in frequencies below 2 Hz. In many cases, over 90 per cent of the energy is even below 1 Hz. What these results suggest is that no appreciable error (certainly not one of an order of magnitude) is incurred by making an energy determination at far field using a long period

Figure 8. The integral $D(f)$ (see section 5) of the spectral energy density versus frequency from strong motion velocity (cm/sec) traces for the San Fernando, Parkfield, Imperial Valley, and Bucharest earthquakes. Different curves for each earthquake correspond to different records, (see Table 3) The curves for the San Fernando, Parkfield, and Imperial Valley earthquakes suggest that, even close to the source, by far most of the energy radiated is below 1 to 2 Hz. in frequency. Far field energy determinations using long period instruments thus may not be in gross error, despite their bandlimited nature.







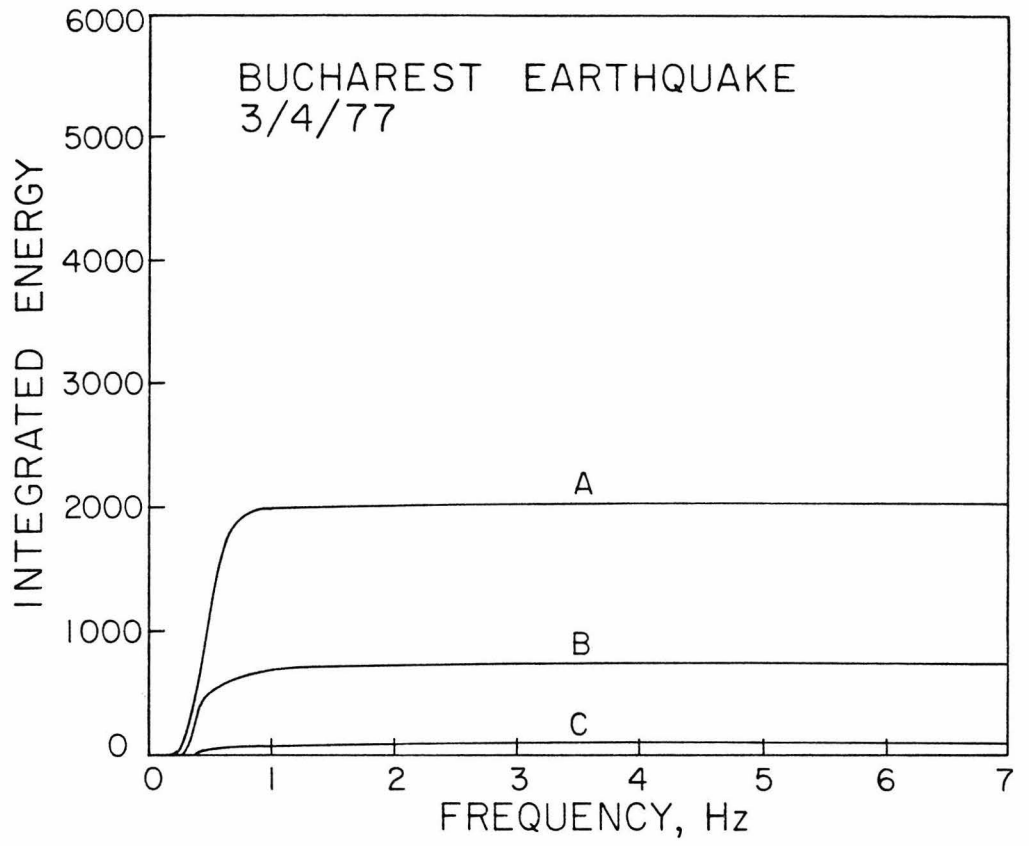


TABLE 3
ENERGY SPECTRAL DENSITY FROM STRONG-MOTION RECORDS (SEE FIGURE 8)

Earthquake	Station	Ref.*	Comp.	Δf (km)	D (10)†	D (1) + D (10)	D (2) + D (10)	D (4) + D (10)	Figure and Curve
San Fernando	Pacoima	C041	S16E	~0	4747.3	0.83	0.92	0.99	8a, A
San Fernando	Pacoima	C041	S74W	~0	1590.8	0.47	0.71	0.98	8a, D
San Fernando	Holiday Inn, Orion	C048	N00W	14.5	1575.6	0.89	0.97	1.0	8a, B
San Fernando	Holiday Inn, Orion	C048	S90W	14.5	1425.0	0.95	0.98	1.0	
San Fernando	15250 Ventura Blvd.	H115	N11E	21.0	1269.2	0.95	0.97	0.99	8a, C
San Fernando	15250 Ventura Blvd.	H115	N79W	21.0	861.6	0.95	0.96	1.0	
Parkfield	Cholame, Array 2	B033	N65E	22.8, 0.08	1709.1	0.77	0.97	1.0	8b, A
Parkfield	Cholame, Array 5	B034	N85E	23.5, 5.5	311.1	0.72	0.81	0.99	8b, B
Parkfield	Cholame, Array 5	B034	N05W	23.5, 5.5	155.4	0.47	0.72	0.99	
Parkfield	Cholame, Array 12	B036	N40W	27.7, 15.4	122.2	0.96	0.99	1.0	
Imperial Valley	El Centro, Array 6	IIZ004	S50W	24.5, 1.2	7307.5	0.98	0.99	1.0	8c, A
Imperial Valley	El Centro, Array 5	IIZ007	S50W	21.8, 4.0	6056.4	0.97	0.99	1.0	8c, B
Imperial Valley	El Centro, Array 7	IIZ003	S50W	24.2, 0.8	5102.0	0.92	1.0	1.0	8c, C
Imperial Valley	El Centro, Array 6	IIZ004	S40E	24.5, 1.2	2470.8	0.91	0.99	1.0	8c, D
Imperial Valley	El Centro, Array 8	IIZ006	S50W	23.9, 3.8	2056.1	0.94	0.98	0.99	
Imperial Valley	El Centro, Array 5	IIZ007	S40E	21.8, 4.0	2022.0	0.91	0.97	0.99	
Imperial Valley	El Centro, Bonds Corner	IIZ005	S50W	3.7	1641.4	0.43	0.86	0.98	8c, E
Imperial Valley	El Centro, Array 8	IIZ006	S40E	23.9, 3.8	1499.9	0.91	0.97	0.99	
Imperial Valley	El Centro, Array 7	IIZ003	S40E	24.2, 0.8	1442.9	0.89	0.99	1.0	8c, F
Imperial Valley	El Centro, Bonds Corner	IIZ005	S40E	3.7	1230.6	0.41	0.86	0.98	8c, G
Bucharest	Bld. Res. Inst.		S-N	190	2029.2	0.98	1.0	1.0	8d, A
Bucharest	Bld. Res. Inst.		E-W	190	743.0	0.88	0.99	1.0	8d, B
Bucharest	Bld. Res. Inst.		U-D	190	88.9	0.84	0.96	0.99	8d, C

* Reference number of accelerogram in CalTech Earthquake Engineering Research Laboratory Reports.

† Where two distances are given, the first is that to the epicenter, and the second is that to the nearest point of the fault.

‡ $D(f) = \int_{\rho} |\dot{u} \sim (f')|^2 df'$, where f is frequency in Hertz. D (10) is taken to represent $D(\infty)$. $\dot{u}^N(f)$ is the Fourier transform of $\dot{u}(t)$, and $\dot{u}(t)$ is in centimeters/seconds.

instrument.

Strictly, this only applies to shallow events. Certainly we have no instances of strong motion recordings within 1 km. of the source of a deep focus event, so we cannot directly address the problem of whether there is important energy within a few kilometers of the source which never propagates out to teleseismic distances. We can, however, make some statement about whether or not a long period instrument is broad enough in its frequency response to retrieve adequately the energy that does manage to propagate to the teleseismic range. The curves of Fig. 8(d) for the 100 km. depth Bucharest earthquake in fact show very little energy outside the passband of a long period WWSSN instrument (≈ 60 sec. to 1 to 2 Hz.), and this is encouraging.

6. Energy and Magnitude

In this section we compare our dynamic energy estimates with the energies one would obtain using the Gutenberg-Richter relations. For the shallow events of Table 1, the comparison is relatively straightforward; we may use M_s as a measure of magnitude. Fig. 9(a) shows $\log_{10}E$ in ergs versus M_s for these events. Our estimates seem to be consistently lower than the Gutenberg-Richter line. A best fit line through our points would have slope $1.81(\pm 0.2)$ and intercept $9.06(\pm 1.38)$, compared to 1.5 and 11.8 respectively for Gutenberg-Richter.

The comparison for the deep and intermediate events of Table 2 is more ambiguous. These events generally did not excite appreciable surface waves, so we must use a body wave magnitude. Gutenberg and Richter (1956a,b) derived the relation $\log_{10}E = 2.4m_B + 5.8$. The magnitude m_B is not the same as the m_b now in common use. The latter is a short period (≈ 1 sec) body wave magnitude, while the former is

a longer period one. We have used long period WWSSN records to determine an m_B more compatible than m_b with Gutenberg and Richter's definition.

One difficulty which arises is that when the P wave consists essentially of a single pulse, as is the general case with the simple events we have studied here, the measurement of the dominant period in the wave group becomes ambiguous. We have set the period to twice the pulse width. Another difficulty is that the WWSSN instruments whose records we have employed are peaked at 15 seconds, while Gutenberg and Richter used mechanical instruments with a different period response (flat rather than decaying); thus, one must be careful to use the correct gain for the WWSSN instrument when one is looking at a period different from the peak period. The waveforms from the two instruments differ; we have conducted some numerical experiments to ascertain that no drastic errors occur because of this.

A plot of $\log E$ versus m_B for the intermediate and deep events of table 2 is shown in Fig 9(b). In contrast to the case of the shallow events, the bias here is above the Gutenberg-Richter line. The least squares line through our plotted points has slope $1.97(\pm 0.34)$ and intercept $9.07(\pm 2.13)$. We note that if one allows an error of 0.5 units in m_B , taking into account all the factors mentioned above, as well as an error of an order of magnitude in the energy, the discrepancy is understandable.

Although it is interesting that the shallow events generally plot below the $\log_{10}E - M_s$ line, while the deep and intermediate ones plot above the $\log_{10}E - m_B$ line, we cannot really make meaningful comments about this given the empirical nature of the Gutenberg-Richter relationships.

Figure 9. (a) Common logarithm of the dynamic energy release in ergs plotted against M_s for shallow events of Table 1. The line represents the Gutenberg-Richter relationship.

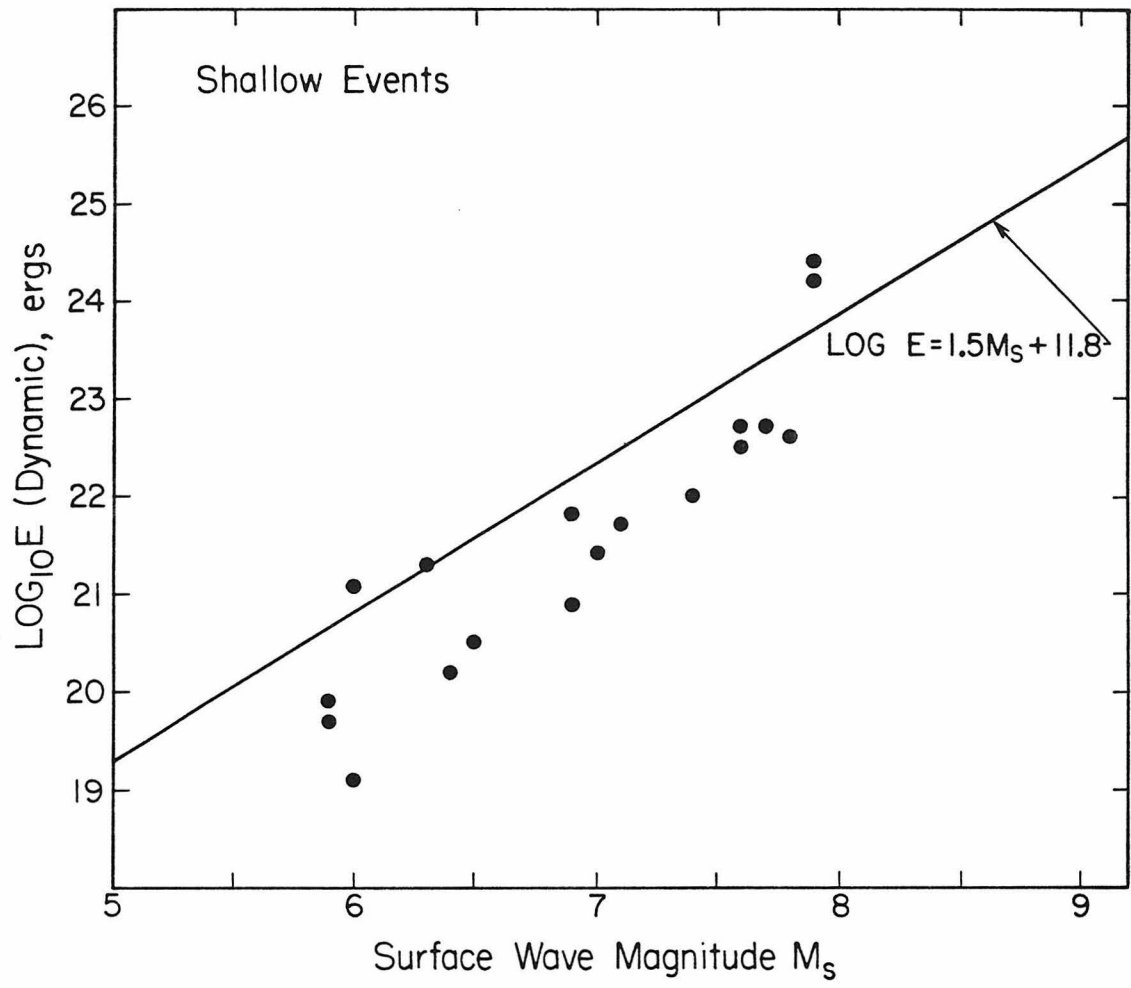
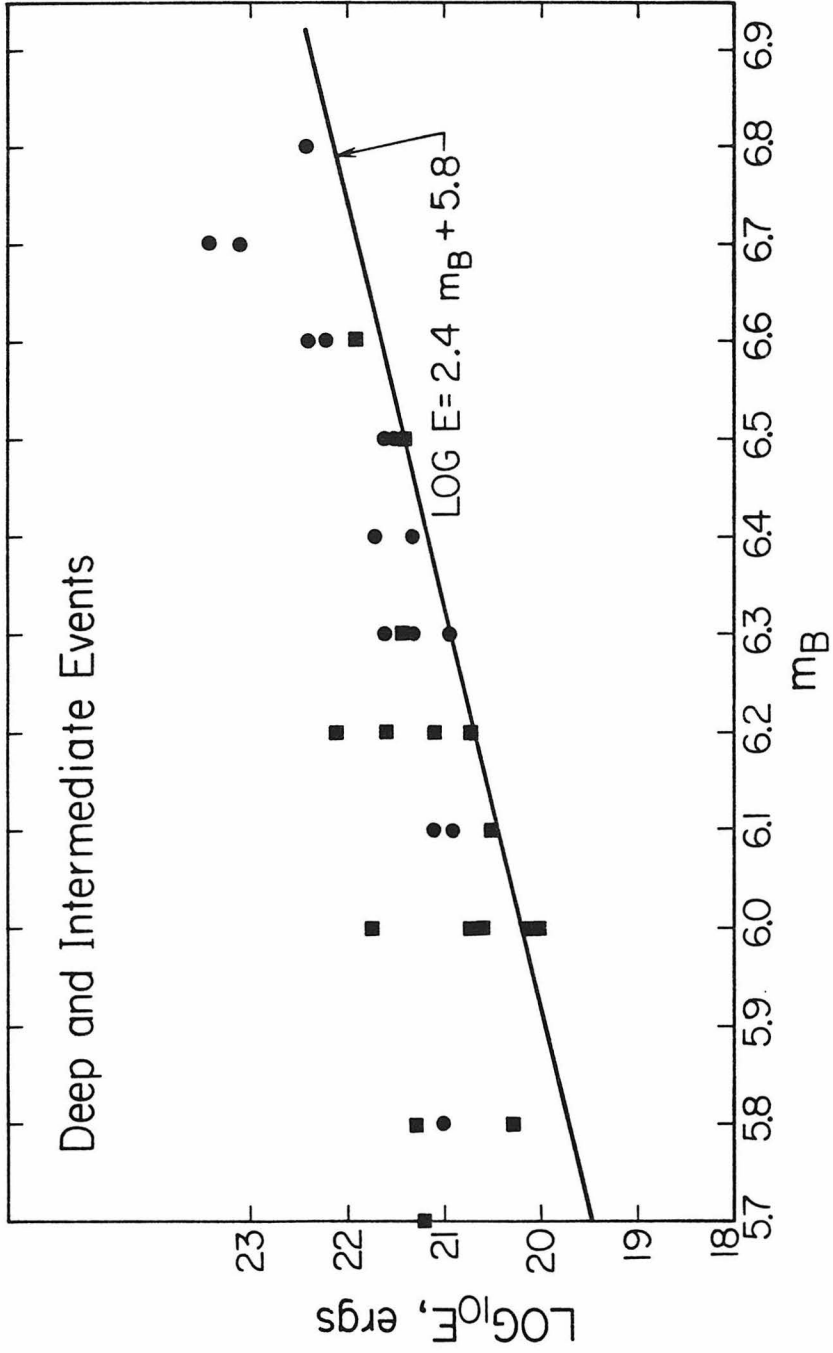


Figure 9. (b) Common logarithm of the dynamic energy release in ergs plotted against m_B (long period body wave magnitude-- see section 6) for the deep and intermediate events of Table 2. Squares represent events also studied by Chung and Kanamori (1980). The line represents the Gutenberg-Richter relationship.



7. Conclusions

(1) The important parameters in the calculation of seismic energy release from body waves are seismic moment M_0 and far field displacement time function duration T_0 , with $E \propto \frac{M_0^2}{T_0^3}$. The important shape effect for the usual trapezoidal time function comes from its ratio x of rise time to total duration. As long as $x \geq 0.1$, which is generally supported by the data, the effect is not important.

(2) Our near source studies suggest that most of the important radiated energy is below 1 to 2 Hz. in frequency, and hence that far field energy determinations using long period WWSSN instruments are not in gross error despite their bandlimited nature.

(3) Dynamic energy estimates for shallow earthquakes made from body waves are in reasonable agreement with expectations from simple static elastic relaxation models, which suggest that $E \approx 5 \times 10^{-5} M_0$ for shallow events when a stress drop of 20-60 bars is assumed.

(4) Deep events, despite their possibly different seismological character, yield dynamic energies which are also compatible with a static energy prediction similar to that for shallow events. Seismic moment M_0 , and hence a moment based magnitude scale, may reliably be used for shallow and deep events alike, as a reasonably accurate measure of energy release.

References

- Bath, M. (1966). Earthquake Energy and Magnitude, in Physics and Chemistry of the Earth vol. 7 (eds. L.H. Ahrens, F. Press, S.K. Runcorn, and H.C. Urey), Pergamon Press, N. Y., 117-165.
- Bollinger, G.A. (1968). Determination of Earthquake Fault Parameters from Long Period P Waves, J. Geophys. Res., 73, 785-807.
- Bracewell, R.N. (1978). The Fourier Transform and Its Applications, 2nded., McGraw Hill, N. Y.
- Burdick, L.J. (1977). Broad Band Seismic Studies of Body Waves, PhD Thesis, California Institute of Technology.
- Burdick, L. J., and G. R. Mellman (1976). Inversion of Body Waves of the Borrego Mountain Earthquake to the Source Mechanism, Bull. Seismol. Soc. Am., 66, 1485-1499.
- Chael, E. P., and G. S. Stewart (1982). Recent Large Earthquakes Along the Middle America Trench and Their Implications for the Subduction Process, J. Geophys. Res., 87, 329-338.
- Chung, W. Y., and H. Kanamori (1980). Variation of Seismic Source Parameters and Stress Drops Within a Descending Slab and Its Implications in Plate Mechanics, Phys. Earth and Plan. Interiors, 23, 134-159.
- Cipar, J. (1979). Source Processes of the Haicheng, China Earthquake from Observations of P and S Waves, Bull. Seismol. Soc. Am., 69, 1903-1916.
- Cipar, J. (1980). Teleseismic Observations of the 1976 Friuli, Italy Earthquake

- Sequence, *Bull. Seismol. Soc. Am.*, 70, 963-1983.
- Cipar, J. (1981). Broadband Time Domain Modeling of Earthquakes from Friuli, Italy, *Bull. Seis. Soc. Am.*, 71, 1215-1231.
- Ebel, J.E., L.J. Burdick and G. Stewart (1978). The Source Mechanism of the August 7, 1966 El Golfo Earthquake, *Bull. Seismol. Soc. Am.*, 68, 1281-1292.
- Fukao, Y. (1970). Focal Process of a Deep Focus Earthquake as Deduced from Long Period P and S Waves, *Bull. Earthquake Res. Inst.*, 48, 707-727.
- Geller, R.J. (1976). Scaling Relations for Earthquake Source Parameters and Magnitudes, *Bull. Seismol. Soc. Am.*, 66, 1501-1523.
- Gutenberg, B., and C. F. Richter (1942) Earthquake Magnitude, Intensity, Energy, and Acceleration, *Bull. Seismol. Soc. Am.*, 32, 163-191.
- Gutenberg, B., and C. F. Richter (1956a). Earthquake Magnitude, Intensity, Energy, and Acceleration (Second Paper) *Bull. Seismol. Soc. Am.*, 46, 105-145.
- Gutenberg, B., and C. F. Richter (1956b) Magnitude and Energy of Earthquakes, *Ann. di Geofis.*, 9, 1-15.
- Hartzell, S. (1980). Faulting Process of the May 17 1976 Gazli, USSR Earthquake, *Bull. Seismol. Soc. Am.*, 70, 1715-1736.
- Haskell, N.A. (1964). Total Energy and Energy Spectral Density of Elastic Wave Radiation from Propagating Faults, *Bull. Seismol. Soc. Am.*, 54, 1811-1841.
- Heaton, T. H. (1982). The San Fernando Earthquake: A Double Event? *Bull. Seismol. Soc. Am.*, 72, 2037-2060
- Kanamori, H. (1972). Determination of Effective Tectonic Stress Associated with Earthquake Faulting. *Phys. Earth and Plan. Int.*, 5, 426-434.
- Kanamori, H. (1977). The Energy Release in Great Earthquakes, *J. Geophys. Res.*, 82, 2981-2987.

- Kanamori, H., and D. L. Anderson (1975). Theoretical Basis of Some Empirical Relations in Seismology, *Bull. Seismol. Soc. Am.*, 65, 1073-1095.
- Kanamori, H., and G. S. Stewart (1976). Mode of the Strain Release Along the Gibbs Fracture Zone, Mid-Atlantic Ridge, *Phys. Earth Plan. Int.*, 11, 312-332.
- Knopoff, L. (1958). Energy Release in Earthquakes, *Geophys. J. Roy. Astr. Soc.*, 1, 44-52.
- Langston, C.A. (1976). A Body Wave Inversion of the Koyna, India Earthquake of Dec. 10 1967 and Some Implications for Body Wave Focal Mechanisms, *J. Geophys. Res.*, 81, 2517-2529.
- Langston, C.A. and Blum, D.E. (1977). The April 29 1965 Puget Sound Earthquake and the Crustal and Upper Mantle Structure of Western Washington, *Bull. Seismol. Soc. Am.*, 67, 693-711.
- Langston, C.A. and Butler, R. (1976). Focal Mechanism of the August 1 1975 Oroville Earthquake, *Bull. Seismol. Soc. Am.*, 66, 1111-1120.
- Langston, C. A., and D. V. Helmberger (1975). A Procedure for Modeling Shallow Dislocation Sources, *Geophys. J. Roy. Astr. Soc.*, 42, 117-130.
- Lay, T., and H. Kanamori (1980). Earthquake Doublets in the Solomon Islands, *Phys. Earth and Plan. Int.*, 21, 283-304.
- Liu, H. L., and H. Kanamori (1980). Determination of Source Parameters of Mid-Plate Earthquakes from the Waveforms of Body Waves, *Bull. Seismol. Soc. Am.*, 70, 1989-2004.
- Mikumo, T. (1971). Source Process of Deep and Intermediate Earthquakes as Inferred from Long Period P and S Waveforms: 1. Intermediate Depth Earthquakes in S.W. Pacific Region, *J. Phys. Earth* 19, 1-19.
- Orowan, E. (1960). Mechanism of Seismic Faulting, *Geol. Soc. Am. Mem.* 79, 323-345.

- Rudnicki, J. W., and L. B. Freund (1981). On Energy Radiation from Seismic Sources, Bull. Seis. Soc. Am., 71, 583-595.
- Savage, J. C. and M. D. Wood (1971). The Relation Between Apparent Stress and Stress Drop, Bull. Seismol. Soc. Am., 61, 1381-1388.
- Stewart, G. S., and D. V. Helmberger (1981). The Bermuda Earthquake of March 24, 1978: A Significant Oceanic Intraplate Event, J. Geophys. Res., 86, 7027-7036.
- Stewart, G. S., E. P. Chael, and K. C. McNally (1981). The November 29, 1978 Oaxaca Earthquake: A Large Simple Event, J. Geophys. Res., 86, 5053-5060.
- Yoshiyama, R. (1963). Note on Earthquake Energy, Bull. Earthquake Res. Inst., 41, 687-697.

**PART II: SUBDUCTION ZONE SEISMICITY AND STRESS IN
SLABS**

Abstract

The pattern of seismicity as a function of depth in the world, and the orientation of stress axes of deep and intermediate earthquakes, are explained using viscous fluid models of subducting slabs, with a barrier in the mantle at 670 km. 670 km is the depth of a seismic discontinuity, and also the depth below which earthquakes do not occur. The barrier in the models can be a viscosity increase of an order of magnitude or more, or a chemical discontinuity where vertical velocity is zero. Log N versus depth, where N is the number of earthquakes, shows (1) a linear decrease to about 250-300 km depth, (2) a minimum near that depth, and (3) an increase thereafter. Stress magnitude in a subducting slab versus depth, for a wide variety of models, shows the same pattern. Since there is some experimental evidence that N is proportional to $e^{k\sigma}$, where k is a constant and σ is the stress magnitude, the agreement is encouraging. In addition, the models predict down-dip compression in the slab at depths below 400 km. This has been observed in earlier studies of earthquake stress axes, and we have confirmed it via a survey of events occurring since 1977 which have been analysed by moment tensor inversion. At intermediate depths, the models predict an approximate but not precise state of down-dip tension when the slab is dipping. The observations do not show an unambiguous state of down-dip tension at intermediate depths, but in the majority of regions the state of stress is decidedly closer to down-dip tension than it is to down-dip compression. Chemical discontinuities above 670 km, or phase transitions with an elevation of the boundary in the slab, predict, when incorporated into the models, stress peaks which are not

mirrored in the profile of seismicity versus depth. Models with an asthenosphere and mesosphere of appropriate viscosity can not only explain the state of stress observed in double Benioff zones, but also yield stress magnitude profiles consistent with observed seismicity. Models where a nonlinear rheology is used are qualitatively consistent with the linear models.

1. Introduction

In this study we use simple models of subducting slabs to explain observations of the distribution of earthquakes versus depth, and observations of the orientation of stress axes of deep (> 300 km) and intermediate (70 to 300 km) earthquakes.

The distribution of earthquakes with depth has been discussed by many investigators (e.g., Gutenberg and Richter, 1954; Sykes, 1966; Isacks et al, 1968), who have variously noted the presence of seismicity minima near 250 km, and the existence of deep peaks in seismicity. Richter (1979) has recently explored the possibility of a barrier to mantle flow at the 670 km seismic discontinuity (e.g., Whitcomb and Anderson, 1968) being responsible for the large increase in seismicity above this depth in the Tonga-Kermadec region. He also argues that such a barrier may explain the tendency toward down-dip compression at depth for earthquakes in this region (previously noted by Isacks and Molnar, 1969, 1971).

We proceed here in the same spirit as Richter, extending the observational base to the whole world, and exploring a wide range of models of subducting slabs. In section 2 we present observations of seismicity versus depth, using the large amount of catalog data that has become available since the studies of Sykes (1966) and Isacks et al (1968). We also analyse the orientations of stress axes of earthquakes studied using the new methods of moment tensor inversion (Kanamori and Given, 1981; Dziewonski et al, 1981; Appendix A). In Section 3 we present calculations of stress in subducting slabs.

2. Observations

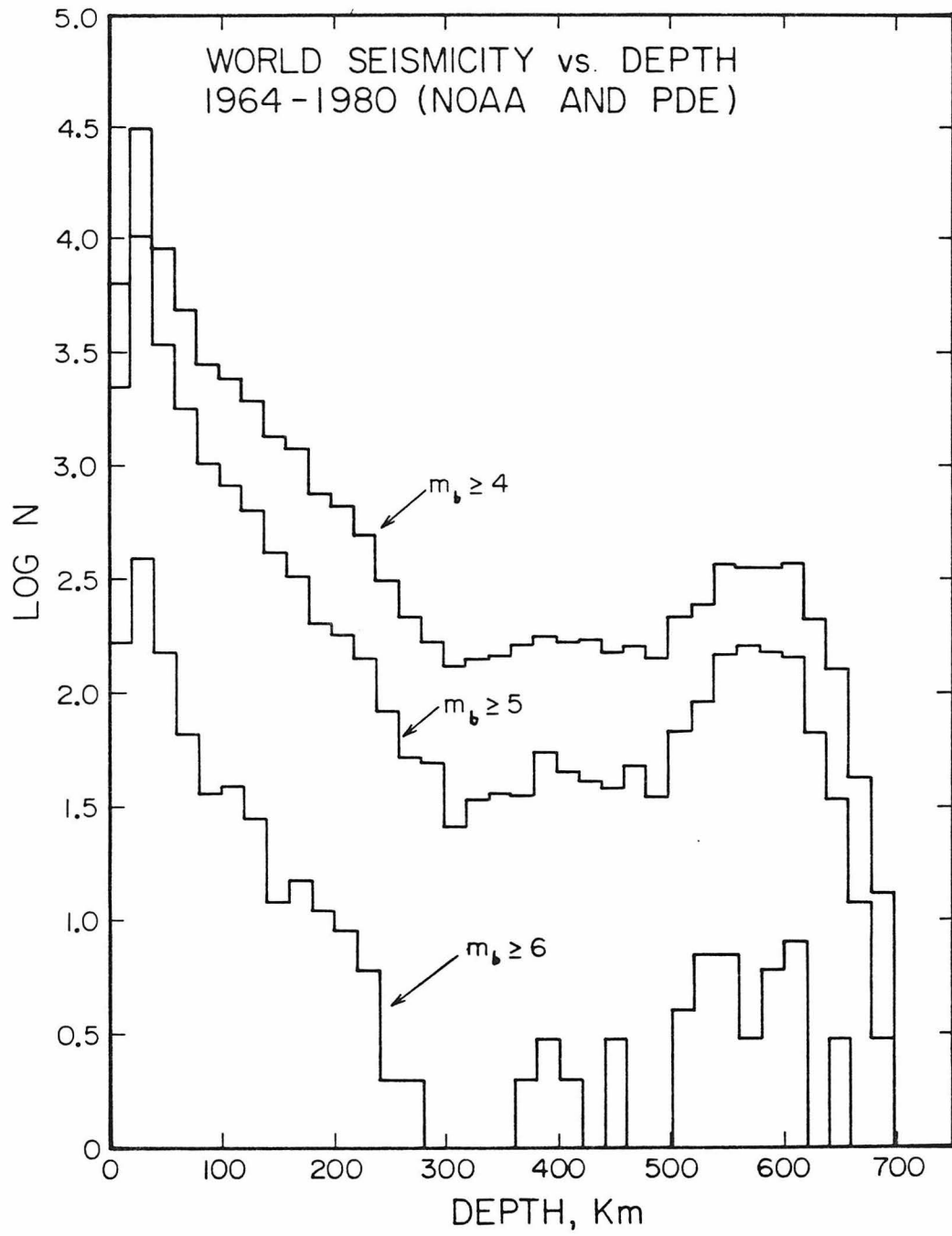
2.1 Seismicity as a Function of Depth

Fig. 1 shows histograms of the logarithm of the total number of earthquakes in the world versus depth. The different curves correspond to different cutoff magnitudes: one represents the earthquakes with a one-second body wave magnitude m_b greater than or equal to 4; in the other two, the cutoffs are $m_b = 5$ and $m_b = 6$. The time period covered is 1964 to 1980, 1964 being the year in which the one-second body wave magnitude began to be applied uniformly. The data sources are the NOAA (1964-1977 inclusive) and PDE (1978-1980) catalogs.

The curves have some striking features. First, we note the well established fact (Isacks et al., 1968) that there are no earthquakes below a depth of about 700 km. Second, we observe a roughly linear decrease in $\log N$ from the surface to a depth of approximately 250 - 300 km. This exponential behavior was noticed by Sykes (1966), and Isacks et al. (1968); it has not been discussed very much in the literature since. After the linear-log decrease, there appears to be a seismicity minimum, followed by a resurgence in activity from 500 to 700 km. The three curves behave very similarly in these respects, although the curve for $m_b \geq 6$ is spottier than the other two, probably showing the effects of incomplete sampling of larger earthquakes in the time period covered.

The worldwide curves of fig. 1 represent what might be termed an "average subduction zone". Although these curves contain very important information, it is necessary also to examine similar plots for individual subducting regions. Such plots are presented in Appendix C. In deciding how to divide up the regions, we have relied on the physiography of trenches, the planform of seismicity observable on global

Figure 1. Logarithm of the total number of earthquakes in the world versus depth, in 20 km intervals. The sources are the NOAA and PDE catalogs, from 1964-1980. The three curves are for three different cutoff magnitudes, as noted, where m_b denotes the one-second body wave magnitude reported by the ISC.



maps such as that of Tarr (1974), the stereo plots of Johnson and Richter (1979), and previous studies of the lateral segmentation of subduction zones (e.g., Isacks and Barazangi, 1977). We have tried to isolate portions of regions where the structure of the Wadati-Benioff zone is as close to two-dimensional as possible.

If we examine the seismicity curves of individual regions, we find that many of them faithfully reproduce the global pattern in whole or in part. Regions without deep seismicity tend to reproduce the upper part of the pattern, that is, the roughly linear-log decrease down to 250-300 km. Regions with deep seismicity tend to reproduce the entire pattern, with the roughly linear decrease down to 250-300 km., followed by a minimum and a deep peak of varying position and intensity.

As we can see from the plots, however, several regions do not conform precisely to these specifications. Many of the shallow regions have a decay pattern of seismicity with depth which deviates significantly from linearity. Note the pattern in the Hindu-Kush, which is more a zone of continental convergence than a subduction zone (Molnar and Tapponier, 1975). Some of the shallow dipping South American zones show patterns more similar to this than to the patterns of other circum-Pacific zones.

To first order, however, the features of the seismicity curves which we have listed do appear to be global, and bear explanation.

2.2 Orientations of Stress Axes of Intermediate and Deep Focus Earthquakes

2.2.1 A First Look

We now turn our attention to observational evidence concerning the orientation of stress in subducting slabs. In a pair of classic papers, Isacks and Molnar (1969,1971) examined the relationship of earthquake stress axes, derived from first motion studies, to the geometry of Benioff zones. In the 1969 paper they established the result that stress axes (tension or compression) are more closely aligned with slab geometry than are nodal planes. That is, the evidence does not suggest that earthquakes represent shear motion along a fault plane marking the interface between slab and mantle. Actually, some evidence for this has been discovered (e.g., Umino and Hasegawa, 1982), but this is for depths shallower than 60 km.

In the 1971 paper, Isacks and Molnar performed a detailed regional analysis. Globally, the evidence seems to suggest down-dip compression or tension at depths from 70 to 300 km, depending on the region, and down-dip compression below 300 km. Of course, "down-dip" is to some extent in the eye of the beholder. In this section and the next we will attempt to quantify how close to down-dip the stress axes of earthquakes are, in the mean. Fujita and Kanamori (1981), who have performed a global survey of focal mechanism solutions for intermediate earthquakes, and had more data at their disposal than did Isacks and Molnar, argue for a state of "in-plate" rather than down-dip stress.

First-motion solutions vary greatly in the degree to which the nodal planes and stress axes can be constrained by the data. Heaton (1982) has compiled a very useful table of the best constrained solutions for earthquakes deeper than 30 km. Several of Isacks and Molnar's solutions are included, as are first-motion studies by

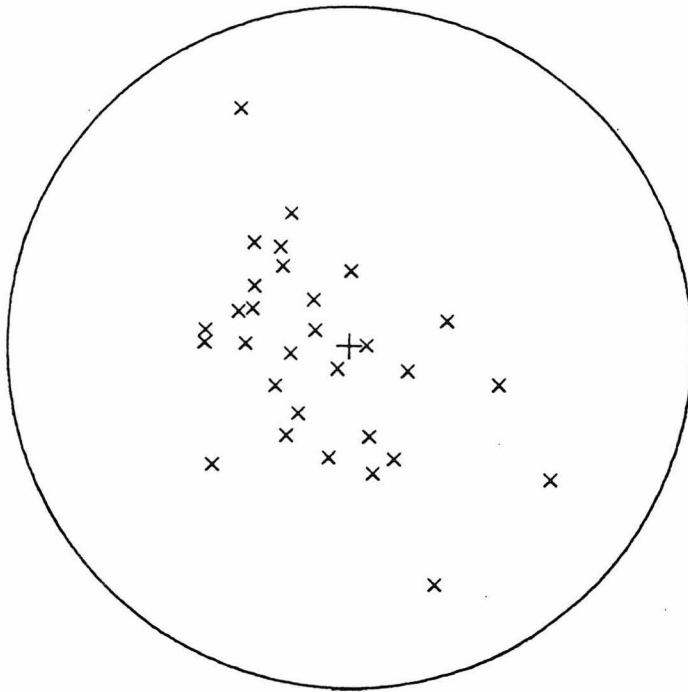
more recent investigators, and some more detailed studies involving the use of synthetic seismograms. In fig. 2, we plot the stress axes from Heaton's list on lower-hemisphere stereographic projections. The data from different regions are combined by rotating all axes such that the slab is always vertical and striking North. The dips and strikes of the various slabs are taken from Uyeda and Kanamori (1979) and Fujita and Kanamori (1981). There is some scatter introduced by the fact that slabs are not everywhere even approximately two dimensional in structure, but we have tried to minimise this by eliminating events where the average dips and strikes cannot clearly be used. Particular care must be taken in the Tonga, Indonesian, and Philippine regions.

Looking at fig. 2, we see considerable scatter in the data. However, a general tendency towards down-dip compression is definitely observable in the deep events. In the intermediate events there is less of an obvious cluster, although the tension axes do seem to line up with the down-dip direction better than does anything else. If we choose for each earthquake the stress axis closest to the down-dip direction and plot that axis, then the cluster improves for intermediate events, although not for deep ones. This is because of the more universal nature of down-dip compression at depth, as opposed to the more region-dependent state of stress above 300 km. In any case, we can see that the stress axes, rather than the nodal planes, are what align best with the geometry of the slab.

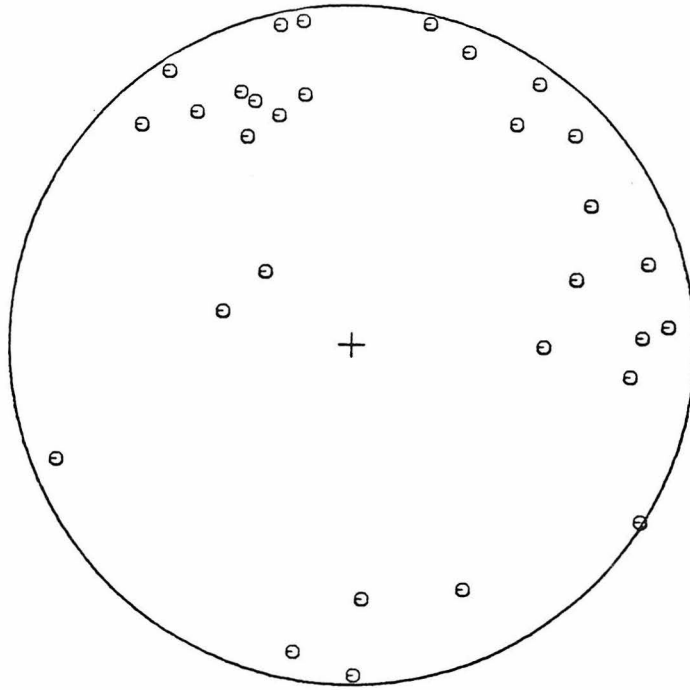
Figure 2. Stereographic (equal-area, lower hemisphere) projections of stress axes and nodal plane poles for earthquakes drawn from Heaton's (1982) list of well constrained solutions. Some of Isacks and Molnar's (1971) mechanisms are included, as well as more recent ones. Figure 2(a) is for deep (≥ 300 km) earthquakes, and figure 2(b) is for intermediate (70 to 300 km) earthquakes. All quantities are plotted in a slab coordinate system. The slab is always vertical and striking North-South. The down-dip direction is at the center of the stereonet. Compression and tension axes are shown. Also shown is a drawing where the stress axis (compression or tension) closest to the down-dip direction is plotted.

a

WELL CONSTRAINED DEEP EVENTS



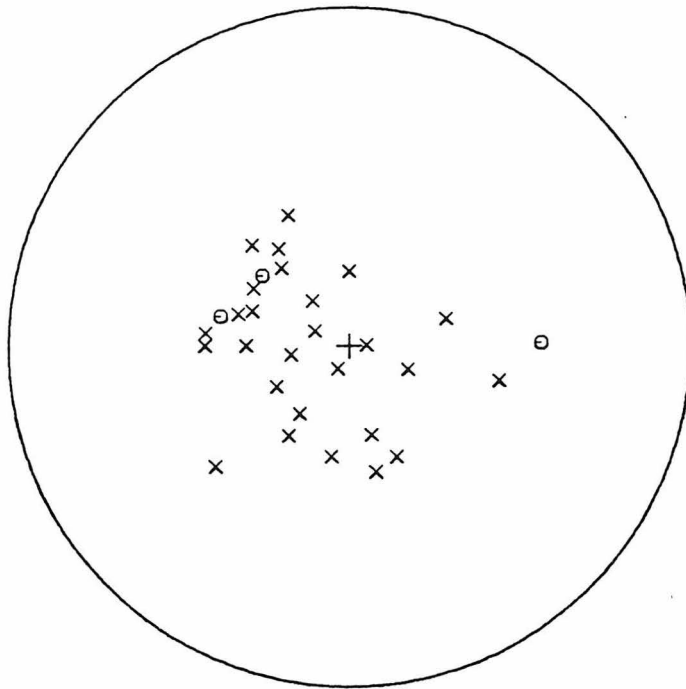
COMPRESSION
AXES



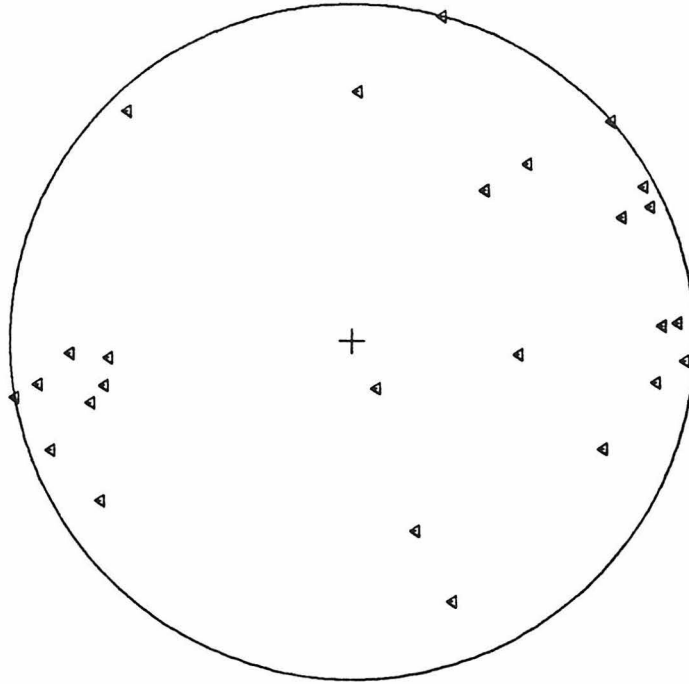
TENSION
AXES

a

WELL CONSTRAINED DEEP EVENTS



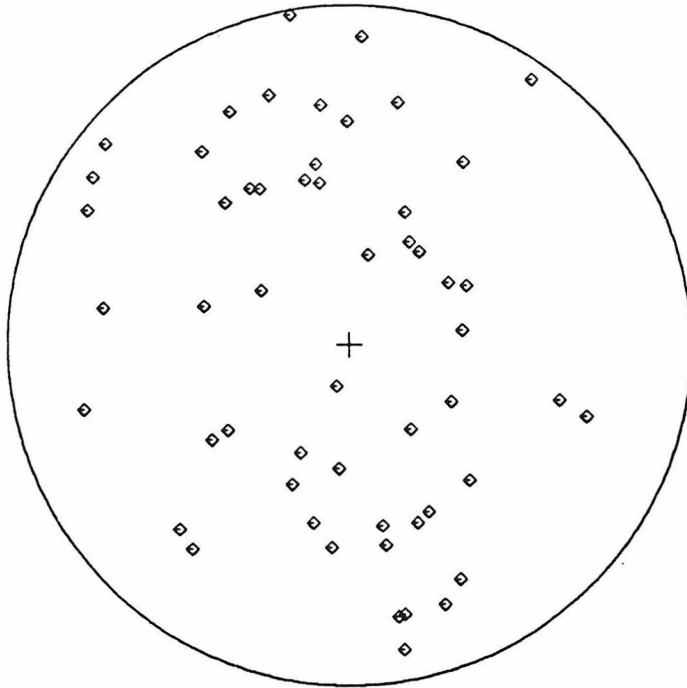
CLOSEST STRESS
AXIS



NULL
AXES

a

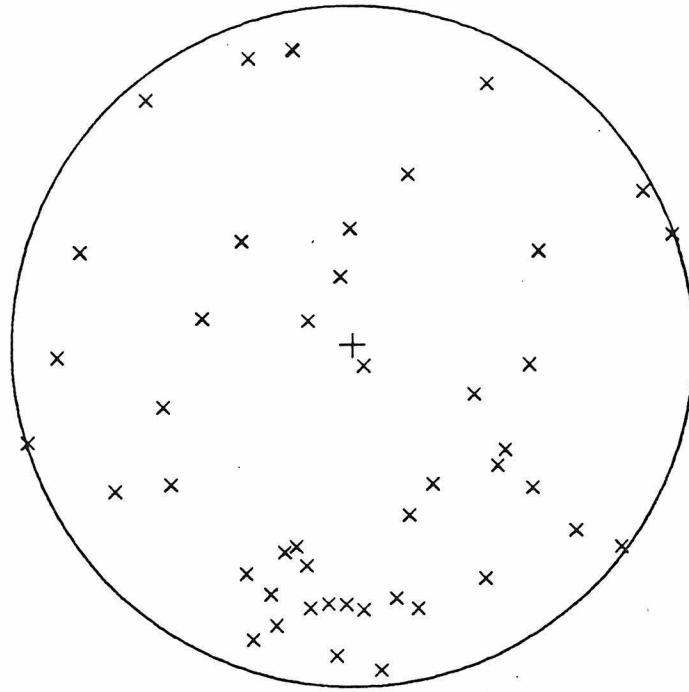
WELL CONSTRAINED DEEP EVENTS



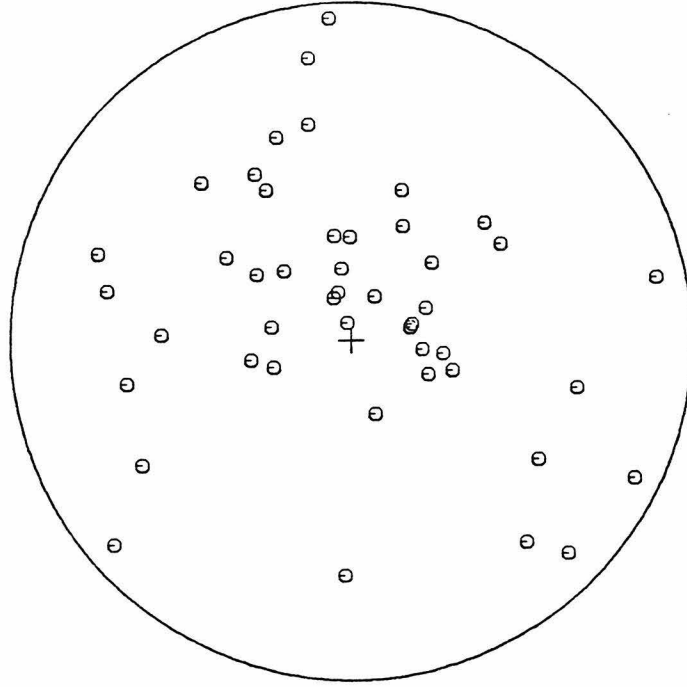
POLES TO NODAL PLANES

WELL CONSTRAINED INTERMEDIATE EVENTS

b



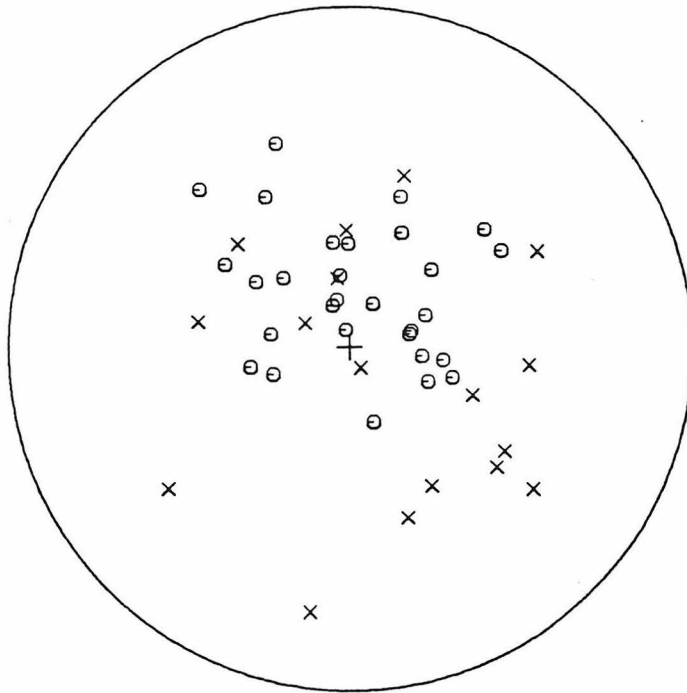
COMPRESSION AXES



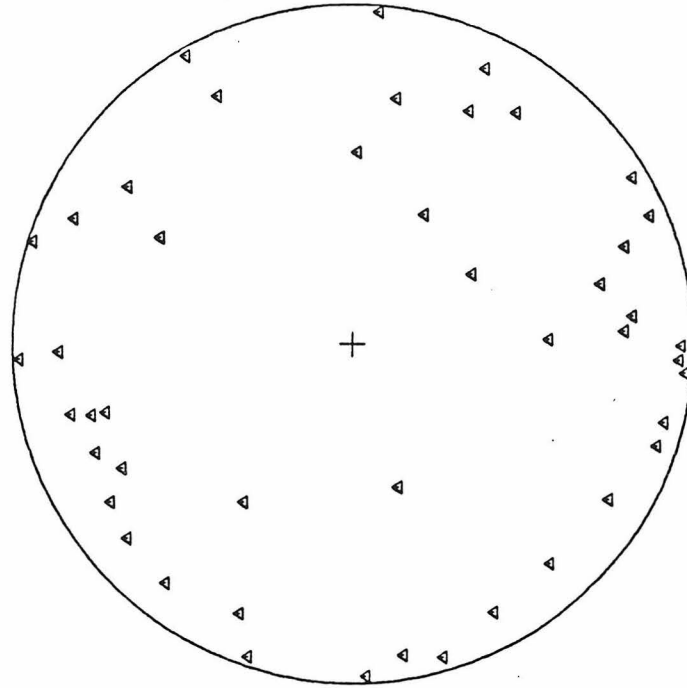
TENSION AXES

b

WELL CONSTRAINED INTERMEDIATE EVENTS



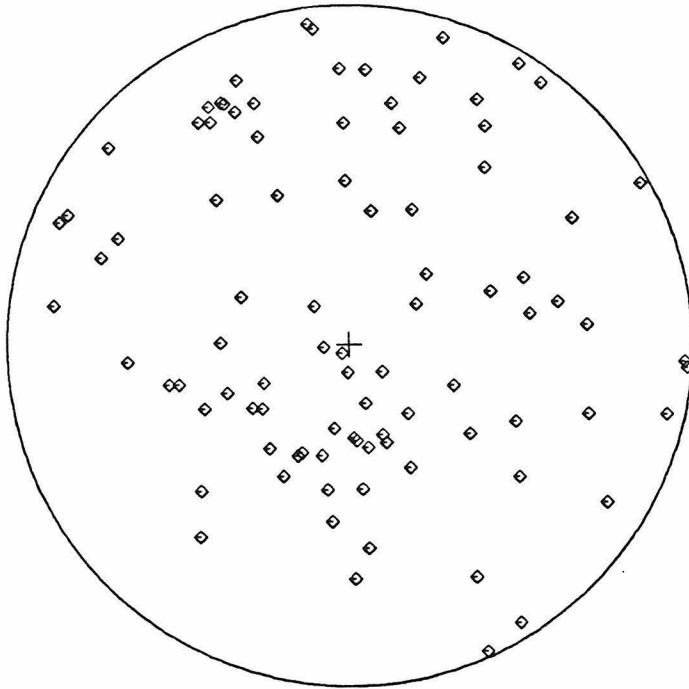
CLOSEST STRESS AXIS



NULL AXES

b

WELL CONSTRAINED INTERMEDIATE EVENTS



POLES TO NODAL PLANES

2.2.2 Events Studied by Moment Tensor Inversion

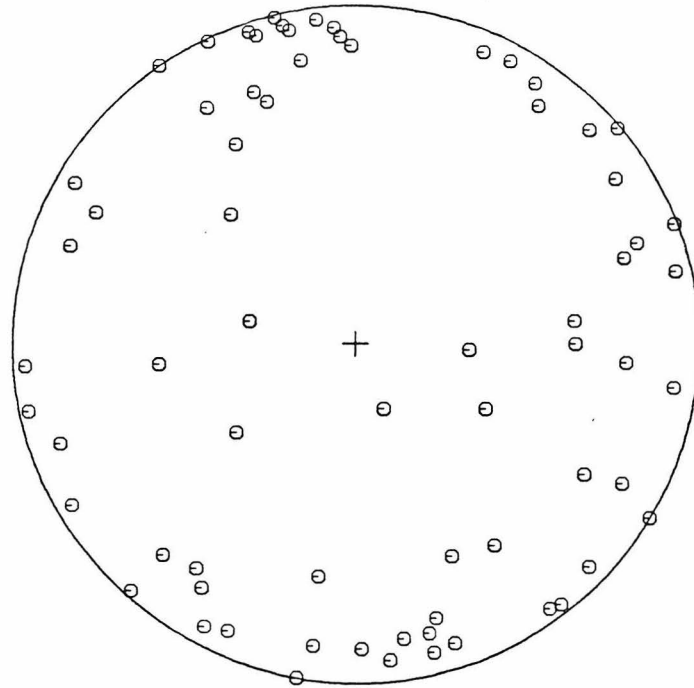
An important new development in seismology has been the development of methods for performing routine moment tensor inversions for earthquakes using now available digital data. In the years preceding the availability of this data and the development of the new methods, an investigator who wanted to do a more detailed study of an earthquake mechanism than a first-motion analysis had to commit a sizeable amount of time to the digitization and forward modelling of the records. The number of events that could be studied in this manner was therefore quite limited. The new moment tensor inversion methods offer the advantages of objectivity, as well as thoroughness and speed. We have studied several of the larger ($M_0 \geq 10^{26}$ dyn-cm) intermediate and deep events which have occurred in the world since 1978, using the method of Kanamori and Given (1981) for inverting IDA data. Details are given in Appendix A. In addition, we have available several solutions performed in independent studies by Dziewonski and Woodhouse (1983) and Giardini (1982,1983). These investigators have obtained reasonable solutions for events with $M_0 \geq 10^{24}$ dyn-cm. Their lower threshold stems from their effective use of body waves from the SRO; our IDA inversions are carried out on surface waves at periods exceeding 200 seconds. We now ask ourselves: do these earthquakes studied in this more objective and thorough manner lend support to the general conclusions discussed in the last section?

In general, they appear to. Fig. 3 shows the stress axes for intermediate and deep events studied by moment tensor inversion, plotted as before, with data from different regions rotated such that the slab is striking North and vertical. In this set of figures, too, the most readily apparent feature in the considerably scattered data is the tendency toward down-dip compression for the deep events. In the

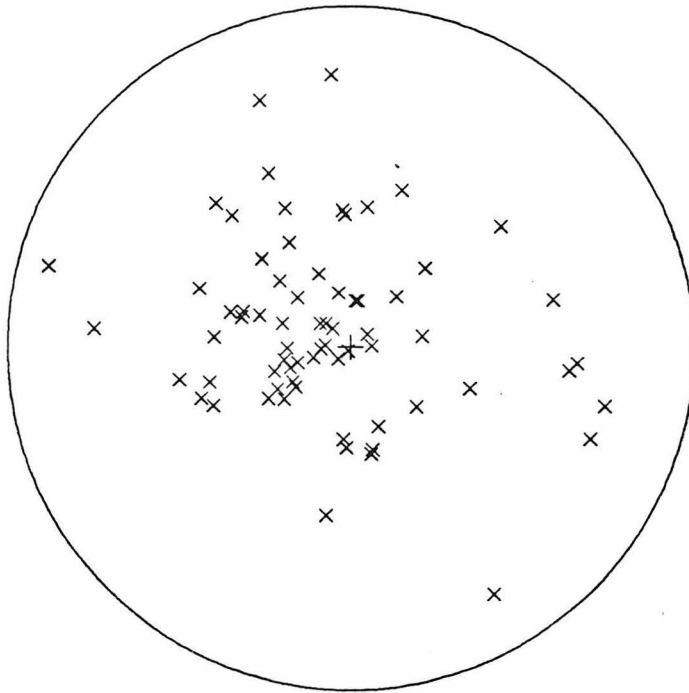
Figure 3. As Figure 2, but for events from 1977-1981 analysed by moment tensor inversion, in this study (Appendix A), and in Dziewonski and Woodhouse (1983) and Giardini (1983). Figure 3(a) is for deep events, and Figure 3(b) is for intermediate events. We recall that down-dip is always in the center of the stereonet.

DEEP EVENTS STUDIED BY MOMENT TENSOR INVERSION

a



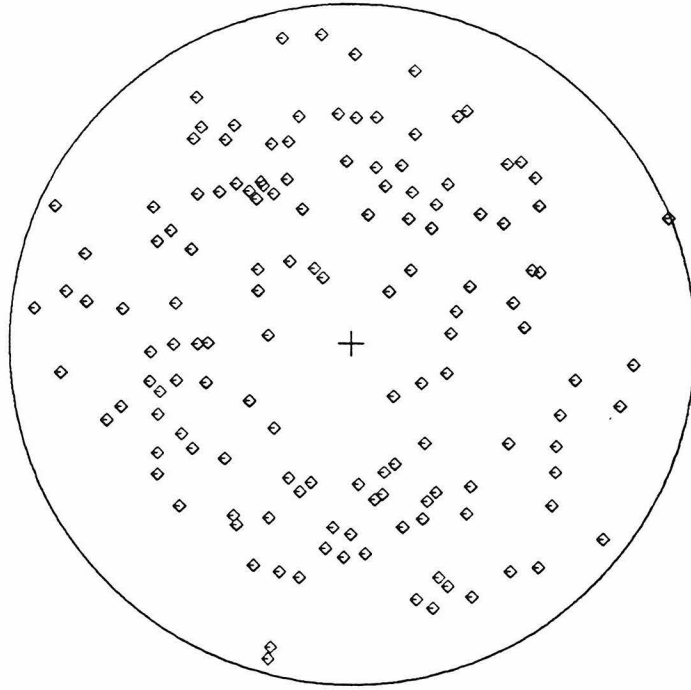
TENSION AXES



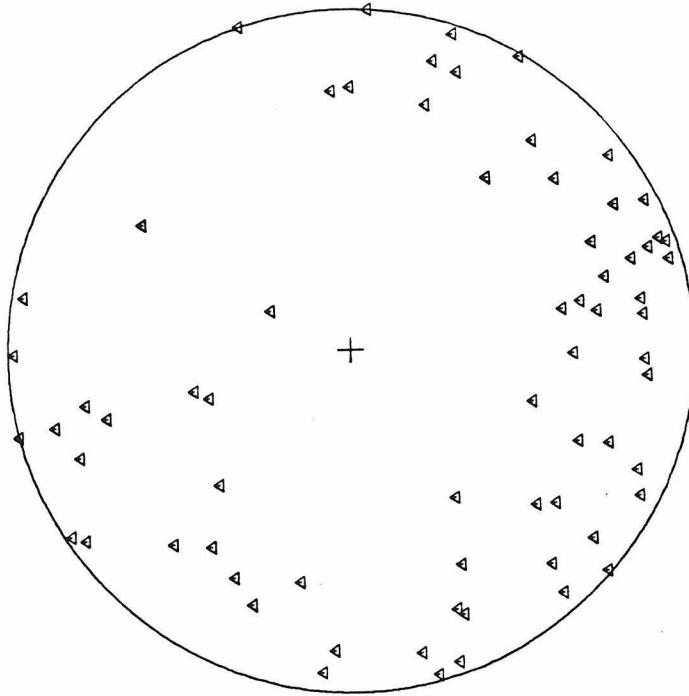
COMPRESSION AXES

DEEP EVENTS STUDIED BY MOMENT TENSOR INVERSION

a



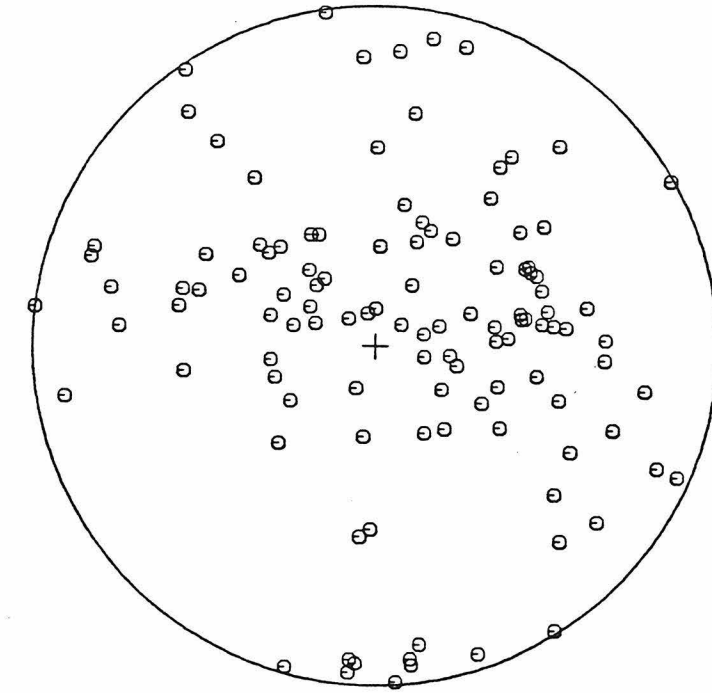
POLES TO NODAL PLANES



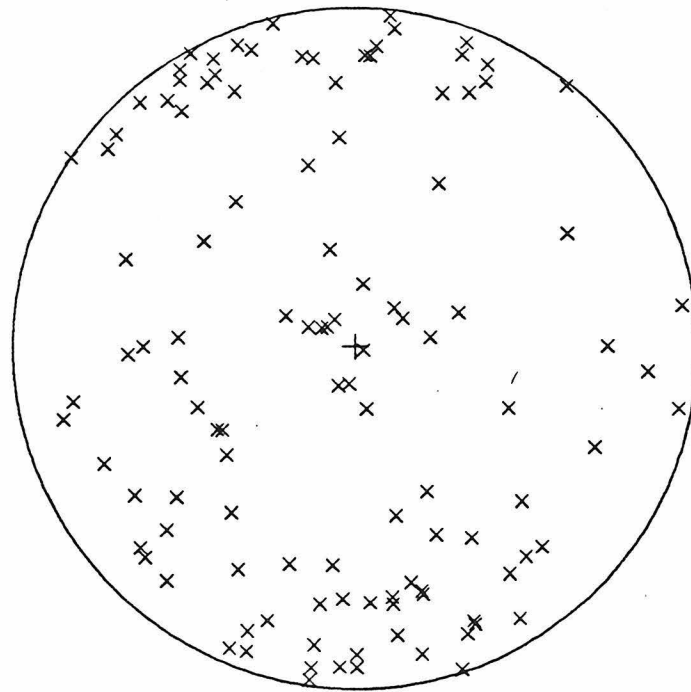
NULL AXES

INTERMEDIATE EVENTS STUDIED BY MOMENT TENSOR INVERSION

b



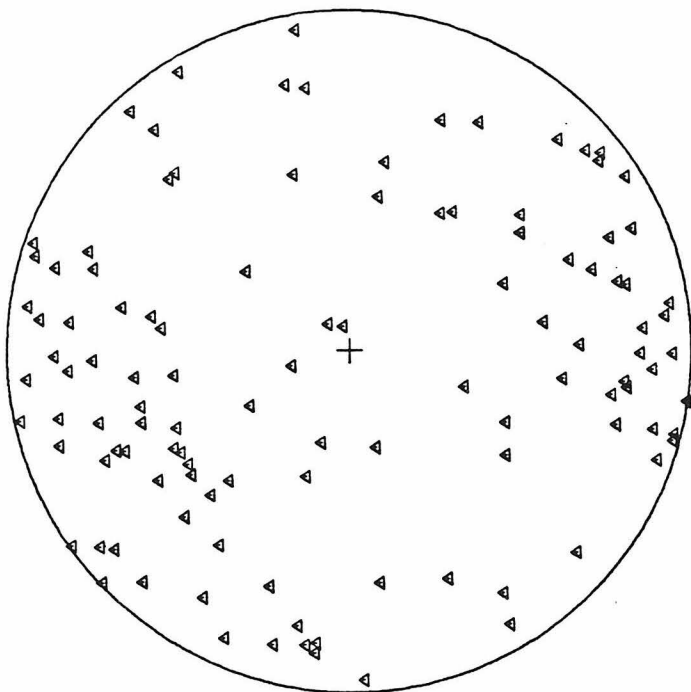
TENSION AXES



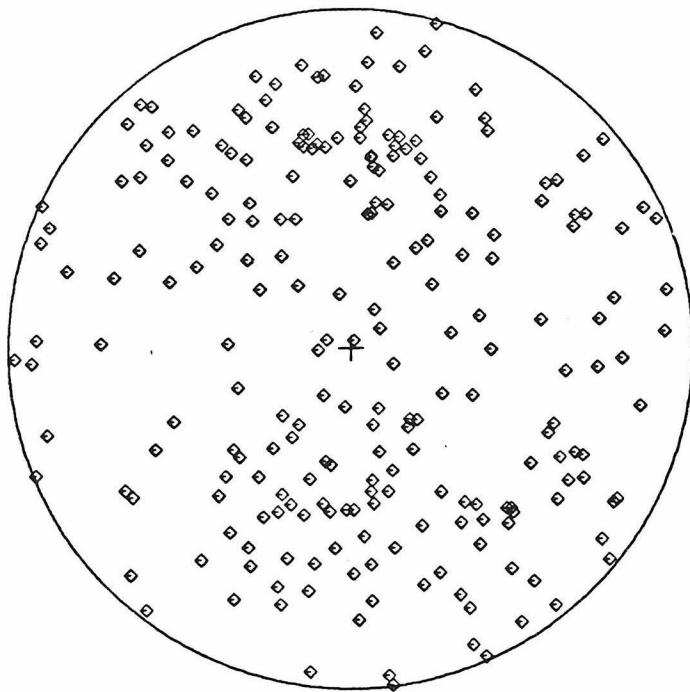
COMPRESSION AXES

INTERMEDIATE EVENTS STUDIED BY MOMENT TENSOR INVERSION

b



NULL AXES



POLES TO NODAL PLANES

intermediate events, a pattern is more difficult to discern, but the tension axes do show the tightest group around the plate in general, if not convincingly around the down-dip direction.

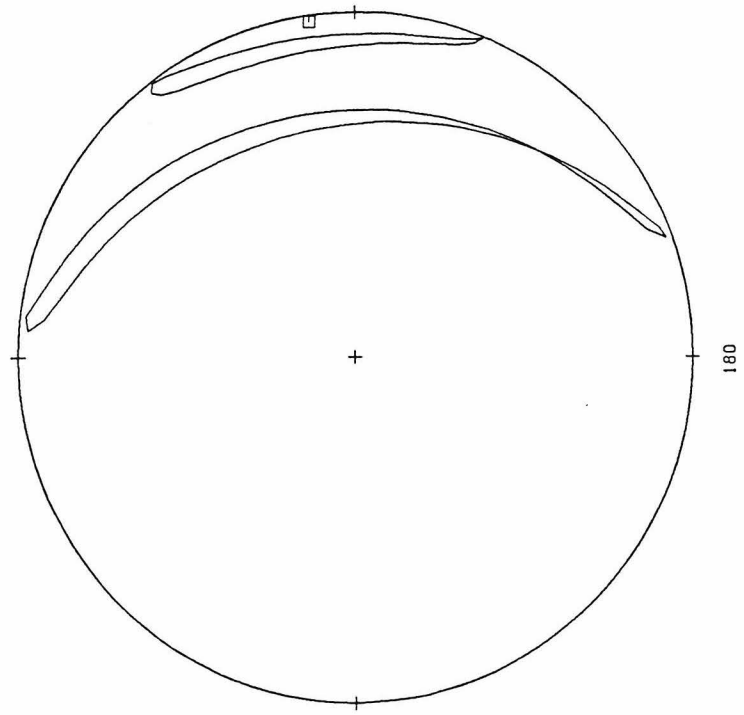
Fig. 4 shows the results of some simple statistical analysis of the data in fig. 3. Since we are dealing here with the statistics of *directions* rather than conventional linear statistics, some special techniques must be applied. The techniques are well developed and have long been in use in paleomagnetism and biometry; a brief description and references are given in Appendix B. Fig. 4 shows both Bingham and Fisher statistics for the tension and compression axes of the intermediate and deep focus earthquakes. The Bingham and Fisher means are quite similar. In all cases, the hypothesis of uniformity can be rejected to 99% level or better. This means that there is 1% chance or less that the data are drawn from an isotropic distribution, and a preferred direction does not exist. The larger circle or ellipse in each plot represents the standard deviation of the data, while the smaller one represents the boundary of the region of 95% confidence for the mean direction.

From these figures we can conclude, despite large scatter, that the deep events are consistent with down-dip compression but not down-dip tension, while the intermediate events are marginally consistent with down-dip or in-plate tension, but not down-dip compression.

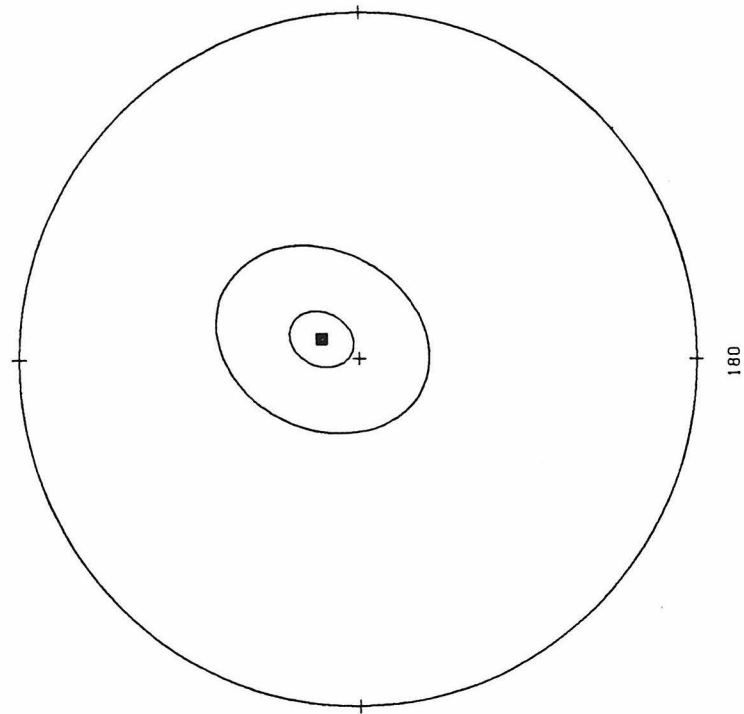
We must remember, however, that our sample contains data from many different regions. While we do not have enough events to conduct an exhaustive individual survey of each of the world's subduction zones, it is still worthwhile to present some of the data by region, or class of region. One important subdivision we must perform for the deep earthquakes is to isolate the Tonga region. This is the most active area of the world at depths below 300 km, and accounts for 46% of the deep events in

Figure 4. Some simple statistical parameters for the data shown in figure 3. Both Fisher and Bingham statistics are shown (Appendix B). For convenience of plotting, the projections are now Wulff projections, and cover the whole sphere. An open square indicates a mean position in the upper hemisphere, while a filled square indicates one in the lower hemisphere. Small ellipses or circles show 95% confidence limits for the true mean directions. In all cases, a preferred or mean direction does exist, to 99% confidence or better. Large ellipses or circles delineate standard deviation limits.

DEEP EVENTS STUDIED BY MOMENT TENSOR INVERSION
BINGHAM STATISTICS

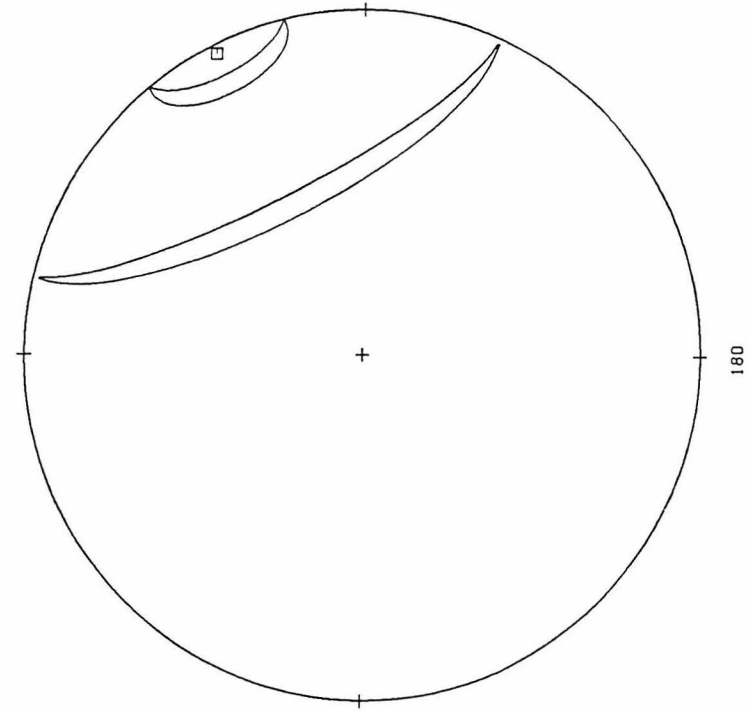


TENSION

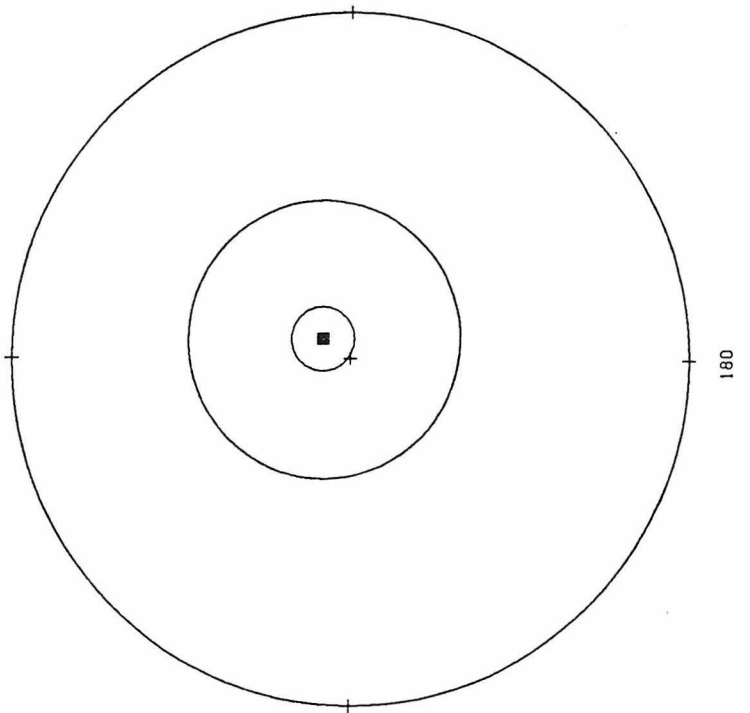


COMPRESSION

DEEP EVENTS STUDIED BY MOMENT TENSOR INVERSION
FISHER STATISTICS

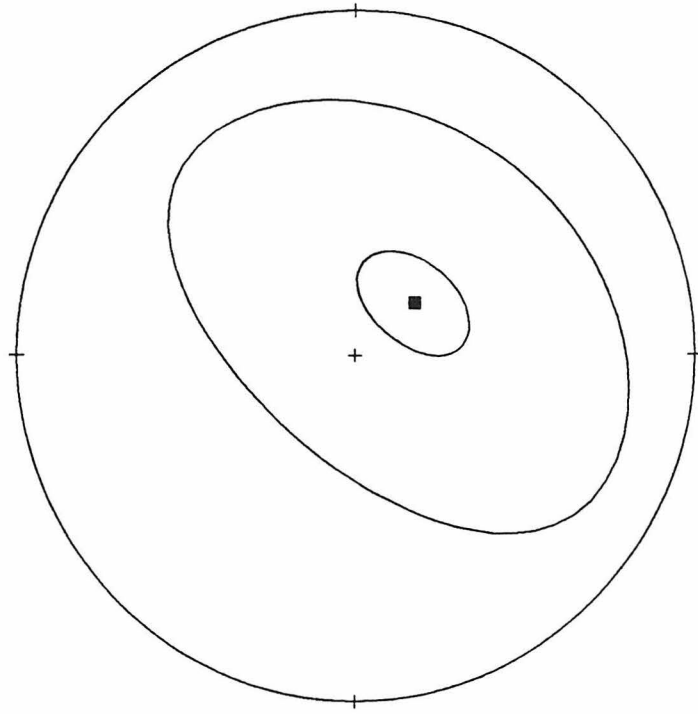


TENSION



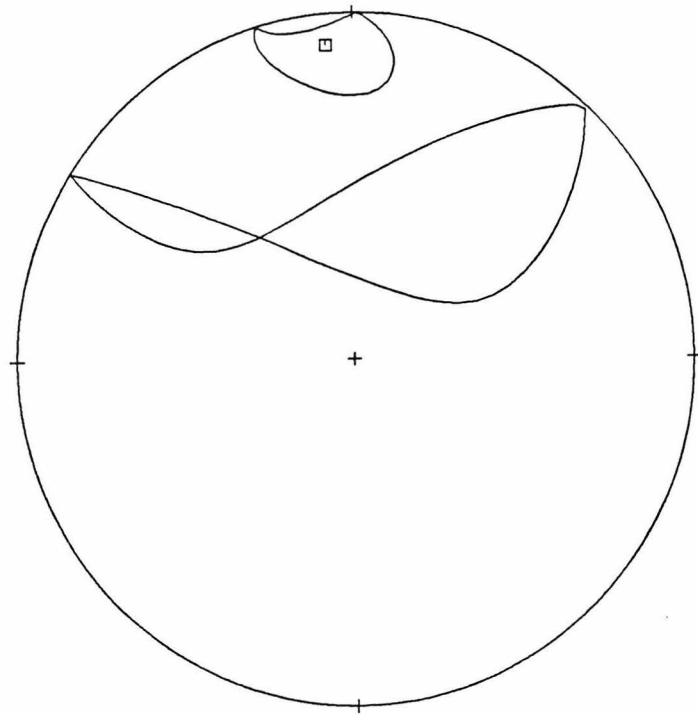
COMPRESSION

INTERMEDIATE EVENTS STUDIED BY MOMENT TENSOR INVERSION
BINGHAM STATISTICS



180

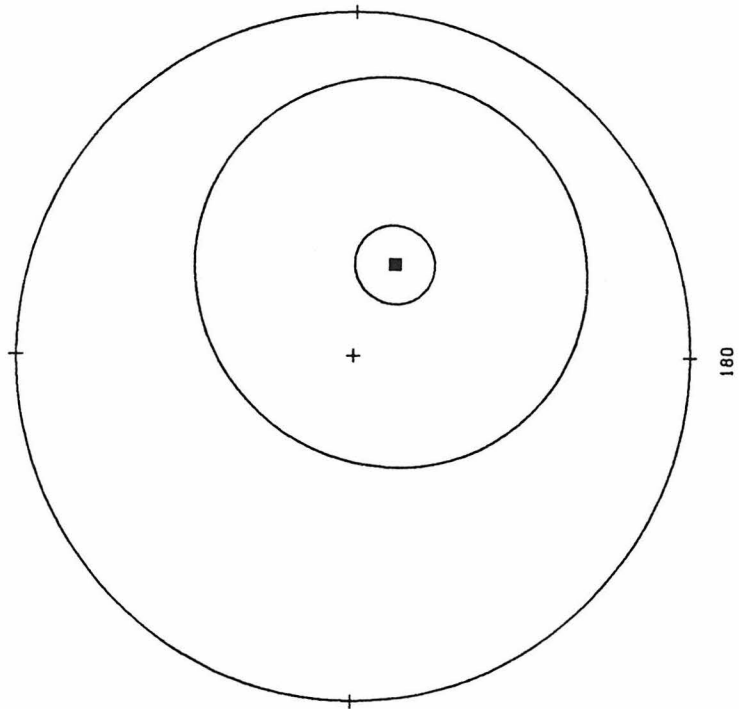
TENSION



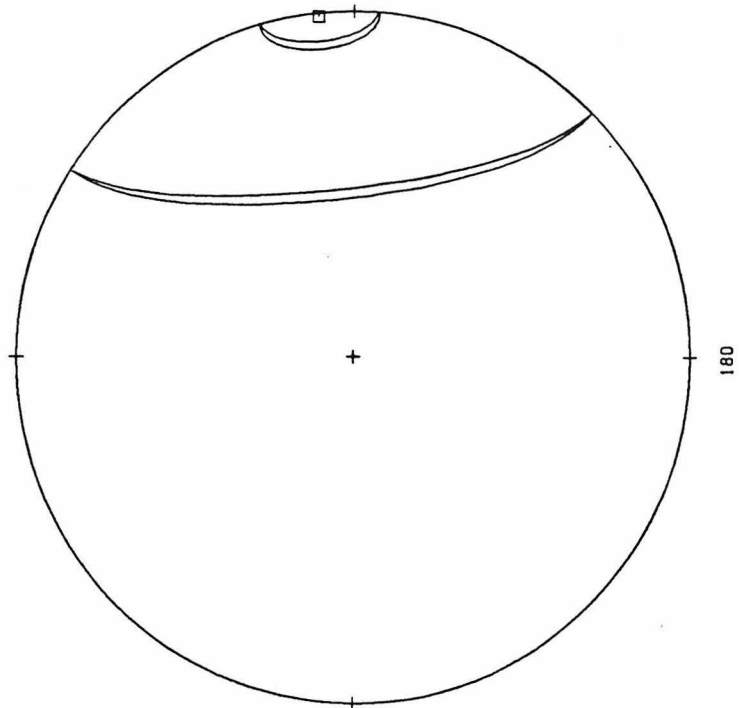
180

COMPRESSION

INTERMEDIATE EVENTS STUDIED BY MOMENT TENSOR INVERSION
FISHER STATISTICS



TENSION



COMPRESSION

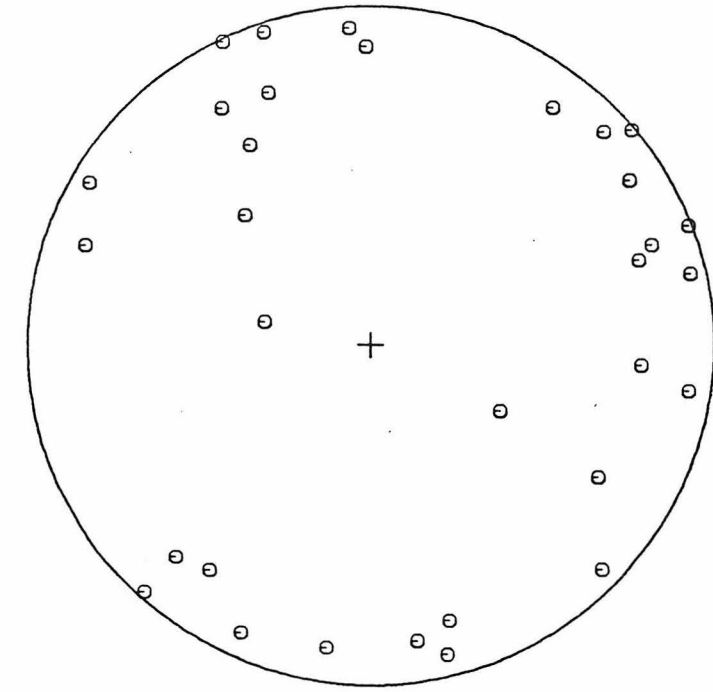
our sample. Fig. 5 plots stress axes for deep earthquakes separately for Tonga and for the rest of the world. The tendency toward down-dip compression at depth is not restricted to Tonga, as we can see from the statistics in fig. 6. Fig. 7 shows compression axes for individual regions where we have more than four events. The number of events in each case is small enough such that it is difficult to draw a confident conclusion for the region. We can see, however, that North Honshu, Mindanao, and Izu-Bonin are all more or less consistent with down-dip compression. The large scatter in the case of Izu-Bonin is probably at least partially due to the assignment of an average dip to the entire subduction zone, whereas this zone appears to change dip from North to South (Katsumata and Sykes, 1969). This may also be a factor in the case of Java, whose state of stress is not well resolved in the figure.

Turning now to intermediate depths, we are faced with the problem that Tonga and the New Hebrides are really the only regions which are individually well represented in our sample. Tonga shows some tendency toward down-dip compression, in agreement with the findings of Richter (1979) and Isacks and Molnar (1971) (see fig. 8). The New Hebrides show some tendency toward down-dip tension, as was also observed by Pascal et al (1978), as well as Isacks and Molnar. In both cases, actually, "in-plate" might be a more accurate expression than "down-dip" (Fujita and Kanamori, 1981). Shown also are the axes for North Honshu, the Marianas, and Mindanao. These are all deep extending slabs, but they do not show down-dip compression at intermediate depths the way Tonga does. Mindanao seems closer to tension than compression (see also Cardwell et al. , 1980). However, these regions are not well represented at all in our sample, and we cannot make any strong statement about them. Other regions are represented, individually, even worse.

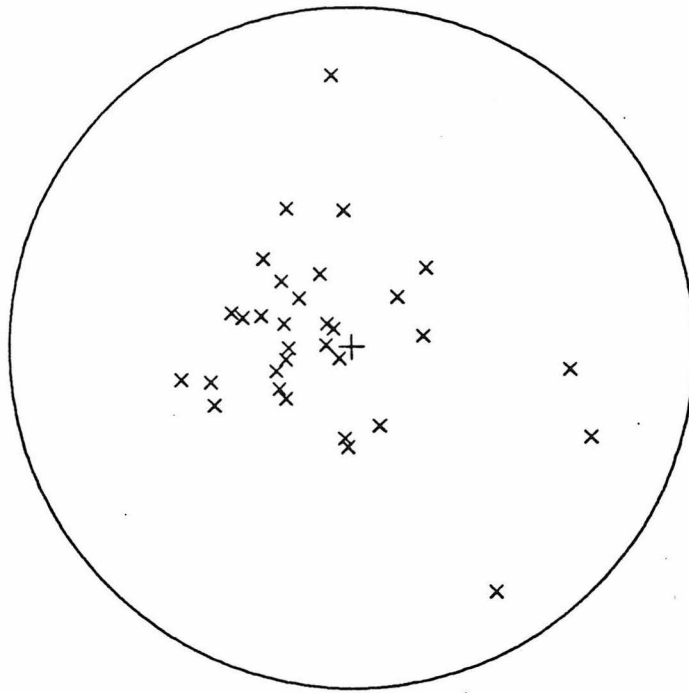
Figure 5. As figure 2, but plotting axes separately for Tonga and the rest of the world.

DEEP EVENTS

TONGA



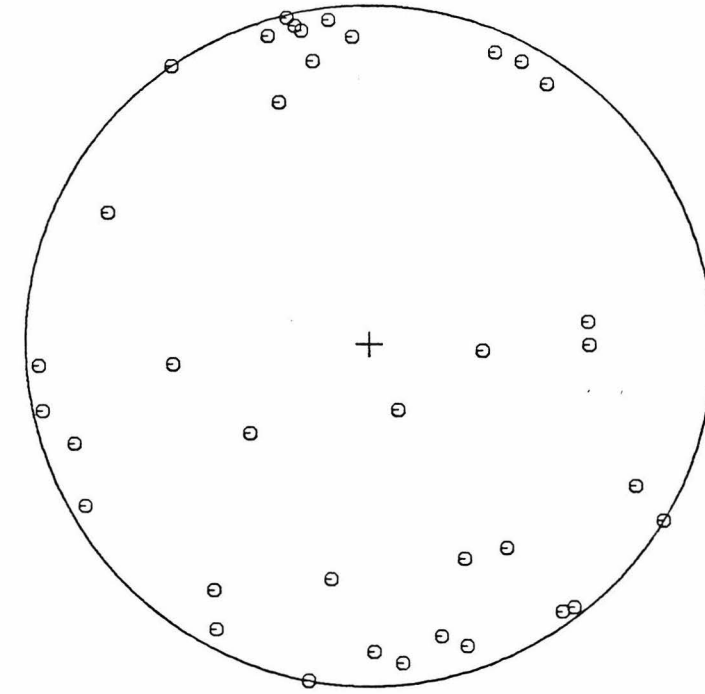
TENSION
AXES



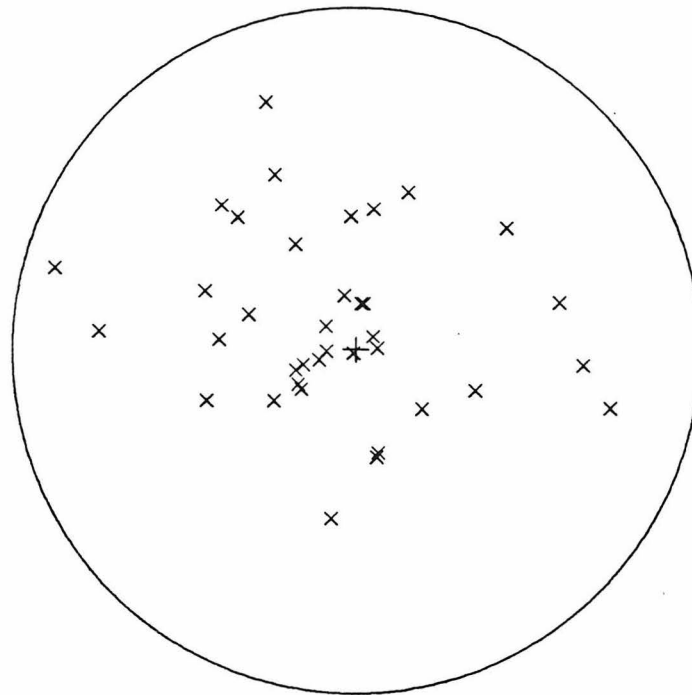
COMPRESSION
AXES

DEEP EVENTS

WORLD MINUS TONGA



TENSION
AXES



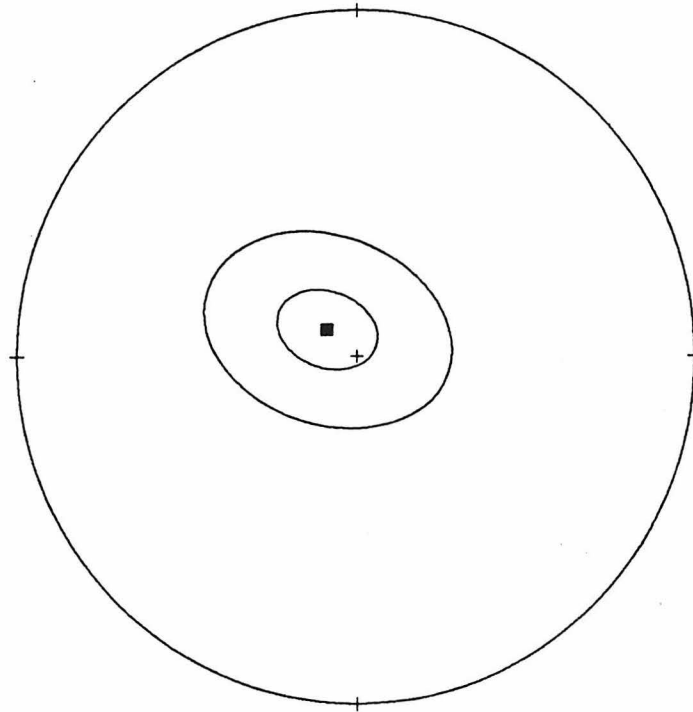
COMPRESSION
AXES

Figure 6. Bingham statistics, plotted as in figure 4, for the data representing the world except for Tonga (figure 5).

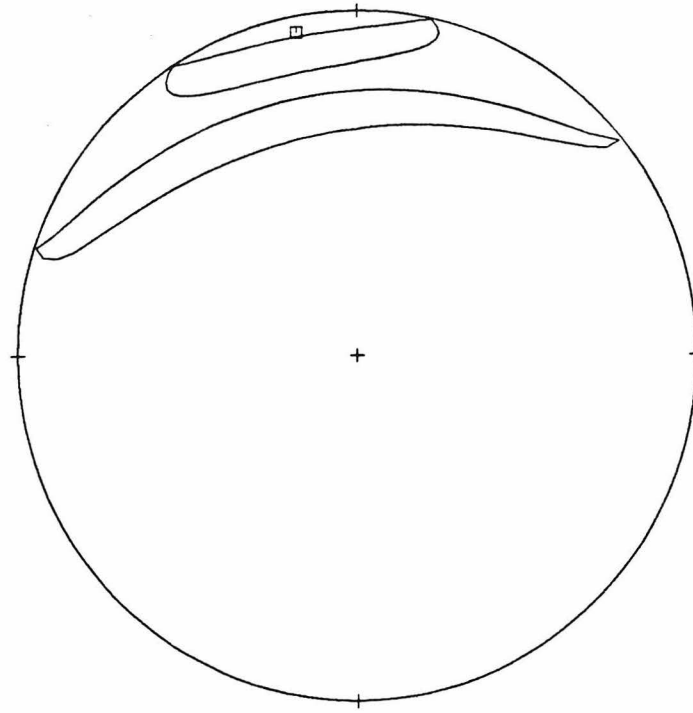
DEEP EVENTS

Bingham Statistics

World Minus
Tonga



Compression



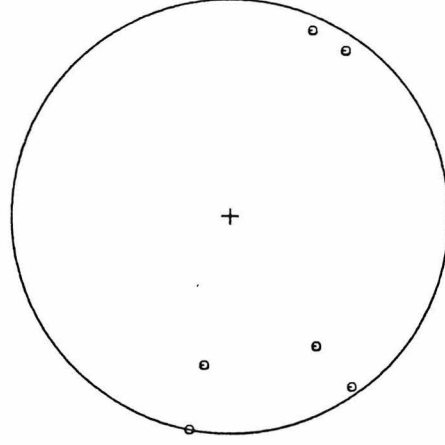
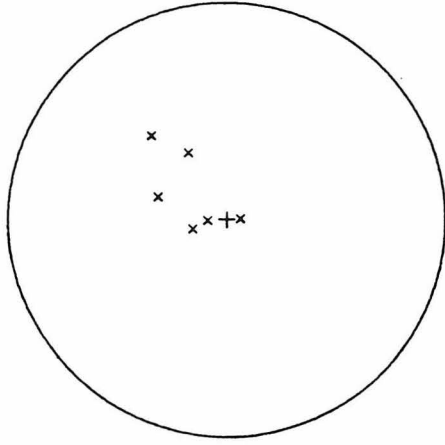
Tension

One potentially instructive way to look at the data is shown in figs. 9 and 11. Here we plot stress axes for intermediate depth earthquakes occurring in slabs that do not extend below 300 km (fig. 9), and for intermediate depth earthquakes occurring in deep-extending slabs other than Tonga (fig. 10). Again, the scatter is large, and it is difficult for us to draw conclusions as confidently as we have for deep earthquakes. As we can see from the mean directions in fig. 10, shallow-extending slabs are closer to down-dip tension than compression. This also appears to be true of the deep-extending slabs other than Tonga (fig. 12). This disagrees with one of the conclusions of Isacks and Molnar (1971), who believed that deep extending slabs in general were in down-dip compression at all depths.

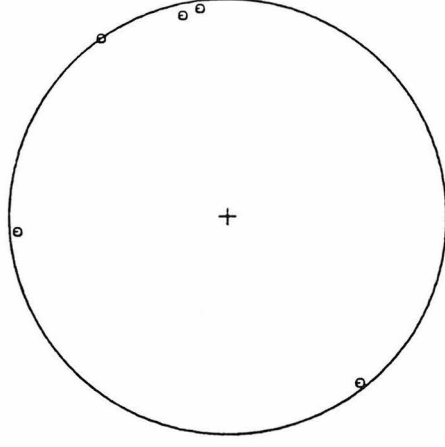
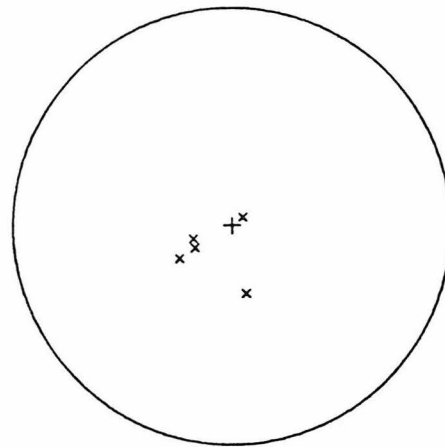
Figure 7. As figure 2, for deep events in individual regions where more than 4 events are available.

DEEP EVENTS

Mindanao



North Honshu

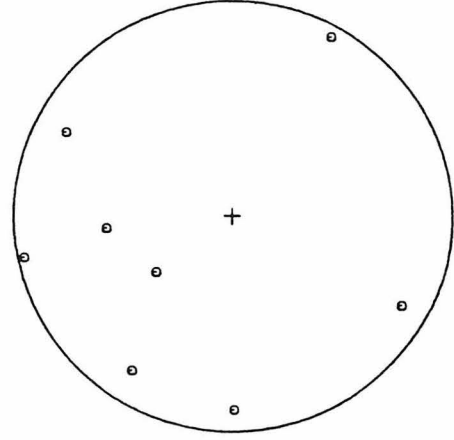
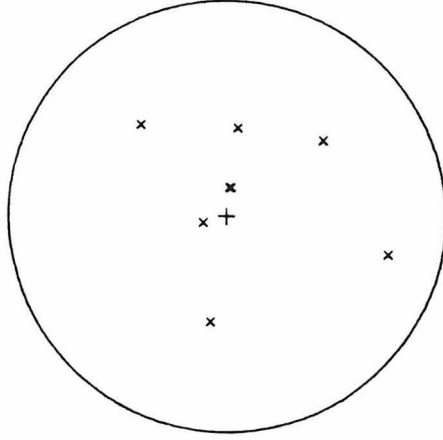


Compression

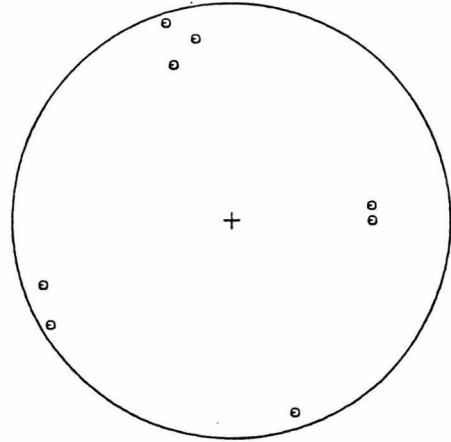
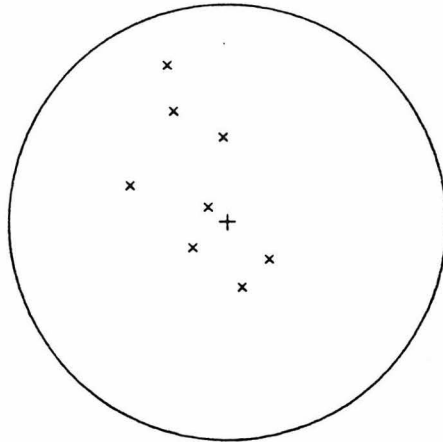
Tension

DEEP EVENTS

Java



Izu-Bonin



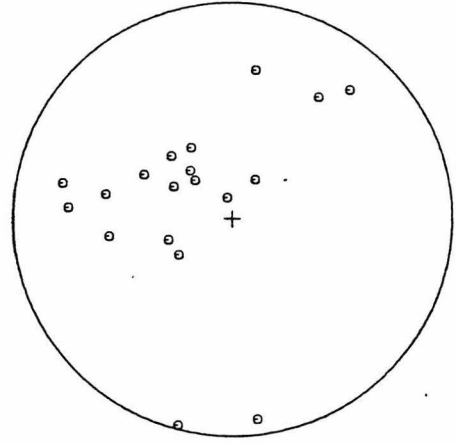
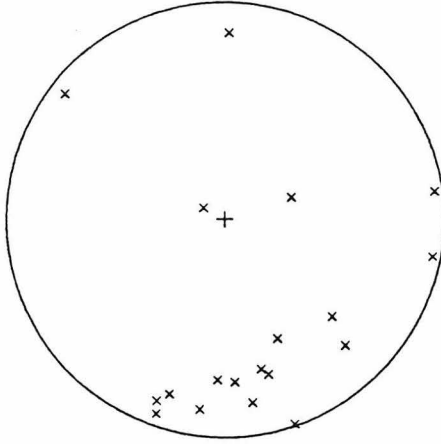
Compression

Tension

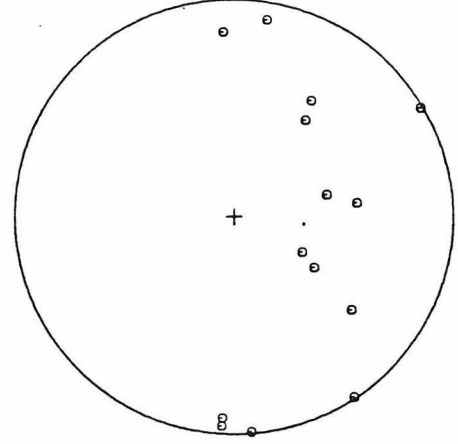
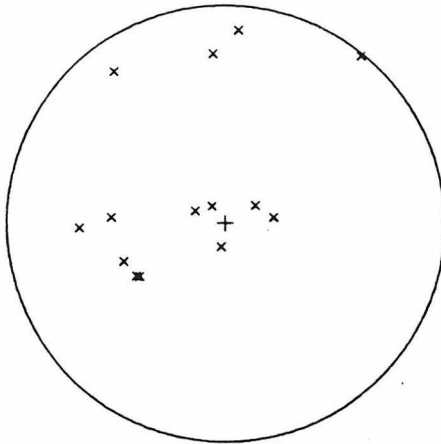
Figure 8. As figure 2, for intermediate events in individual regions where more than 4 events are available.

INTERMEDIATE
EVENTS

New Hebrides



Tonga

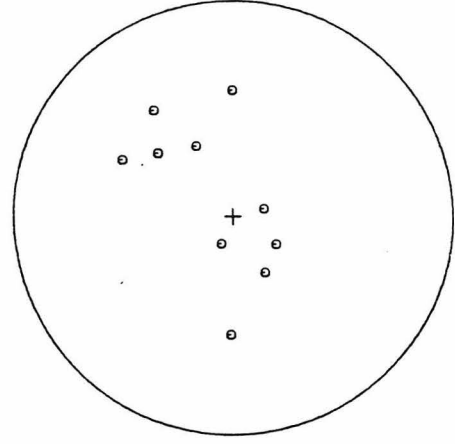
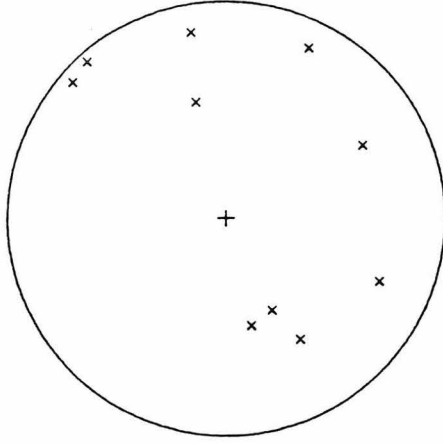


Compression

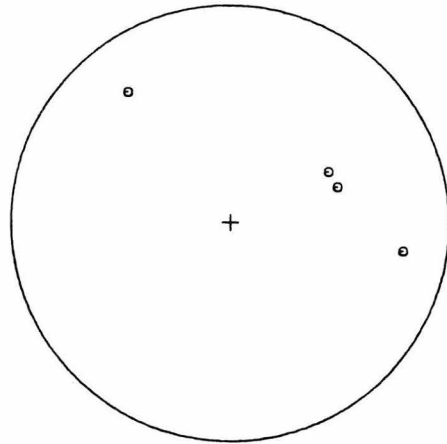
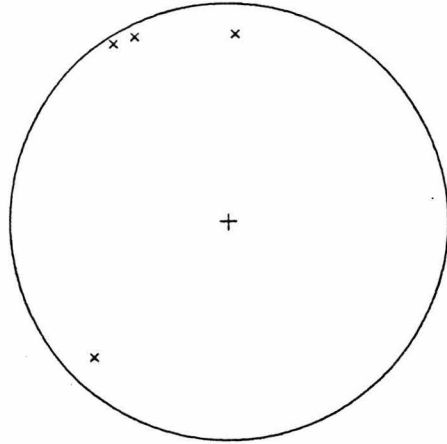
Tension

INTERMEDIATE
EVENTS

Mindanao



Marianas

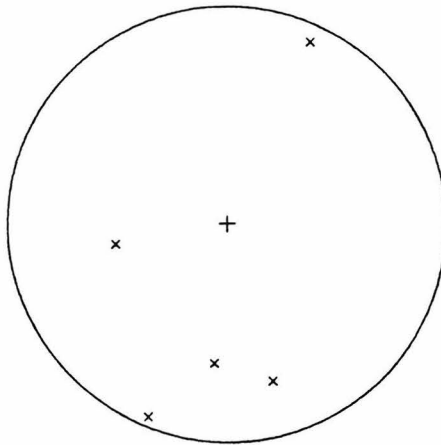


Compression

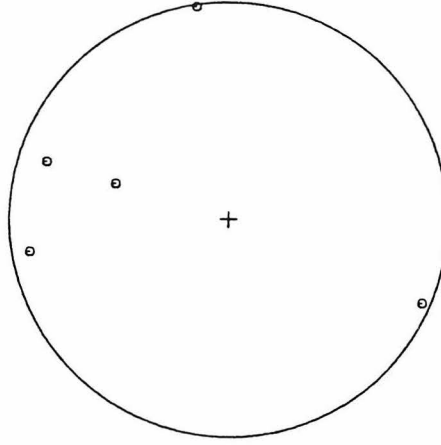
Tension

INTERMEDIATE
EVENTS

North Honshu



Compression

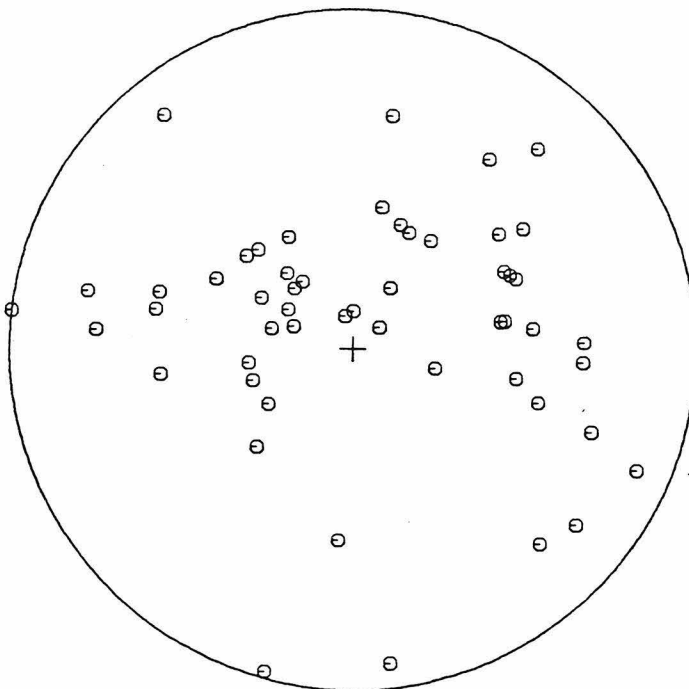


Tension

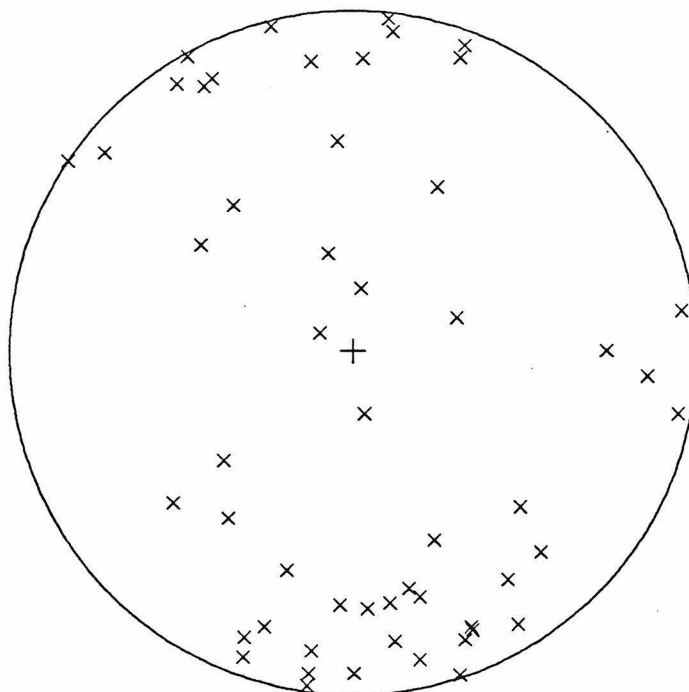
Figure 9. As figure 2, for intermediate events in slabs with maximum depths at 300 km or less.

INTERMEDIATE
EVENTS

Shallow Slabs



TENSION
AXES



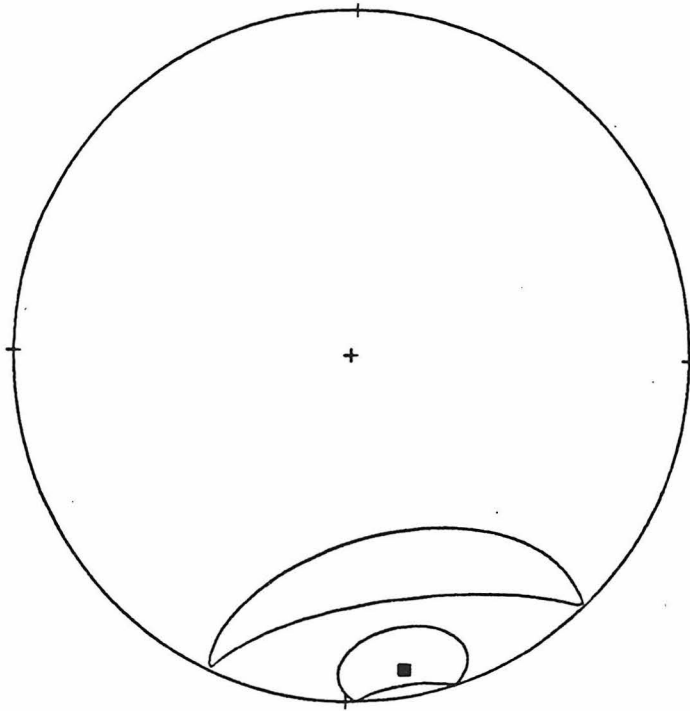
COMPRESSION
AXES

Figure 10. Bingham statistics, plotted as in figure 4, for events in shallow-extending slabs (figure 9).

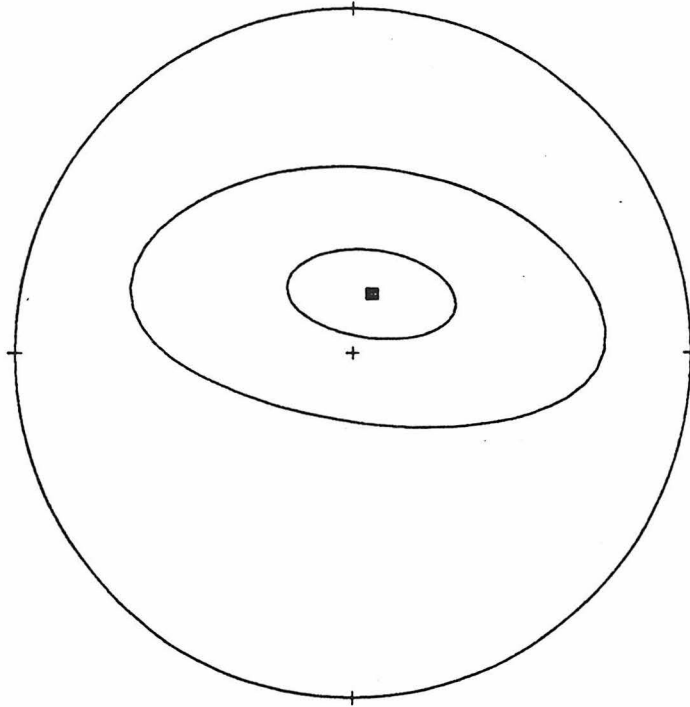
INTERMEDIATE
EVENTS

Bingham Statistics

Shallow Slabs



Compression

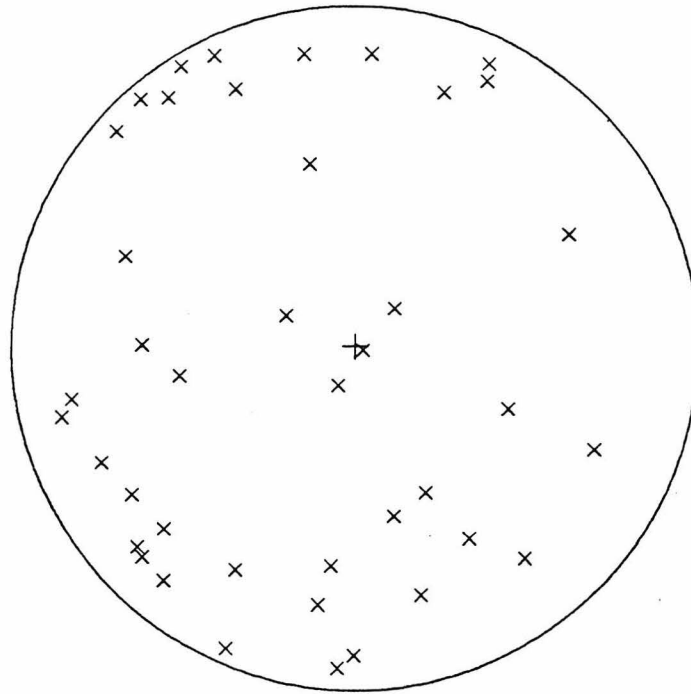


Tension

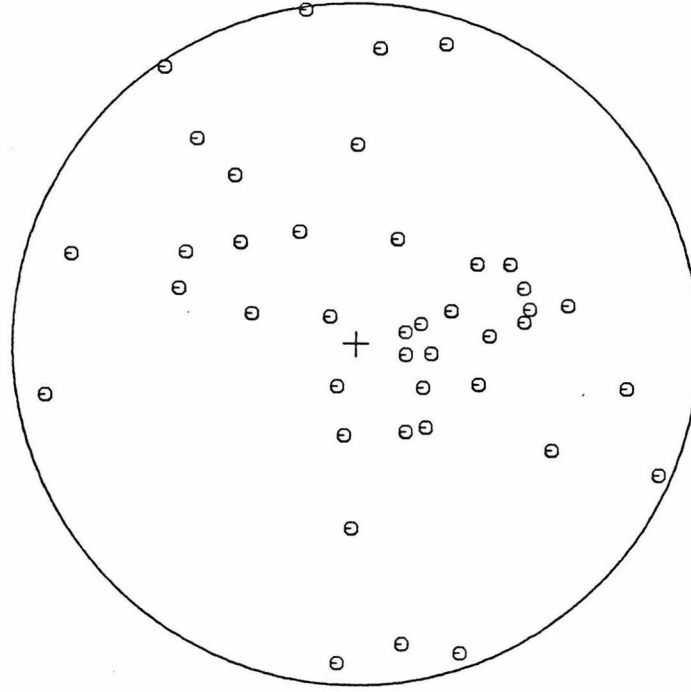
Figure 11. As figure 2, for intermediate earthquakes in slabs other than Tonga with maximum depths below 300 km. We separate Tonga because of its tendency, visible in figure 8, toward down-dip compression.

INTERMEDIATE
EVENTS

Deep Slabs Except
Tonga



COMPRESSION
AXES

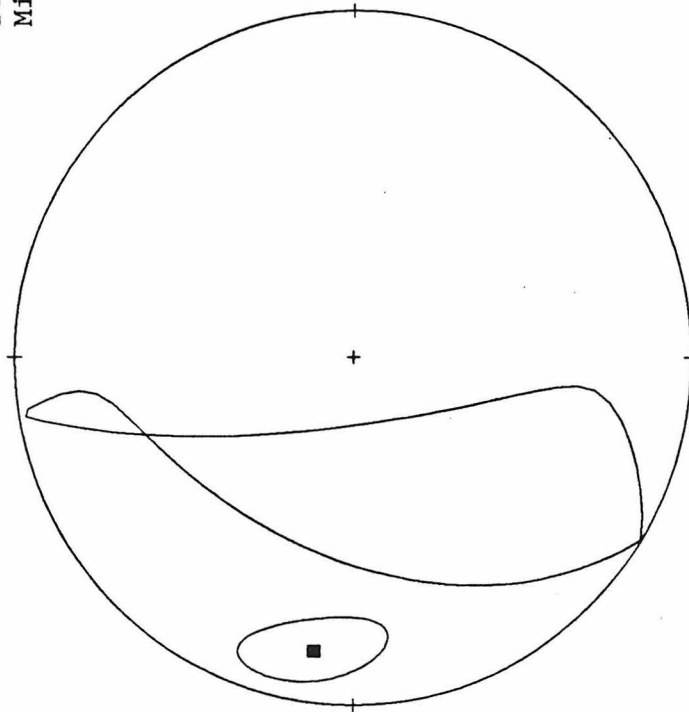


TENSION
AXES

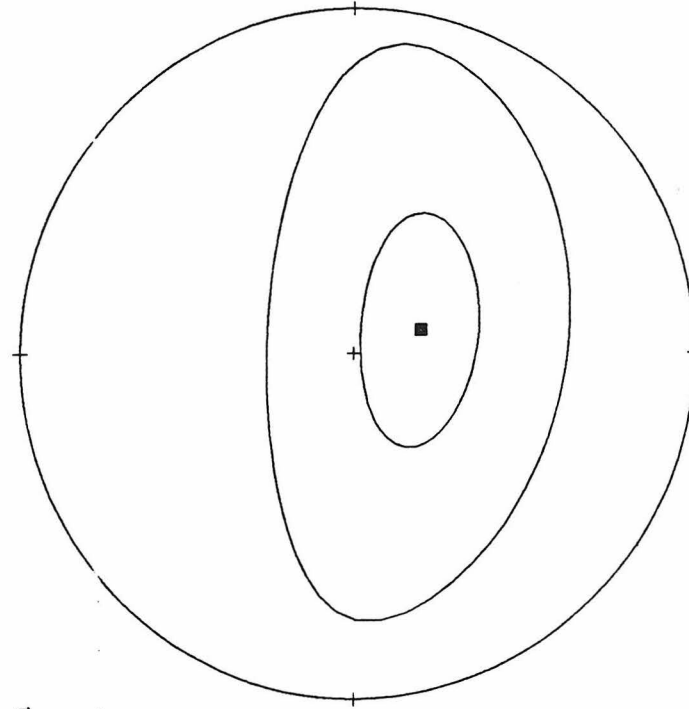
Figure 12. Bingham statistics, plotted as in figure 4, for data shown in figure 11.

INTERMEDIATE
EVENTS

Deep Slabs
Minus
Tonga



Compression



Tension

Bingham Statistics

3. Calculations of Stress in Subducting Slabs

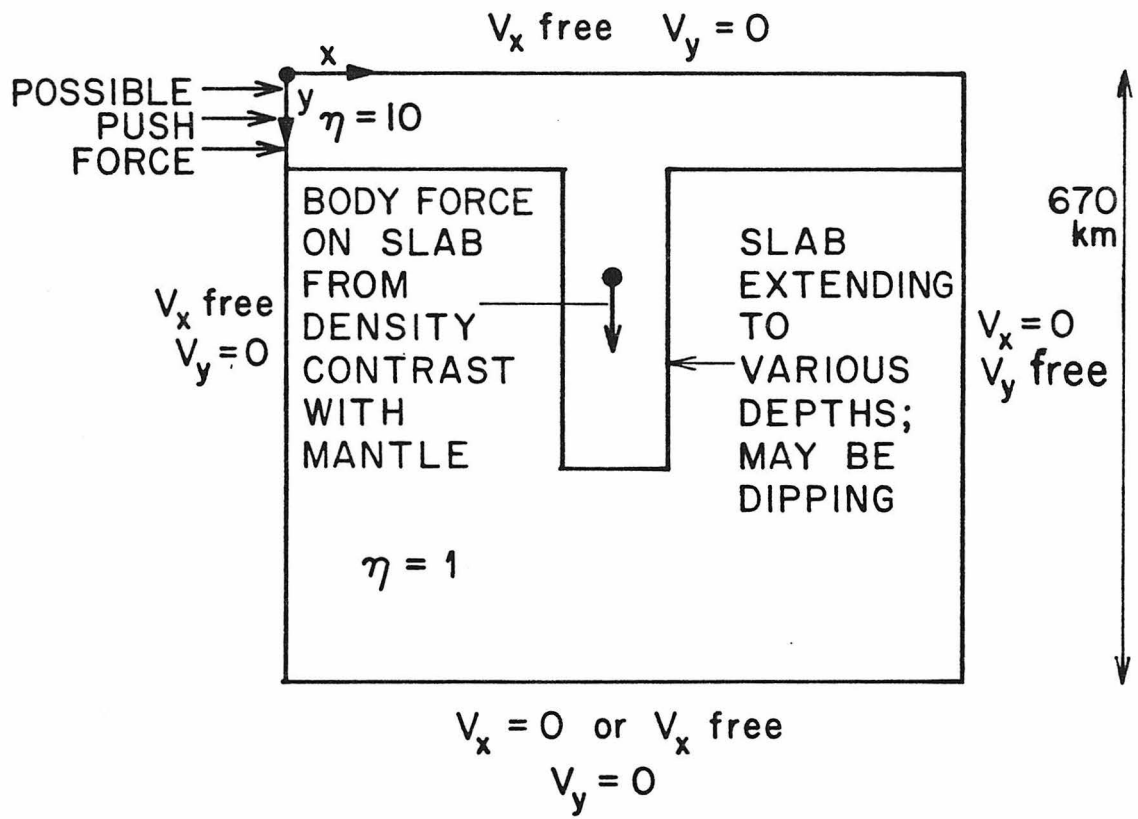
3.1 Introduction to the Models

We presume that, other things being equal, the number of earthquakes which will occur in a given area is related to the level of stress. Section 3.4 discusses this in more detail. We thus adopt some simple models of a subducting slab and calculate the stresses therein. We must emphasize that what we seek is not a detailed numerical simulation of any individual subduction zone-- a futile task given the complexity and many unknowns involved-- but a series of models which can elucidate the basic physical processes and give us qualitative insight.

It has long been thought that at long time scales the Earth's mantle behaves as a fluid, and that plate tectonic processes are associated with a large scale thermally driven mantle circulation. The literature on this topic is extensive. Hager and O'Connell (1981), O'Connell (1977), and McKenzie et al. (1974) are good starting points for one who is interested. We will not be reviewing here the solid state processes by which a solid mantle might creep or flow over geologic time. The literature here is also extensive, but we can quote Ashby and Verrall (1977) and Gueguen and Nicolas (1980) as general references.

Our models consist of a box of fluid, as shown in fig. 13. The slab is modelled as a denser and more viscous fluid than the surrounding mantle, as we will discuss shortly. We solve the Stokes problem for viscous incompressible flow via a penalty function, finite element method (Hughes et al., 1979). Typically we use grids of square or rectangular elements. We always have at least 20 elements depthwise in the box (y direction), and at least 40 in the x direction. All elements have a maximum dimension of 0.05 dimensionless units. We have slabs which are at least four

Figure 13. Boundary conditions used in the models.



elements thick. In cases where we are modelling the presence of discontinuities of some kind (Section 3.8), we double this resolution.

The surface of the Earth marks the top boundary, and we have the reasonable conditions (Sleep, 1975; Richter, 1973) that the fluid is free to move horizontally, but has zero vertical velocity. The depth 670 km. marks a bottom boundary which we begin by assuming marks an obstruction of some sort to the motion of the slab (e.g. Richter, 1979). We thus set vertical velocity to zero at this boundary. Horizontal velocity can be set to zero or left free. If horizontal velocity is set to zero, the boundary assumes the character of an extreme viscosity jump. A free horizontal velocity might be better for simulating a density discontinuity arising from chemical layering, where lateral motions might be occurring along the deforming chemical boundary. Of course, vertical motions would occur also, in the dynamic situation. We are obtaining instantaneous solutions; we cannot track the dynamic deformation of a chemical boundary. We accept $v_y = 0$ and v_x free as an approximation to the steady state at the boundary in the case of chemical layering. Leaving v_x free is a constant pressure boundary condition, with pressure equal to zero at the boundary. As we will soon see, the bottom boundary condition on v_x has very little influence on our important results-- it is the condition on v_y which is important.

The boundary conditions on the side of the box are more arbitrary and more artificial. Since the Earth, or a part thereof, cannot be regarded as an isolated box, it seems reasonable to allow fluid to enter and leave our model box. We have thus left the horizontal velocity free on the left hand side. In some models, we will be pushing the slab from the left. We have somewhat arbitrarily chosen to set v_x equal to zero on the right hand side. It turns out that the boundary conditions on the right, while they may influence some of the details of the flow field, make essentially no

difference to the results for the stresses in the slab, which are our primary concern. This can be seen on fig. 17, and figs. D17.

There are some other assumptions we are making. We are ignoring inertia and Coriolis forces, which are much smaller in our problem than the viscous forces (Sleep, 1975). We are also, obviously, ignoring the curvature of the Earth. As discussed by Richter (1973), this may cause some geometric distortion in the computed flow field compared to what might actually be happening in the Earth, but the basic dynamics will not be changed.

There are many things we do not know about subducting slabs, and the subject can usually offer much room for debate. One thing everyone seems to agree on, however, is that subducting slabs are colder and denser than the surrounding mantle. Gravitational forces on the slab are likely to be an important factor in the kinematics of the subduction process. How much colder one believes the slab to be than the mantle depends, of course, on one's thermal model. McKenzie (1969) solved the heat conduction equation for a subducting slab in a mantle of constant temperature T_0 . His 50 km thick, 45° dipping slab moving at 10 cm/yr warms to roughly $0.8T_0$ at its coldest by the time it reaches a depth of 700 km. Hence, for $T_0 = 1300^\circ$, it is over 250° cooler than the surrounding mantle. Howard and Hager (1983) have performed a very interesting calculation which refines McKenzie's model to include the effect of the cooling of the mantle as well as the heating of the slab. The material parameters they use in their model are the same as McKenzie's. In their model, the slab stays colder to a significantly greater depth than does McKenzie's slab, because of the buildup of a layer of cooler mantle on the sides of the slab. A 50 km slab in the Howard-Hager model warms up to $0.67T_0$ by 700 km; a 100 km slab warms up to $0.46T_0$. Thus, for $T_0 = 1300^\circ$, the slab may be about 700° cooler than the

surrounding mantle near the 670 km seismic discontinuity.

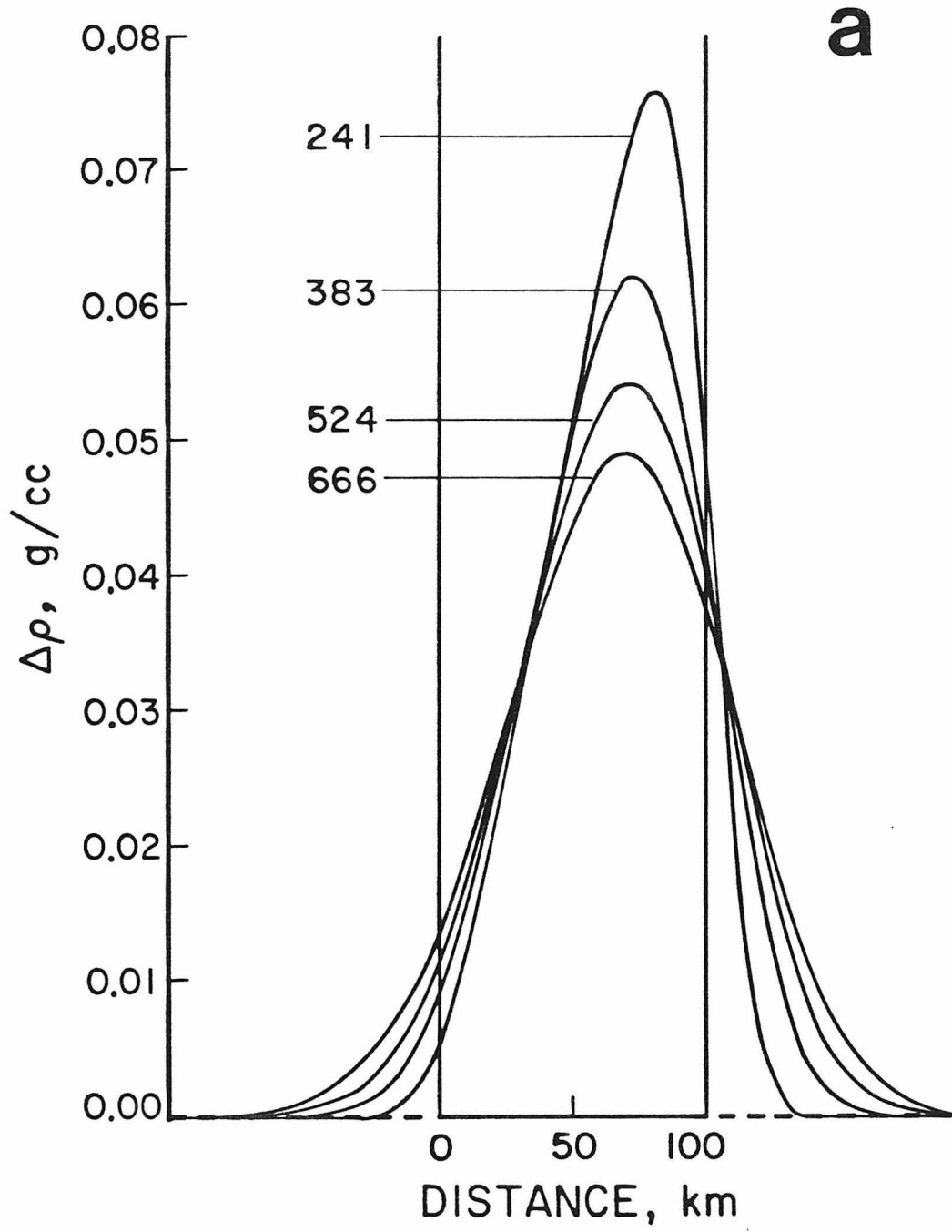
Howard and Hager, like McKenzie, have not considered the adiabatic gradient in the mantle, or the possible effects of shear heating and mantle phase transitions. Such effects have variously been considered in many studies: Minear and Toksöz (1970a,b); Toksöz et al (1971,1973); Hsui and Toksöz (1979); Turcotte and Schubert (1973); and Schubert et al (1975), among others. In several of these studies, the numerical calculations are so involved that it is sometimes difficult to isolate the effect of each individual factor, and it is also difficult to compare the models to each other. The coolest slab appears to be that of Schubert et al (1975), which at 650 km or so is a maximum of 800° cooler than the surrounding mantle. A highly exothermic olivine-spinel phase transition in the model may be partially responsible for this. We note that none of the models to which we have just referred treat the issue of the entrainment of the mantle, as Howard and Hager (1983) do.

Fig. 14(a) shows calculations of the density difference between slab and mantle for the Howard-Hager model with a 45° dipping slab moving at 5 cm/yr. The coefficient of thermal expansion is not well known, but is thought to be of order 10⁻⁵ (e.g. Sleep, 1975). We have somewhat arbitrarily adopted for α a value of 5 X 10⁻⁵, and 3.5 g/cc for the density of the mantle at 0° C. As we can see from the figure, the density contrast varies across the slab and with depth. In most of the models, we have assumed the density difference between slab and mantle to be 0.07 g/cc throughout the slab. As we shall see in Section 3.7, this does not affect our results.

Fig. 14(b) shows calculations of the viscosity ratio of the slab to the mantle. This ratio is of the form

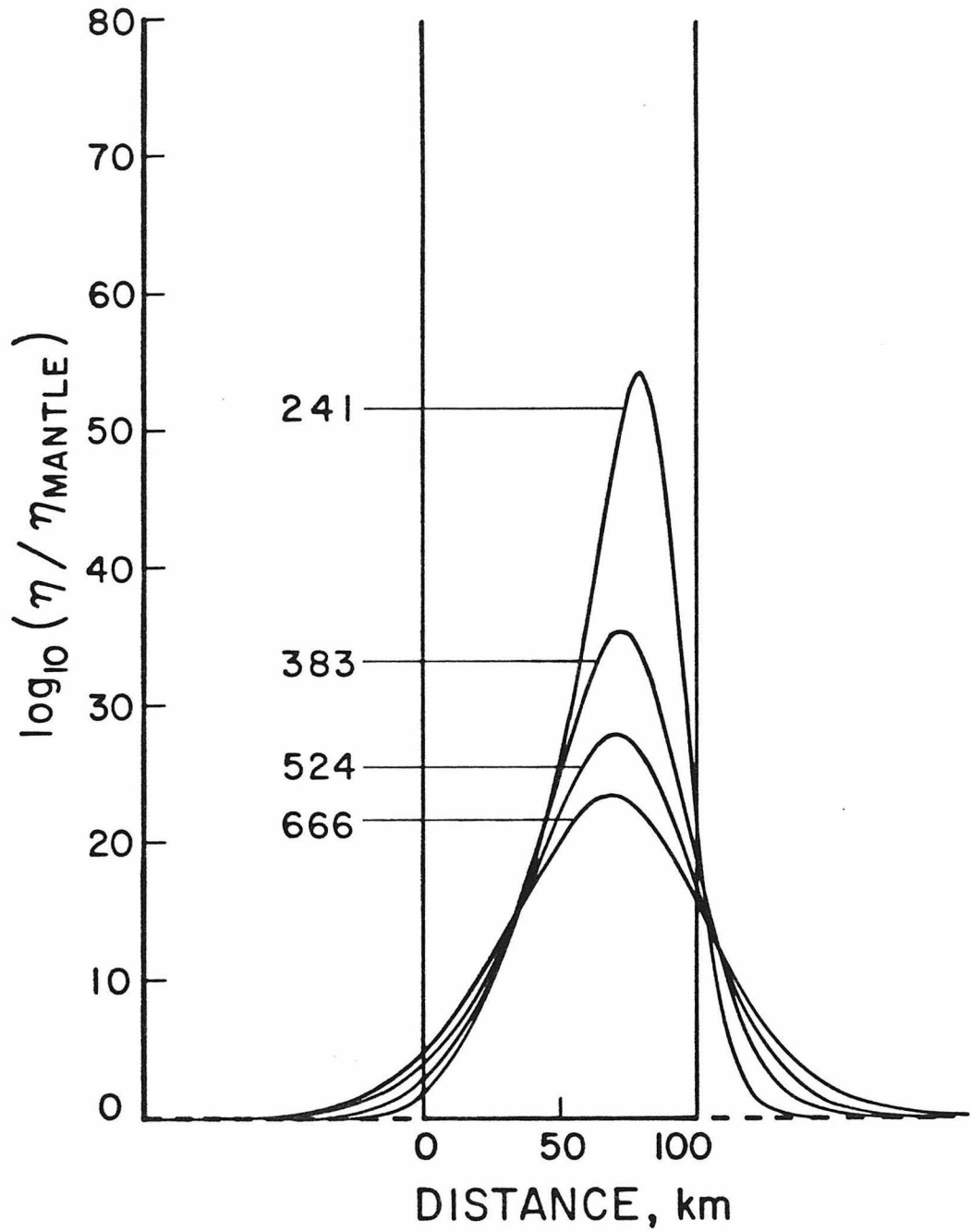
$$\frac{\eta_{T_1}}{\eta_{T_0}} = \frac{T_1}{T_0} e^{\frac{E}{R} \left(\frac{T_0 - T_1}{T_0 T_1} \right)}$$

Figure 14. Variation within the slab of (a) density contrast with respect to the mantle and (b) logarithm of the ratio of slab viscosity to mantle viscosity. In both cases, the slab is dipping 45° and travelling 5 cm/yr. Calculations are from the model of Howard and Hager (1983). Vertical parallel lines indicate boundaries of slab. Each curve is a perpendicular section through the slab, taken at the depth indicated by the curve label.



a

b



where T_1 is calculated temperature, T_0 is assumed initial mantle temperature, E is the activation energy for creep, and R is the universal gas constant. We have ignored a term dependent on the activation volume, since activation volume is essentially unknown. Since the precise composition of the slab is not known, we can only guess at E . We use Ashby and Verrall's (1977) value for olivine, 5.2×10^4 J/mol. The figure shows that we can expect viscosity in the slab to be everywhere essentially infinite with respect to the mantle.

Note, however, that the equation above calculates microscopic viscosity. Although we expect from the temperature that the slab is absolutely rigid microscopically, there is evidence that its macroscopic viscosity is lower. Macroscopic and microscopic viscosities can differ if, for example, the slab is fractured. Melosh and Raefsky (1980) found that an effective viscosity of about 6×10^{22} p is required to explain the outer arc bulge and trench if these are formed by bending a viscous lithosphere. The mantle is believed to have a viscosity of roughly 10^{22} p from post-glacial rebound studies (Cathles, 1975; Peltier and Andrews, 1976). Thus our assumption of a slab viscosity ten times greater than the mantle viscosity is probably reasonable.

3.1.1 A Word About Units

We solve a series of problems for a box which has depth h equal to 1. The two fluids in the box simulating mantle and slab have viscosities of 1 and 10 respectively. We apply a downward body force of 1000 to the slab. The results we obtain are not in any conventional unit. The reader will notice, however, that in all our figures we report stress in bars and velocity in cm/yr. These results are correct when the problem is scaled such that $h = 670$ km, the viscosity of the mantle is 10^{22} p,

and a body force of 1000 corresponds to a density contrast of 0.07 g/cc between slab and mantle. Stress scales as $\Delta\rho gh$, and velocity scales as $\frac{\Delta\rho gh^2}{\eta}$, where g is acceleration due to gravity and η is viscosity. It is important to note that stresses do not depend on the absolute value of the viscosity, whereas velocities do. To convert back to the "natural" dimensionless units of the problem, one needs only to divide stress in bars by 4.72, and no conversion is required for the velocities.

3.1.2 Presentation of Results

We have calculated stresses and flow fields for a large number of models. For all these models, we present plots of stress magnitude versus depth in the slab (see 3.2 below) in the main body of the text. In a number of cases, we also present spatial stress plots (showing stress orientation) and velocity fields; however, the large number of models would have made it impractical to include these in the text for every case. Since the spatial stress plots and the flow diagrams do contain important information, we have placed the ones not included in the text in Appendix D. The figures in Appendix D, as we explain there, are labelled so as to allow them to be easily identified with the corresponding figures in the text.

3.2 A Sinking Vertical Slab

We now examine the results of some simple calculations which yield much insight in explaining the seismicity curves. The slab sinks under its own weight, and is not subjected to external push forces. Consider the model of a vertical slab, with parameters as discussed in the previous section. Fig. 15 shows the flow field. The slab is moving at a velocity on the order of centimeters a year. Fig. 16 plots the axes of compression of the deviatoric stress at points throughout the model box (at

the center of each finite element). The axes of tension are perpendicular to the axes of compression, and of equal magnitude. We see that the slab is in vertical (i.e., down-dip) tension on top, and down-dip compression on the bottom. In fig. 17, we plot the average stress magnitude in the slab versus depth. We define the stress magnitude as

$$\sigma = \sqrt{1/2 (\tau_{xx}^2 + \tau_{yy}^2 + 2\tau_{xy}^2)}$$

where the τ_{ij} are stress components. This is actually the expression for the second stress invariant. At each depth, we calculate σ for all points in the slab, take the average, and plot on fig. 17.

The calculated stress profile has the following features: (1) a linear decrease down to ≈ 300 km, (2) a minimum between 300 and 400 km, and (3) a resurgence at depth. In a rough sense, it seems to follow the same pattern as the curves of $\log N$ versus depth. The linear decrease in the upper part of the stress profile could explain the linear-log decrease of seismicity in the upper parts of subducting slabs quite nicely if the number of earthquakes depended exponentially on the stress. (e.g. Mogi, 1962a,b, and section 3.4). The position of the stress minimum also suggests that the seismicity minima might be occurring at a depth dictated by the 670 km length scale to a bottom barrier. We note that whether v_x is free or zero at the bottom boundary makes essentially no difference. The barrier can be a chemical one or a viscosity jump.

Figure 15. Flow field for a vertical sinking slab extending to 670 km, subjected only to gravitational forces, as described in Section 3.2.

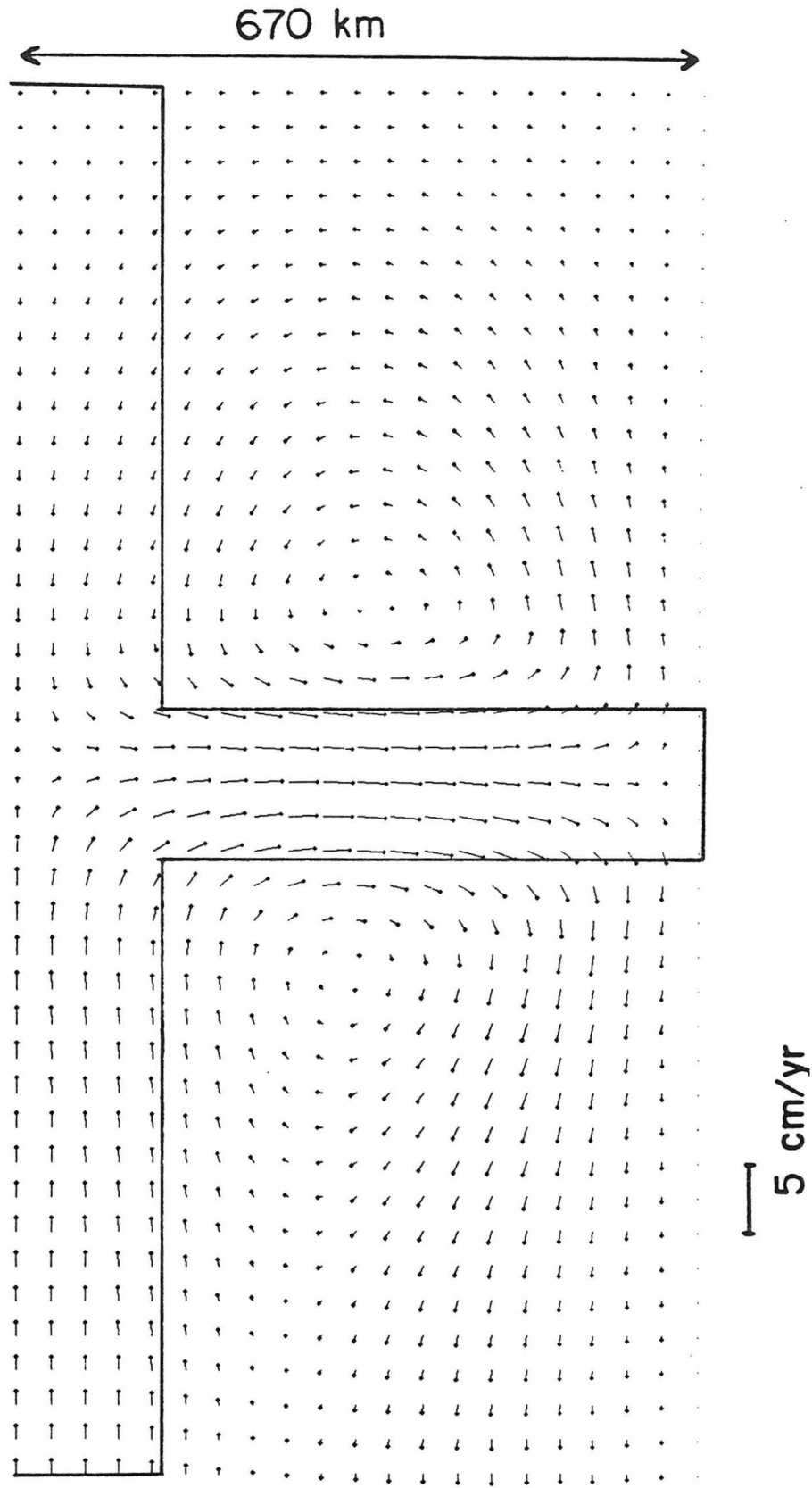


Figure 16. Deviatoric compression axes for the slab of figure 15 and section 3.2.
Tension axes are of equal magnitude, and perpendicular in direction.

— | Kbar

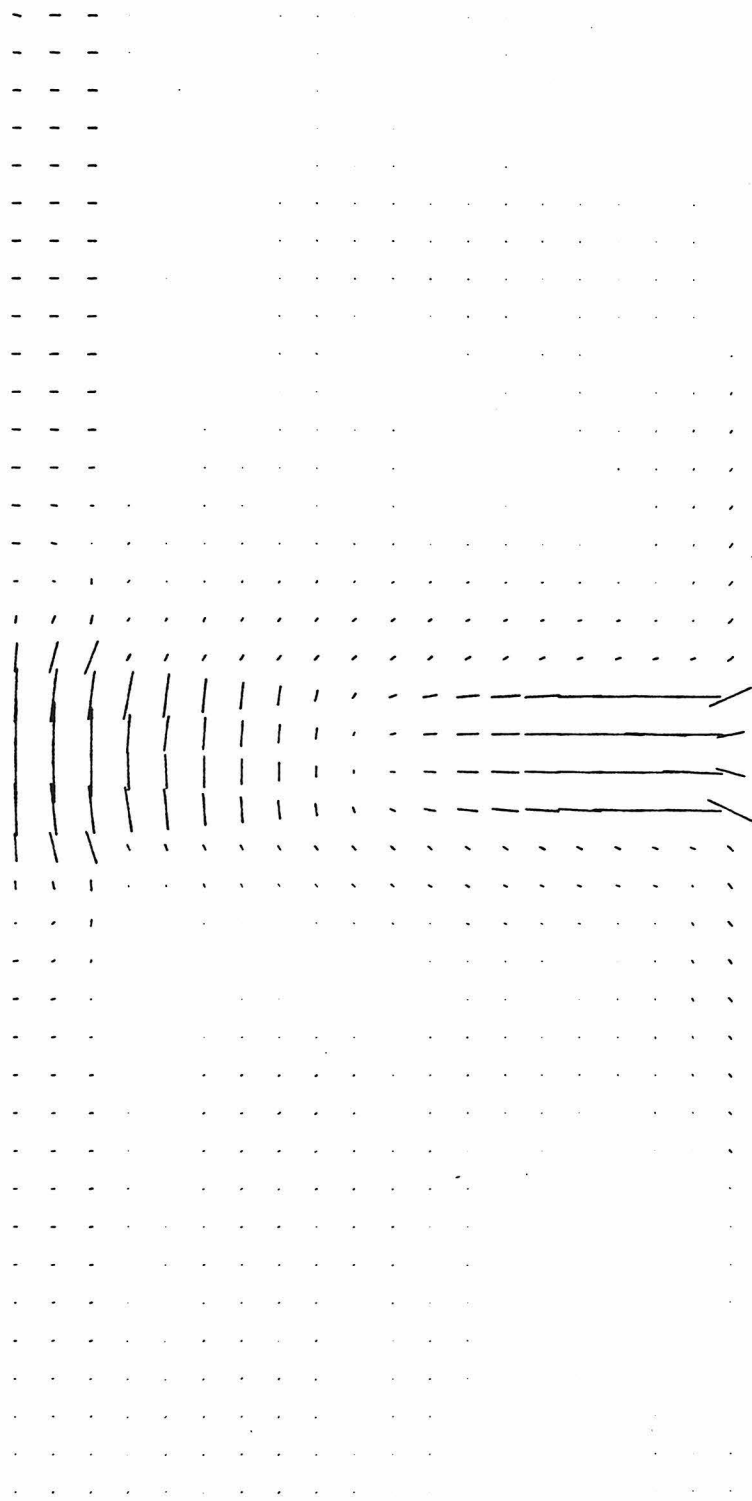
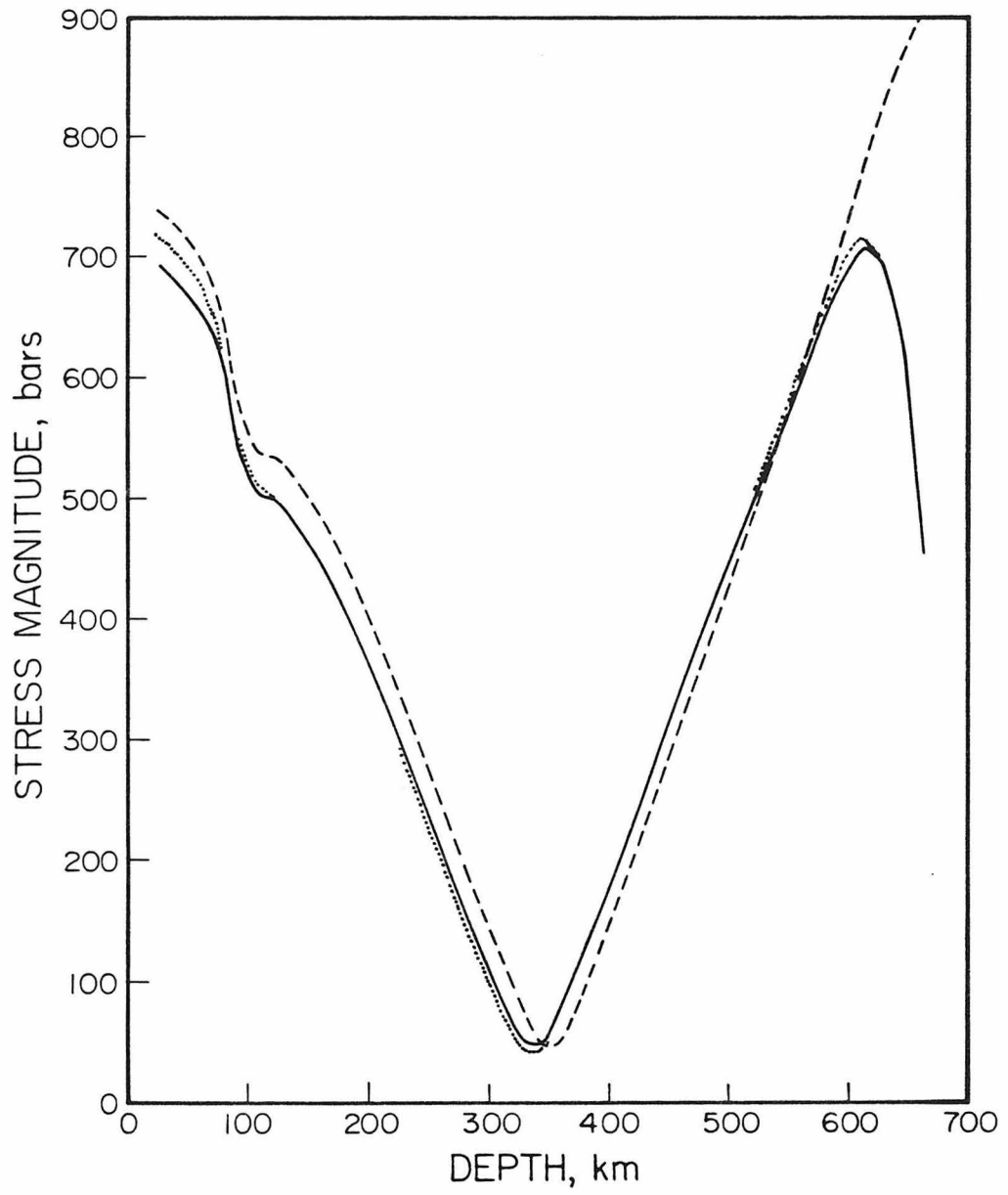


Figure 17. Solid line shows average stress magnitude versus depth for the slab of section 3.2 and figure 15. Dashed line shows result for the same slab except that v_x is left free on the bottom boundary instead of being set to zero. Dotted line shows result for the same slab when v_x is left free on the right hand boundary instead of being set to zero.



3.3 Viscosity Contrast at 670 km

Suppose now that there is no barrier at 670 km. Fig 18 shows the stress profile for a slab extending to 670 km, but underlain by mantle fluid of viscosity 10^{22} p. (Our model box is now twice as big in both dimensions). We do not see the minimum or the resurgence, but rather a smooth decay. The slab is in tension, except at its very tip.

Fig. 19 shows what happens if we increase the viscosity of the lower mantle, creating a contrast at 670 km. As the viscosity contrast increases, the stress minimum, below which compression prevails, moves up in depth. A viscosity contrast of a factor of 5 produces a significant peak. A contrast factor of 25-50 produces a large peak, which is not much different in position or intensity from the case when the contrast is 1000-- or essentially infinite, as in fig. 17.

How viscous is the lower mantle in fact? At present, this question is not completely resolved, but there is some evidence that it could be more viscous than the upper mantle. A good discussion of the literature is given in O'Connell (1977). As we have noted, the upper mantle appears, from analysis of post-glacial rebound data, to have a viscosity of 10^{22} p (There is a possible low viscosity channel below the lithosphere; how low its viscosity can be depends on its thickness). Cathles (1975) has fit the data with a 75 km thick channel with viscosity of order 10^{20} p). The earlier literature (MacDonald, 1963; McKenzie, 1966) favored a large increase of viscosity with depth in the mantle. McKenzie (1966) concluded that the lower mantle had a viscosity four orders of magnitude greater than the upper mantle. His conclusion was based on interpreting the Earth's nonhydrostatic "fossil" bulge. However, it appears that his results were an artifact of his use of spherical harmonic coefficients. They were questioned by Goldreich and Toomre (1969), who placed an upper bound of 10^{24} p on the viscosity of the lower mantle from the rate of polar wander obtained

Figure 18. Average stress magnitude versus depth for a vertical slab subjected only to gravitational forces and extending to 670 km, when there is no barrier at 670 km. depth.

(X 10)

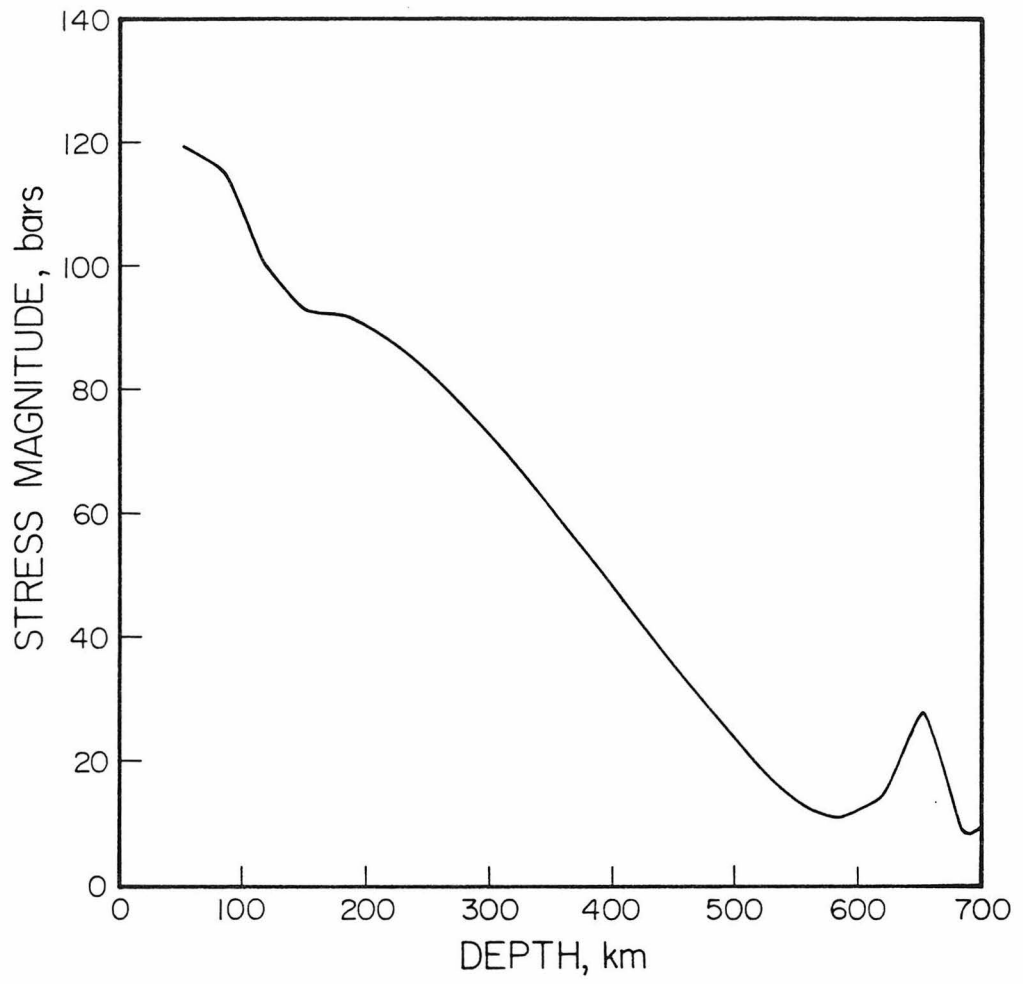
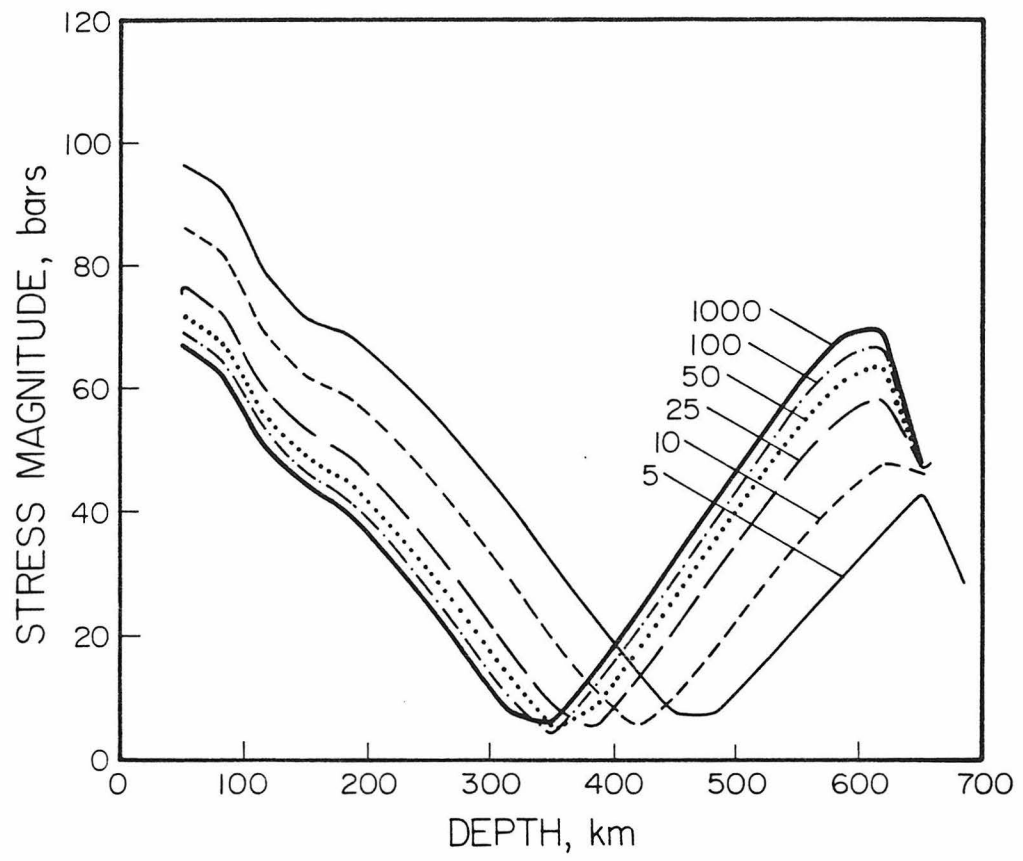


Figure 19. Average stress magnitude versus depth for a vertical sinking slab extending to 670 km when there is a viscosity contrast at 670 km depth. The number labelling each curve denotes the ratio of viscosity below to viscosity above the discontinuity. Viscosity above the discontinuity is 10^{22} p.

(x 10)



from paleomagnetic studies. Cathles (1975) interpreted the Canadian post-glacial rebound data to indicate a lower mantle viscosity of 10^{22} p the same as the upper mantle. Walcott (1973) believed the data to indicate a lower mantle viscosity of at least 10^{23} p. As O'Connell (1977) points out, Walcott's analysis considered the residual gravity anomalies in Canada associated with unrecovered rebound. Cathles (1975) believed the data to be consistent with either his or Walcott's model, the choice depending in large measure on the significance attached to the residual gravity anomalies. More recently, Yuen et al. (1982) estimated the viscosity of the lower mantle to be larger than that of the upper mantle by analysing observed secular motions of the Earth's rotation axis. They found it to be larger than the viscosity of the upper mantle, at most by a factor of 4. Hager (1983), by considering geoid anomalies, has found that the contrast factor must be as high as 30 in subduction zones. Thus we see that, overall, the available data are consistent with enough of a viscosity barrier at 670 km to produce stress patterns in the slab matching observed seismicity profiles.

3.4 Relationship of Seismicity to Stress Levels

Before exploring more models, we pause to consider the important question of the relationship of seismicity to stress levels. Qualitatively, our results make sense if we assume only that a higher level of stress leads to a larger number of events. They make even more sense if the number of events depends exponentially on the stress. The linear-log decrease of seismicity in the shallow portion of slabs, as well as the relative numerical levels of deep and shallow seismicity, are nicely explained. All this assumes that the dependence of seismicity on stress does not change drastically with depth.

Let us further examine the idea that $N \propto e^{k\sigma}$, where k is some constant, and σ denotes the stress magnitude. It has long been known (Ishimoto and Iida, 1939) that earthquakes follow a frequency-magnitude relation of the form

$$\log N = a - bM$$

where a and b are positive constants known universally in the seismological literature as the " a value" and the " b value" (Richter, 1958; Bath, 1981). We may rewrite this as

$$\log N = b(M_{\text{max}} - M)$$

where M_{max} , the maximum magnitude of earthquake is equal to $\frac{a}{b}$ — provided, of course, that the linear relationship holds throughout the magnitude range. If b is not a function of stress, we have that $N \propto e^{M_{\text{max}}}$. If $M_{\text{max}} \propto \sigma$, then $N \propto e^{k\sigma}$. There is no compelling reason to assume that $M_{\text{max}} \propto \sigma$. We are merely trying to see the conditions under which the empirical distribution of earthquake sizes might lead to the type of exponential dependence on stress which has been observed experimentally, and which would provide a link between our slab stress calculations and observed seismicity curves.

The experiments where $N \propto e^{k\sigma}$ has been observed have been acoustic emission studies on the brittle failure of rock samples. In evaluating such experiments in connection with our problem, we are faced with the omnipresent difficulty of scaling. How relevant rock mechanics experiments on small samples are to the real Earth is a long standing unresolved question (e.g. Iio, 1982). We are also faced with the difficulty of applying results from brittle fracture experiments to deep focus earthquakes whose mechanisms, albeit consistent with shear dislocations, are not known to result

from brittle failure. However, the results of the experiments are worth reviewing. This is because, first of all, these results are all we now have at our disposal. Secondly, we must bear in mind that brittle failure, although not a certain mechanism for earthquakes at depth, is still a possible one, particularly if the slab retains significant amounts of pore fluid. This is particularly true for the relatively shallow depths (above 250 km) where we are interested in finding an explanation for the linear-log decrease in number of events with depth.

Mogi (1962a,b) performed experiments establishing that microfractures in rock samples obey a frequency-magnitude relation similar to that of earthquakes. He found in his experiments that the number of events was proportional to the exponential of the applied stress. This dependence was subsequently used in certain seismic hazard studies (Hagiwara, 1974). Scholz (1968) conducted more rock mechanics experiments, and found the b value to decrease with stress. This complicates the exponential dependence of number of events on stress. However, this stress dependence of the b value has subsequently been disputed. Mogi (1981) presents data showing that under a constant load, the b value of the microfractures decreases before the main rupture. Ohnaka and Mogi (1981) argue that "the relative increase in the number of emission events with larger amplitude [i.e., the decrease in the b value] is not due directly to the increase in the stress level itself. The effect can be explained reasonably if the stress drop and/or the source dimension (crack size) of emission events become larger in statistical terms as the rock approaches failure". Other data (Kusunose et al., 1980; Sano et al., 1982) have also displayed the effect of a relatively constant b value until the sample comes close to failure. The b values of Kusunose et al. (1980) are constant until the stress exceeds 85% of the fracture strength. Sano et al. (1982) believe that their b values show evidence of

decreasing stress, but this is, again, for a deformation regime close to the macroscopic failure of the rock. There is thus no convincing experimental evidence that the b value changes significantly with stress.

If the b value did change with stress, then we might expect from our calculations that it would change with depth in the Earth. Gutenberg and Richter (1954) reported b values for shallow, intermediate, and deep earthquakes respectively as 0.9 ± 0.02 , 1.2 ± 0.2 , and 1.2 ± 0.2 . Fig. 20 shows frequency-magnitude plots for the catalogs we have used in this study for shallow, intermediate, and deep earthquakes. We focus our attention on the magnitude range between 5 and 6, where the linearity of the frequency-magnitude relation is most apparent. For the smaller events the relationship breaks down, because of inadequate detection capability. For larger events, it breaks down again, both because of the saturation of the m_b scale (Kanamori, 1978) and possibly because of inadequate sampling of larger events over the sixteen year time period. There is no evidence in fig. 20 that b value changes with depth. Plotting a figure like fig. 20 for 100 km depth intervals also fails to provide such evidence. Chouhan and Srivastava (1970) report a depth dependence of b value based on an analysis of Gutenberg and Richter's (1954) data in 100 km depth intervals. Their results indicate a roughly constant b value of 0.65 for events above 400 km in depth, a value of nearly 0.8 below 500 km, and a value of almost 1.1 from 400-500 km. We do not believe these results are significant given the small number of events in each sample. The observation by Abe (1981) of a b value increasing with depth for the large events in the data set of Abe and Kanamori (1979) suffers from the same limitation, as we can see by examining fig. 21. The b value for the deep events is not well constrained. We note, finally, that Kagan and Knopoff (1980), in a rigorous statistical study of the NOAA catalog, find no

Figure 20. Logarithm of the number of earthquakes versus one-second body wave magnitude m_b , in intervals of 0.1 magnitude unit. A is for shallow (less than 70 km) events; B is for intermediate (between 70 and 300 km) events; and C is for deep (greater than 300 km) events. Data sources are the NOAA and PDE catalogs, 1964-1980.

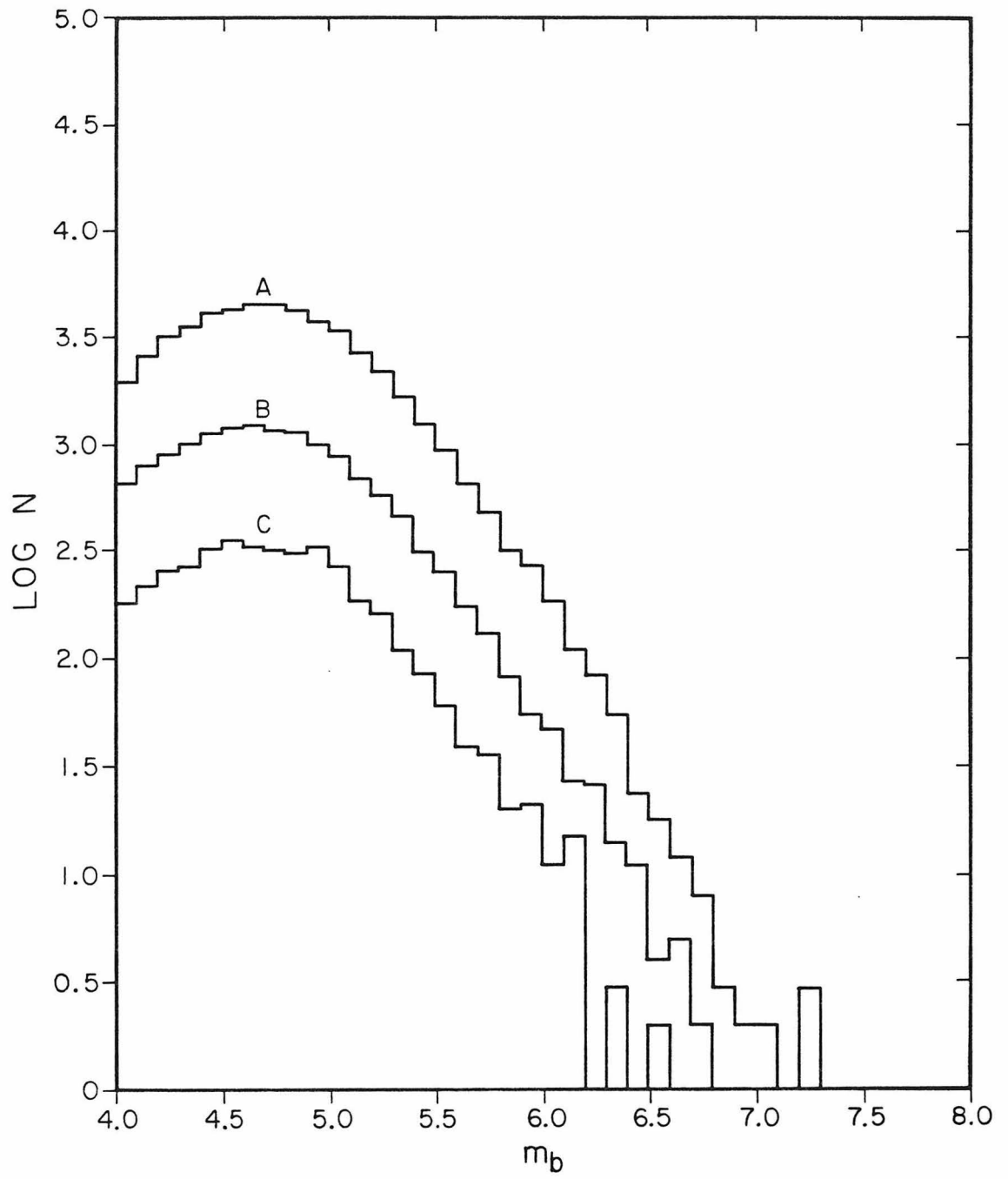
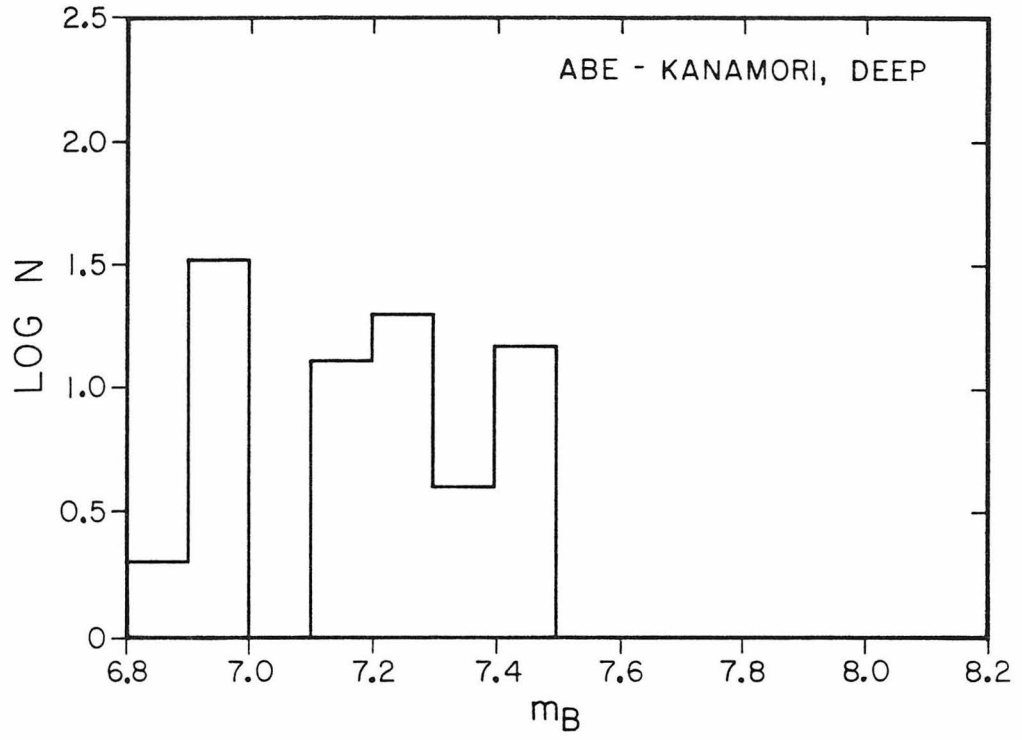
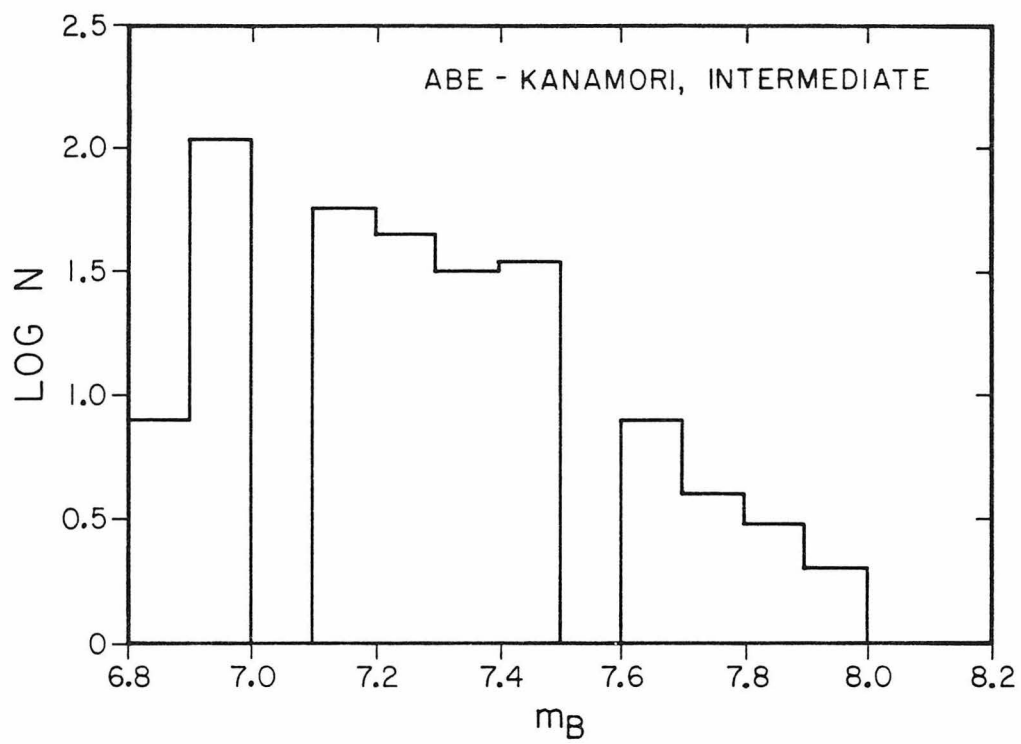


Figure 21. Logarithm of number of earthquakes versus long period body wave magnitude m_B for large events of the twentieth century compiled by Abe and Kanamori (1979). Figure 21(a) is for deep events; figure 21(b) is for intermediate events.

a



b



significant differences in the b values of shallow, intermediate, and deep events.

3.5 Finite, Dipping Slabs

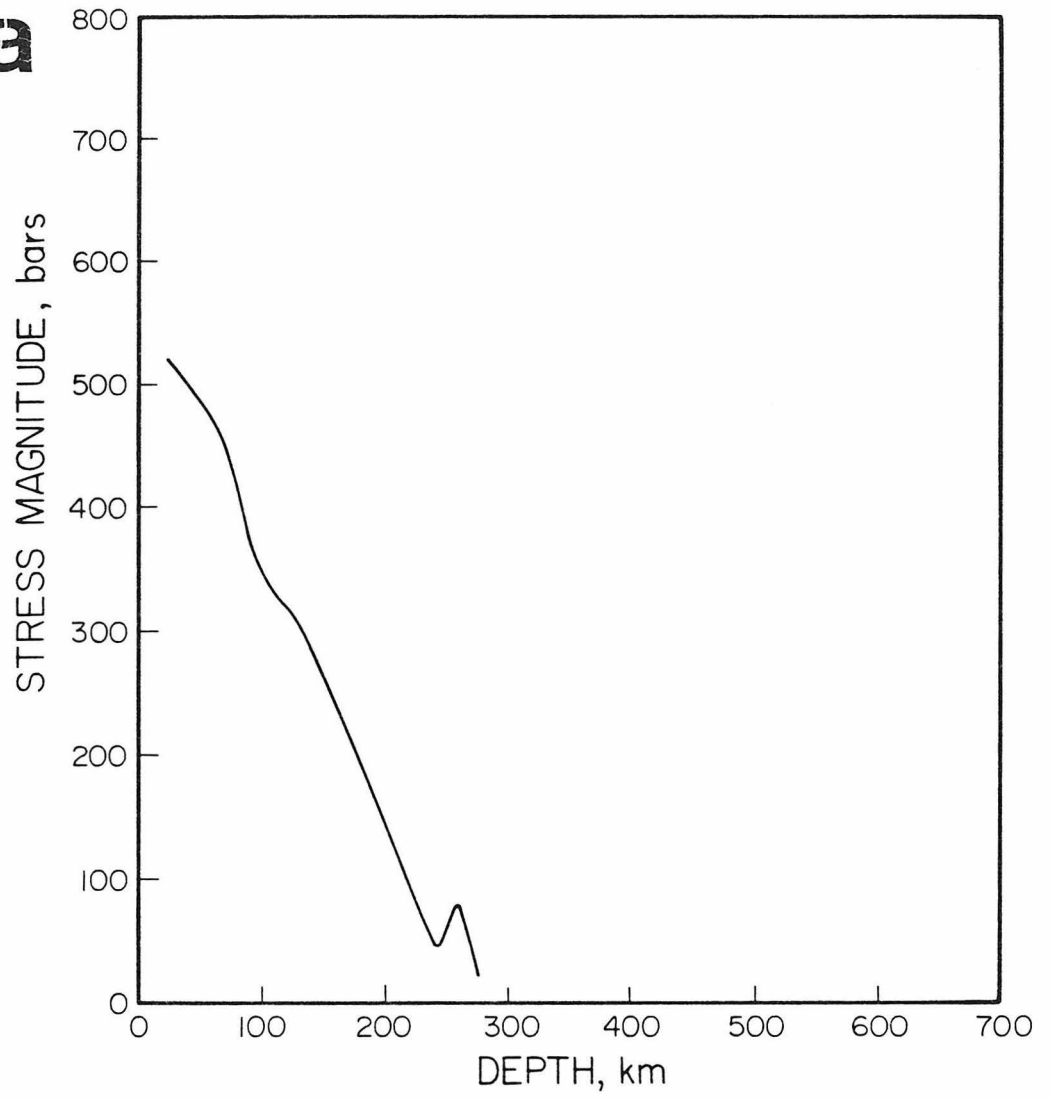
All slabs do not extend to 670 km, and we might raise the question of whether finite slabs in our model can give us acceptable stress profiles. Fig. 22 shows that this is in fact the case. A vertical slab extending to less than 300 km, sinking under its own weight, has a smooth decay of σ with depth. One extending deeper develops a peak, as the bottom boundary begins to be felt. We note that the shallow slab of fig. 22 is in tension, while deeper ones are in tension on top and compression on the bottom below the stress minimum.

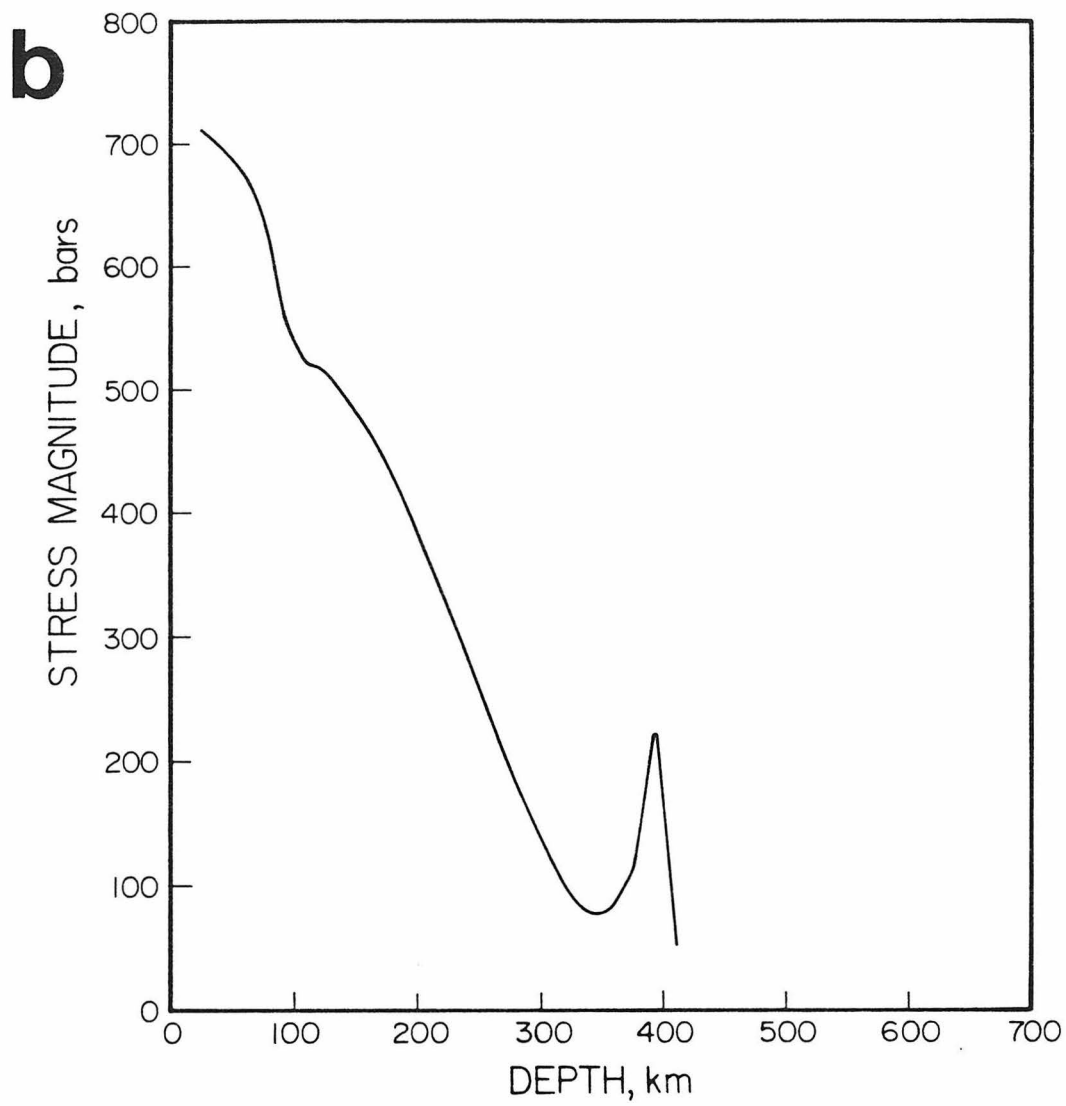
What happens when the slab is dipping? Fig. 23 shows the results for a 60° slab, and fig. 24 for a 45° slab. All parameters in the models are the same as for the vertical slab, except that the slab is now dipping. The overall stress levels are lower than in the vertical slab because the body force is the same, but is not directed down-dip. Overall, the dipping slabs show the same qualitative features as the vertical one. There is more difference between the v_x free and the $v_x=0$ case when the slab extends to 670 km, but this is still not a difference resolvable in the seismicity data.

In general, the shallow decay, the minimum, and the resurgence are there. There is some complexity caused by the dip, because of sagging effects. The shallow decay is less smooth, the deep peak is not as pronounced, and the minimum is somewhat broader in the 45° case than in the 60° case, and this is also true of the 60° slab with respect to the vertical one. Of course, $\log N$ versus depth for the various regions is not always smooth in the shallow portion, and does not always show a pronounced deep peak. We cannot, however, see any pattern of the complexity of the

Figure 22. Stress profile for a vertical slab subjected only to gravitational forces, extending to (a) 270 km, (b) 400 km, and (c) 540 km.

a





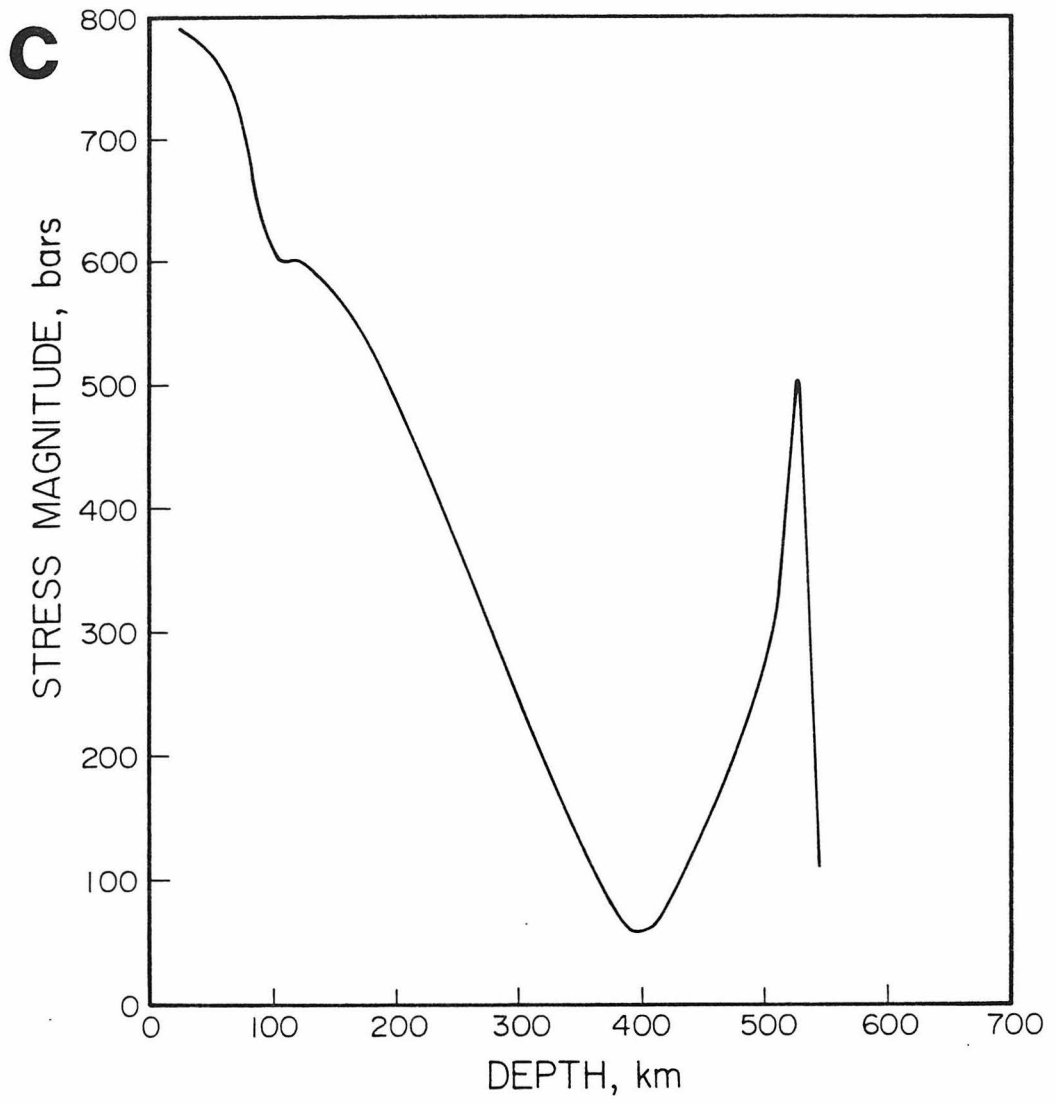
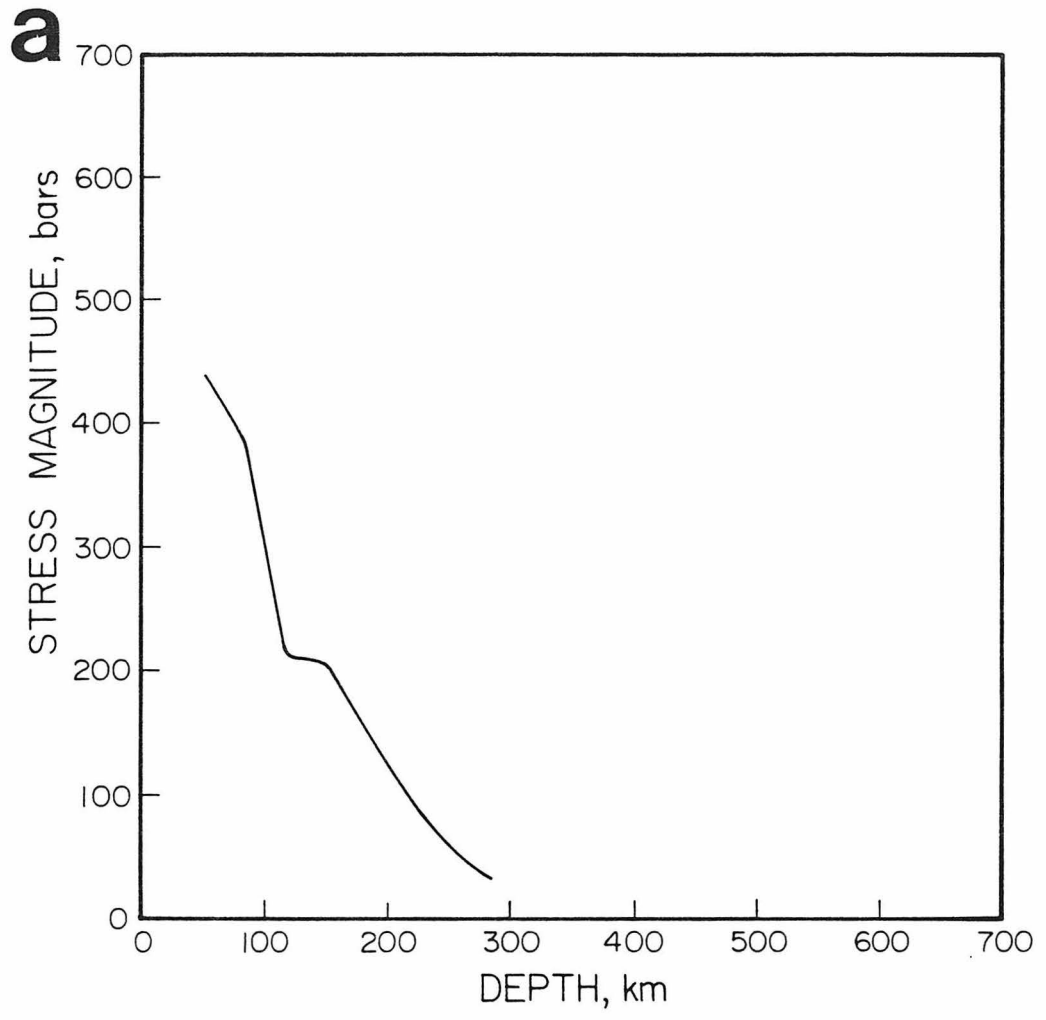
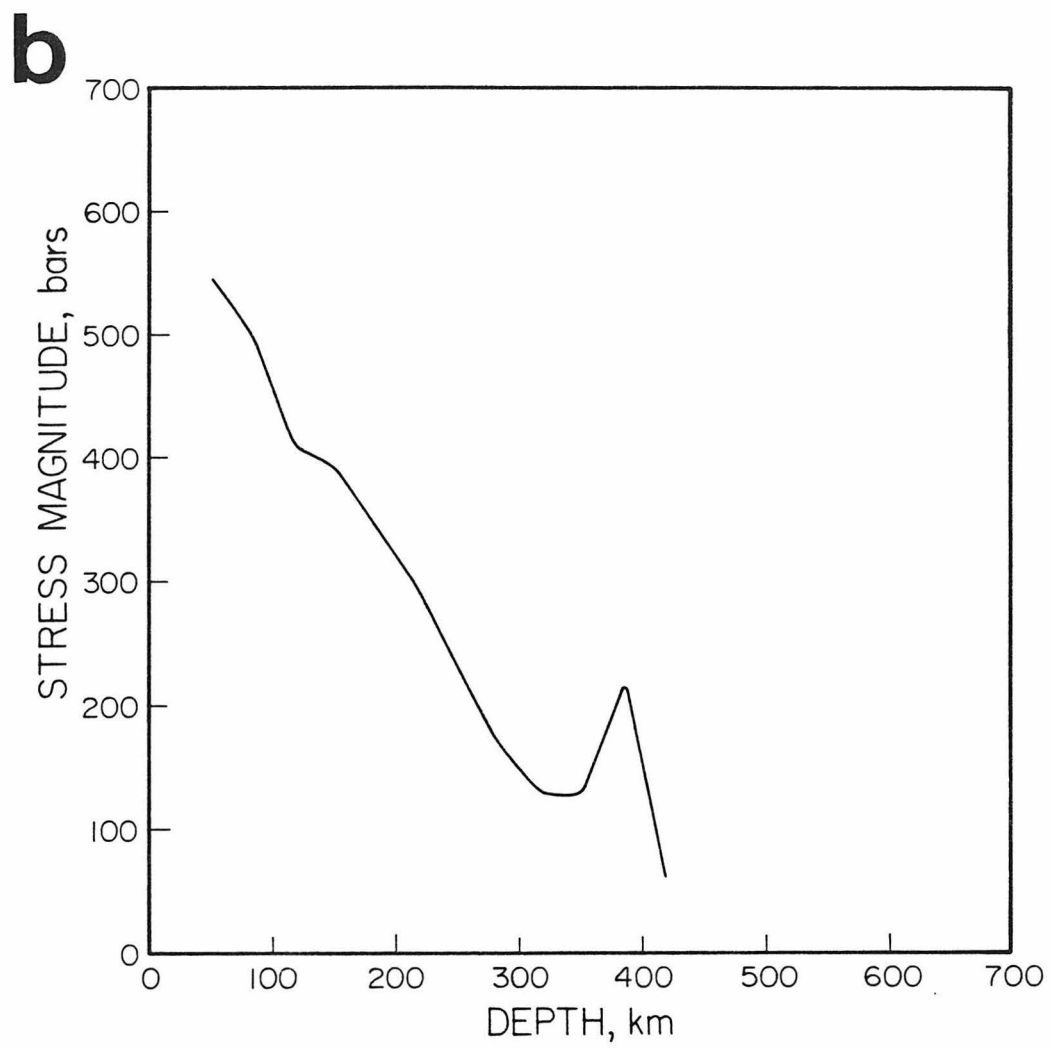
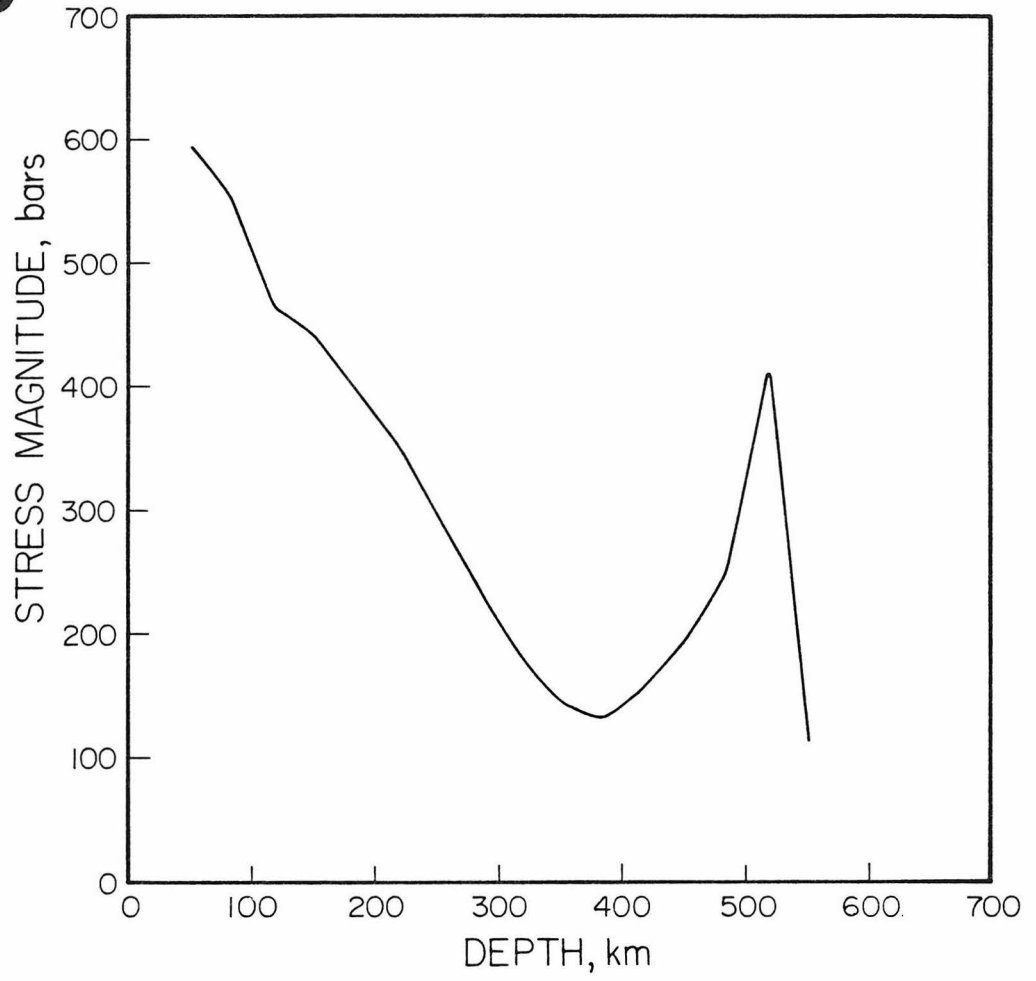


Figure 23. Stress profile for a 60° dipping slab extending to (a) 270, (b) 402, (c) 540, and (d) 670 km. Dashed curve in (d) is for v_x free on the bottom boundary; solid curve is for $v_x=0$ on the bottom boundary. Figure 23(d) is the only case where the two curves do not effectively coincide. The slab is subjected only to gravitational forces.





C



d

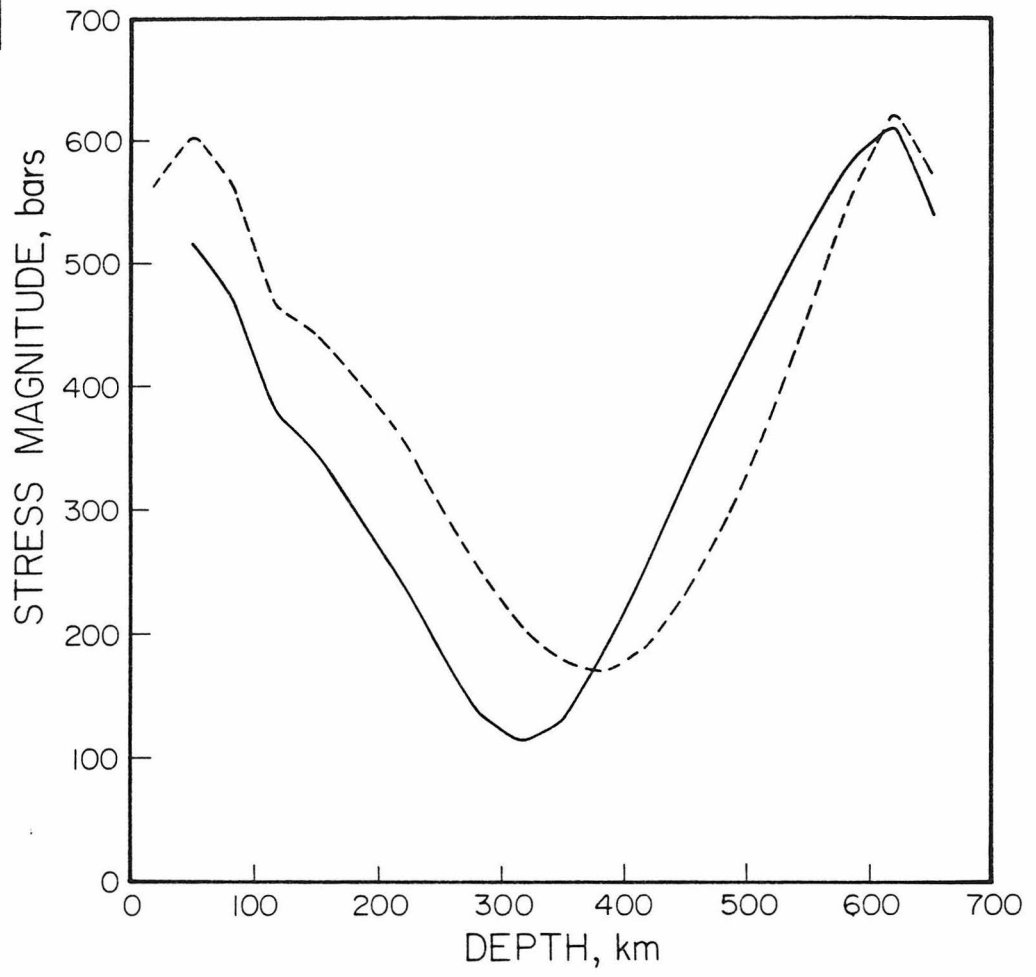
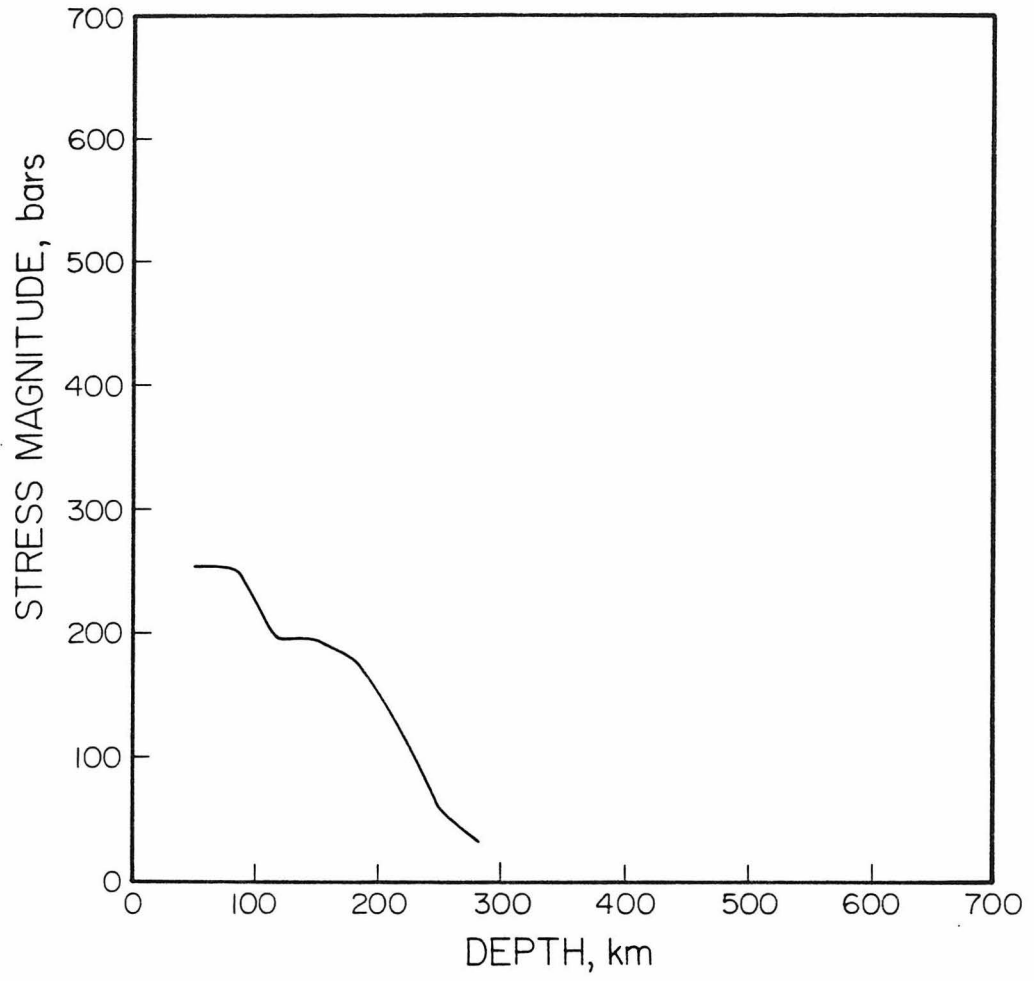
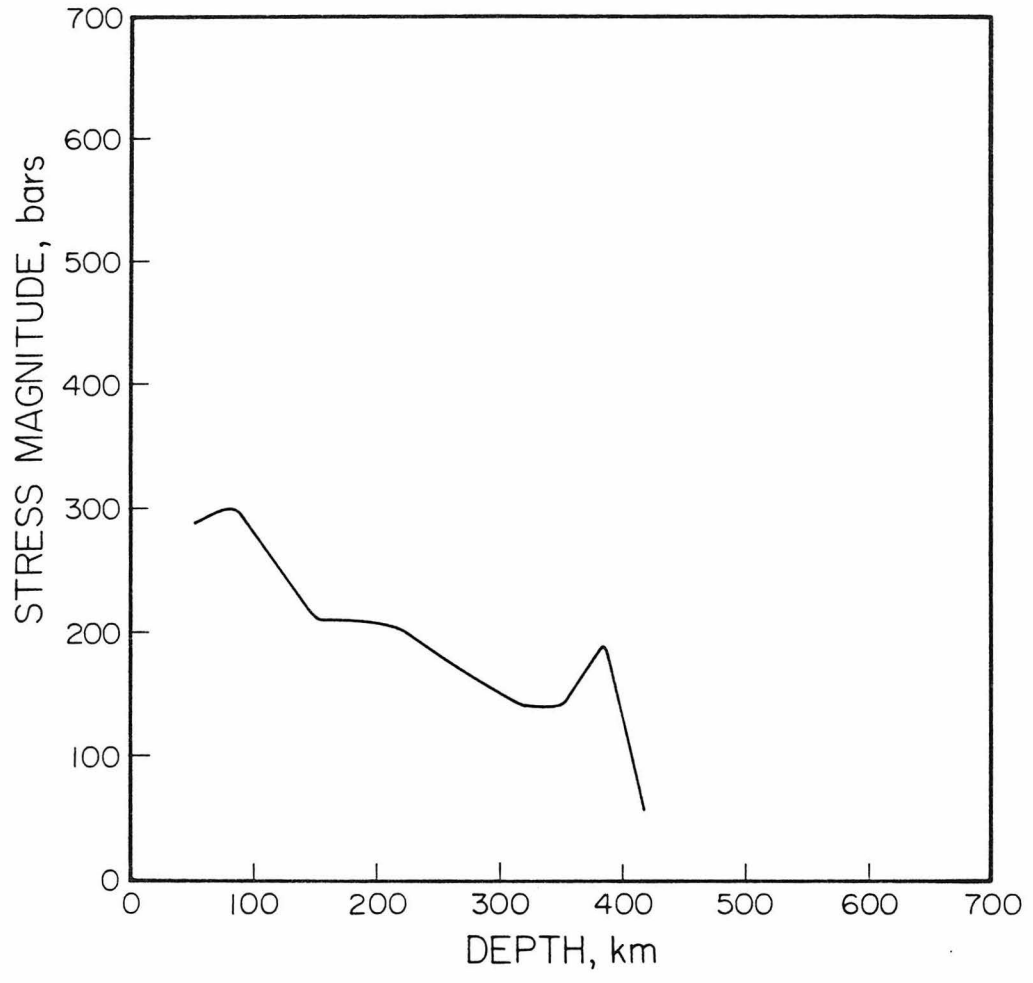


Figure 24. Precisely as figure 23, but for a 45° dipping slab.

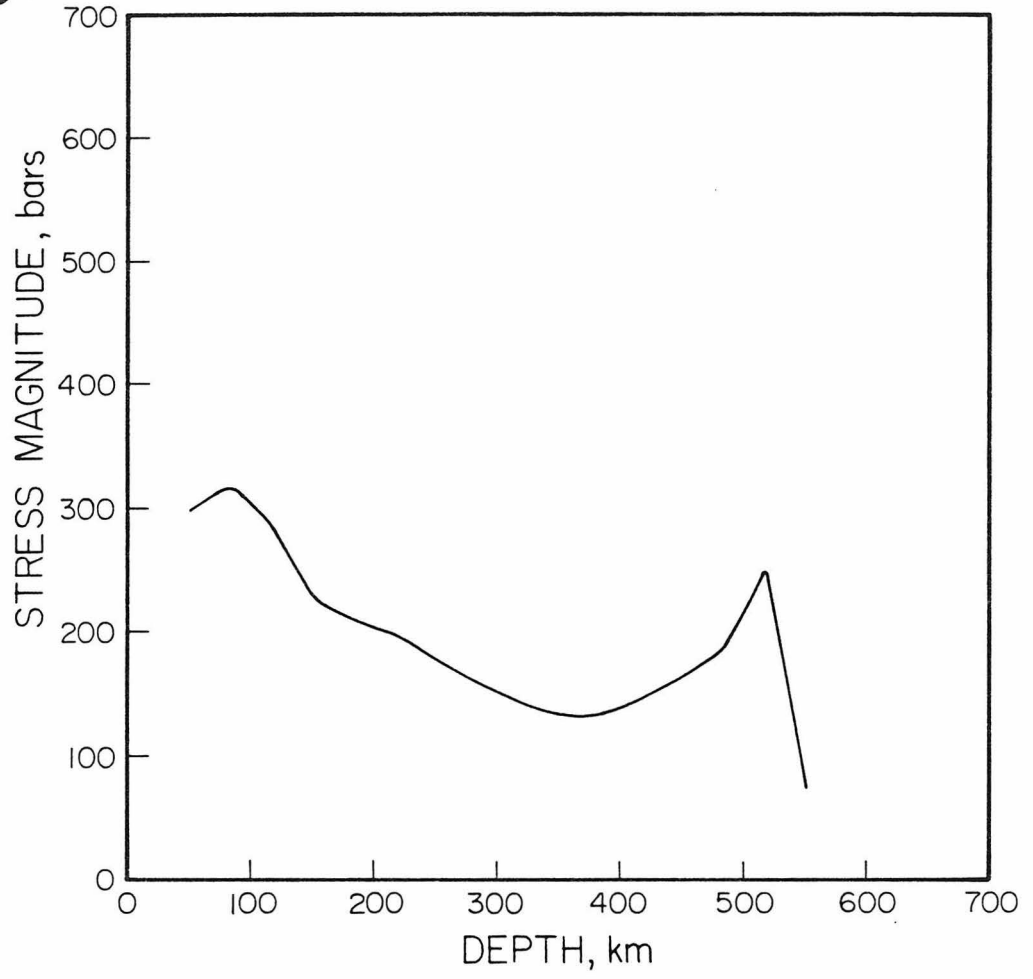
a



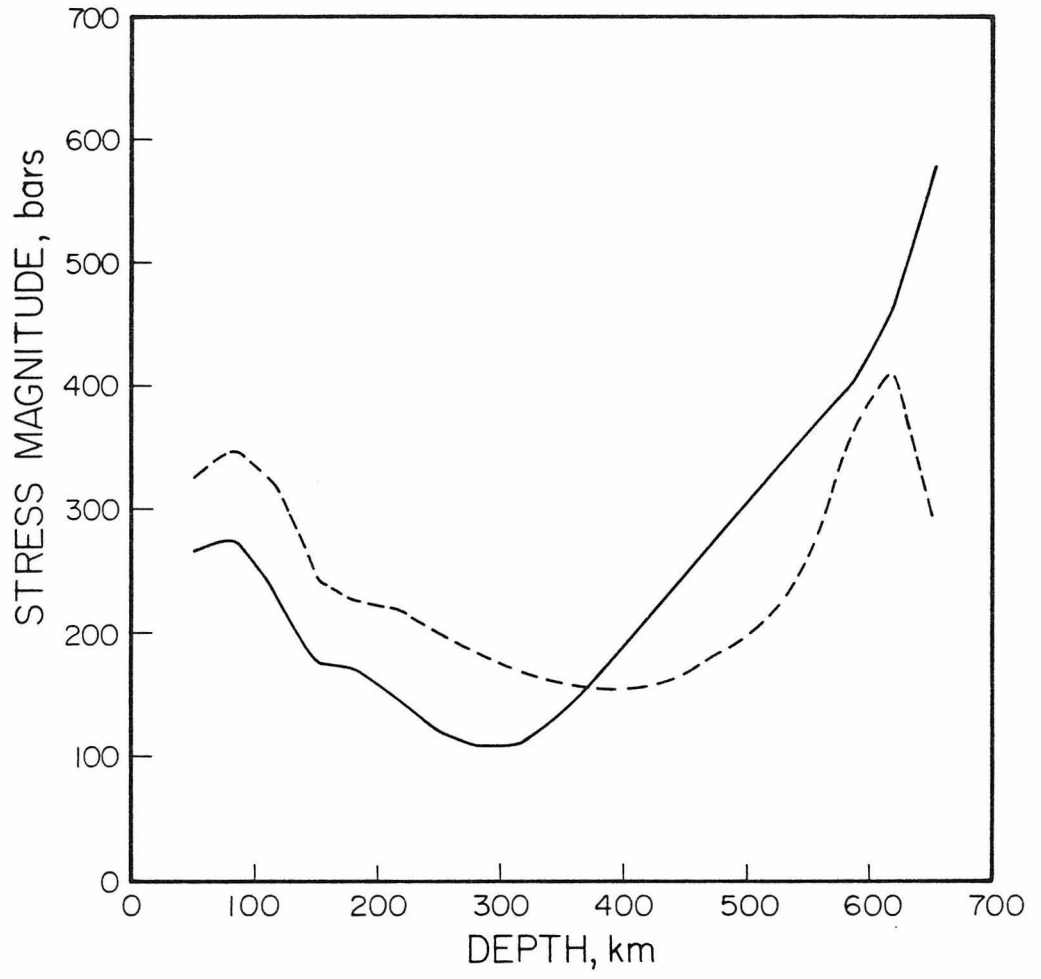
b



C



d



seismic profiles varying with the dip. It is, in fact, almost impossible to identify any trends in the seismicity profile which we might ascribe solely to the dip.

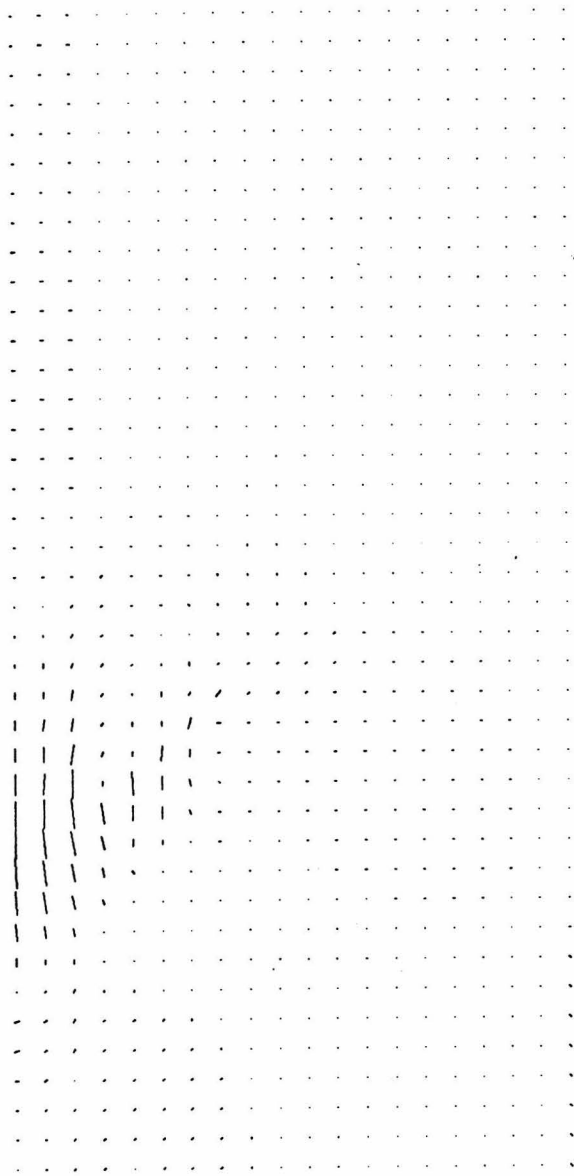
The stress orientation for a 45° slab is shown in fig 25. Unlike when the slab is vertical, the stresses in the depths above 300 km are not precisely down-dip tensile. There are both tensile and compressive components down the dip. The state of stress in the lower portions of a deeply extending slab, however, is clearly down-dip compressive. This is consistent with the famous conclusions of Isacks and Molnar (1971), and also with our own analyses of earthquake stress axes obtained by moment tensor inversion (Section 2.2.2, Appendix A).

3.6 Slabs Pushed from the Side

The models we have been considering so far have all been subjected to a body force only. While gravitational forces on the slab are likely to constitute an important driving mechanism for plate tectonics (e.g., McKenzie, 1969), ridge-push is also a possible force. Fig 26 shows a series of stress profiles for a slab pushed from the side so as to produce stress levels in the slab comparable to those produced by body forces in our previous models. We see that we can match the smooth decay in the shallow portion, but we do not produce a deep peak. As shown in fig 27, stress is down-dip compressive throughout the slab. In general, a model with push force only is not adequate to satisfy the observations. We have no trouble, however, if we add a push force to a body force, as shown in fig 28. As we can see in fig. 29, the state of stress in the shallow portion of the slab is less down-dip tensile when we add a push force.

Figure 25. Compression axes for the 45° slab of figure 24, extending to (a) 270 km, (b) 400 km, (c) 540 km and (d) 670 km.

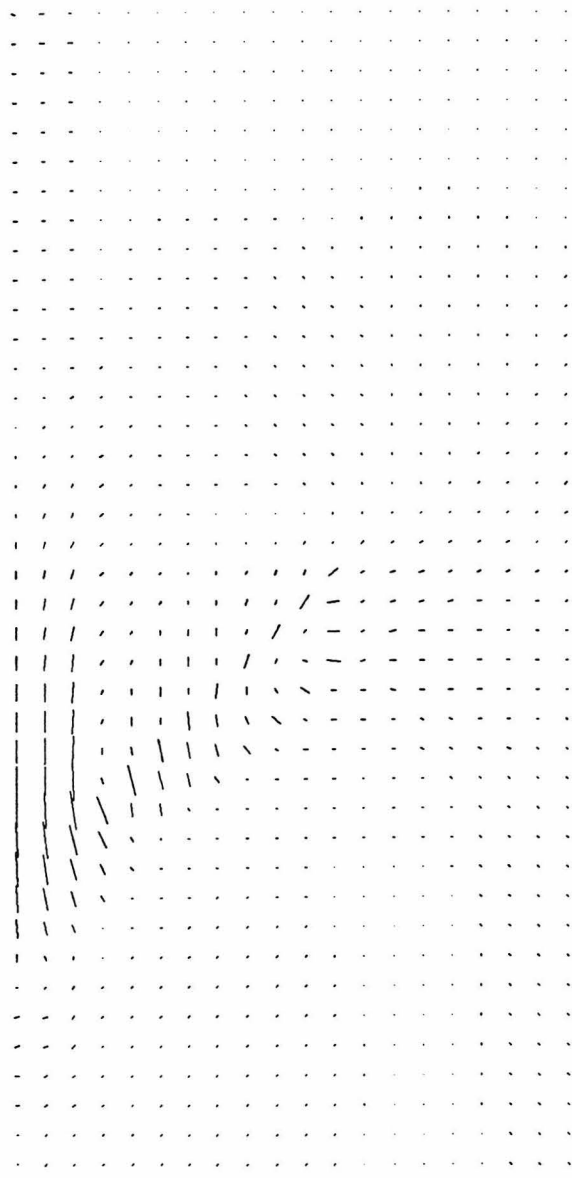
670 km
←—————→



a

—
| kbar

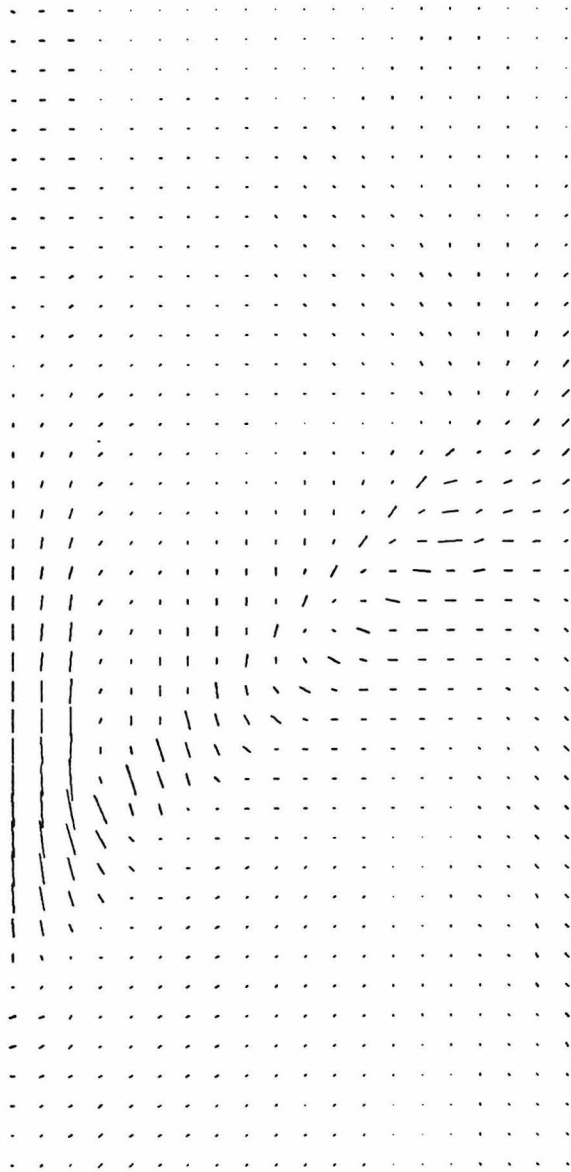
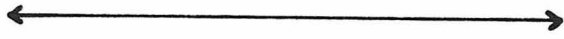
670 km
←—————→



b

—
| kbar

670 km

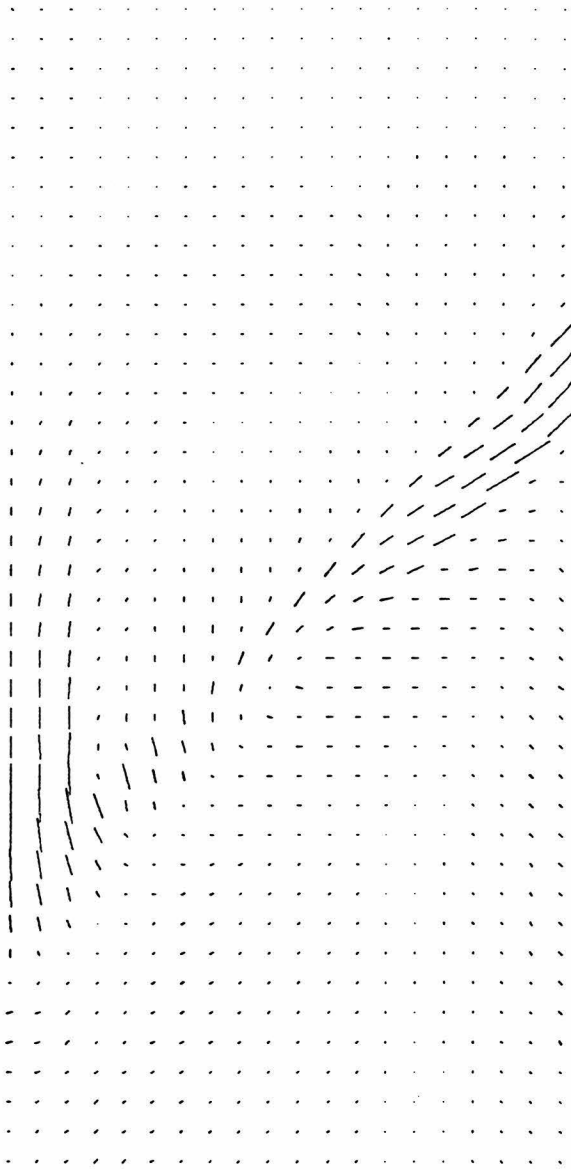
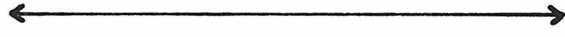


C

I

I kbar

670 km



d



1 kbar

Figure 26. Stress profiles for a 45° slab subjected only to a push force from the left side. Different curves are for slab extending to different depths: 270, 400, and 670 km.

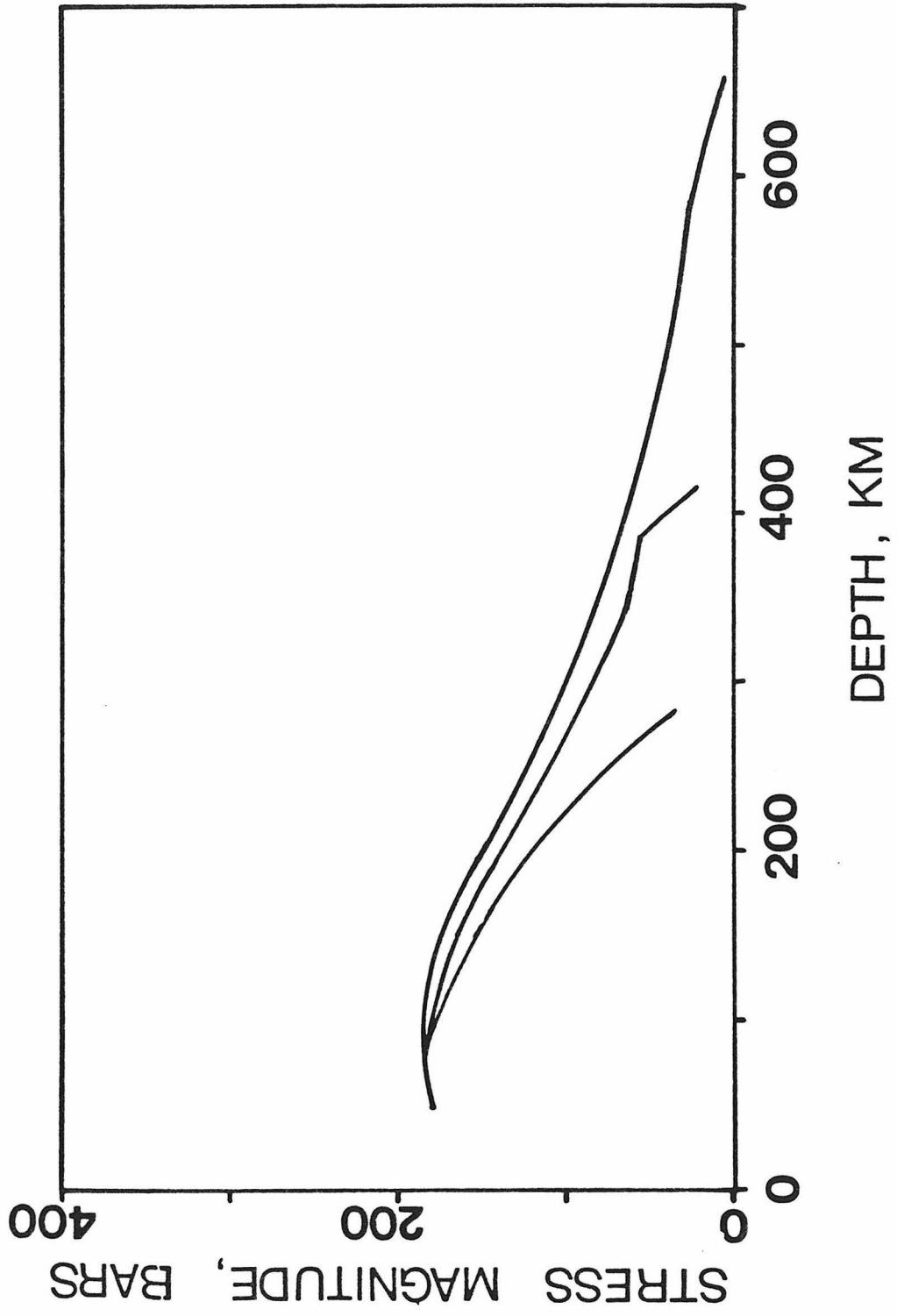
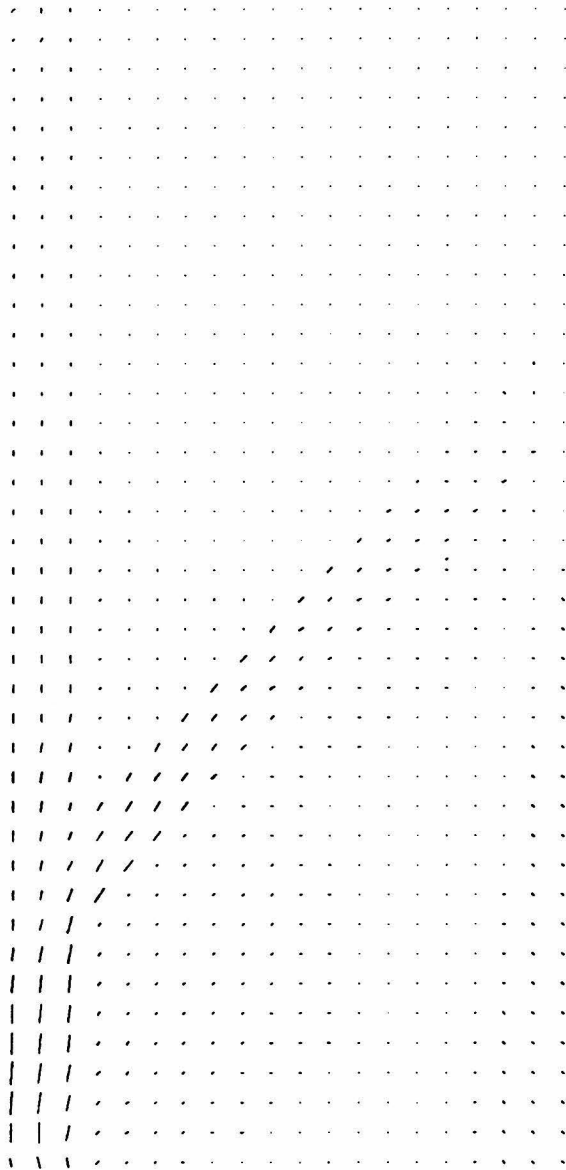


Figure 27. Compression axes for the slab of figure 26 extending to 670 km. We recall that the slab is dipping 45° and is not subjected to gravitational forces, but only to a push from the left side.

670 km



—
| kbar

Figure 28. Stress profiles for a 45° slab extending to various depths (270, 400, 540, and 670 km). The slab is subjected both to the push force of figure 26 and to a gravitational body force as in figure 24.

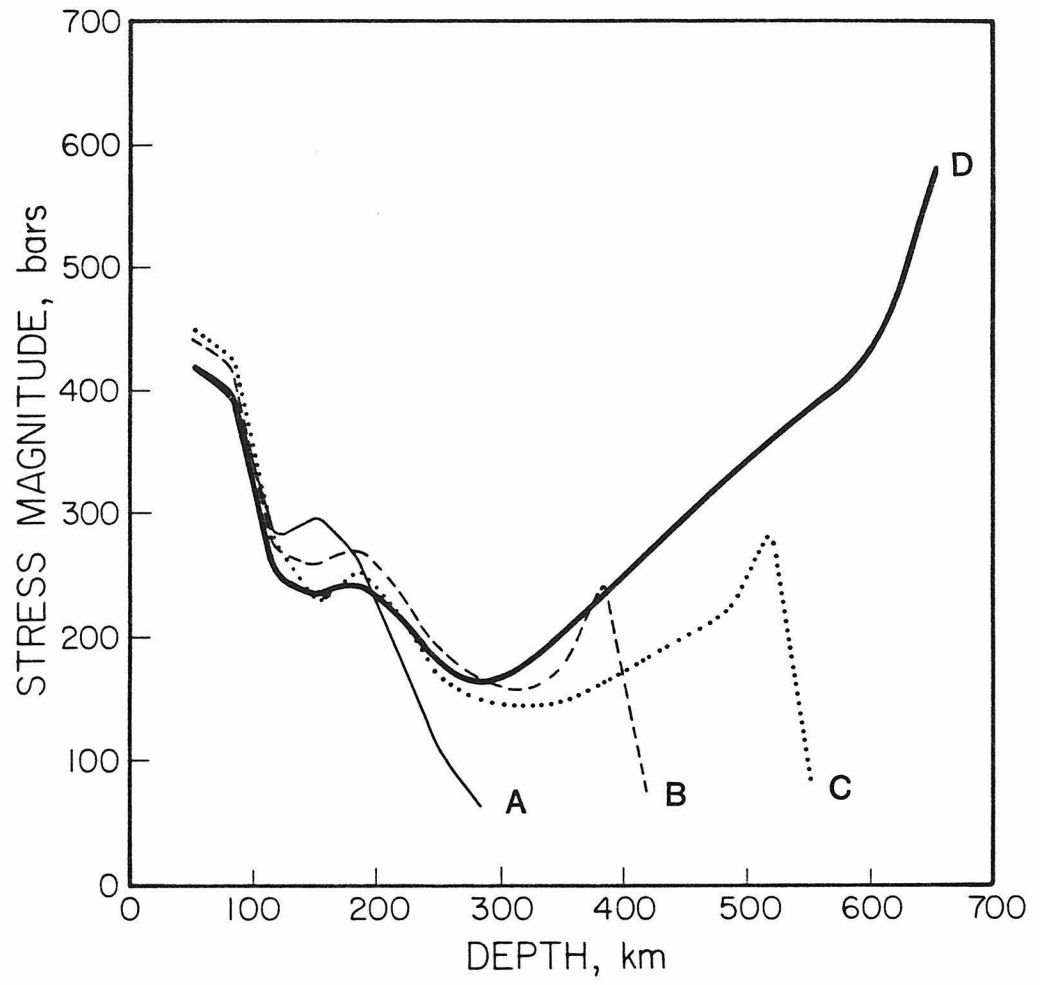
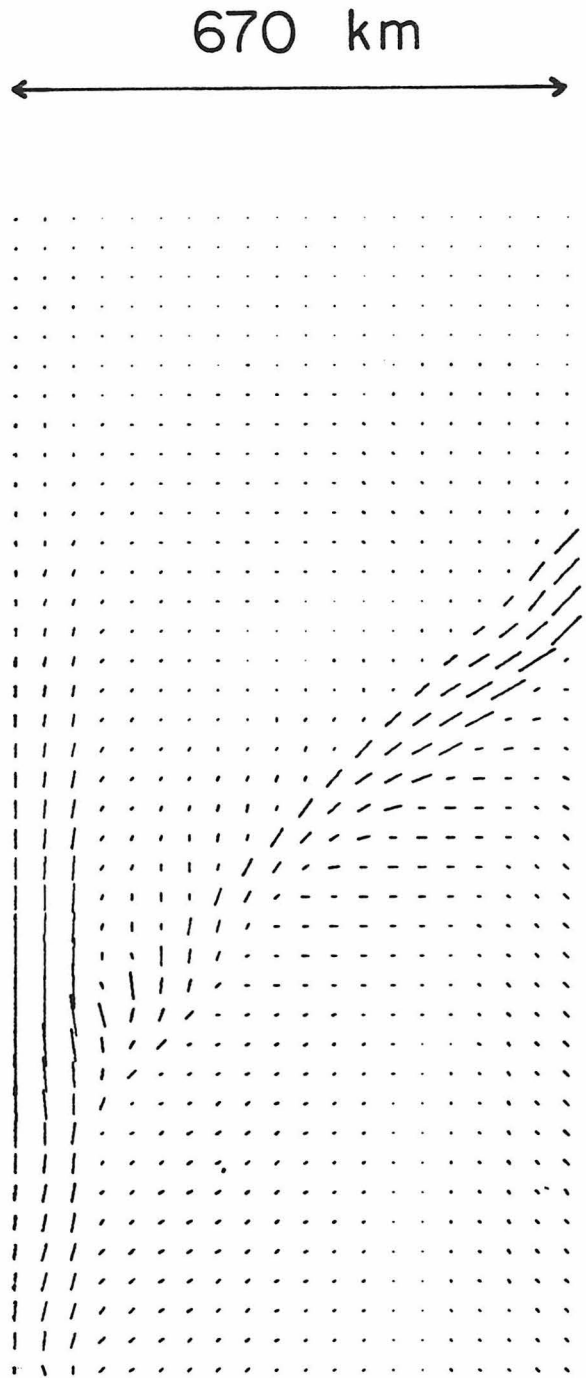


Figure 29. Compression axes for the slab of figure 28 extending to 670 km. We recall that this slab is dipping 45° and is subjected both to a push from the side and to gravitational body forces.



I
I kbar

3.7 A Slab More Consistent with Thermal Models

As we have noted, the assumption of a uniform density throughout the slab is somewhat oversimplified. If we look at fig 14, the calculation of density differences between the slab and mantle for Howard and Hager's (1983) model, we see that $\Delta\rho$ varies both across the slab and with depth. Fig 30 shows a stress profile for a slab with body force decreasing smoothly with depth, and one for a slab with a laminated body force. Clearly, we may regard constant density throughout the slab as a reasonable approximation for our purposes.

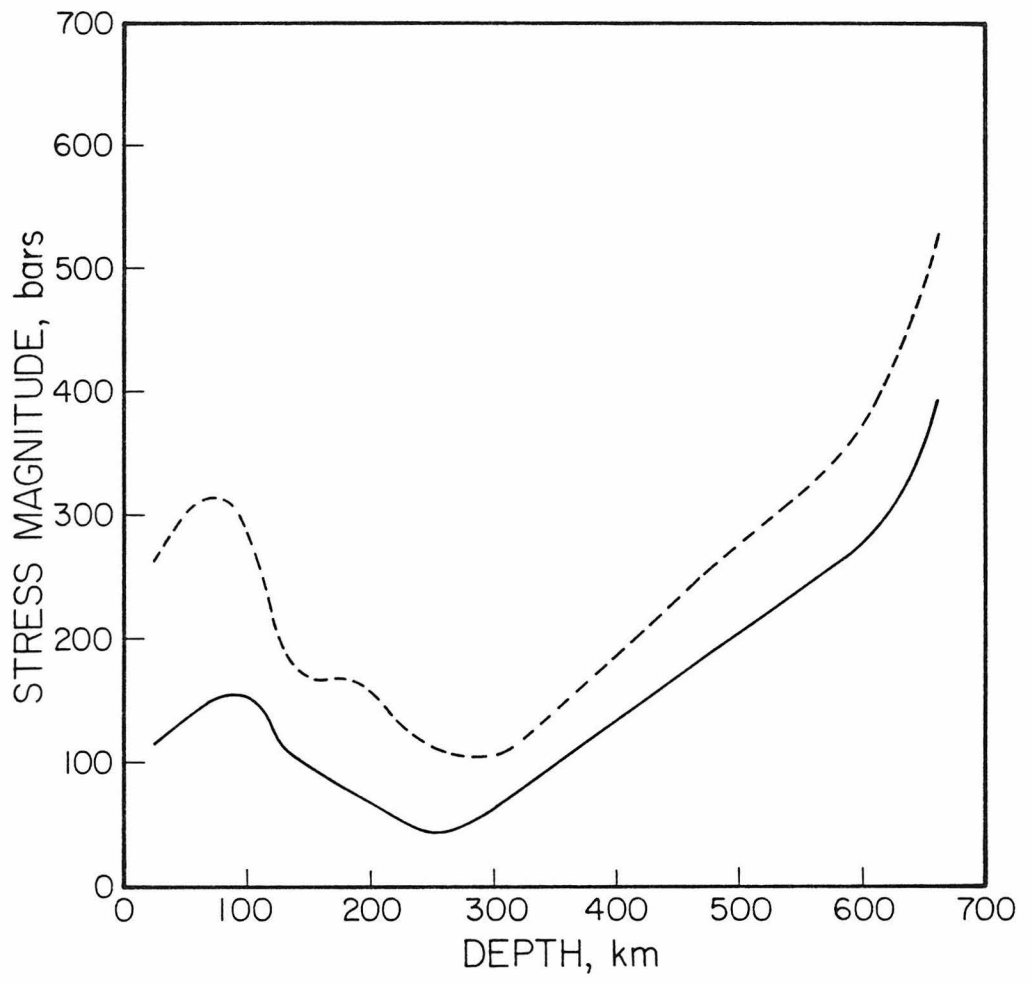
3.8 Discontinuities and Phase Transitions Above 670 km

All our slabs thus far have been descending in a uniform mantle with the barrier at 670 km being the only discontinuity. There are known seismic discontinuities between the Moho and 670 km, however. One is the Lehmann discontinuity (Lehmann, 1961; Hales et al., 1976) In Anderson's (1979a,b) compositional model of the mantle, this discontinuity represents a chemical boundary between peridotite and eclogite.

Fig 31 shows a stress profile for a 45° slab when there is a barrier to vertical flow at 200 km. Horizontal flow is allowed, as discussed in Section 3.1 for a chemical boundary. The barrier does not extend into the slab. Hence, we leave v_z free and set v_y equal to zero at the internal surface representing the barrier, and that surface does not include the 11 element nodes representing the slab. We see that a chemical discontinuity in the mantle would be expected to produce a peak in stress. Thus, within the framework of our assumption that the seismicity profile follows the stress profile, there is no evidence for a barrier of this sort above 670 km.

Another discontinuity is the better known one at 400 km (e.g., Anderson, 1967). This second discontinuity has been widely thought to represent a phase transition of

Figure 30. Stress profiles for slabs more consistent with the results of the thermal model shown in figure 14. The solid line is for a slab dipping 45° and extending to 670 km, with a density structure such that the upper surface of the slab is densest, with a gradient down to the lower surface which is the least dense. The dashed line is for a similar slab, but with density decreasing with depth to half its shallow value.



upper mantle olivine into the spinel structure (Meijering and Rooymans, 1958; Ringwood and Major, 1970). The proposed olivine-spinel change has been thought to have significance in plate tectonic processes, in that its positive Clapeyron slope implies an elevation of the phase boundary in the cold slab, this possibly providing a significant additional downward body force (Turcotte and Schubert, 1971). Schubert et al (1975), have calculated this body force in their model descending slab. They estimate a quadrupling of the body force above the 400 km discontinuity. Fig 32 shows the stress profile for a 45° slab where this effect is included. The influence of this increase in body force on the stress profile is very significant, and no evidence for such behavior is seen in the seismicity profiles.

Thus we affirm once more that the distribution of seismicity with depth in the world appears, to first order, to be dictated by the presence of a barrier at 670 km. Other proposed chemical discontinuities and phase transitions do not appear to be necessary to account for the observations, and in fact show evidence of being inconsistent. Phase transitions where the phase boundary is not significantly elevated in the slab may be consistent. It is interesting to note that the phase transition of clinopyroxene to the garnet structure, favored by Anderson (1979a) for explaining the 400 km discontinuity, may have a Clapeyron slope lower than that for olivine \rightarrow spinel, although the value is not well constrained at present (Akaogi and Akimoto, 1977). It should be borne in mind, however, that for any phase transition, kinetic factors might prevent a significant change in elevation of the phase boundary in the slab (Hager, personal communication, 1983).

Figure 31. Stress profile for a 45° slab extending to 670 km, but with a barrier to vertical flow at 200 km arising from a hypothetical chemical discontinuity. The barrier does not extend into the slab, which in this scenario is assumed to have pierced the discontinuity.

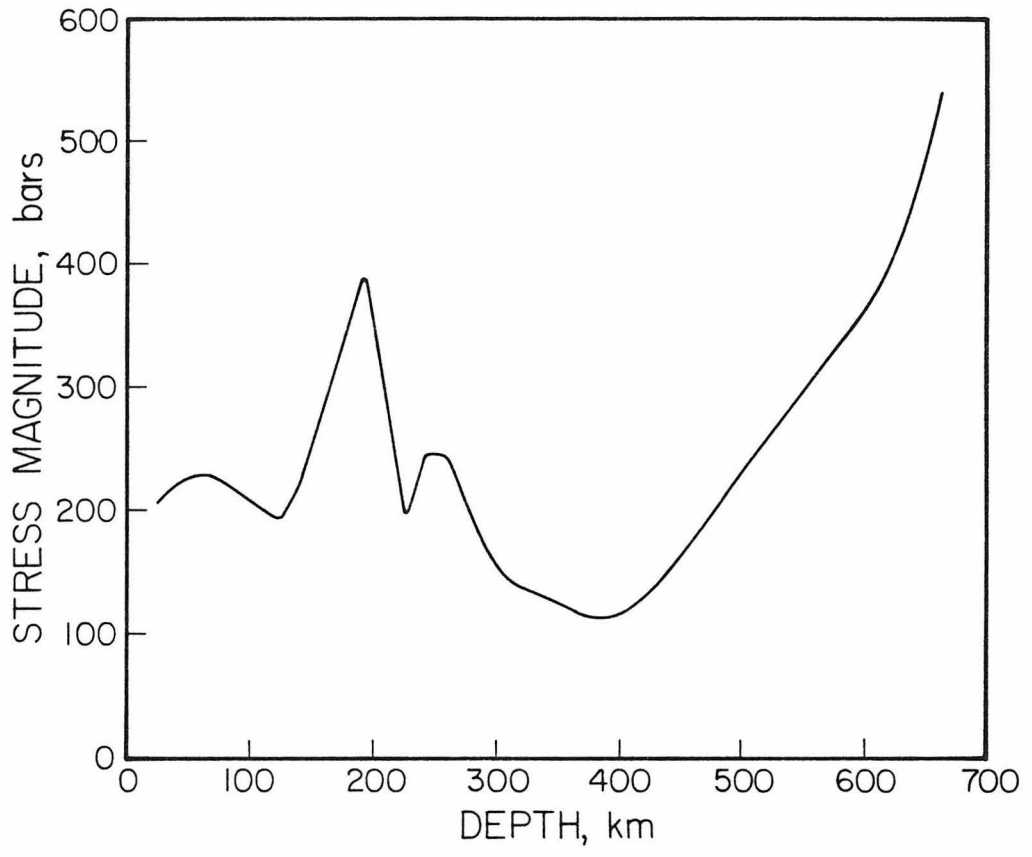
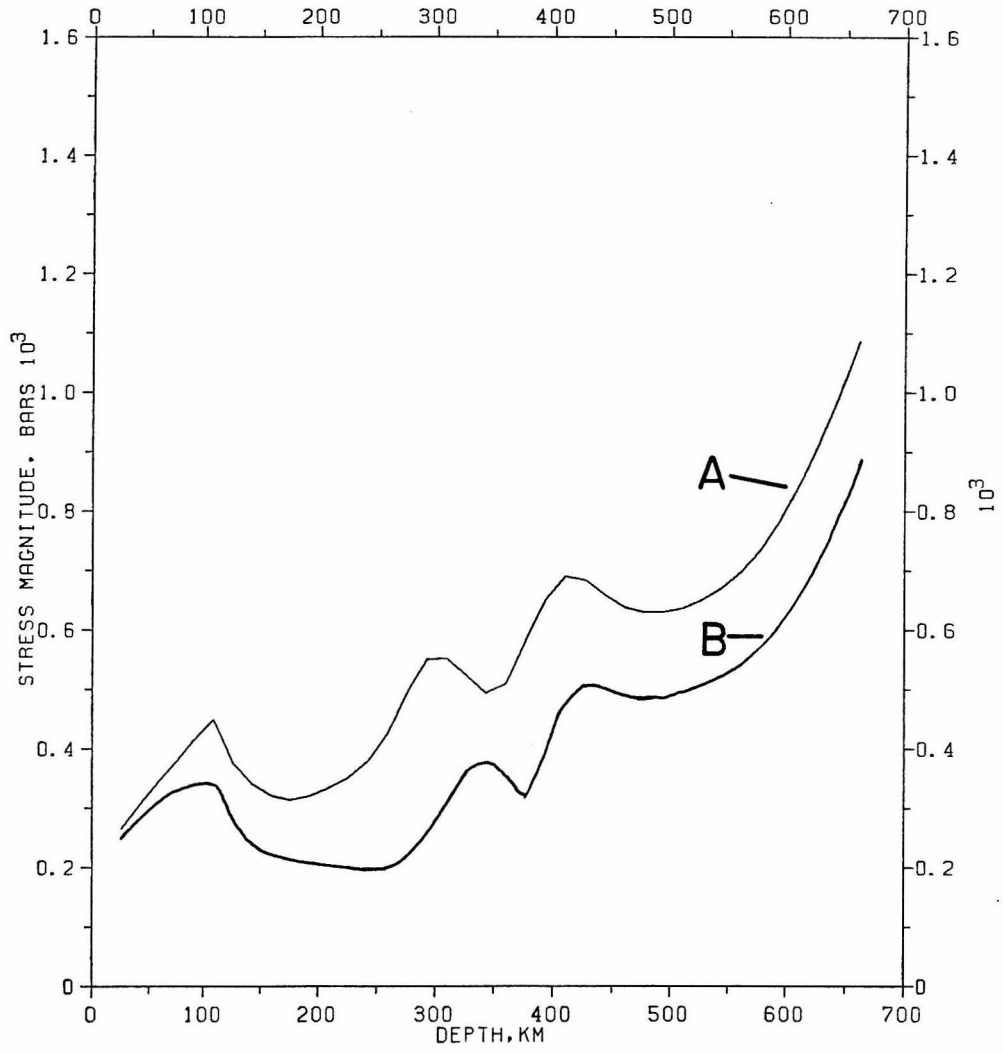


Figure 32. Stress profile for a 45° slab with an elevated olivine-spinel phase boundary as calculated by Schubert et al. (1975). A is for a phase boundary elevated by ≈ 100 km, as in that paper, and B is for a phase boundary elevated by 50 km.



3.9 Viscosity Increasing with Depth in the Mantle

If we do not impose a step function increase in viscosity at 670 km, but rather allow viscosity to increase smoothly with depth in the mantle, do we get the same results? Fig. 33 shows the results of a model where viscosity in the upper mantle increases linearly with depth such that the viscosity is 25 times greater at 670 km than it is immediately below the lithosphere (where it is 1, that is, 10^{22} p in our scaling). The lower mantle, below 670 km, has a viscosity of 25. The viscosity of the slab is kept at a value of 10 as in previous models. The stress profile is smoothed out somewhat; the deep peak is not as intense. However, the profile still shows some of the first order features observed in the seismicity.

This is less true of the profile in fig 34. We arrive at this profile by using the model of fig 33, except that we now allow viscosity to increase with depth in the slab as well as in the mantle. The slab is now ten times more viscous than the mantle *at every depth*. There is no reason to presume, if viscosity increases with depth in the mantle, that it should not also do so in the slab. Thus we might say that, based on the poorer match of fig. 34, an increasing-viscosity model is not as successful in explaining the variation of seismicity with depth as is a sharp increase at 670 km.

3.10 The Asthenosphere, Mesosphere, and Double Benioff Zones

We explore here the effect of a low viscosity zone in the mantle just below the lithosphere (Cathles, 1975). We refer to this zone, to which we assign a viscosity of 0.01 relative to the rest of the mantle, as the "asthenosphere", following established convention, and the more viscous mantle below it as the "mesosphere", following Sleep (1979). The sagging stresses in the slab as it meets the asthenosphere-mesosphere contact have been proposed (Sleep, 1979) as a possible explanation of

Figure 33. Stress Profile for a 45° dipping slab subjected to gravitational forces only, when viscosity in the mantle increases linearly with depth from a value of 1 (10^{22} p) immediately below the lithosphere to one of 25 at 670 km. The viscosity of the slab is 10 at all depths.

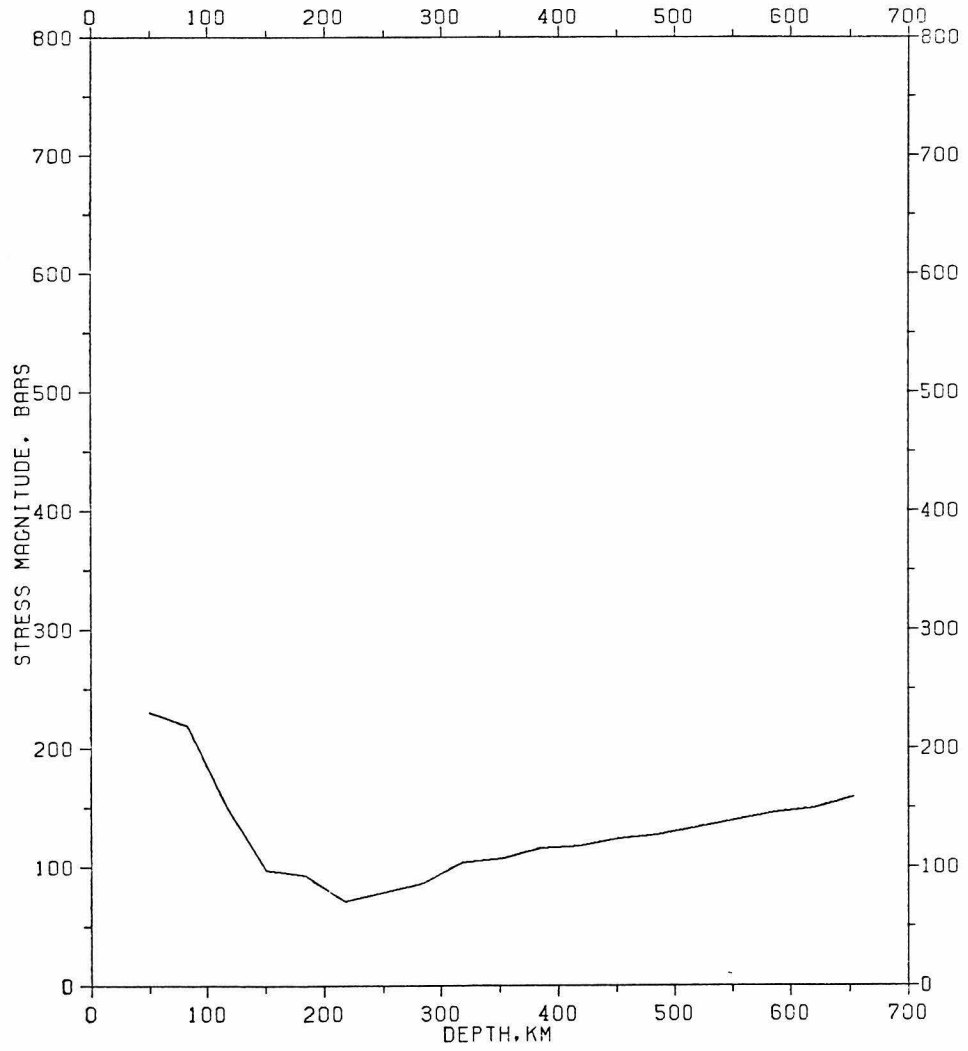
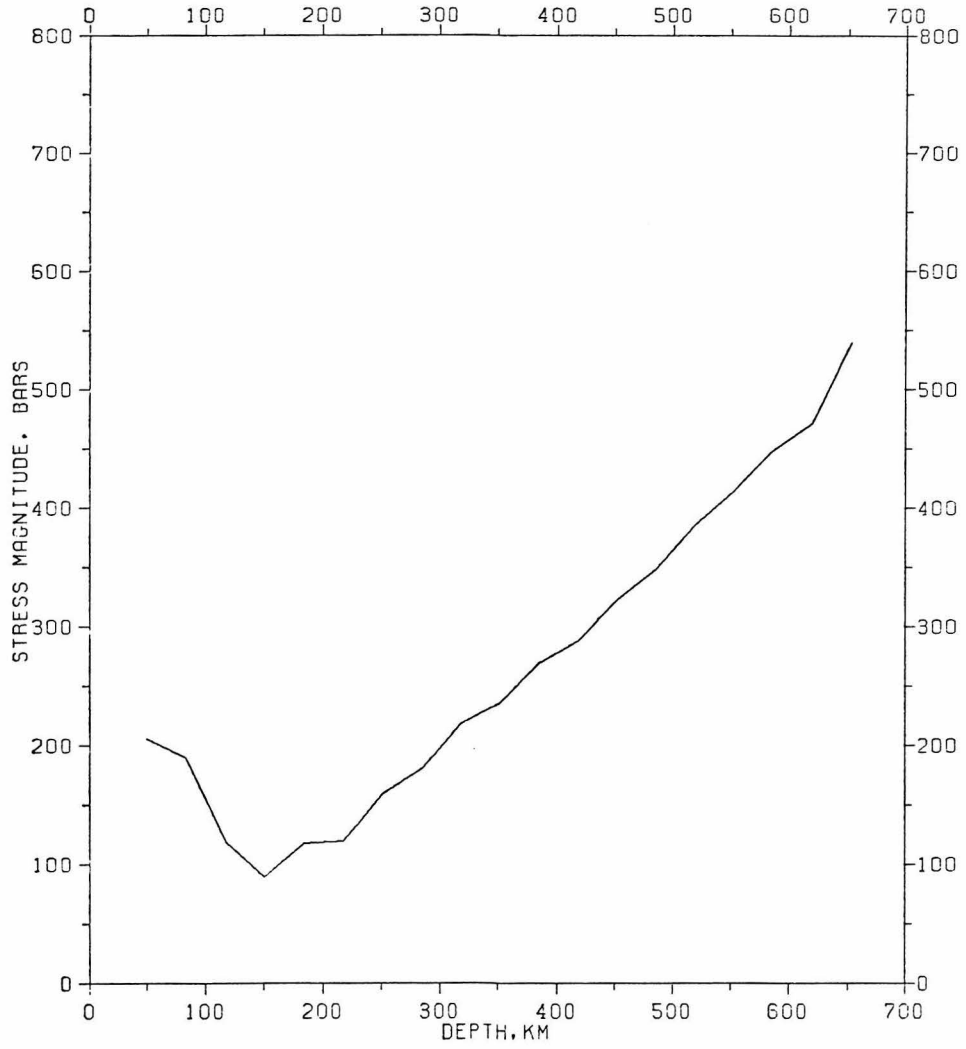


Figure 34. The same model as that in fig. 33, except that viscosity increases with depth in the slab as well as in the mantle, so that the viscosity of the slab is ten times that of the mantle at every depth.



double Benioff zones. We will see below that models of the kind considered by Sleep also yield stress profiles consistent with observed seismicity.

The literature on double Benioff zones has been reviewed by Fujita and Kanamori (1981). A double Benioff zone is a structure of seismicity involving two parallel planar earthquake belts, separated by about 30-40 km, and existing between approximately 65 and 185 km depth. The upper zone is characterised by down-dip (or, as Fujita and Kanamori call it, "in-plate") compression, while the lower zone is tensile. This stress orientation is opposite to what one would expect for a bending plate, and in fact "unbending" of the plate was an early proposed explanation for the observations (Engdahl and Scholz, 1977). Fujita and Kanamori cast some doubt on the unbending hypothesis, because they argue that if this were the explanation, one might expect double Benioff zones to be a global feature. In fact the only true double Benioff zones known are in Japan (Tsumura, 1973; Umino and Hasegawa, 1975, 1982; Hasegawa et al., 1978) and the Kuriles (Veith, 1974, 1977). Engdahl and Scholz (1977) reported a double Benioff zone for the Aleutians. However, the existence of this zone has been called into question by Topper (1978, cited by Fujita and Kanamori), who believes that what one is actually seeing in the Aleutians is a tear in the Benioff zone, which shows up as an extra plane when all events are projected onto a vertical cross section. Reyners and Coles (1982), who continue to treat the Aleutian data as a double Benioff zone, report that the stress orientation in the upper and lower planes is opposite to what one might expect from unbending, that is, opposite to what is seen in Japan.

Sleep's (1979) models have a lithosphere of 2×10^{23} p viscosity, an asthenosphere of 2×10^{20} p, an accretionary wedge of viscosity varying between 2×10^{21} and 2×10^{23} p, and a mesosphere of viscosity varying between 10^{21} and 2×10^{22} p. The

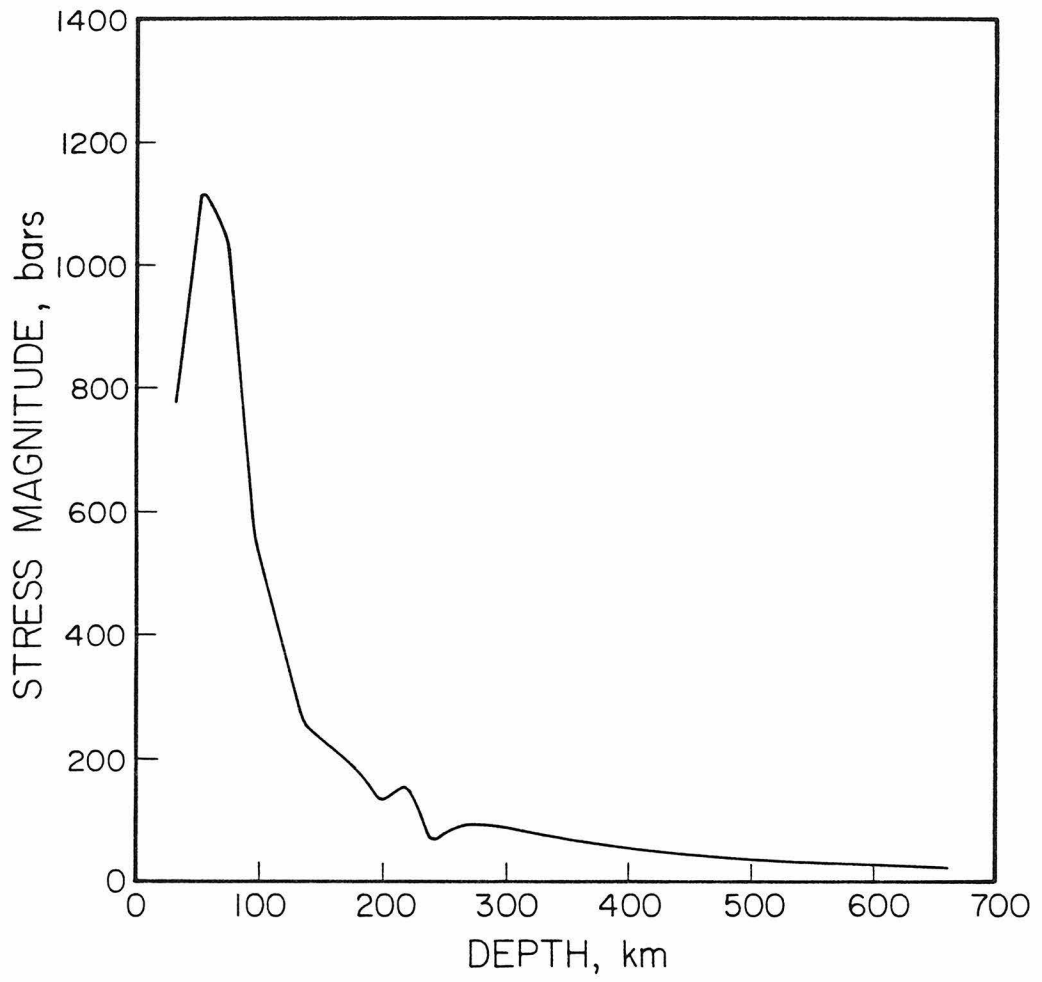
accretionary wedge does not have much effect on Sleep's results, but the mesosphere does. If mesospheric viscosity is less than about 2×10^{22} p, the stress in the slab is down-dip tensile. If it is higher than 5×10^{22} p, the stress is down-dip compressive. Between these two viscosities, a double Benioff zone develops.

Fig. 35 shows a calculation very similar to Sleep's for a mesospheric viscosity of 2×10^{22} p. (Note that Sleep's boundary conditions are somewhat different from those we have used in our other models. He imposes a velocity of 5.7 cm/yr on the lithosphere on the left side. We have applied similar boundary conditions). The slab extends to 230 km depth and dips 60° -- Sleep was trying specifically to explain the situation then thought to prevail in the Aleutians. The top of the mesosphere is at 160 km. Examining fig. 35(b), we see that below about 100 km, the upper plane of the slab is in compression, and the lower plane is (somewhat weakly) in tension. Fig 35(a) plots the stress magnitude as in our other calculations. It behaves like our other shallow profiles, showing a fairly smooth decay. If we let the slab extend to 670 km, with our customary barrier at that depth (fig. 36), the stress profile is not qualitatively different from that in a uniform mantle. The minimum is just somewhat broader. At depths below about 400 km, the stress is down-dip compressive throughout the slab, while at depths from about 120-400 km, the stress is as in a double Benioff zone. This is deeper than the range associated with double zones.

3.11 Non-Linear Rheology

All calculations so far in this study have assumed that the mantle and slab behave as Newtonian fluids. Other than computational convenience, there is no *a priori* reason to assume this. While some proposed deformation mechanisms for the mantle, such as point defect diffusion (Nabarro, 1948; Herring, 1950; Raj and

Figure 35. (a) Stress profile for a 60° slab extending to 230 km, with an asthenosphere-mesosphere contact at 160 km depth. The viscosity of the asthenosphere is 0.02×10^{22} p, and of the mesosphere 2×10^{22} p. Figure 35(b) shows compression axes for this slab.



a

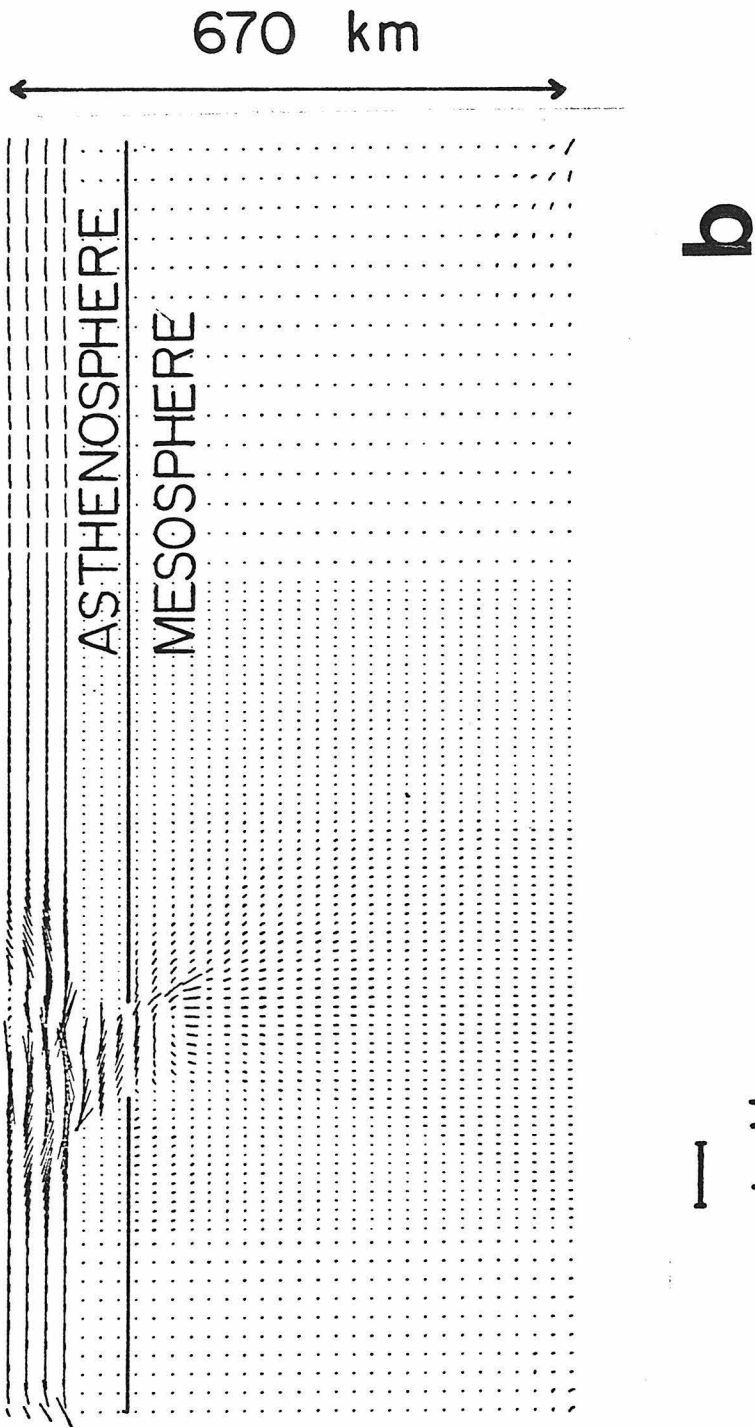
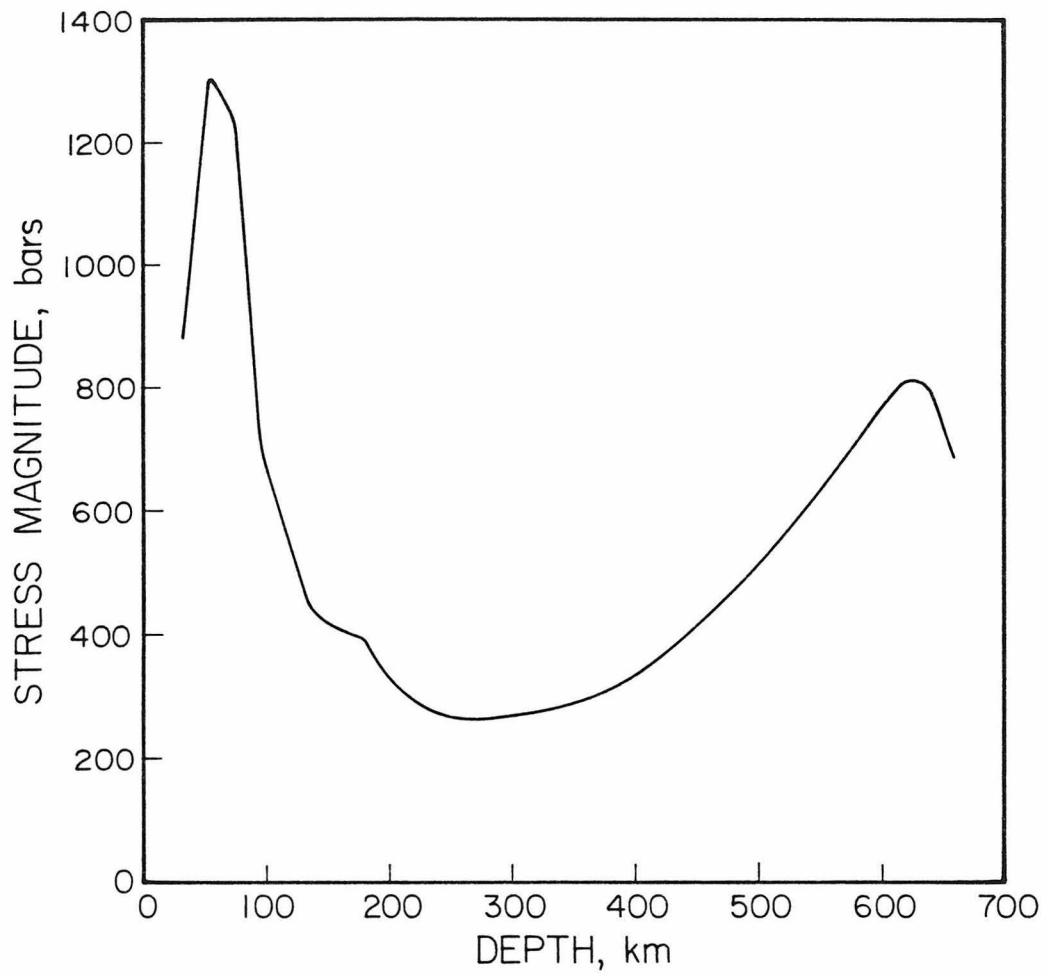
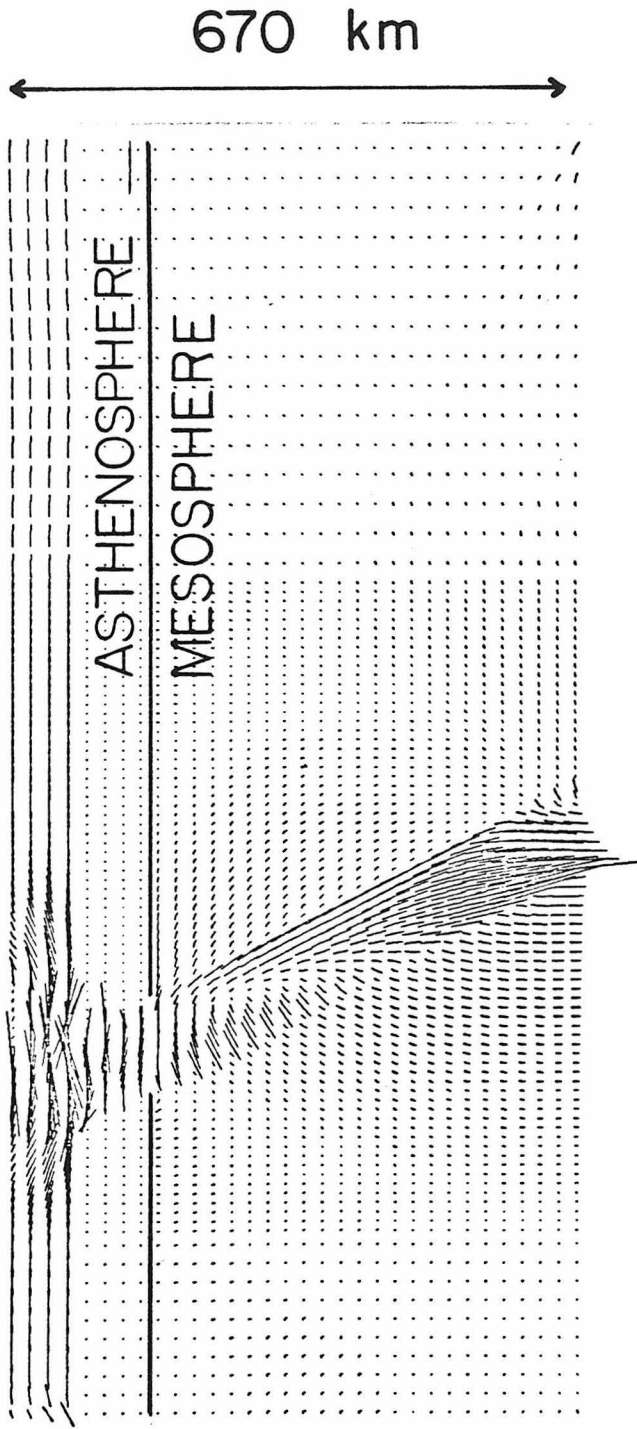


Figure 36. As Figure 35, but for a slab extending to 670 km. (a) plots the stress profile, and (b) plots the compression axes.



a



b

—
| kbar

Ashby, 1971) or superplastic creep (Twiss, 1976) have linear constitutive relations, others do not. Diffusion controlled dislocation climb, known as "dislocation creep", has a strain rate proportional to some power n of the stress. n can be between 3 and 10, tending to the higher end of the range with increasing temperature and decreasing stress (Stocker and Ashby, 1973).

We have calculated stress profiles for models with a nonlinear rheology. As n is not known, we have chosen a value of 3 for computational reasons. The results for a 45° slab extending to 670 km and subjected only to gravitational forces are shown in fig 37. They are very similar qualitatively to the linear results, and we find no cause to suspect that nonlinear mantle rheology will alter or invalidate our conclusions. We note that the calculation assumes a slab viscosity 100,000 times greater than the mantle viscosity of 10^{22} p at unit stress (4.72 bars, as discussed in Section 3.1.1). The contrast in effective viscosity, however, is far lower-- viscosity is stress dependent. We can see this in fig. 38, which shows contours of effective viscosity, where a viscosity of 1 represents the starting mantle viscosity. The slab has an effective viscosity of order 10, while the mantle varies from order 0.01 to 1. The nonlinear rheology tends to create a low viscosity zone where the slab is bending, and on the underside near the bottom where the slab approaches the barrier. We can see hints of a tensional lower surface and a compressive upper surface in the slab (fig. D37S), as we observed in our previous linear models containing an asthenosphere (Section 3.10).

We note that the choice of the factor 10^5 was made in order to obtain reasonable flow velocities of order 1 - 10 cm/yr. In the linear case, this is achieved by choosing $\eta_{SLAB} = 10\eta_{MANTLE}$, and contrasts of 10^5 would lead to very small velocities. In the nonlinear case ($n = 3$), choosing $\eta_{SLAB}^0 = 10 \eta_{MANTLE}^0$ leads to

Figure 37. Results for a nonlinear rheology ($n = 3$). Slab dips 45° and is subjected only to gravitational forces. Viscosity of slab at unit stress is 10^5 times that of mantle.

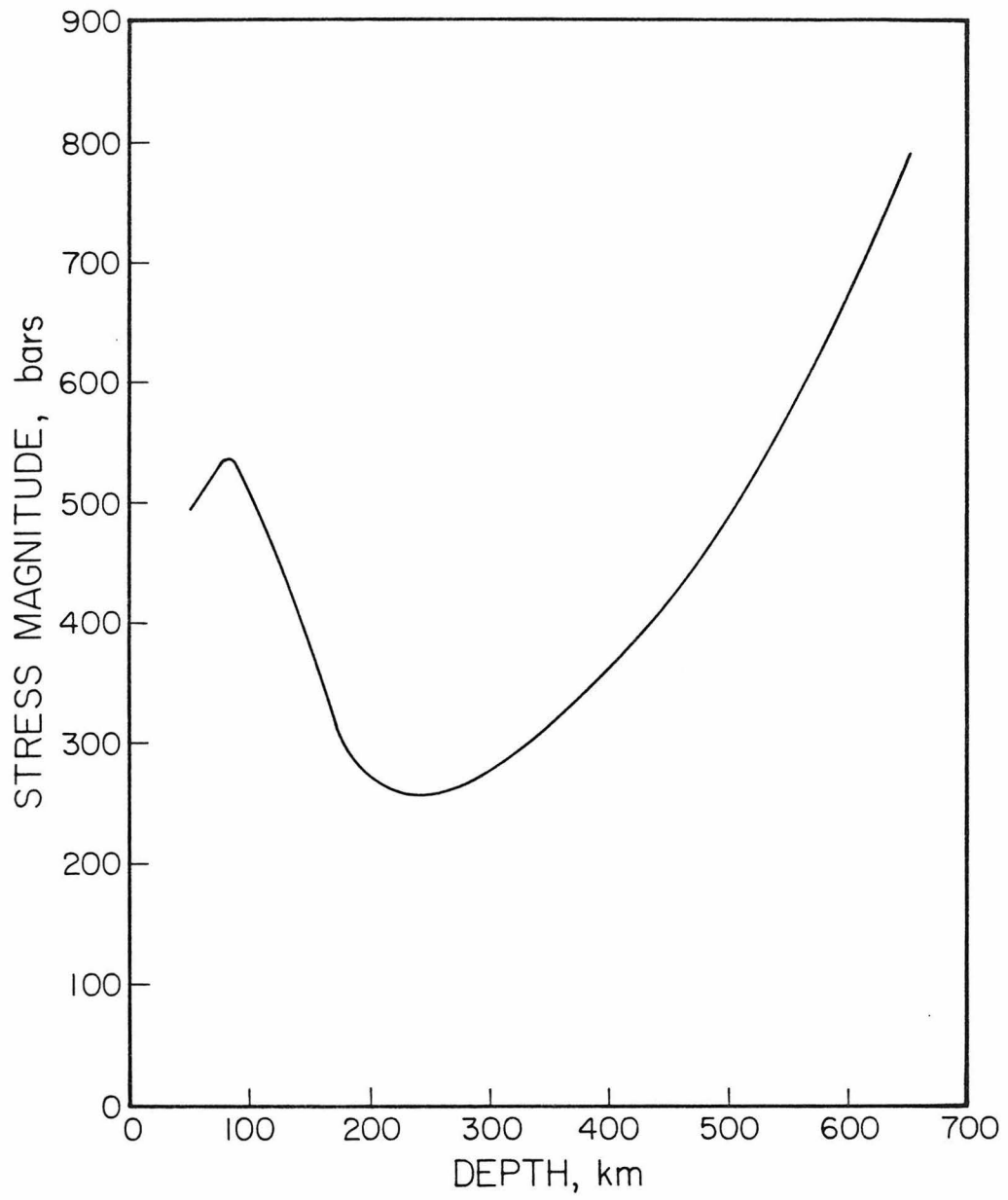
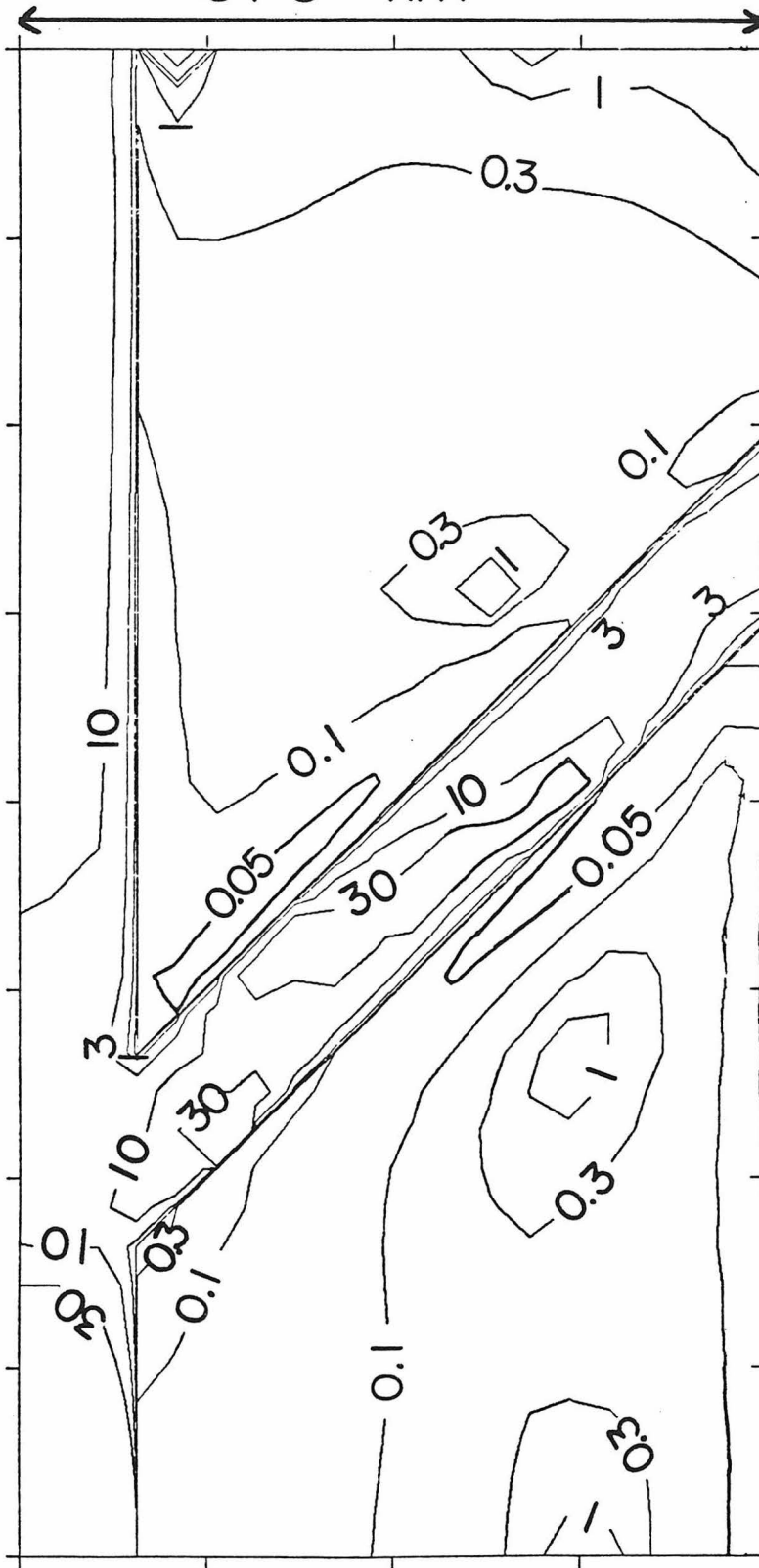


Figure 38. Contours of effective viscosity for the slab of fig. 37. A viscosity of 1 represents the starting mantle viscosity. Contours are drawn at effective viscosities of 0.05 ,0.1 ,0.3, 1.0, 3.0, 10.0, and 30.0.

670 km



velocities on the order of tens or hundreds of meters a year.

3.12 The Nature of the 670 km Barrier

Whether the 670 km barrier is a chemical discontinuity or a viscosity jump is not resolvable by our data. The stress patterns-- both orientation and magnitude-- are explainable, to first order, either way. The flow patterns, however, may provide some constraint. If we look at fig. 39, the flow field for a slab running into an impenetrable barrier, we see that the flow lines near the bottom of the slab do not parallel the dip of the slab, but rather flatten out. The slab looks as if it is about to distort into a sigmoidal shape. This kind of shape is not observed. Looking at fig. 40, the flow lines for the slab when there is a viscosity jump of an order of magnitude at 670 km, we see that the flow roughly parallels the slab, and no distortion is implied, particularly when the slab is allowed to extend into the lower mantle. This result is related to that obtained by Hager and O'Connell (1978). They calculated global mantle flow fields driven by observed surface plate motions. They were able to predict subduction zone dip angles successfully when they allowed flow to extend into the lower mantle, but not when they confined flow to the upper mantle.

There are other arguments favoring the viscosity contrast as well. Some of the most powerful are the ones given by Hager (1983). He finds that geoid anomalies over subduction zones are positive, contrary to what one might expect in a model Earth of uniform viscosity; a factor of 30 or more increase in viscosity with depth is required to account for this observation. Moreover, Hager finds that the density contrasts in the seismically active parts of Benioff zones are insufficient to account for the magnitude of the observed geoid anomalies. Allowing slabs to penetrate aseismically into the lower mantle can account for this discrepancy. Another way to account

for it, under the hypothesis of a chemically layered mantle, is to have 350 km of dead slab at the base of the upper mantle. Hager argues that this would require a substantial deflection of the 670 km discontinuity, which has not been observed.

The finer features of the seismicity patterns in some of our regions may be better explained by a viscosity contrast of a factor of 10 to 30 than by a very large viscosity contrast or a chemical discontinuity. If we refer back to fig. 19, and then to the plots in Appendix C, we see that many of the deep regions have deep peaks whose size relative to shallow seismicity levels might imply a "soft" boundary at 670 km. The Marianas, for instance, have a deeply positioned seismicity minimum, and a small deep peak. This pattern is better matched by a vertical slab sinking into a viscosity contrast of an order of magnitude, or even less, than by one sinking into a hard boundary. The seismicity pattern observed in Mindanao is also suggestive of a relatively soft boundary, while that seen in Tonga is more suggestive of a hard one. Perhaps we are seeing the effects of lateral variations in mantle viscosity.

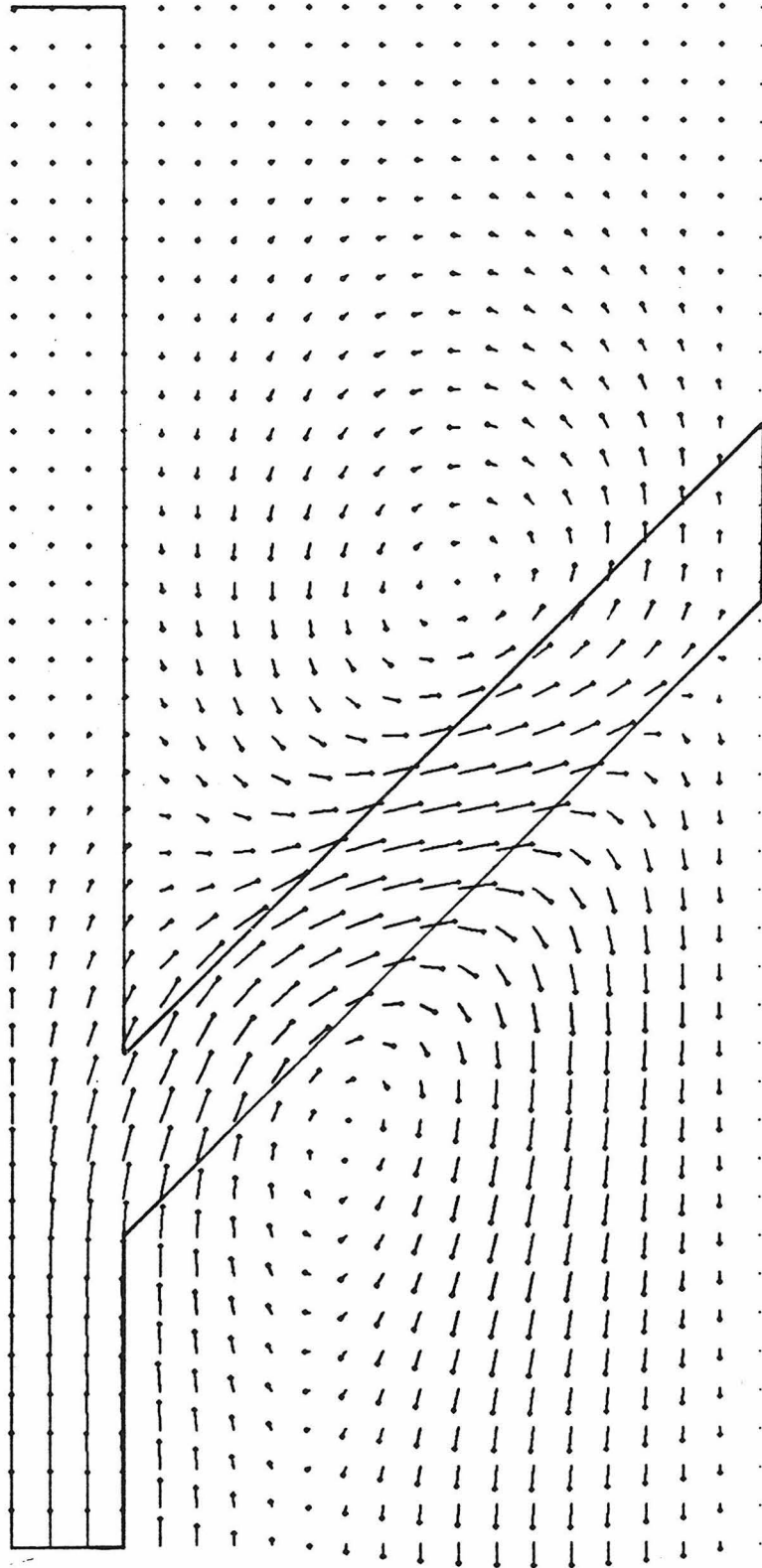
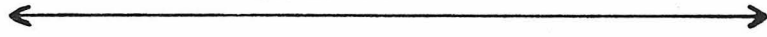
So can we conclude that the boundary at 670 km is a viscosity contrast rather than a chemical discontinuity? Not necessarily; consider fig. 41, which plots the stress profile for the slab of fig. 40(b). The upper mantle stress pattern is adequate to explain observed seismicity, but the stress in the slab is still high at depths below 670 km. Why, then, do earthquakes not occur there? One can adopt the somewhat *ad hoc* explanation (e.g., Wortel, 1982) that ≈ 700 km simply happens to be the depth at which a critical temperature is reached and the slab loses its mechanical integrity, becoming aseismic. Such an explanation is not satisfying, however; it seems like too much of a coincidence that earthquakes should stop, after a very high level of activity, at a depth where there is also a possibly very sharp seismic discontinuity (Richter, 1979). Thus, the question is not resolved.

The sharpness of the discontinuity (Whitcomb and Anderson, 1968) has been used by Anderson (1976) as an argument against its being caused by a phase transition. Bell (Geological Sciences Seminar, Caltech, 1983), however, has disputed this argument, stating that the transition of upper mantle phases to the perovskite structure may indeed be sharp enough to explain the discontinuity. Thus, a phase transition is still a possibility, so we examine the possible effects of one kind of transition which has the potential to help us explain the seismicity patterns. If a phase transition at 670 km has a negative Clapeyron slope, the phase boundary may be depressed in the slab. This may then cause an upward body force on the slab, producing compressive stress at depth, and possibly a stress profile with a minimum and a deep peak. It was once believed that upper mantle olivine in the spinel structure might disproportionate into mixed oxides (Birch, 1952), a transition which might involve a negative Clapeyron slope (Ahrens and Syono, 1967). Since the discovery that olivine and pyroxene transform to the perovskite structure at high pressure (Liu, 1975, 1976), there is less reason to suspect a negative Clapeyron slope. However, it is still possible, as the slope for the perovskite transition is not known.

Fig. 42 shows a curve for the spinel to mixed-oxides transition as calculated by Schubert et al. (1975), with a density contrast of 0.4 g/cc, and a \approx 30 km depression of the boundary in the slab. We see that a model of this sort is capable of adequately matching the seismicity profiles, without an increase in mantle viscosity or a chemical barrier at 670 km. However, as we have said, we have no reason to suppose a negative Clapeyron slope. A viscosity change or a chemical discontinuity still constitute more straightforward explanations of the phenomena at hand.

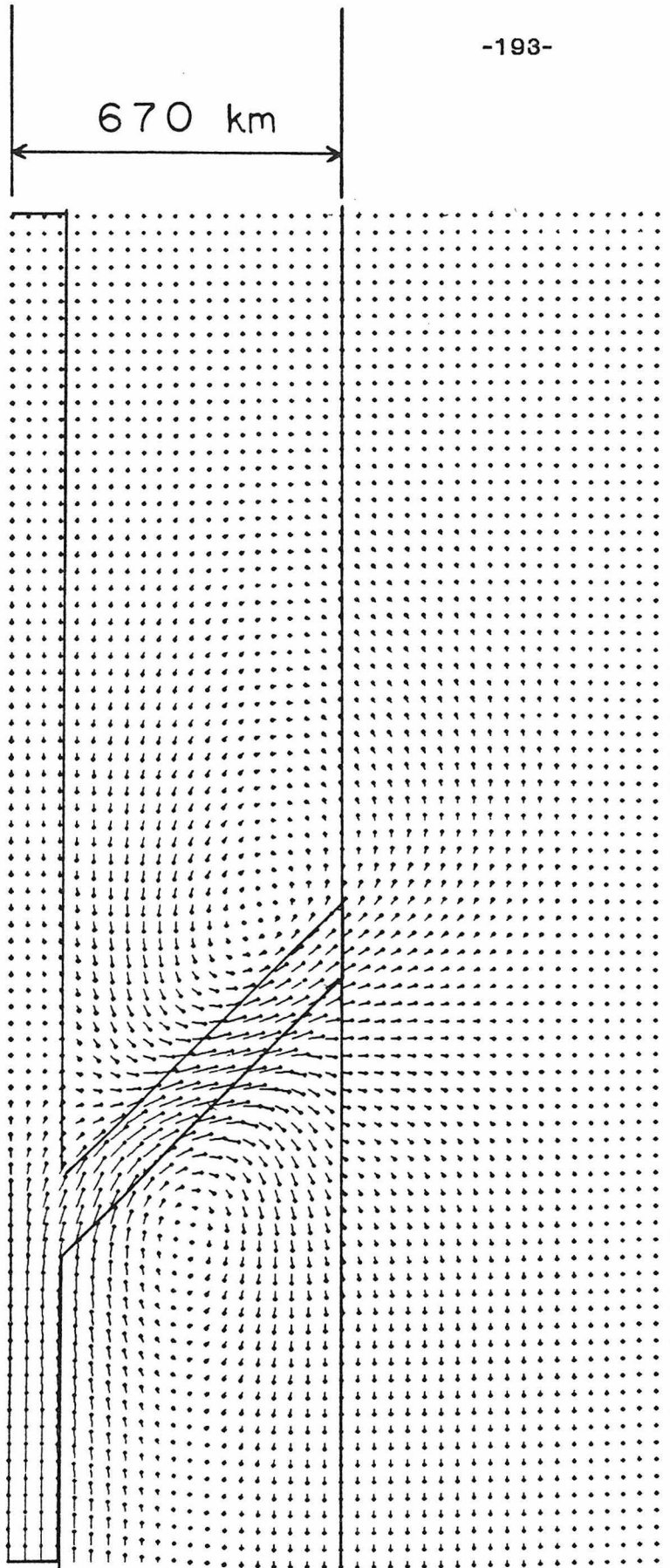
Figure 39. Flow field for a 45° slab sinking under its own weight when there is a barrier at 670 km. The stress field for this slab is shown in figs. 24 and 25. The flow lines appear to flatten out at the boundary, suggesting that the slab may be about to distort into a sigmoidal shape.

670 km



5 cm/yr

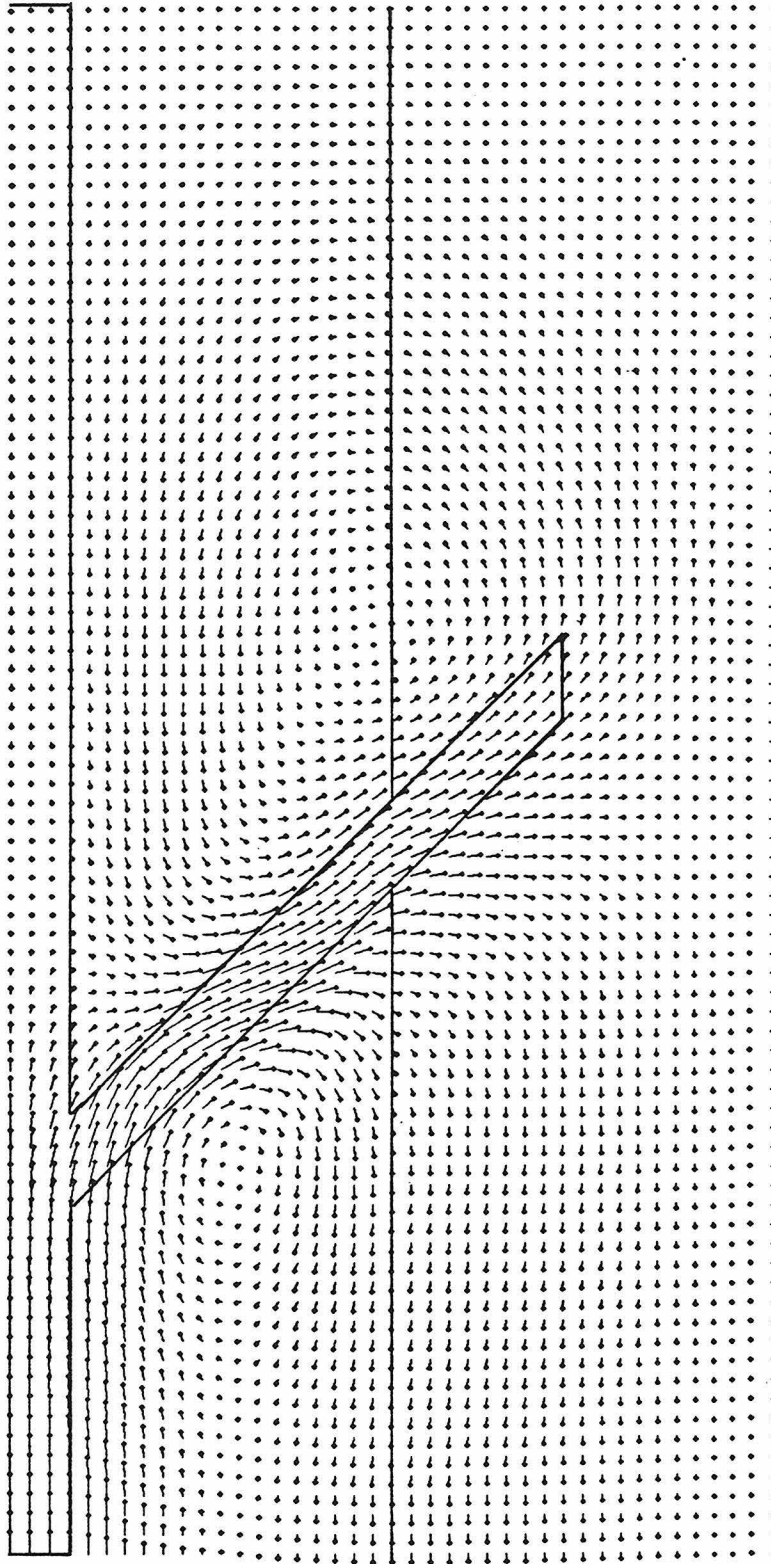
Figure 40. Flow fields for a 45° slab sinking under its own weight when there is a viscosity contrast of an order of magnitude at 670 km. In (a), the slab extends to 670 km depth. In (b), it penetrates into the lower mantle, to a depth of 1000 km. The flow lines are more aligned with the dip of the slab than they are in fig. 39.



a

10 cm/yr

670 km



b

10 cm/yr

Figure 41. Stress profile for the slab of fig. 40(b), a 45° slab sinking under its own weight into the lower mantle to a depth of 1000 km, when there is a viscosity contrast of an order of magnitude at 670 km. The stress in the upper mantle portion of the slab is consistent with observed seismicity, but we note that the stress in the lower mantle portion is still high.

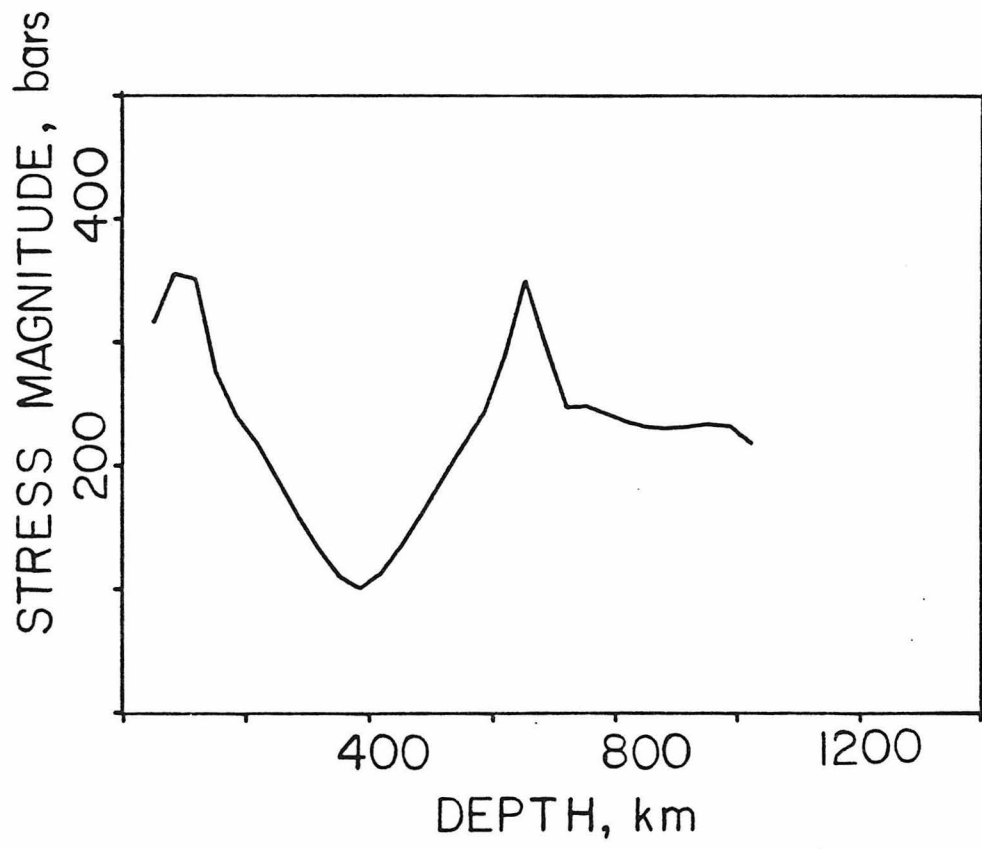
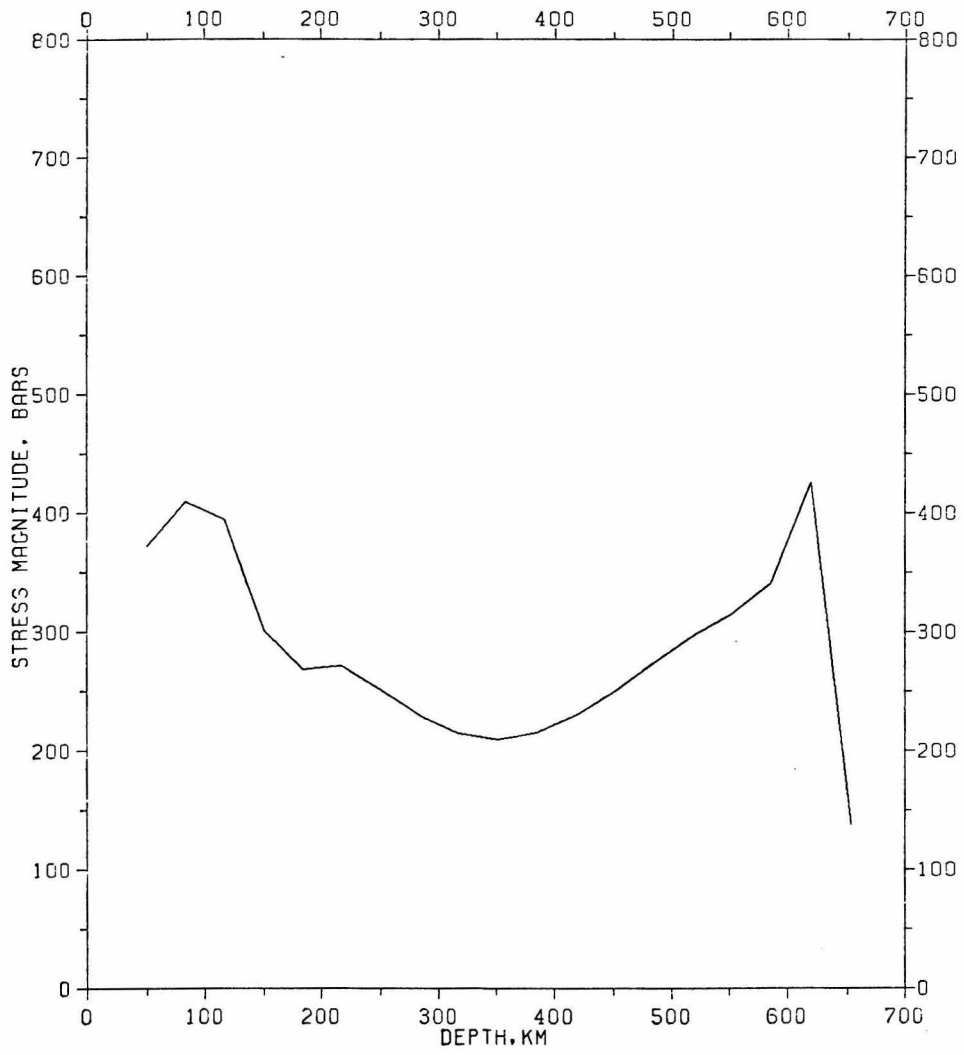


Figure 42. Stress profiles for a 45° slab sinking under its own weight when there is a phase transition at 670 km with a negative Clapeyron slope, as calculated by Schubert et al. (1975).



4. Summary and Conclusions

(1). The distribution of earthquakes with depth in the world has the following features: (a) an exponential decrease from shallow depths down to ≈ 250 to 300 km, (b) a minimum level near 250 to 300 km, and (c) a deep peak below 300 km. Many shallow subducting slabs show only feature (a). Deeper extending regions tend to show (a), (b), and (c), with the deep peak varying in position and intensity.

(2). A survey of events analysed by moment tensor inversion has confirmed some earlier ideas concerning the state of stress in the slab. Deep earthquakes (below 300 to 400 km) tend to have compression axes aligned with the dip of the slab. This appears to be a global tendency. The behavior of intermediate earthquakes is less clear, and more region-dependent. Both shallow-extending slabs and deep-extending slabs other than Tonga have intermediate earthquakes which are, in orientation, closer to down-dip tension than they are to anything else, but whose tension axes are not as well aligned with slab geometry as are the compression axes of deep events. The Tonga region shows some tendency toward down-dip compression at intermediate depths. In general, however, we do not agree with earlier conclusions (Isacks and Molnar, 1971) that deep-extending slabs in general are in down-dip compression at all depths.

(3). Simple viscous fluid models of subduction can explain observations (1) and (2) very well if there is a barrier of some sort at 670 km depth. A wide variety of models have stress magnitudes in the slab which display the following features as a function of depth: (a) a roughly linear decrease from shallow depths to about 250-

300 km, (b) a minimum near 250-300 km, and (c) a deep peak whose position and intensity depend on the depth of penetration of the slab. If the 670 km depth marks a viscosity contrast, the position and intensity of the deep peak are also affected by the magnitude of the viscosity increase: "softer" boundaries produce deeper and smaller peaks. Curves of stress magnitude versus depth look very much like curves of $\log N$ versus depth, where N is the number of earthquakes. The minimum at ≈ 300 km seems to be dictated by the 670 km length scale. The linear decrease in $\log N$ with depth down to ≈ 300 km is understandable if the number of events depends exponentially on the stress, for which there is some experimental evidence. Slab models with a barrier at 670 km yield down-dip compression below 300 to 400 km, in concordance with observation (2). At intermediate depths, dipping slabs in the models have a state of stress which is neither down-dip tensile nor down-dip compressive, although it is closer to the former. This, too, agrees with (2).

(4). The observations are explainable if the slab sinks under its own weight and is not subjected to push forces. They are also explainable if push forces exist in conjunction with gravitational forces. However, a slab subjected to push forces alone does not develop a deep peak in stress, and thus is not adequate to explain the observations.

(5). Chemical discontinuities above 670 km, or phase transitions with a phase boundary elevated in the slab relative to the mantle, produce peaks in stress which do not appear to be mirrored in the seismicity. Phase transitions whose boundaries are not elevated in the slab may be consistent with the observations.

(6). The data are consistent with a uniform viscosity mantle above the important barrier at 670 km. Inclusion of a low viscosity asthenosphere below the lithosphere does not destroy the match between calculated stress profiles and observed

seismicity, and can also help explain the stress orientations associated with double Benioff zones (Sleep, 1979).

(7). The results for a nonlinear rheology ($n = 3$) are qualitatively similar to the linear results.

(8). Observations (1) and (2) are equally well explained if the barrier at 670 km is a chemical discontinuity or a viscosity contrast where viscosity increases by an order of magnitude or more. A viscosity contrast yields flow fields in the models which are more consistent with observed slab shapes. However, if we allow the slab to penetrate into the lower mantle, we find that stresses in the slab below 670 km are as high as they are at upper mantle depths. We are thus faced with the problem of explaining why these stresses do not produce earthquakes.

REFERENCES

- Abe, K. (1981). Magnitudes of Large Shallow Earthquakes from 1904 to 1980, *Phys. Earth Plan. Int.*, 27, 72-92.
- Abe, K., and H. Kanamori (1979). Temporal Variation of the Activity of Intermediate and Deep Focus Earthquakes, *J. Geophys. Res.*, 84, 3589-3595.
- Ahrens, T. J., and Syono, Y. (1967). Calculated Mineral Reactions in the Earth's Mantle, *J. Geophys. Res.*, 72, 4181-4188.
- Akaogi, M., and S. Akimoto (1977). Pyroxene-Garnet Solid Solution Equilibria in the Systems $Mg_4Si_4O_{12}-Mg_3Al_2Si_3O_{12}$ at High Pressures and Temperatures, *Phys. Earth Plan. Int.*, 15, 90-106.
- Anderson, D. L. (1967). Phase Changes in the Upper Mantle, *Science*, 157, 1165-1173.
- Anderson, D. L. (1976). The 650 km Mantle Discontinuity, *Geophys. Res. Lett.*, 3, 347-349.
- Anderson, D. L. (1979a). The Upper Mantle Transition Region: Eclogite ? *Geophys. Res. Lett.*, 6, 433-436.
- Anderson, D. L. (1979b). The Deep Structure of Continents, *J. Geophys. Res.*, 84, 7555-7560.
- Ashby, M. F., and R. A. Verrall (1977). Micromechanisms of Flow and Fracture, and Their Relevance to the Rheology of the Upper Mantle, *Phil. Trans. Roy. Soc. Lond.*, A, 288, 59-95.
- Bath, M. (1981). Earthquake Magnitude-- Recent Research and Current Trends, *Earth*

- Sci. Rev., 17, 315-398.
- Batschelet, E. (1981). Circular Statistics in Biology, Academic Press, N. Y.
- Bingham, C. (1964). Distributions on the Sphere and on the Projective Plane, PhD Dissertation, Yale University, New Haven, CT.
- Bingham, C. (1974). An Antipodally Symmetric Distribution on the Sphere, Ann. Statist., 2, 1201-1225.
- Birch, F. (1952). Elasticity and Constitution of the Earth's Interior, J. Geophys. Res., 57,227-286.
- Cardwell, R. K., B. L. Isacks, and D. E. Karig (1980). The Spatial Distribution of Earthquakes, Foci Mechanism Solutions, and Subducted Lithosphere in the Philippine and Northeastern Indonesian Islands, in Dennis E. Hayes, ed., The Tectonic and Geologic Evolution of Southeast Asian Seas and Islands, Geophysical Monograph 23, American Geophysical Union, Washington, 1-35.
- Cathles, L. M. (1975). The Viscosity of the Earth's Mantle, Princeton University Press, Princeton, N. J.
- Chouhan, R. K. S. and V. K. Srivastava (1970). Global Variation of b in the Gutenberg-Richter's Relation $\log N = a - bM$ with Depth, Pageoph., 82, 124-132.
- Dziewonski, A. M., T. A. Chou, and J. H. Woodhouse (1981). Determination of Earthquake Source Parameters from Waveform Data for Studies of Global and Regional Seismicity, J. Geoph. Res., 86, 2825-2852.
- Dziewonski, A. M. and J. H. Woodhouse (1983). An Experiment in Systematic Study of Global Seismicity: Centroid-Moment Tensor Solutions for 201 Moderate and Large Earthquakes of 1981, J. Geophys. Res., in press.
- Engdahl, E. R. and C. H. Scholz (1977). A Double Benioff Zone Beneath the Central Aleutians: An Unbending of the Lithosphere, Geoph. Res. Lett., 4, 473-476.

- Fisher, R. A. (1953). Dispersion on a Sphere, *Proc. Roy. Soc. A*, 217, 295-305.
- Fujita, K., and H. Kanamori (1981). Double Seismic Zones and Stresses of Intermediate Depth Earthquakes, *Geophys. J. Roy. Astr. Soc.*, 66, 131-156.
- Giardini, D. (1982). Depth Dependence of Deviations of Earthquake Source Mechanisms from "Double Couple" Model, *EOS*, 63, 1027.
- Giardini, D. (1983). Manuscript in Preparation.
- Gilbert, F. (1981). An Introduction to Low Frequency Seismology, in A. M. Dziewonski and E. Boschi (eds.), *Physics of the Earth's Interior*, North Holland, Amsterdam, 41-81.
- Goldreich, P., and A. Toomre (1969). Some Remarks on Polar Wandering, *J. Geophys. Res.*, 74, 2555-2567.
- Gueguen, Y. and A. Nicolas (1980). Deformation of Mantle Rocks, *Ann. Rev. Earth Plan. Sci.*, 8, 119-144.
- Gutenberg, B. and C. F. Richter (1954). *Seismicity of the Earth and Associated Phenomena*, Hafner Pub. Co., N. Y. (1965 facsimile)
- Hager, B. H. (1983). Subducted Slabs and the Geoid: Constraints on Mantle Rheology and Flow, to be submitted for publication.
- Hager, B. H., and R. J. O'Connell (1978). Subduction Zone Dip Angles and Flow Driven by Plate Motion, *Tectonophys.*, 50, 111-133.
- Hager, B. H., and R. J. O'Connell (1981). A Simple Global Model of Plate Dynamics and Mantle Convection, *J. Geophys. Res.*, 86, 4843-4867.
- Hagiwara, Y. (1974). Probability of Earthquake Occurrence from Results of Rock Fracture Experiments, *Tectonophysics*, 23, 99-103.
- Hales, A. L., K. Muirhead, and J. Rynn (1976). Upper Mantle Travel Times in Australia, *Phys. Earth Plan. Int.*, 11, 109-118.

- Hasegawa, A., N. Umino, and A. Takagi (1978). Double Planed Structure of the Deep Seismic Zone in N.E. Japan Arc, *Tectonophys.*, 47, 43-58.
- Heaton, T. H. (1982). Tidal Triggering of Earthquakes, *Bull. Seismol. Soc. Am.*, 72, 2181-2200.
- Herring, C. (1950). Diffusional Viscosity of a Polycrystalline Solid, *J. Appl. Phys.*, 21, 437.
- Howard, A. and B. H. Hager (1983). Entrainment of the Mantle and the Lifetime of the Subducting Slab, Manuscript in Preparation.
- Hsui, A. T. and M. N. Toksöz (1979). The Evolution of Thermal Structures Beneath a Subduction Zone, *Tectonophysics*, 60, 43-60.
- Hughes, T. J. R., W. K. Liu, and A. Brooks (1979). Finite Element Analysis of Incompressible Viscous Flows by the Penalty Function Formulation, *J. Comp. Phys.*, 30, 1-60.
- Iio, Y. (1982). Scaling of Rupture Size-- From Earthquake to Acoustic Emission, *Zisin*, 35, 183-193.
- Isacks, B., and M. Barazangi (1977). Geometry of Benioff Zones: Lateral Segmentation and Downwards Bending of the Subducted Lithosphere, in M. Talwani and W. C. Pitman (eds.), *Island Arcs, Deep Sea Trenches and Back-Arc Basins*, Ewing Series, vol. 1, American Geophysical Union, Washington, D. C., 99-114.
- Isacks, B., and P. Molnar (1969). Mantle Earthquake Mechanisms and the Sinking of the Lithosphere, *Nature*, 223, 1121-1124.
- Isacks, B., and P. Molnar (1971). Distribution of Stresses in the Descending Lithosphere from a Global Survey of Focal Mechanism Solutions of Mantle Earthquakes, *Rev. Geophys. Sp. Phys.*, 9, 103-174.
- Isacks, B., J. Oliver, L. R. Sykes (1968). Seismology and the New Global Tectonics, *J.*

- Geophys. Res., 73, 5855-5899.
- Ishimoto, M., and K. Iida (1939). Observations sur les Seismes Enregistres par le Microsismographe Construit Dernierement, Bull. Earthquake Res. Inst., 17, 443-478.
- Jarosch, A., and E. Aboodi (1970). Towards a Unified Notation of Source Parameters, Geophys. J. Roy. Astr. Soc., 21, 513-529.
- Johnson, C. E., and F. M. Richter (1979). Stereoviews of Seismicity Associated with Subduction Zones, J. Geol., 87, 467-474.
- Kagan, Y. Y., and L. Knopoff (1980). Dependence of Seismicity on Depth, Bull. Seismol. Soc. Am., 70, 1811-1822.
- Kanamori, H. (1978). Quantification of Earthquakes, Nature, 271, 411-414.
- Kanamori, H., and J. W. Given (1981). Use of Long Period Surface Waves for Rapid Determination of Earthquake Source Parameters, Phys. Earth Plan. Int., 27, 8-31.
- Kanamori, H., and J. W. Given (1982). Use of Long Period Surface Waves for Rapid Determination of Earthquake Source Parameters, 2. Preliminary Determination of Source Mechanism of Large Earthquakes ($M_S \geq 6.5$) in 1980, Phys. Earth Plan. Int., 30, 260-268.
- Katsumata, M., and L. R. Sykes (1969). Seismicity and Tectonics of the Western Pacific: Izu-Mariana-Caroline and Ryukyu-Taiwan Regions, J. Geophys. Res., 74, 5923-5948.
- Knopoff, L., and J. Randall (1970). The Compensated Linear Vector Dipole-- A Possible Mechanism for Deep Earthquakes, J. Geophys. Res., 75, 4957-4963.
- Kusunose, K., K. Yamamoto, and T. Hirasawa (1980). Source Process of Microfracture in Granite with Reference to Earthquake Prediction, Sci. Rep. Tohoku University, Ser. 5, Geophys., 26, 111-121.

- Lehmann, I. (1961). S and the Structure of the Upper Mantle, *Geophys. J. Roy. Astr. Soc.*, 4, 124-138.
- Liu, L. G. (1975). Post-Oxide Phases of Forsterite and Enstatite, *Geoph. Res. Lett.*, 2, 417-419.
- Liu, L. G. (1976). The Post Spinel Phase of Forsterite, *Nature*, 262, 770-772.
- MacDonald, G. J. F. (1963). The Deep Structure of the Continents, *Rev. Geophys. Sp. Phys.*, 1, 587-665.
- Mardia, K. V. (1972). *Statistics of Directional Data*, Academic Press, N. Y.
- McKenzie, D. P. (1966). The Viscosity of the Lower Mantle, *J. Geophys. Res.*, 71, 3995-4010.
- McKenzie, D. P. (1969). Speculations on the Consequences and Causes of Plate Motions, *Geophys. J. Roy. Astr. Soc.*, 18, 1-32.
- McKenzie, D. P., J. M. Roberts, and N. O. Weiss (1974). Convection in the Earth's Mantle: Towards a Numerical Simulation, *J. Fluid Mech.*, 62, 465-538.
- Melosh, H. J. and A. Raefsky (1980). The Dynamical Origin of Subduction Zone Topography, *Geophys. J. Roy. Astr. Soc.*, 60, 333-354.
- Meijering, J. L., and C. J. M. Rooymans (1958). On the Olivine-Spinel Transition in the Earth's Mantle, *Koninkl. Ned. Akad. Wetenschap. Proc., Ser. B.*, 61, 333-344.
- Minear, J. W., and M. N. Toksöz (1970a). Thermal Regime of a Downgoing Slab and the New Global Tectonics, *J. Geophys. Res.*, 75, 1397-1419.
- Minear, J. W., and M. N. Toksöz (1970b). Thermal Regime of a Downgoing Slab, *Tectonophys.*, 10, 367-390.
- Mogi, K. (1962a). Study of Elastic Shocks Caused by the Fracture of Heterogeneous Materials and its Relations to Earthquake Phenomena, *Bull. Earthq. Res. Inst.*, 40, 125-173.

- Mogi, K. (1962b). Magnitude-Frequency Relation for Elastic Shocks Accompanying Fracture of Various Materials and Some Related Problems in Earthquakes: II, Bull. Earthq. Res. Inst., 40, 851-853.
- Mogi, K. (1981). Earthquake Prediction Program in Japan, in D. W. Simpson and P. G. Richards (eds.), Earthquake Prediction: An International Review, Maurice Ewing Series vol 4, American Geophysical Union, Washington, D. C., 635-666.
- Molnar, P., and P. Tapponier (1975). Cenozoic Tectonics of Asia: Effects of a Continental Collision, Science, 189, 419-426.
- Nabarro, F. R. N. (1948). Deformation of Crystals by the Motion of Single Ions, in Strength of Solids, The Physical Society, London, 75.
- O'Connell, R. J. (1977). On the Scale of Mantle Convection, Tectonophys., 38, 119-136.
- Ohnaka, M., and K. Mogi (1981). Frequency Dependence of Acoustic Emission Activity in Rocks Under Incremental, Uniaxial Compression, Bull. Earthq. Res. Inst., 56, 67-89.
- Ohnaka, M., and K. Mogi (1982). Frequency Characteristics of Acoustic Emission in Rocks Under Uniaxial Compression and Its Relation to the Fracturing Process to Failure, J. Geophys. Res., 87, 3873-3884.
- Onstott, T. C. (1980). Application of the Bingham Distribution Function in Paleomagnetic Studies, J. Geophys. Res., 85, 1500-1510.
- Pascal, G., B. L. Isacks, M. Barazangi, and J. Dubois (1978). Precise Relocations of Earthquakes and Seismotectonics of the New Hebrides Island Arc, J. Geophys. Res., 83, 4957-4973.
- Peltier, W. R. and J. T. Andrews (1976). Glacial-Isostatic Adjustment, I. The Forward Problem, Geophys. J. Roy. Astr. Soc., 46, 605-646.

- Raj, R. and M. F. Ashby (1971). On Grain Boundary Sliding and Diffusional Creep, Trans. Met. Soc. AIME, 2, 1113.
- Reyners, M., and K. Coles (1982). Fine Structure of the Dipping Seismic Zone and Subduction Mechanics in the Shumagin Islands, Alaska, J. Geophys. Res., 87, 356-366.
- Richter, C. F. (1958). Elementary Seismology, Freeman, San Francisco.
- Richter, F. M. (1973). Dynamical Models for Sea Floor Spreading, Rev. Geoph. Sp. Phys., 11, 223-288.
- Richter, F. M. (1979). Focal Mechanisms and Seismic Energy Release of Deep and Intermediate Earthquakes in the Tonga-Kermadec Region and their Bearing on the Depth Extent of Mantle Flow, J. Geophys. Res., 84, 6783-6795.
- Ringwood, A. E., and A. Major (1970). The system $Mg_2SiO_4 - Fe_2SiO_4$ at High Pressure and Temperature, Phys. Earth Plan. Int., 3, 89.
- Sano, O., M. Terada, and S. Ehara (1982). A Study on the Time-Dependent Microfracturing and Strength of Oshima Granite, Tectonophys., 84, 343-362.
- Scholz, C. H. (1968). The Frequency-Magnitude Relation of Microfracturing in Rock and Its Relation to Earthquakes, Bull. Seismol. Soc. Am., 58, 399-415.
- Schubert, G., D. A. Yuen, and D. L. Turcotte (1975). Role of Phase Transitions in a Dynamic Mantle, Geophys. J. R. Astr. Soc., 42, 705-735.
- Sleep, N. H. (1975). Stress and Flow Beneath Island Arcs, Geophys. J. Roy. Astr. Soc., 42, 827-857.
- Sleep, N. H. (1979). The Double Seismic Zone in Downgoing Slabs and the Viscosity of the Mesosphere, J. Geophys. Res., 84, 4565-4571.
- Stephens, M. A. (1964). The Testing of Unit Vectors for Randomness, J. Amer. Statist. Assoc., 59, 160-167.

- Stephens, M. A. (1969a). Tests for Randomness of Directions Against Two Circular Alternatives, *J. Amer. Statist. Assoc.*, 64, 280-289.
- Stephens, M. A. (1969b). Tests for the Von Mises Distribution, *Biometrika*, 56, 149-160.
- Stocker, R. L., and M. F. Ashby (1973). On the Rheology of the Upper Mantle, *Rev. Geophys. Sp. Phys.*, 11, 391-426.
- Sykes, L. R. (1966). Seismicity and Deep Structure of Island Arcs, *J. Geophys. Res.*, 71, 2981-3006.
- Tarr, A. C. (1974). World Seismicity Map, United States Geological Survey.
- Toksöz, M. N., J. W. Minner, and B. R. Julian (1971). Temperature Field and Geophysical Effects of a Downgoing Slab, *J. Geophys. Res.*, 76, 1113-1138
- Toksöz, M. N., N. H. Sleep, and A. T. Smith (1973). Evolution of the Downgoing Lithosphere and the Mechanisms of Deep Focus Earthquakes, *Geophys. J. Roy. Astr. Soc.*, 35, 285-310.
- Topper, R. E. (1978). Fine Structure of the Benioff Zone Beneath the Central Aleutian Arc, M. S. Thesis, Univ. of Colorado.
- Tsumura, K. (1973). Microearthquake Activity in the Kanto District, *Spec. Pub. Earthq. Res. Inst. Tokyo Univ. for 50th Anniv. Great Kanto Earthquake*, 67-87.
- Turcotte, D. L. and G. Schubert (1971). Structure of the Olivine-Spinel Phase Boundary in the Descending Lithosphere, *J. Geophys. Res.*, 76, 7980-7987.
- Turcotte, D. L., and G. Schubert (1973). Frictional Heating of the Descending Lithosphere, *J. Geophys. Res.*, 78, 5876-5886.
- Twiss, R. J. (1976). Structural Superplastic Creep and Linear Viscosity in the Earth's Mantle, *Earth Plan. Sci. Lett.*, 33, 86-100.
- Umino, N., and A. Hasegawa (1975). On the Two-Layered Structure of Deep Seismic

- Plane in Northeastern Japan Arc, *Zisin*, 27, 125-139.
- Umino, N., and A. Hasegawa (1982). A Detailed Structure of the Deep Seismic Zone and Earthquake Mechanism in the N. E. Japan Arc, *Zisin*, 35, 237-257.
- Uyeda, S., and H. Kanamori (1979). Back-Arc Opening and the Mode of Subduction, *J. Geophys. Res.*, 84, 1049-1061.
- Veith, K. F. (1974). The Relationship of Island Arc Seismicity to Plate Tectonics, PhD Dissertation, Southern Methodist University.
- Veith, K. F. (1977). The Nature of the Dual Zone of Seismicity in the Kuriles Arc, *EOS*, 58, 1232.
- Walcott, R. I. (1973). Structure of the Earth from Glacio-Isostatic Rebound, *Ann. Rev. Earth Plan. Sci.*, 1, 15-37.
- Watson, G. S. (1956a). Analysis of Dispersion on a Sphere, *Mon. Not. Roy. Astr. Soc., Geophys. Supp.*, 7, 153-159.
- Watson, G. S. (1956b). A Test for Randomness of Directions, *Mon. Not. Roy. Astr. Soc., Geophys. Supp.*, 7, 160-161.
- Watson G. S. (1966). The Statistics of Orientation Data, *J. Geol.*, 74, 786-797.
- Watson, G. S. and E. Irving (1957). Statistical Methods in Rock Magnetism, *Mon. Not. Roy. Astr. Soc., Geophys. Supp.*, 7, 289-300.
- Whitcomb, J. H., and D. L. Anderson (1970). Reflection of P'P' Seismic Waves from Discontinuities in the Mantle, *J. Geophys. Res.*, 75, 5713-5728.
- Wortel, R., (1982). Seismicity and Rheology of Subducted Slabs, *Nature*, 296, 553-556.
- Yuen, D. A., R. Sabadini, and E. V. Boschi (1982). Viscosity of the Lower Mantle as Inferred from Rotational Data, *J. Geophys. Res.*, 87, 10745-10762.

APPENDICES

NOTE: References mentioned in Appendices are in the same list as the other references for Part II.

Appendix A: Mechanisms of Large Intermediate and Deep Earthquakes, 1978-1981

We present here the results of surface wave inversions for the focal mechanism of large intermediate and deep earthquakes from 1978-1981. Table A1 lists information from the NOAA catalog about these events. In deciding which events were "large", we were guided by the magnitudes. We studied earthquakes with $m_b \geq 6$, and which offered some other evidence of being large, for example, a large listing under M_{other} . Magnitudes, however, are not necessarily reliable indicators of the size of an earthquake (Kanamori, 1978). Thus, some of the events we studied did not in fact turn out to have moments which would place them among the very largest events for the period.

Our data consist of vertical component Rayleigh waves recorded on IDA (International Deployment of Accelerographs) instruments. Generally, we use R2 in the inversions. Often, we also use R1, and sometimes R3. The technique is described by Kanamori and Given (1981,1982). What follows in this paragraph is taken almost directly from Section 2 of the 1981 paper. The parameter vector is $M = [M_{xy}, M_{yy} - M_{xx}, M_{yy} + M_{xx}, M_{yz}, M_{zz}]^T$. Once M is determined, the moment tensor matrix

$$\begin{matrix} M_{xx} & M_{xy} & M_{xz} \\ M_{xy} & M_{yy} & M_{yz} \\ M_{xz} & M_{yz} & M_{zz} \end{matrix}$$

can be diagonalised. The trace of the matrix is zero by assumption in the inversion.

The eigenvectors define the principal stress axes. If the intermediate axis is zero, the moment tensor is a double couple. If it is not, the moment tensor may be decomposed either into a double couple plus compensated linear dipole (Knopoff and Randall, 1970) or two orthogonal double couples (Gilbert, 1981). Generally, one double couple will be larger than the other. Table A2 presents the major and minor double couples we obtained for our events. The notation conventions are the same as those in Kanamori and Given (1981), who follow Jarosch and Aboodi (1970).

General moment tensor solutions often deviate significantly from double couples. Some investigators (Dziewonski et al., 1981; Dziewonski and Woodhouse, 1982; Giardini, 1982, 1983) have attached significance to these deviations. Dziewonski et al. (1981) suggest a possible regional variation in the deviation from double couple. Giardini (1982, 1983) reports a possible depth dependence in the deviation, with high deviations occurring at intermediate depths in deeply penetrating subduction zones. The deviation from double couple is a difficult parameter to interpret. There is at present no way to evaluate the significance of variations in this parameter, and one cannot be certain that the data available can effectively constrain it (Kanamori and Given, 1982).

The double couple is still a very useful model of the earthquake source, and one that has never been convincingly ruled out by the observations. Kanamori and Given (1981) present a technique for inverting IDA data when the source is constrained to be a double couple. We have performed such an inversion for each of our events and the results are shown in Table A3.

In general we see that the inversion of IDA data can be carried out quite successfully on deep and intermediate events, despite the lower signal levels of surface waves as compared to shallow events. There is, however, one difficulty which arises

at intermediate depths: the excitation functions of Rayleigh waves (see Kanamori and Stewart, 1976) go through zeroes, as shown in Fig. A2. Kanamori and Given's matrix equation (equation (7) in the 1981 paper) is

$$AM = V$$

where M is the parameter vector, V is a vector of spectral points from the data, and A is a matrix whose entries depend on the excitation functions. If any of the excitation functions vanish, A becomes singular. When $P_R^{(1)}$ vanishes, the elements M_{xy} and $(M_{yy} - M_{xx})$ are indeterminate. When $S_R^{(1)}$ vanishes $(M_{yy} + M_{xx})$ is indeterminate. The function $Q_R^{(1)}$ does not vanish except at zero depth, so it is not of any concern except for very shallow events. Fig. A2(a) plots $S_R^{(1)}$ versus depth for periods from 190 - 274 seconds; this represents the practically usable range of periods for these inversions. We see that the zero occurs somewhere between 80 and 160 km depth. From fig. A2(b), we see that $P_R^{(1)}$ goes through a zero somewhere between 130 and 200 km depth. Thus IDA inversions are subject to numerical difficulties over a sizeable portion of the intermediate depth range. To some extent, we can avoid the problem by choosing an appropriate period. This technique, however, can push the zero away from the depth of interest by only a limited margin, and complications are caused by the fact that the depth is not known exactly. Reported depths in the NOAA catalog probably have error bars of at least +/- 25 km. The hypocentral depth is not varied as a free parameter in the Kanamori-Given scheme.

One way to improve solutions for events in the problematical depth range is to use first motion data in conjunction with the surface wave data. Kanamori (1982, personal communication) has developed a technique to do this. When $M_{xx} + M_{yy} + M_{zz} = 0$, the standard expression for P-wave displacement in a

homogeneous whole-space can be written

$$u(i_h, \varphi) = M_{xy} \sin^2 i_h \sin 2\varphi - (M_{yy} - M_{xx}) \left(\frac{1}{2} \sin^2 i_h \cos 2\varphi \right) \\ + (M_{xx} + M_{yy}) \left(\frac{1}{2} (1 - 3 \cos^2 i_h) \right) - M_{yz} \sin 2i_h \sin \varphi - M_{zx} \sin 2i_h \cos \varphi$$

where i_h is takeoff angle and φ is azimuth. By estimating u from amplitude data one can, in principle, determine the moment tensor. Because of the extreme scatter typically observed in P wave amplitude data, however, the technique uses a very crude amplitude measure, with +1 for a clear compressional arrival, 0 for an ambiguous arrival, and -1 for a clear tensional one. After obtaining a guess at the moment tensor from this simple method, one then picks the maximum element as a reference element M_R . In the case when $S_R^{(1)}$ vanishes, $\frac{(M_{yy} + M_{xx})}{M_R}$ is constrained to have the same value in the surface wave inversion as is given by the body wave inversion. In the case when $P_R^{(1)}$ vanishes, both $\frac{M_{xy}}{M_R}$ and $\frac{(M_{yy} - M_{xx})}{M_R}$ are constrained. This technique has been used on events 07/22/80 and 05/13/78 indicated in Table A1.

Date	H	M	S	Lat.	Lon.	Depth	m_b	M_{other}	Ref.
07 22 80	07	06	23.0	-20.3	169.6	122	6.1	6.8	1
05 13 78	07	08	46.2	-14.5	167.3	160	6.7	-	1
03 15 78	22	04	40.1	26.4	140.6	263	6.1	6.7	1,3
03 07 78	02	48	39.4	32.0	137.6	442	6.0	6.4	1,3,5
04 28 81	21	14	56.7	-23.7	180.0	540	6.0	-	2
08 16 79	21	31	26.3	41.8	130.8	588	6.1	6.7	1
07 20 80	21	20	04.0	-17.9	-178.6	591	6.0	6.5	1
04 24 79	01	45	09.0	-20.8	-178.7	599	6.0	6.7	1,3
10 17 79	05	43	03.0	18.5	145.3	601	6.1	-	1

References

- (1) Giardini (1983)
- (2) Dziewonski and Woodhouse (1983)
- (3) Dziewonski et al. (1981)
- (4) Gilbert (1981)
- (5) Walck, personal communication (1982)

These references are to investigators who have studied these events independently from us. In most cases, the agreement between our solutions and theirs is excellent. Ref. (1), the as yet unpublished study by Giardini (1983), and Ref. (2) were also the sources for the moment tensor Inversions of smaller earthquakes from 1977-1982, surveyed in Section 2.

Table A2
Moment Tensor Inversions

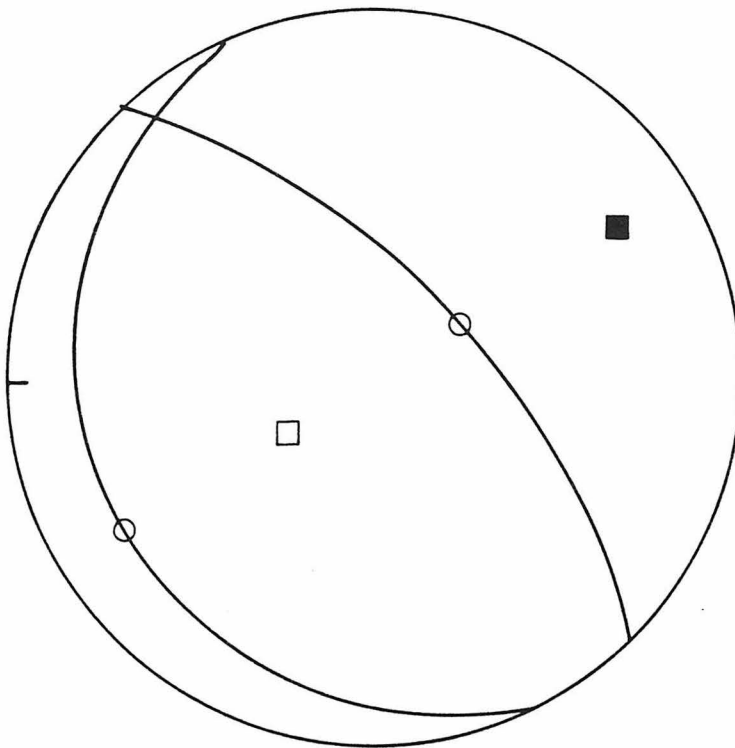
Event	Major Double Couple				Minor Double Couple			
	M_0 10^{27} dyn-cm	δ	λ	φ	M_0 10^{27} dyn-cm	δ	λ	φ
07 22 80	0.04	11.7	-69.8	8.4	0.01	50.7	43.8	-132.1
05 13 78	0.24	57.9	87.7	-126.8	0.012	44.6	-108.5	-48.6
03 15 78	0.098	67.1	183.6	104.1	0.023	61.0	68.8	-44.6
03 07 78	0.58	80.1	63.7	158.9	0.035	48.4	176.3	-54.6
04 28 81	0.21	85.8	44.3	163.0	0.04	83.1	63.7	-76.1
08 16 79	0.137	20.6	135.2	50.6	0.0018	68.5	-57.6	120.3
07 20 80	0.039	81.9	-45.5	-25.7	0.006	86.2	293.6	213.3
04 24 79	0.057	82.2	16.3	-60.1	0.02	53.0	-68.5	-2.0
10 17 79	0.44	59.0	-139.8	143.9	0.08	86.0	91.6	86.8

Table A3
Fault Plane Inversions
(Standard Errors in Parentheses)

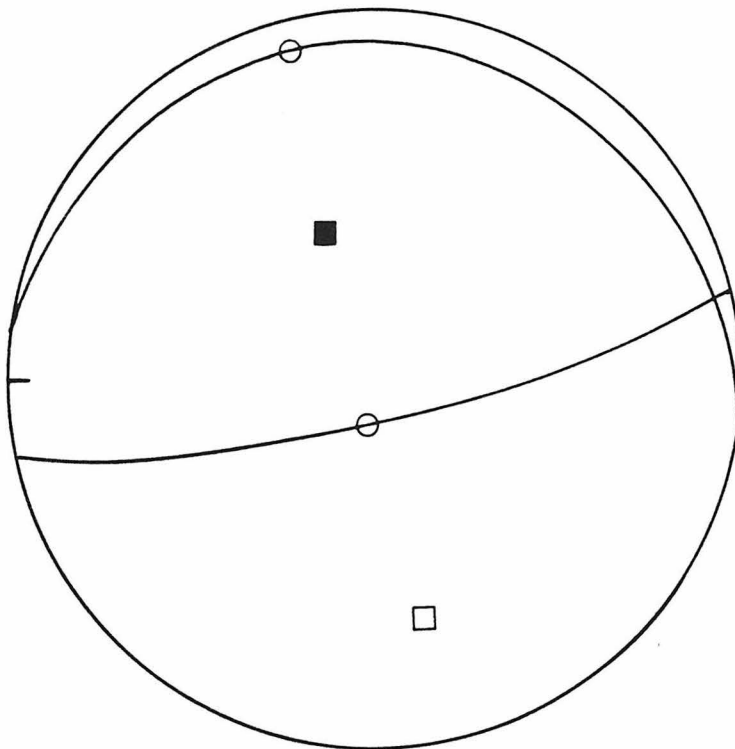
Event	M_0 10^{27} dyn-cm	δ	λ	φ
03 15 78	0.053 (0.011)	47.0 (11.9)	178.2 (4.9)	120.9 (4.8)
03 07 78	0.59 (0.06)	24.1 (11.6)	157.3 (9.9)	48.5 (13.5)
04 28 81	0.18 (0.019)	42.8 (6.4)	-12.3 (3.7)	75.2 (5.6)
08 16 79	0.14 (0.009)	20.5 (5.7)	135.3 (13.9)	50.9 (16.6)
07 20 80	0.035 (0.006)	80.4 (4.2)	-46.8 (11.3)	-33.7 (9.3)
04 24 79	0.024 (0.005)	77.4 (5.6)	268.2 (21.9)	78.8 (10.9)
10 17 79	0.35 (0.03)	55.6 (3.4)	-134.0 (4.6)	146.8 (7.7)

Figure A1. Focal mechanisms for events listed in Table A1. For 05/13/78 and 07/22/80, the major double couple in the combined surface-wave/first-motion inversion is plotted. For the rest of the events, results of the fault plane inversion are plotted. Circles on nodal planes indicate slip vectors. Filled squares are compression axes, and open ones are tension axes.

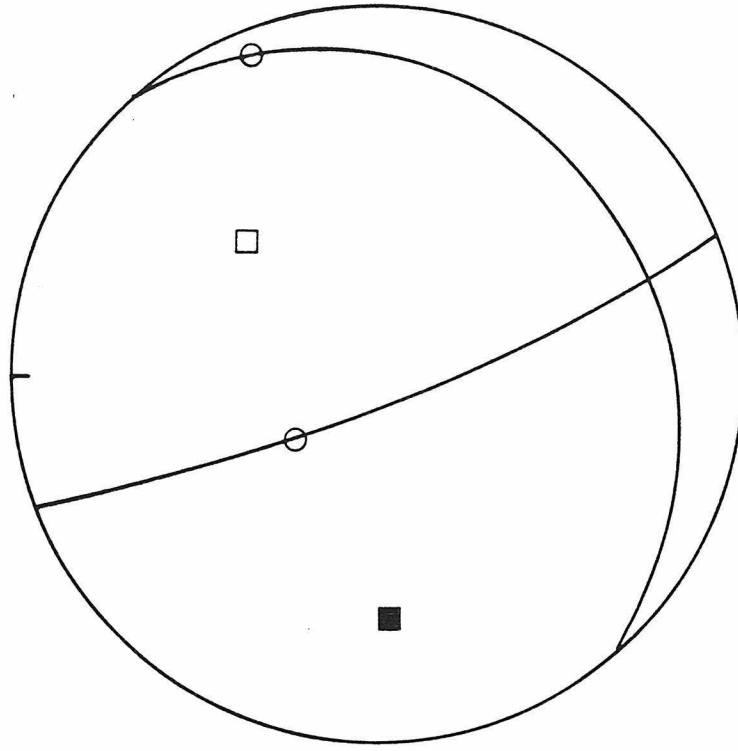
05 13 78



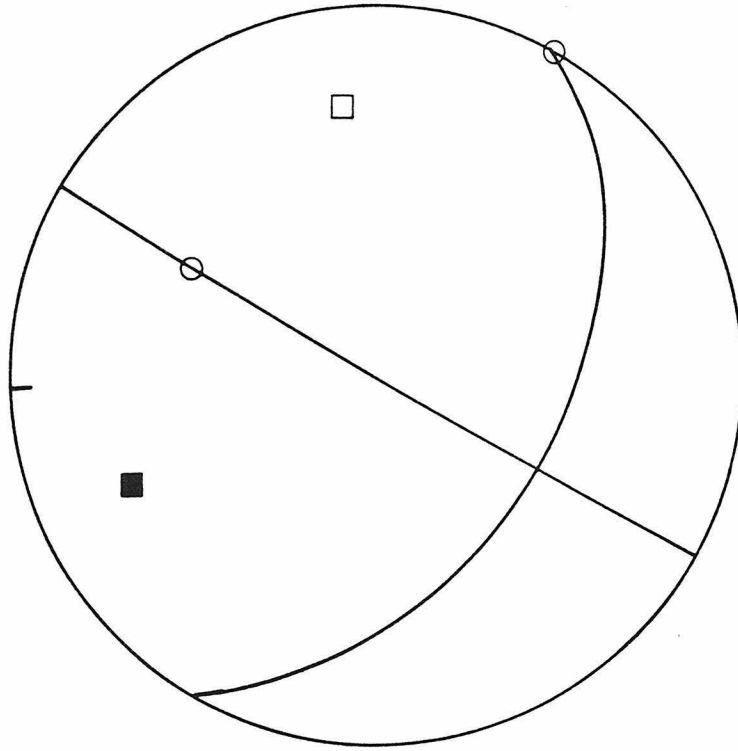
07 22 80



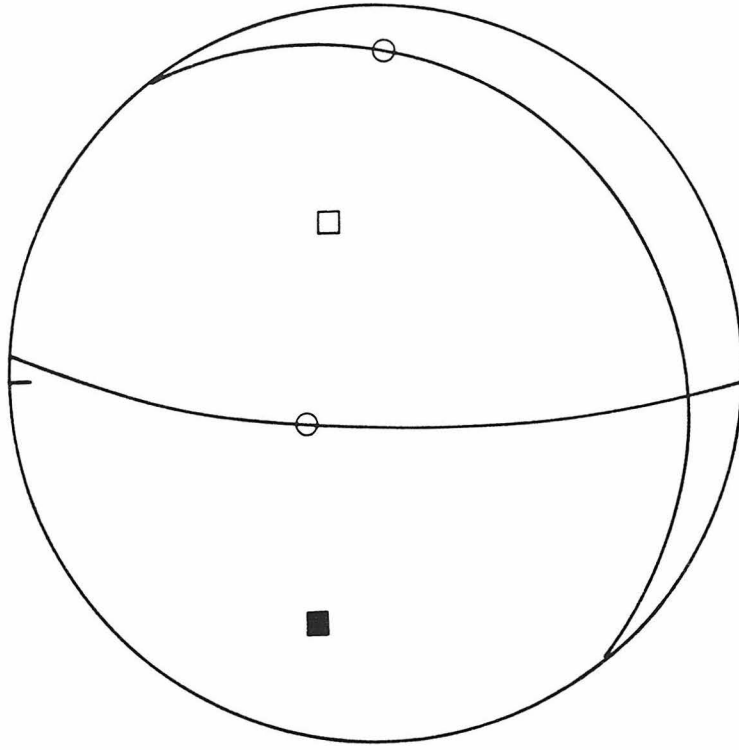
03 07 78



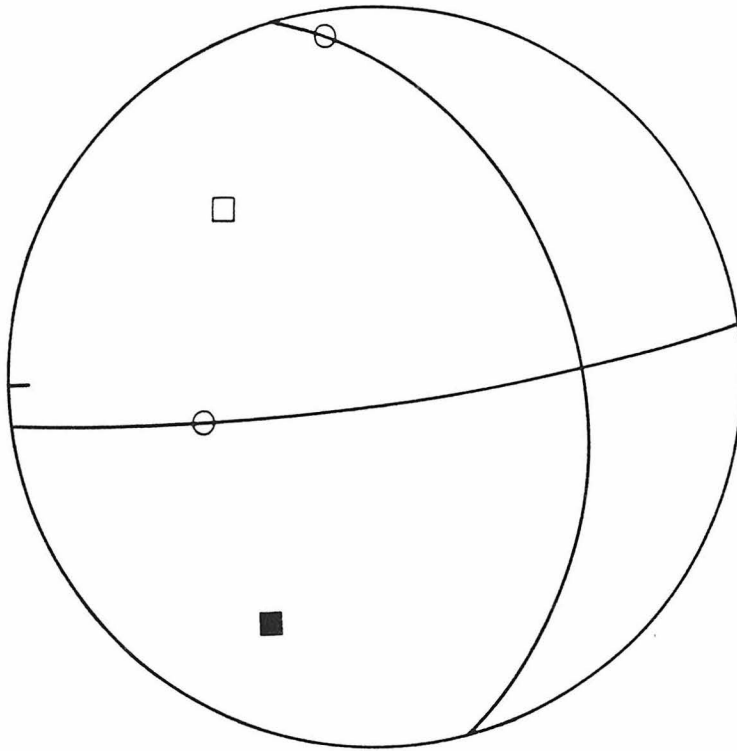
03 15 78



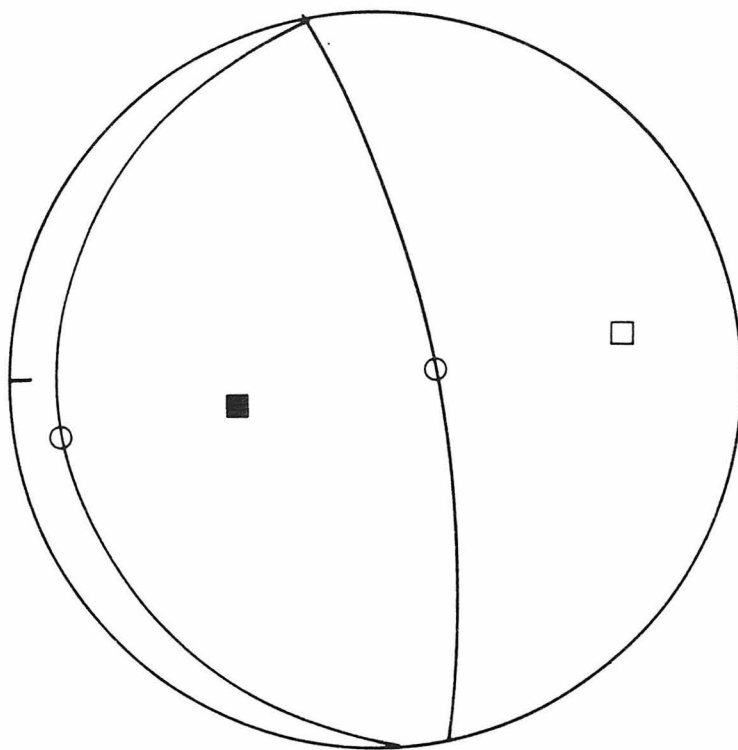
08 16 79



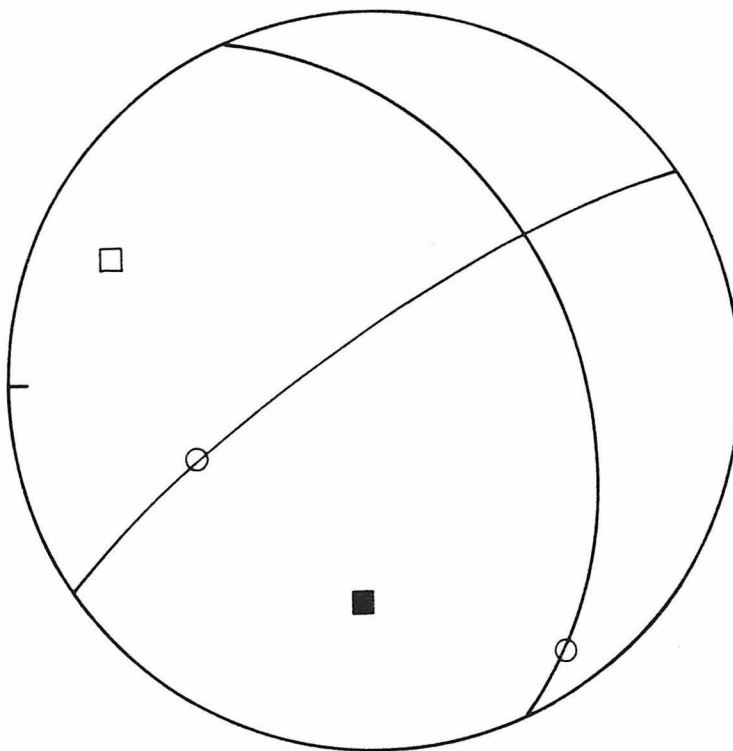
04 28 81



04 24 79



07 20 80



10 17 79

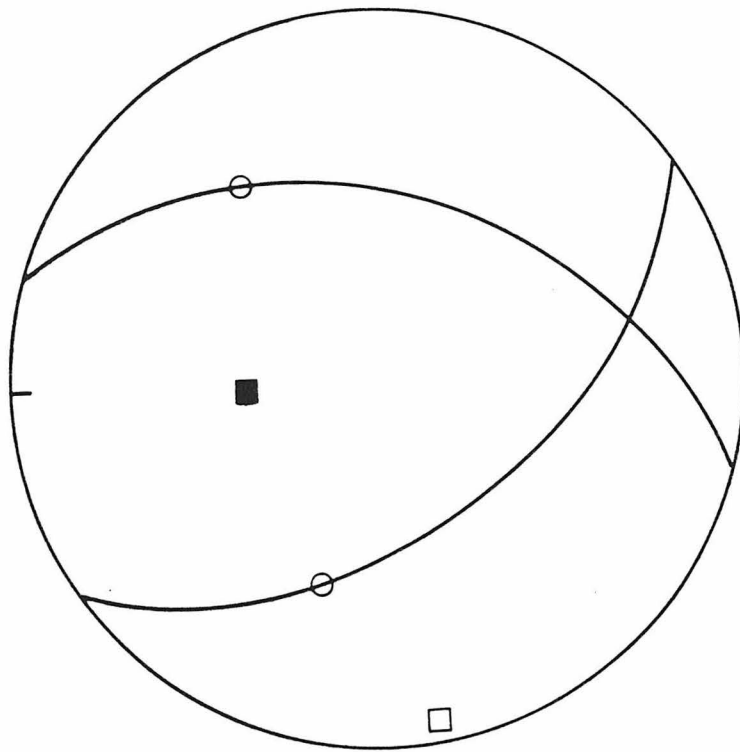
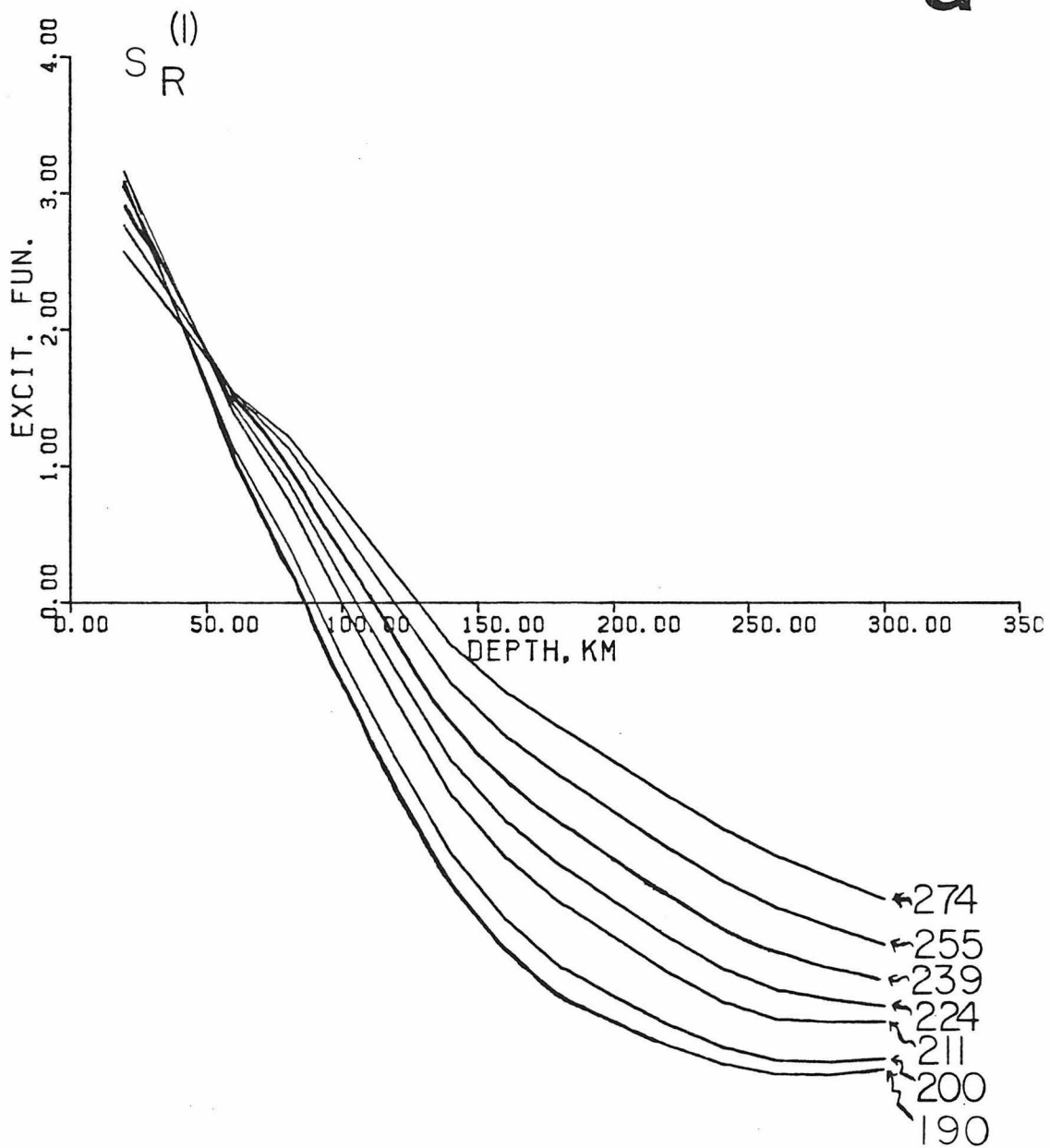
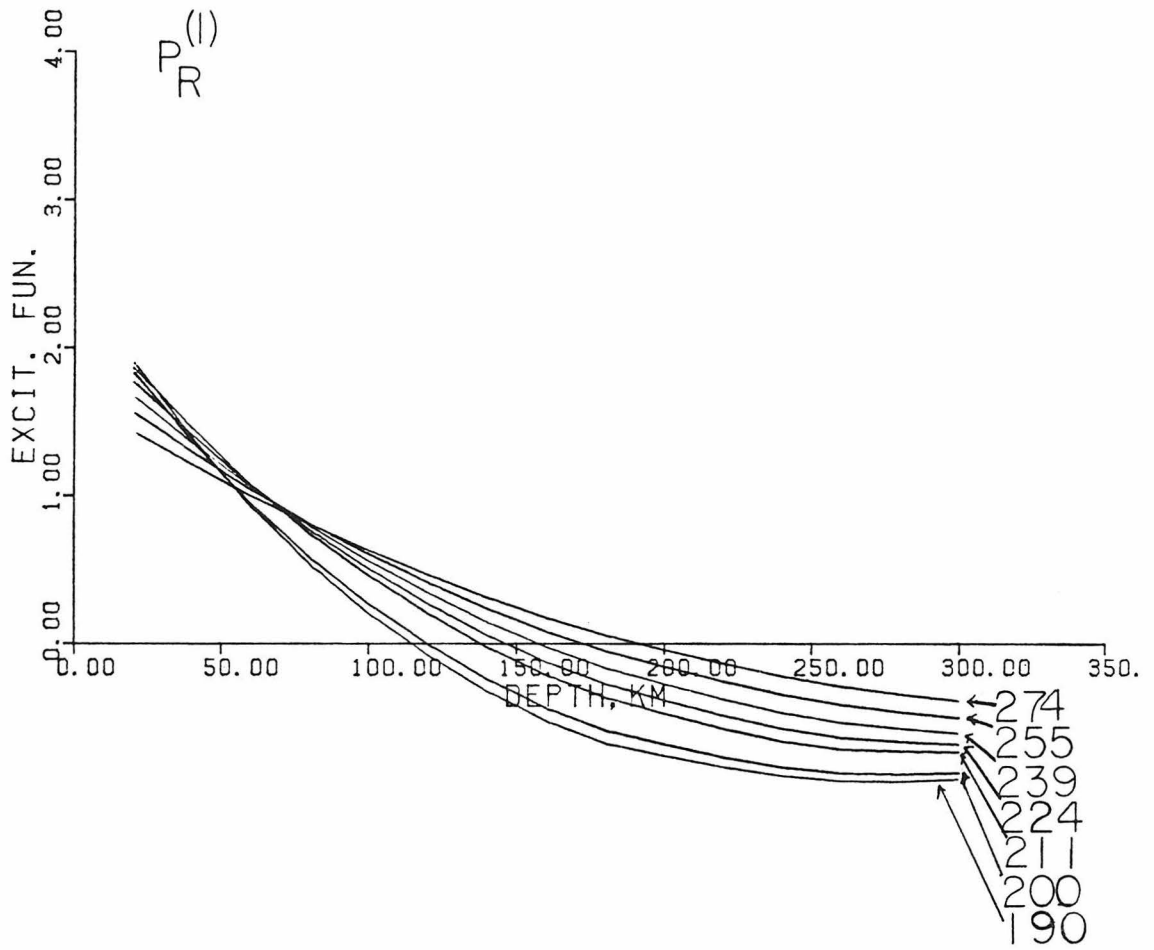


Figure A2. Rayleigh wave excitation functions (a) $S_R^{(1)}$ and (b) $P_R^{(1)}$ as a function of depth. Number labelling each of the curves indicates the period in seconds.

a



b



Appendix B: A Brief Outline of Directional Statistics

When one's data are directions in space, one must use special methods to analyse them statistically. In two dimensions, for instance, a unit vector with azimuth 1° and one with azimuth 359° yield a vector with azimuth 180° if one simply averages azimuths. This is clearly an incorrect mean direction. The literature concerning directional data is extensive, and includes two full length monographs, one by Mardia (1972), and another by Batschelet (1981). Both are good books, but the second is particularly clear for the beginner.

One simple and intuitively pleasing way to average unit directions is to obtain the resultant, and take its direction as the mean direction (Watson, 1966). In the example above, this would give 0° as the mean direction. The resultant can also provide an effective measure of dispersion. The closer a sample of vectors is grouped about a mean direction, the larger will be the resultant. These are measures one might logically choose for data whose exact distribution function were unknown, but which seemed to be grouped about a mean direction.

These simple measures are also the ones applied rigorously in Fisherian statistics (Fisher, 1953), which have been used in paleomagnetism (e.g., Watson and Irving, 1957; Watson, 1956a). The Fisher distribution, also known as the Von Mises distribution on a sphere, is essentially a spherical analogue of the two dimensional Gaussian distribution. The density function is given by

$$f(\theta, \varphi) dA = \frac{\kappa}{4\pi \sinh(\kappa)} e^{\kappa \cos \theta} \sin \theta d\theta d\varphi$$

θ and φ are, respectively, the polar and azimuthal angles, and κ is the Fisher precision parameter. The mean is, as we have said, of the same direction as the resultant, and the circular variance is given by

$$\sigma^2 = \frac{N-R}{N} = \frac{1}{k}$$

where N is the number of samples and R is the magnitude of the resultant vector; k is the maximum likelihood estimate of κ . The confidence cone for the mean direction can be calculated, to significance $(1-\alpha)$, from

$$\alpha = \frac{1}{(N-Rc)^{N-1}} \left\{ (N-R)^{N-1} - N \frac{R(1-c)}{R-Rc+2} (N-R-2)^{N-1} \right. \\ \left. + \frac{N(N-1)}{2} \frac{R(1-c)}{R-Rc+4} (N-R-4)^{N-1} + \dots \right.$$

New terms are taken as the discontinuities $R=N-2, N-4, N-6 \dots$ are passed. Note that $c = \cos \theta$, where θ is the half-angle of the confidence cone. The Fisherian distribution is circularly symmetric about the mean. It is also antipodally asymmetric, or unipolar. That is, a direction is distinct from its antipode. When dealing with data, such as earthquake compression or tension axes, where a direction and its antipode are equivalent, one must take care to project those directions which would cluster about the antipode of the mean back to their antipodes.

A more general distribution than that of Fisher is the Bingham distribution (Bingham, 1964; 1974), which is now also finding use in paleomagnetism (Onstott, 1980). This is not a circularly symmetric distribution, so that elongate probability patches about a mean are allowed. It is also antipodally *symmetric*. The best estimate of the mean direction is not necessarily the direction of the resultant, but follows from a

moment of inertia analysis (Mardia, 1972; Onstott, 1980). Bingham's density function has the form

$$f(l; U; k_j) = \frac{1}{4\pi d(k_1, k_2)} e^{-\{k_1(L \cdot u_1)^2 + k_2(L \cdot u_2)^2\}}$$

where

$$d(k_1, k_2) = \frac{1}{4\pi} \int_0^{2\pi} \int_0^\pi e^{-\{k_1 \cos^2 \varphi + k_2 \sin^2 \varphi\} \sin^2 \theta} \sin \theta \, d\theta \, d\varphi$$

may be evaluated asymptotically (Bingham, 1964) or numerically (Onstott, 1980). k_1 and k_2 are Bingham's "concentration parameters". As Onstott points out, the squaring of $\cos \theta$ reflects the antipodal symmetry of the distribution. Bingham (1964) was able to write the likelihood function of his distribution in terms of the moment-of-inertia matrix. The moment of inertia, about a fixed axis $U(x, y, z)$, of N points on a unit sphere, each point of unit mass and direction (l_i, m_i, n_i) , can be written (Mardia, 1972)

$$M = U^T B U$$

where $B = I - T$, and

$$T = \frac{1}{N} \begin{matrix} \sum l_i^2 & \sum l_i m_i & \sum l_i n_i \\ \sum l_i m_i & \sum m_i^2 & \sum m_i n_i \\ \sum l_i n_i & \sum m_i n_i & \sum n_i^2 \end{matrix}$$

The distribution of the N points is describable by the eigenvalues of the matrix T . As discussed by Mardia and Onstott, Bingham's distribution function may reduce to the uniform distribution, or variously describe symmetric and asymmetric girdle distributions, or distributions about a mean direction (maximum eigenvector). When the

eigenvalues τ_i of T are distinct, with $\tau_1 < \tau_2 \ll \tau_3$, the concentration parameters are such that $k_1 < k_2 < 0$, and we have an elongate distribution about the maximum eigenvector. When $k_1 \rightarrow k_2$, a circularly symmetric distribution is approached, and the maximum eigenvector approaches the resultant vector. That is, we approach a situation similar to the Fisherian one. The variance in Bingham statistics is

$$\sigma_{ij}^2 = \frac{1}{2\Delta_{ij}}$$

where $\Delta_{ij} = (k_i - k_j)(\tau_i - \tau_j)$. σ_{ij} is the semiaxis of the standard deviation ellipse around the i^{th} eigenvector in the direction of the j^{th} eigenvector. Thus we are interested in σ_{31} and σ_{32} , the semiaxes of the ellipse around the mean direction. The semi axes of the confidence region around the mean, to significance $(1 - \alpha)$, are given approximately by

$$c_{ij} = \left(\chi^2_{1-\alpha}(2) \frac{\sigma_{ij}^2}{\sqrt{N}} \right)^{1/2}$$

where $\chi^2_{1-\alpha}(2)$ denotes the χ^2 distribution with 2 degrees of freedom at percentage point $(1 - \alpha)$.

Apart from performing statistical analyses based on a Fisher, Bingham, or other distribution, one can use the resultant vector of the data in a test for randomness. By "randomness" here we really mean "uniformity" or "isotropy", where no preferred direction exists. The null hypothesis is, then, that the parent population is uniformly distributed. One can compute the probability P (Watson, 1956b) that a uniform distribution of vectors will yield a given resultant R_0 . Hence, given a resultant exceeding R_0 in magnitude, one can reject the hypothesis of uniformity, with confidence P . Good explanations and tables for performing the test are given in Stephens (1964;

1969a,b). Variants of this test, as well as other tests, are discussed in Batschelet (1981).

Appendix C: Plots of Seismicity Versus Depth for the World's Subduction Zones

In this appendix we present histograms of the total number of earthquakes with one-second body wave magnitude $m_b \geq 4$, for the time period 1964-1980, versus depth in the world's subduction zones. The data sources are the NOAA and PDE catalogs. We note that we have regionalised such that the isolated areas of very deep seismicity in South America and the New Hebrides do not appear on the plots.

Figure C1. The world's subduction zones for which seismicity is plotted in fig. C2

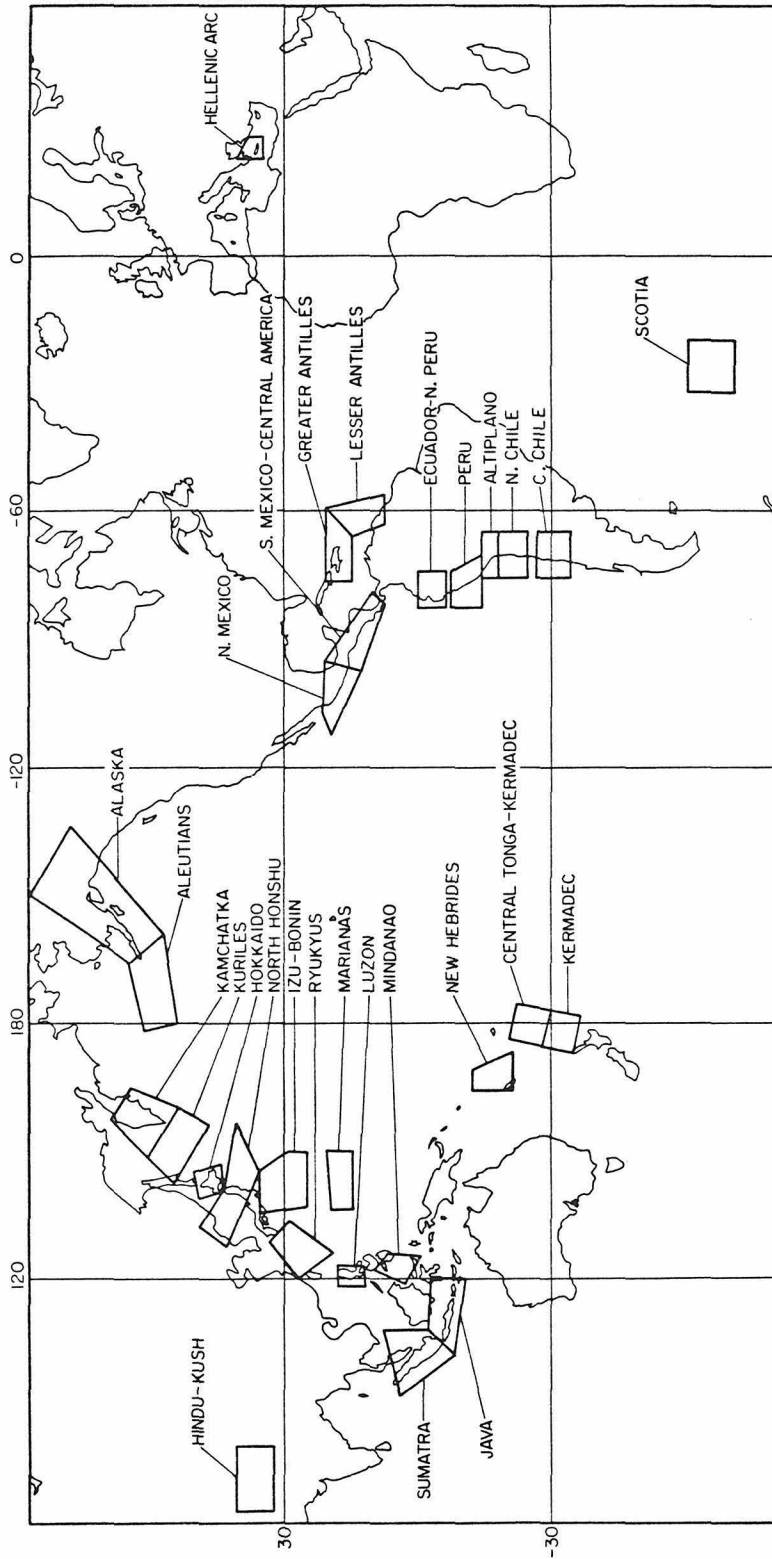
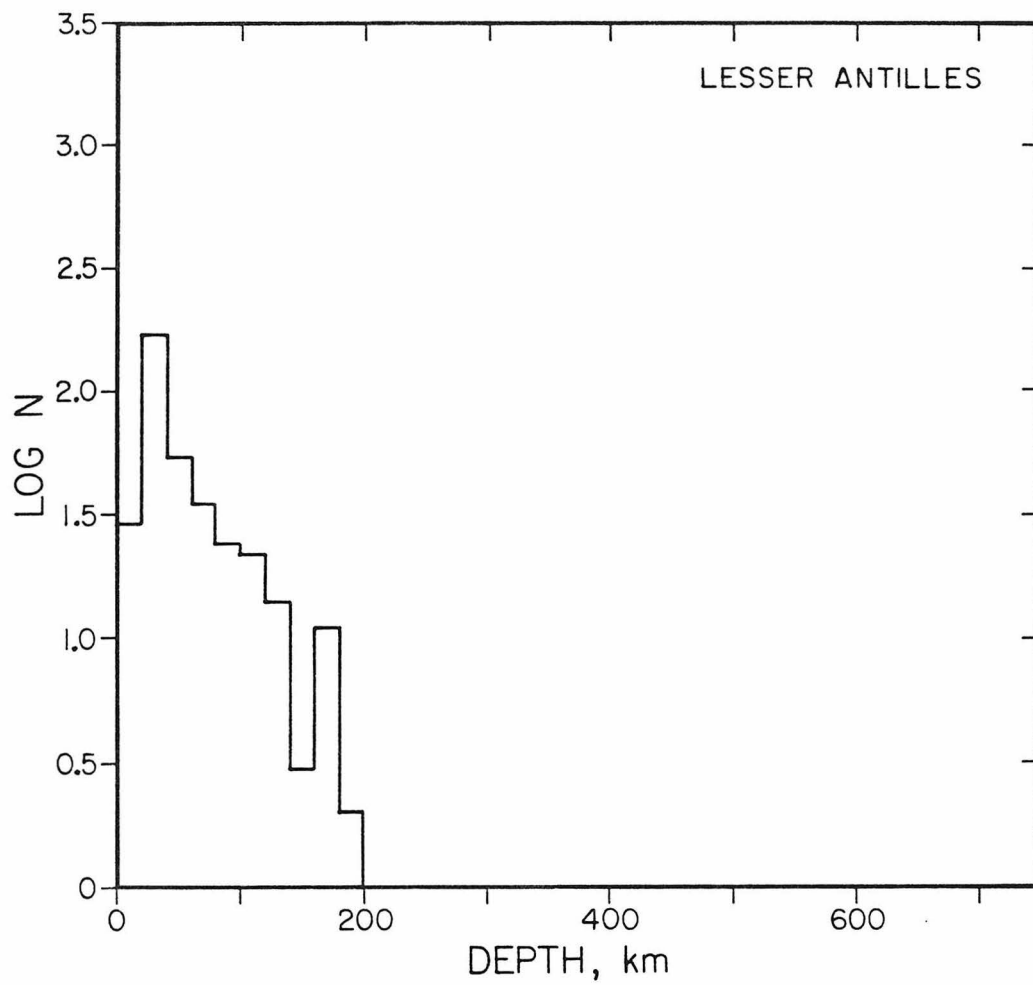
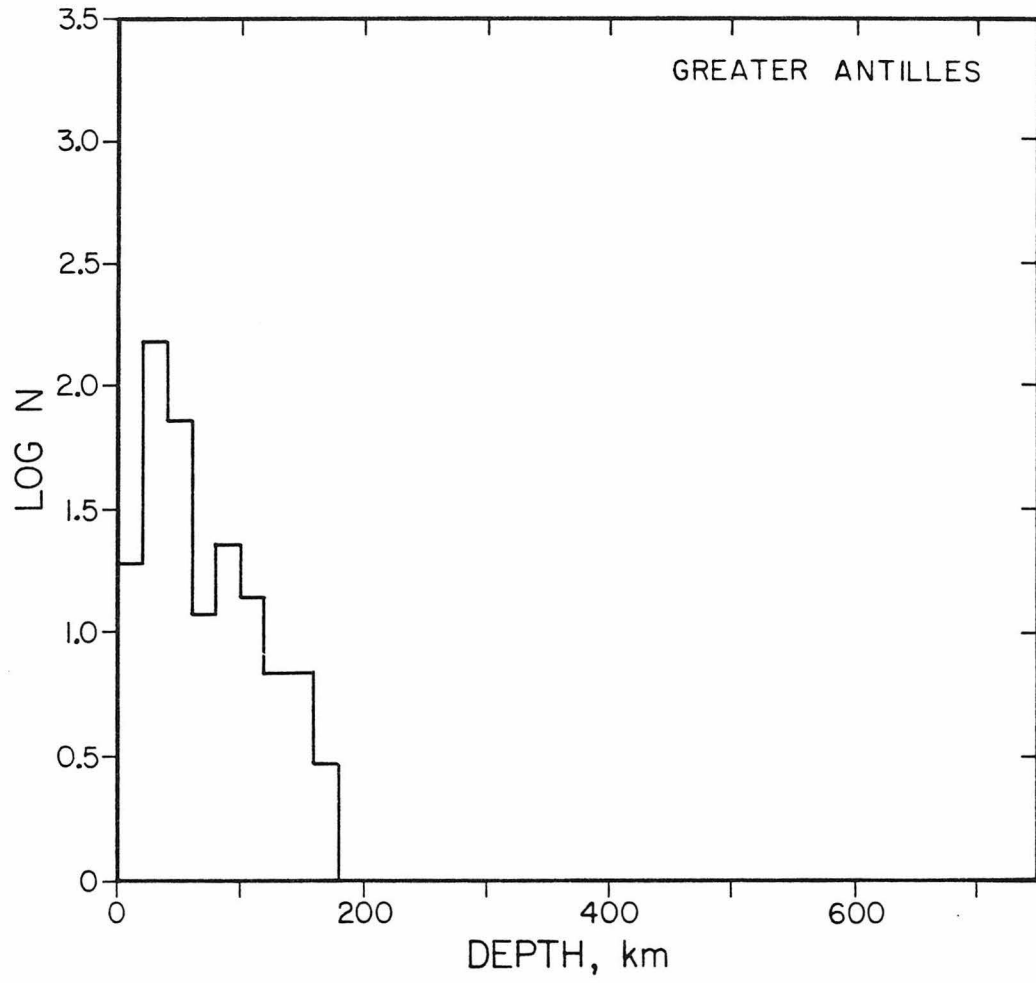
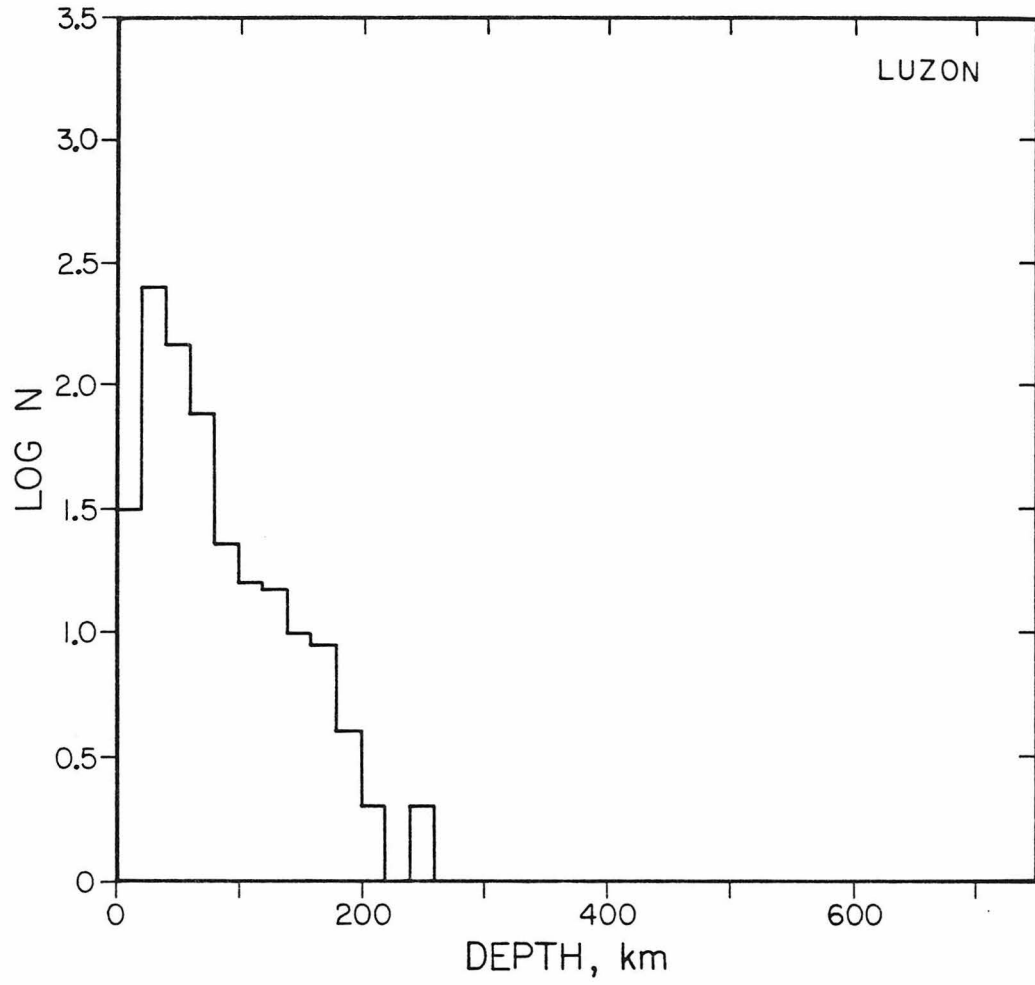
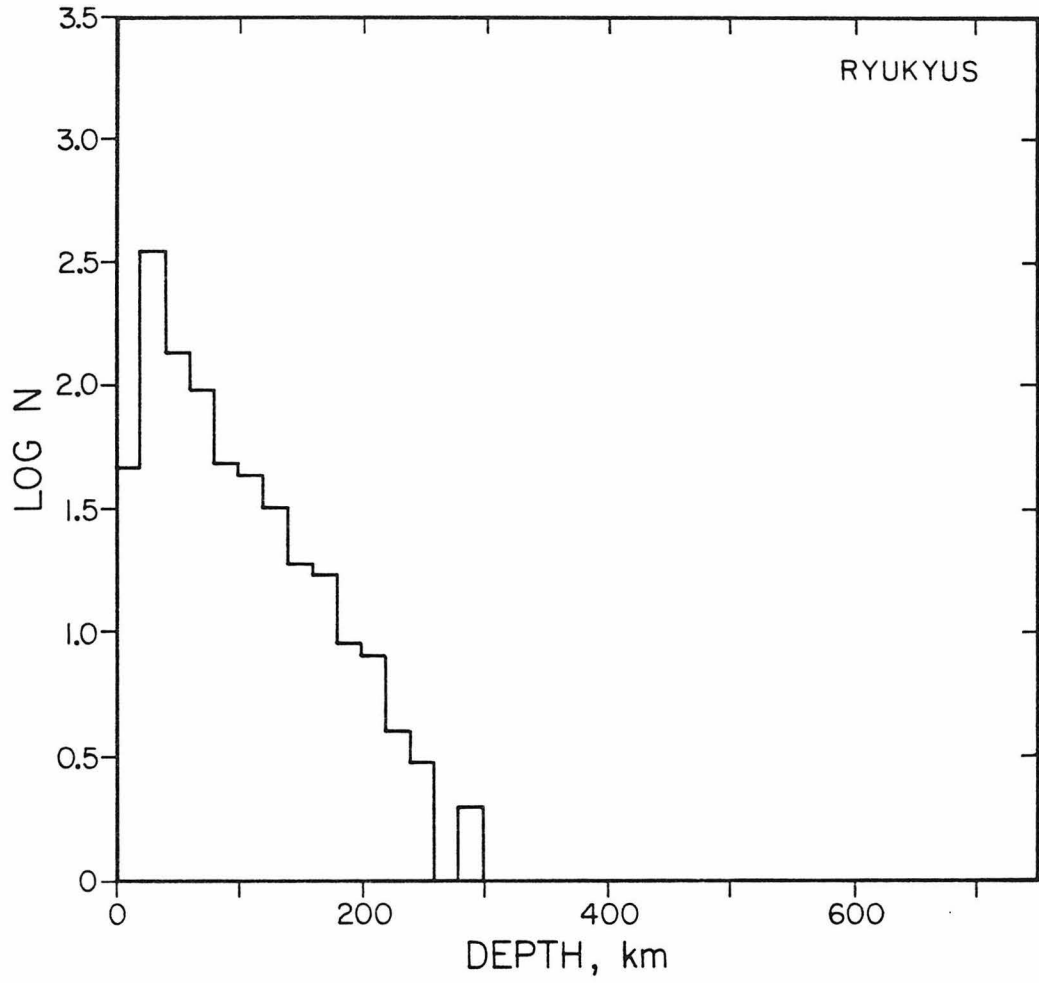


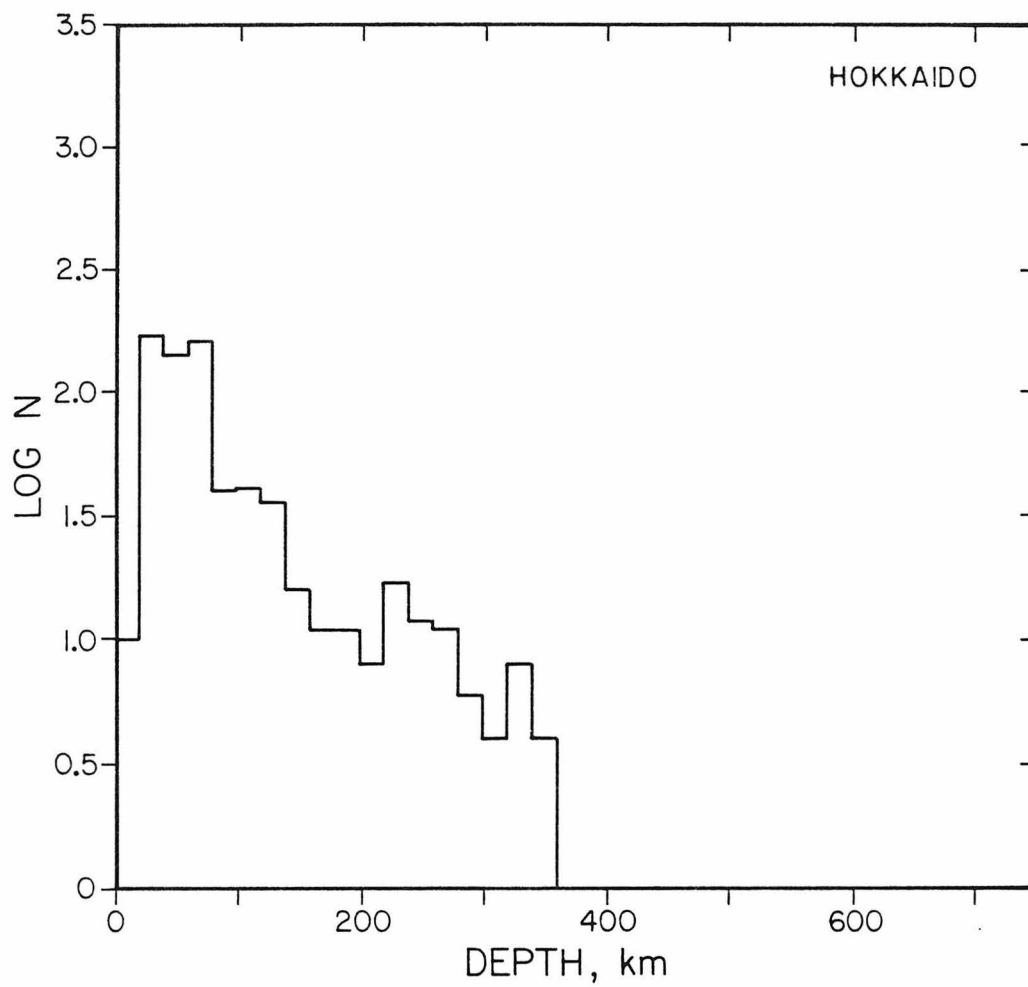
Figure C2. Plots of $\log_{10}N$ versus depth for the regions in fig. C1. N is the total number of events (1964-1980) with $m_b \geq 4$.

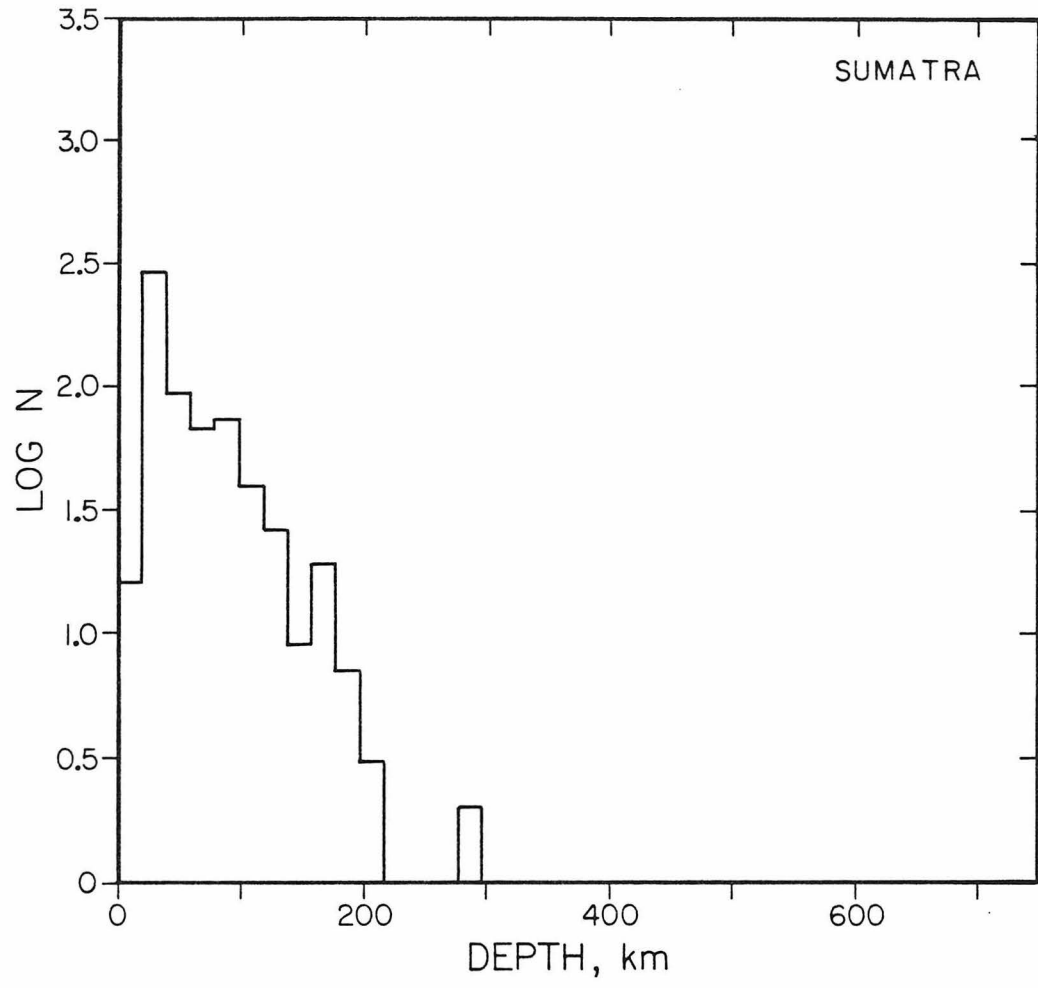


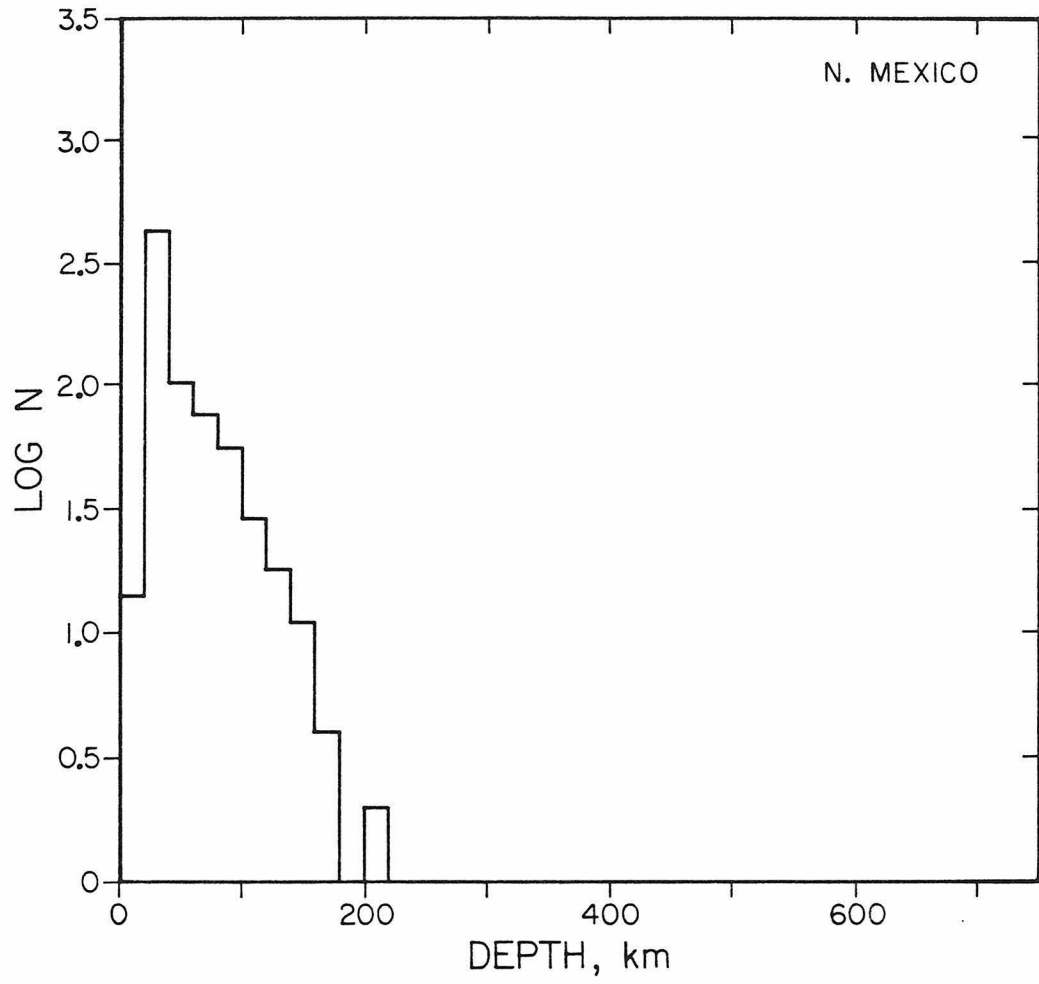


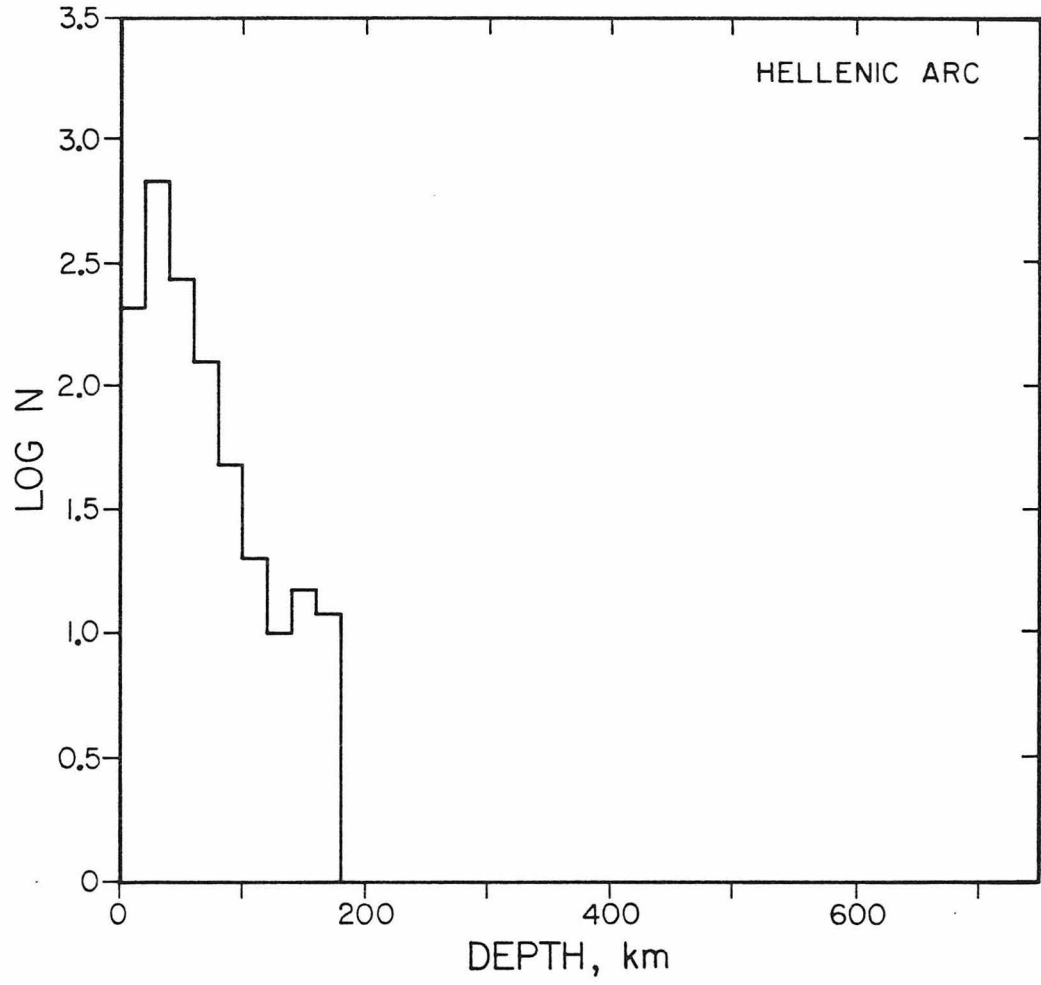


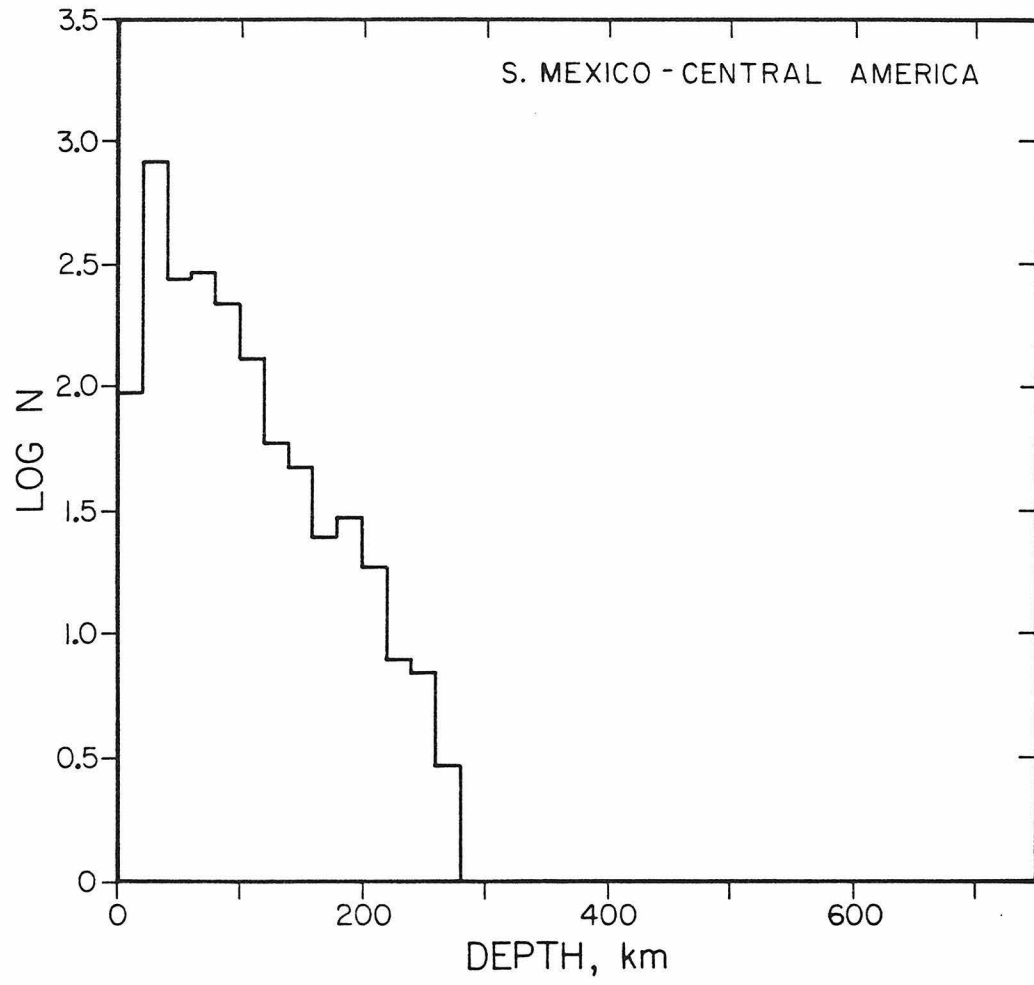


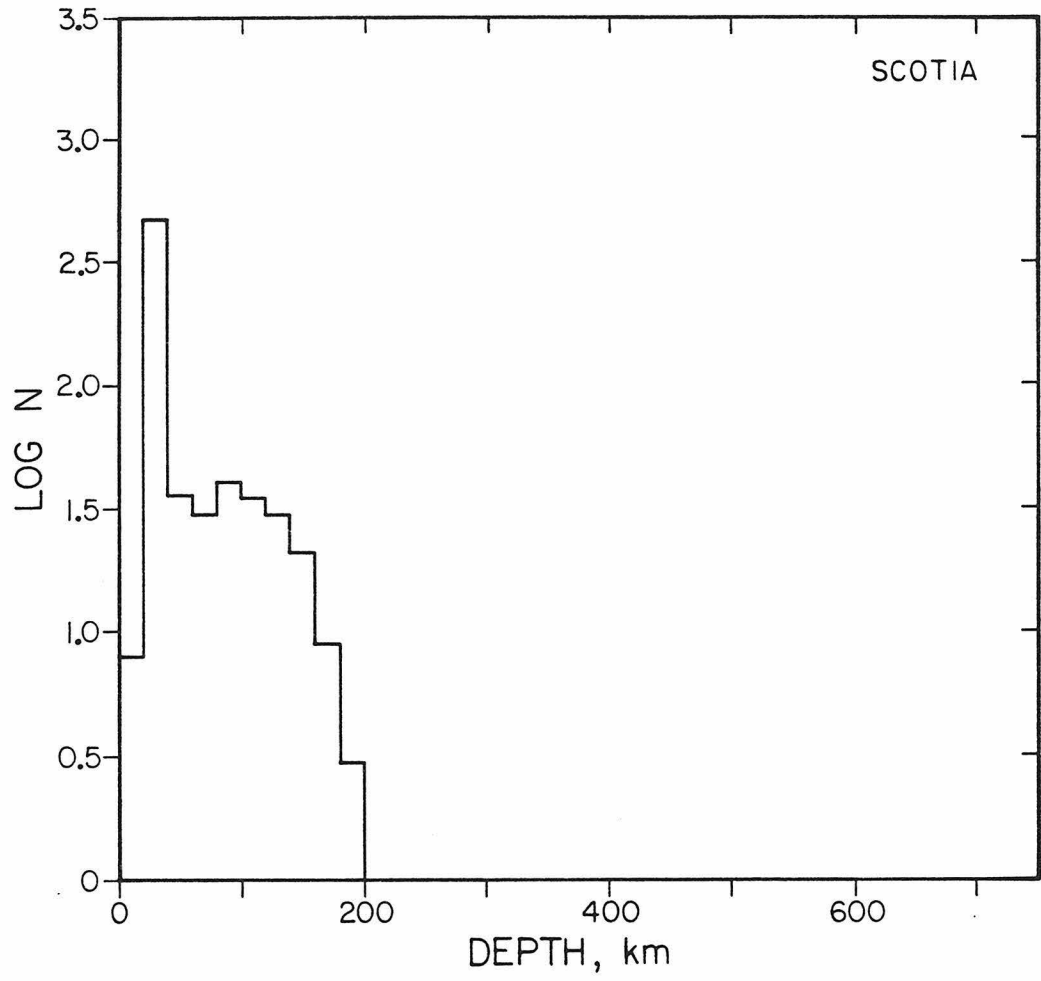


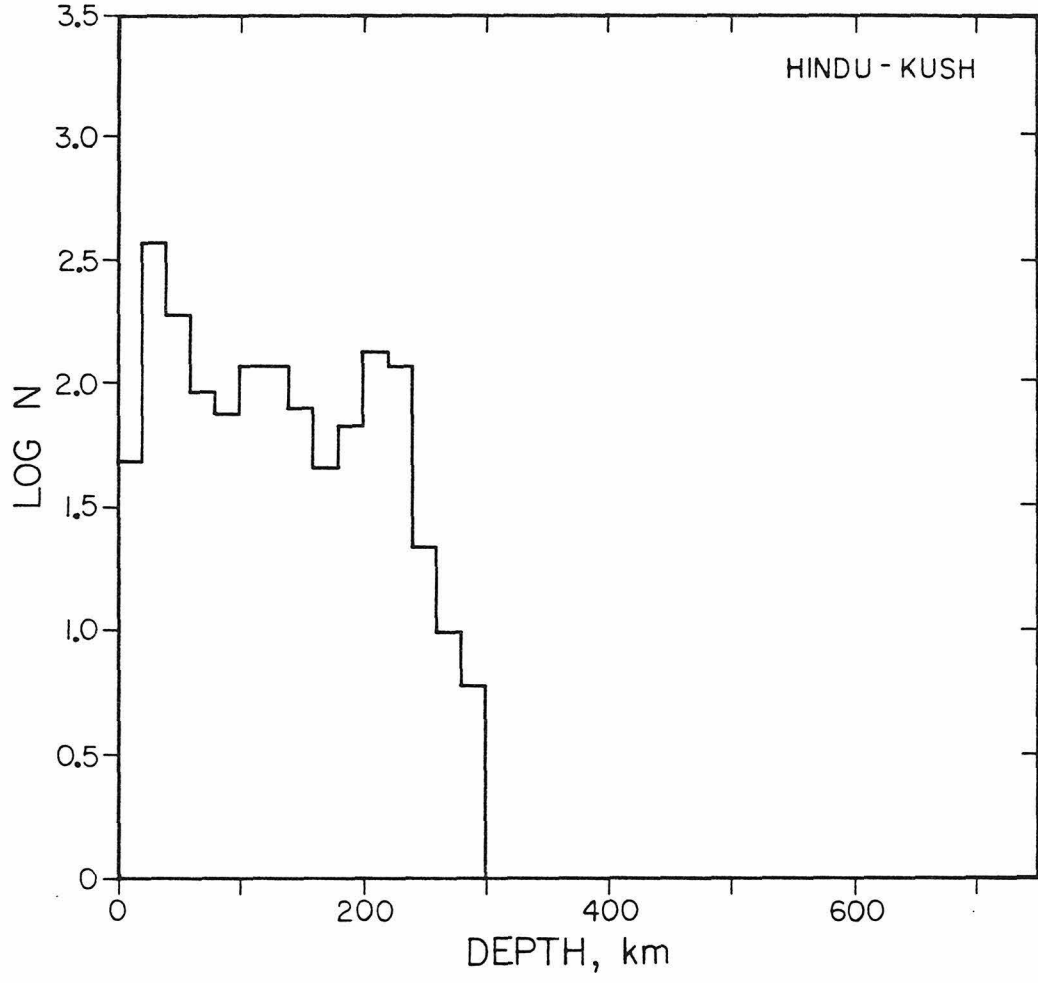


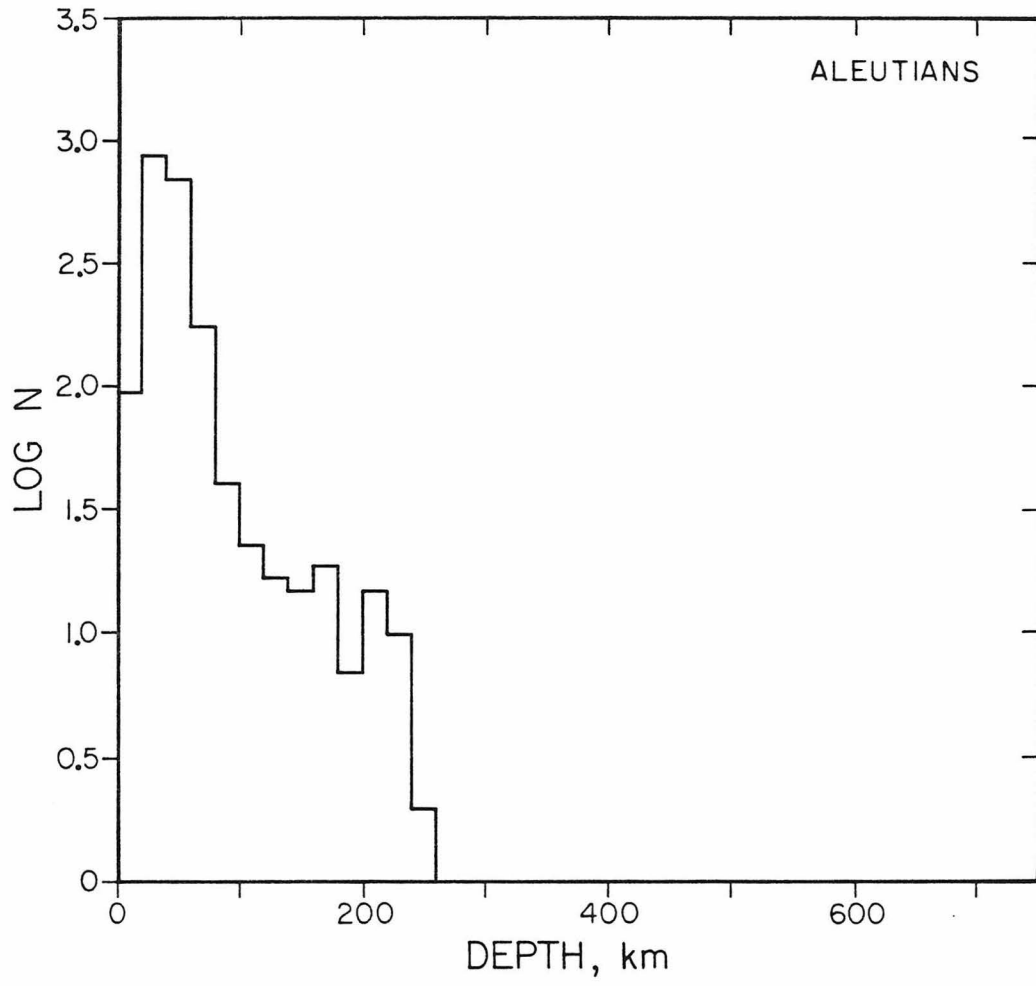


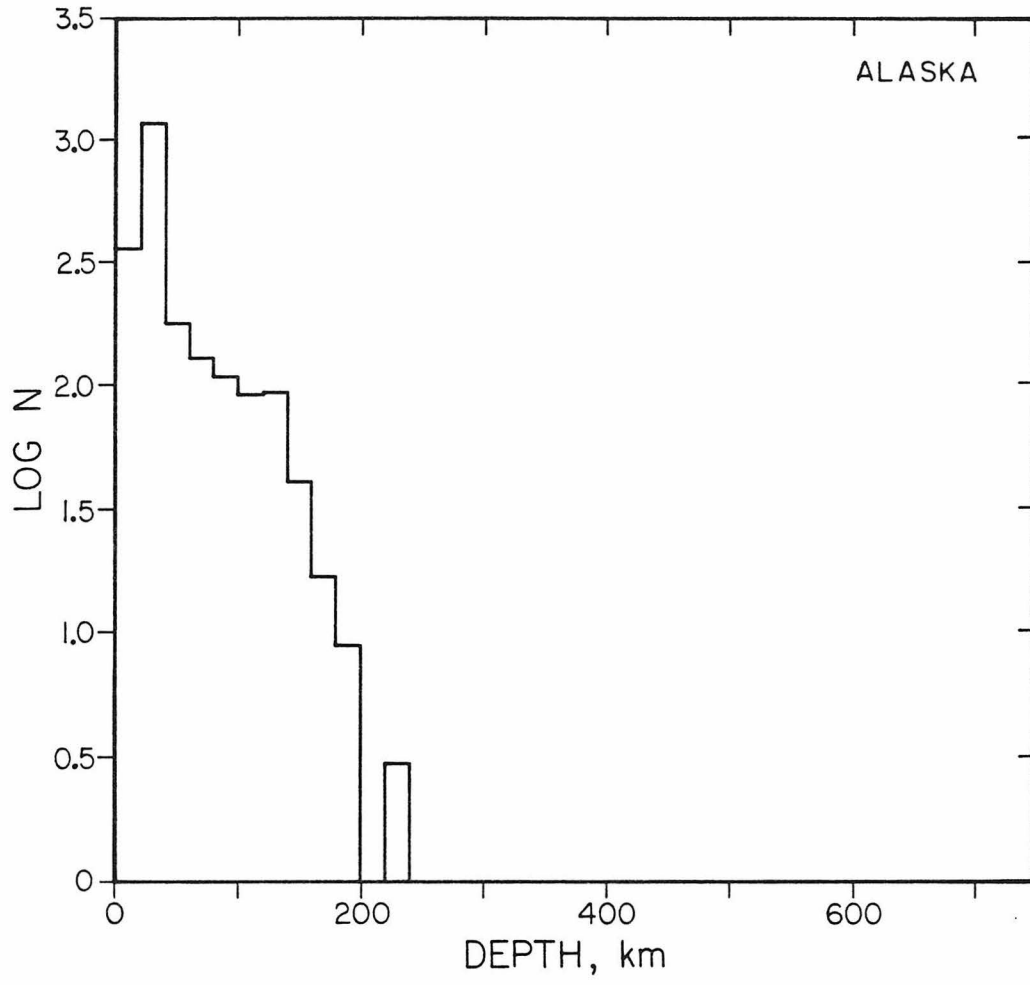


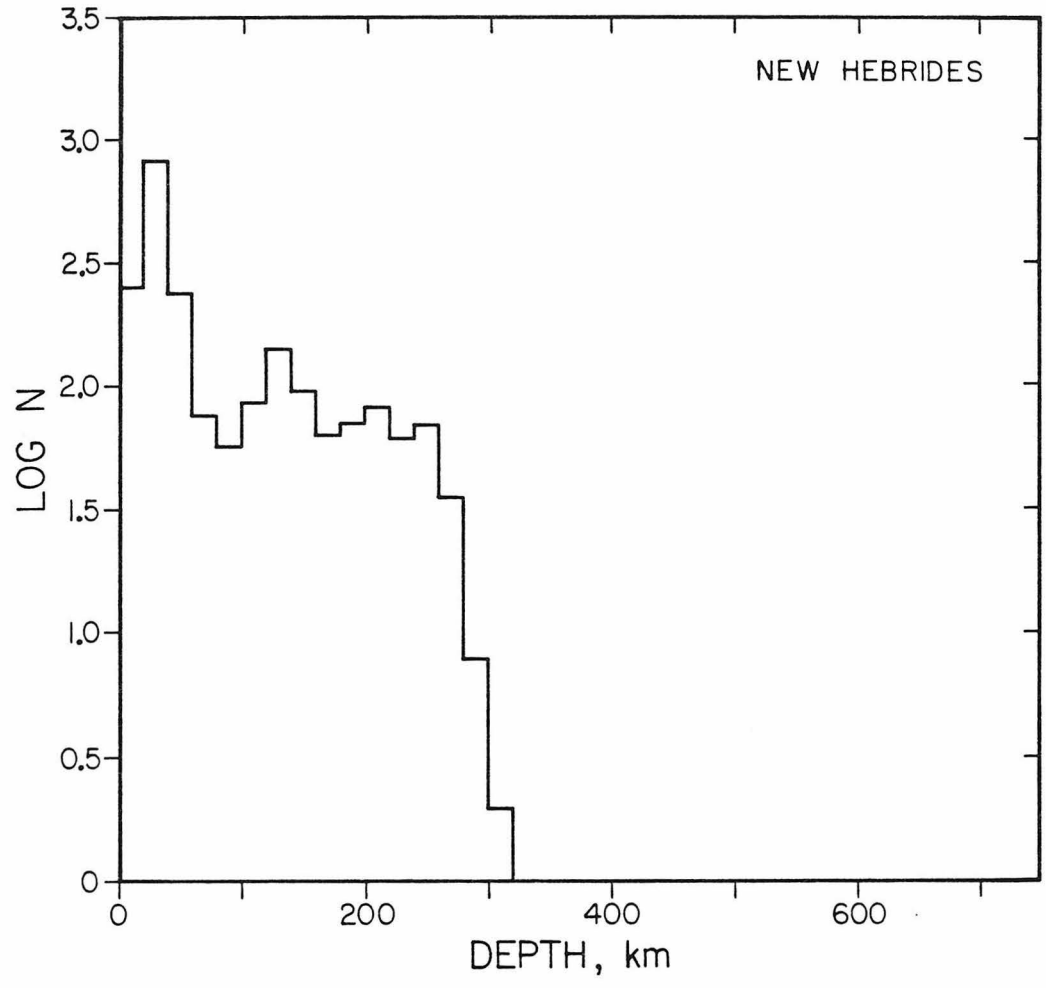


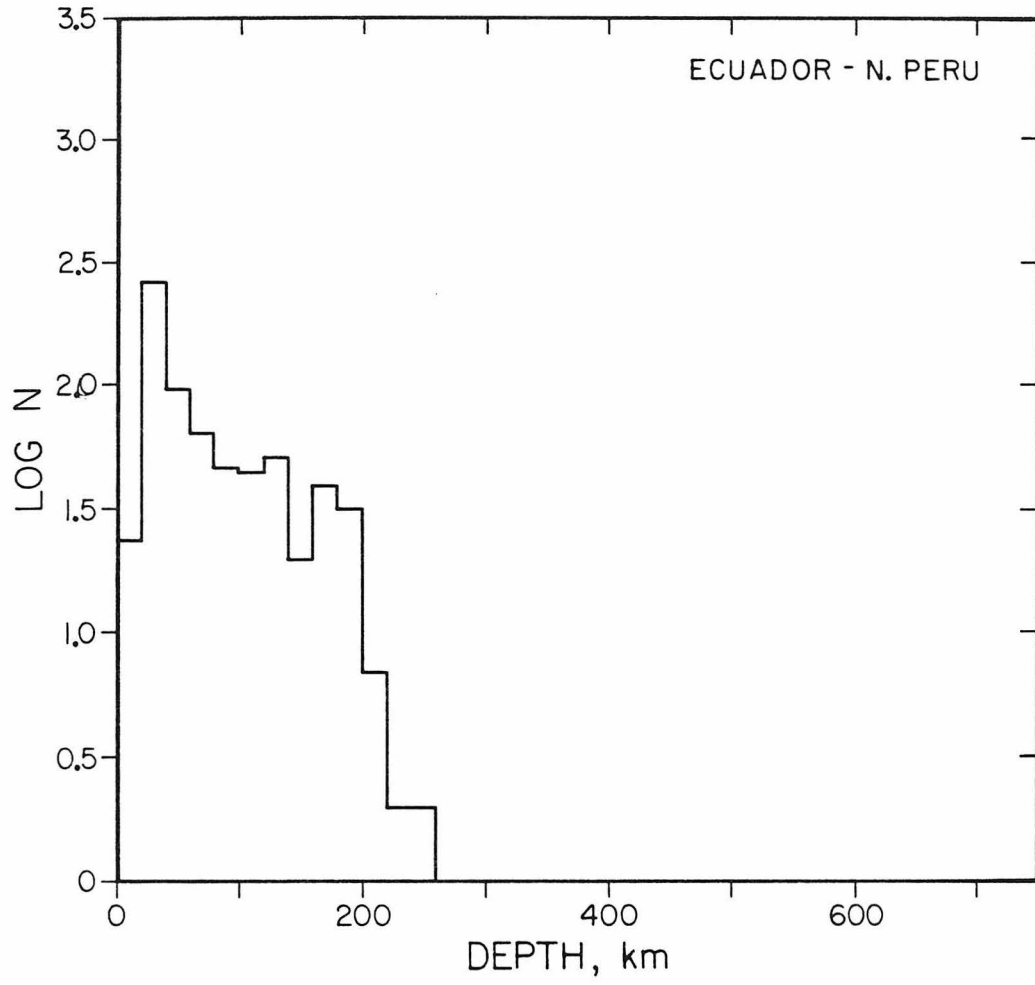


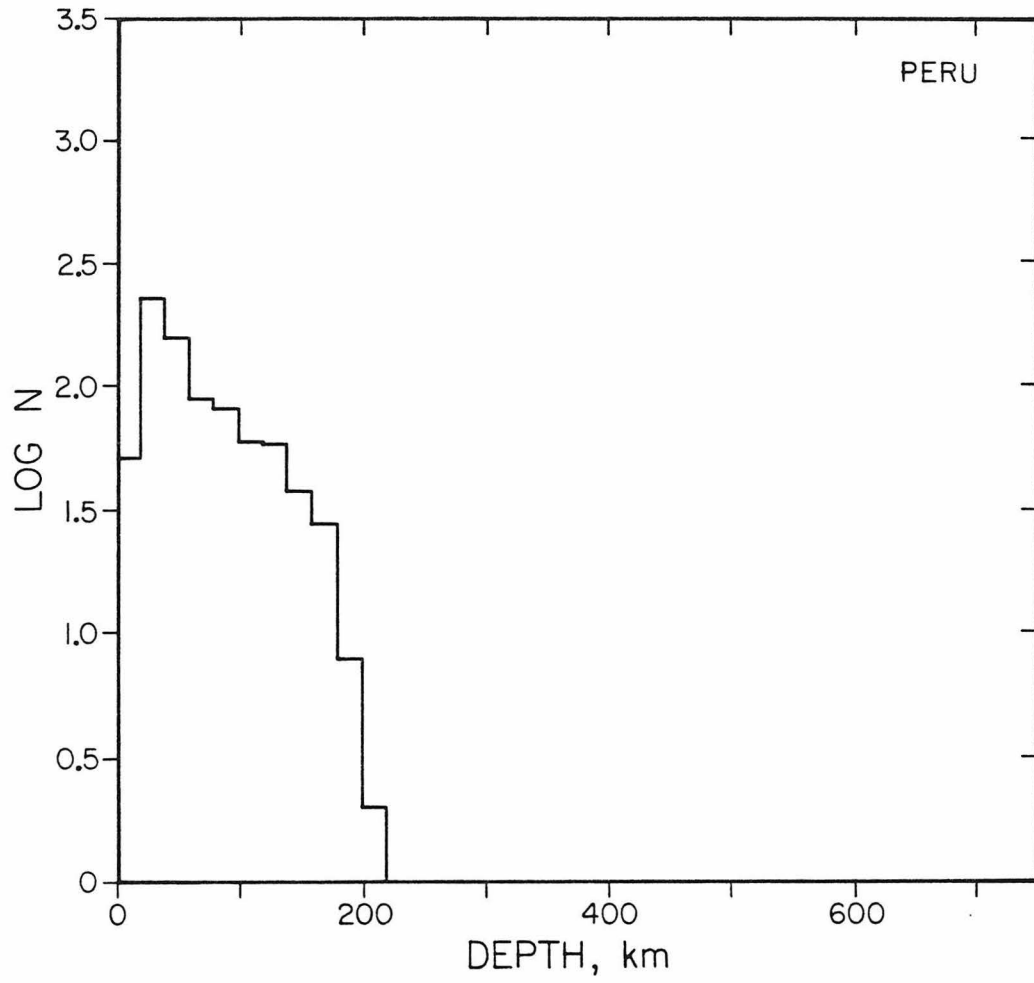


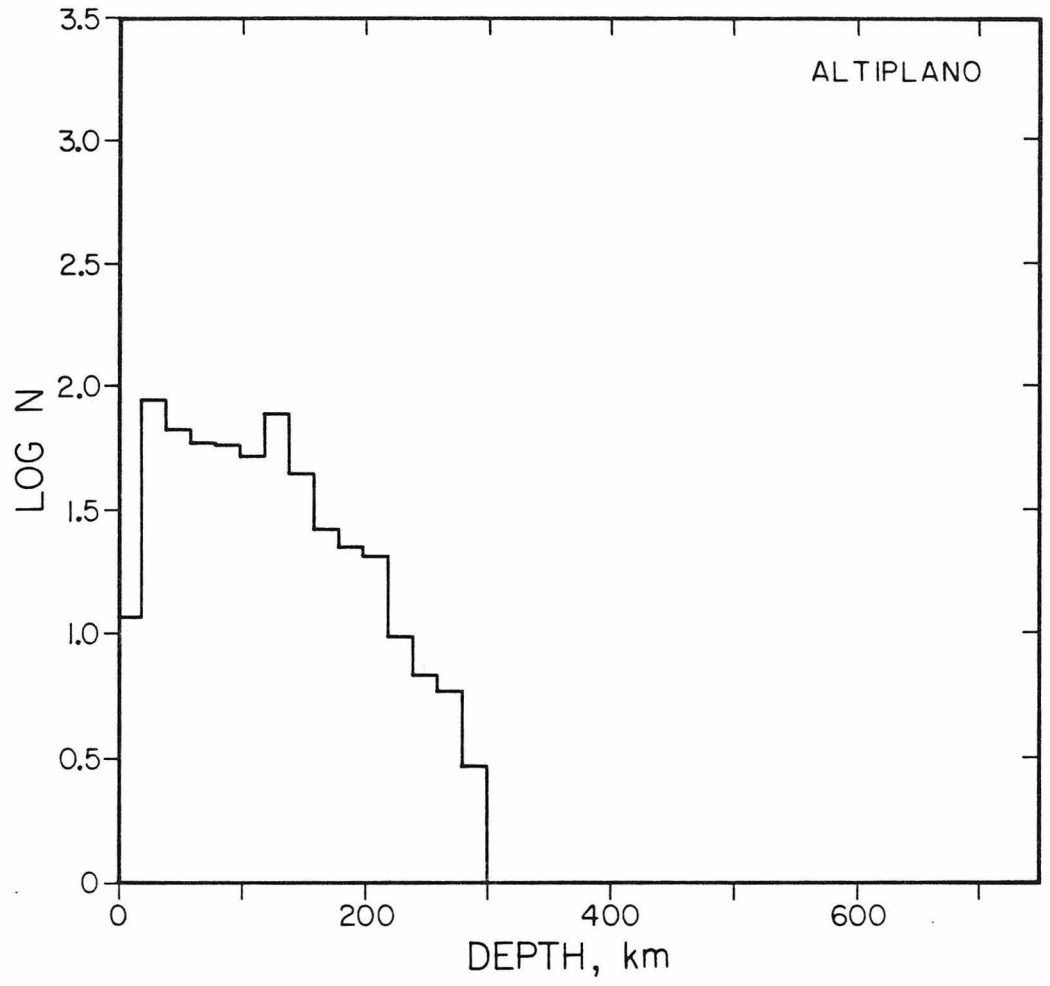


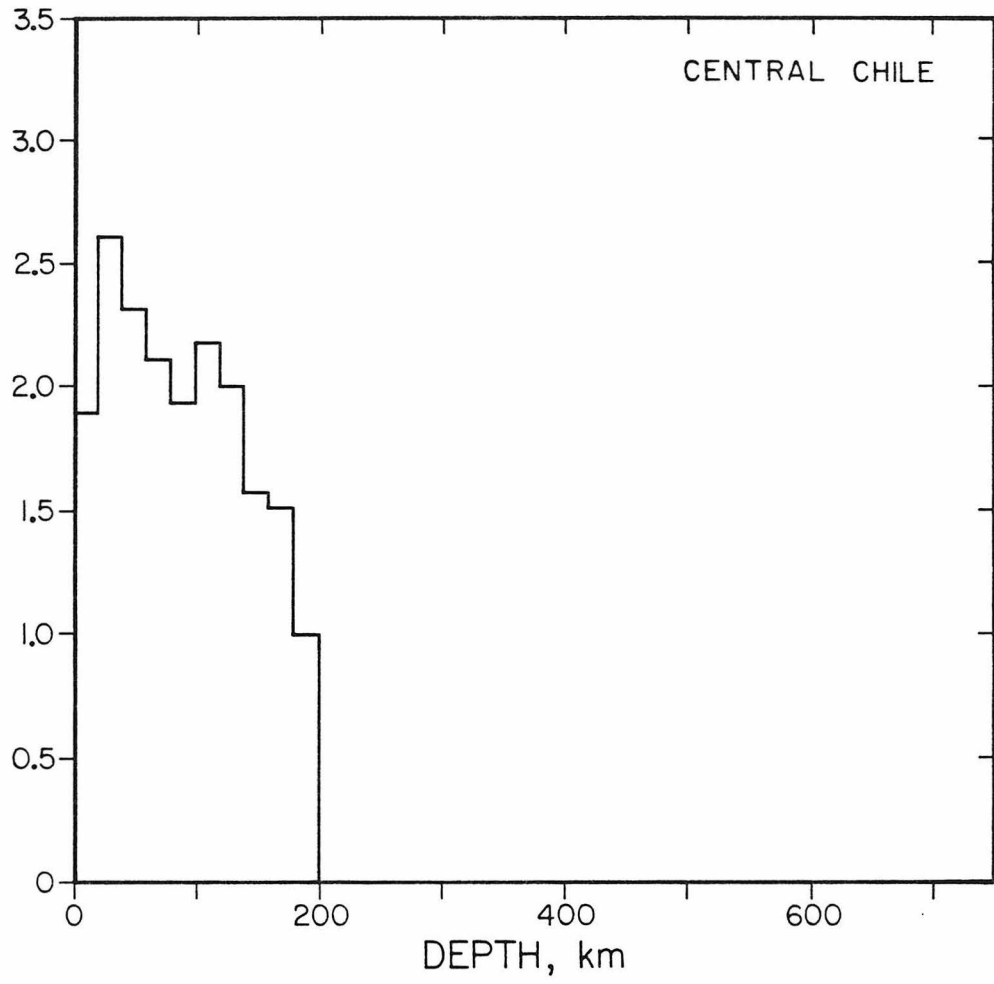


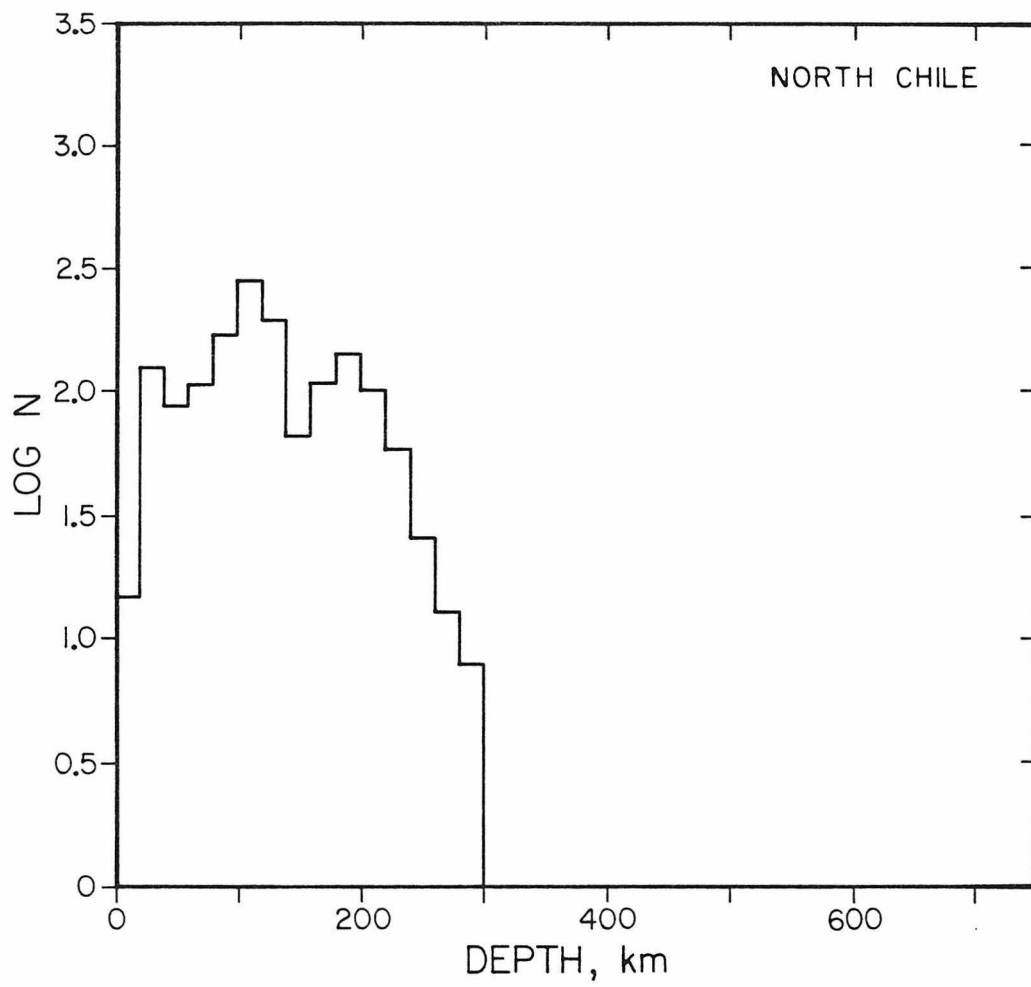


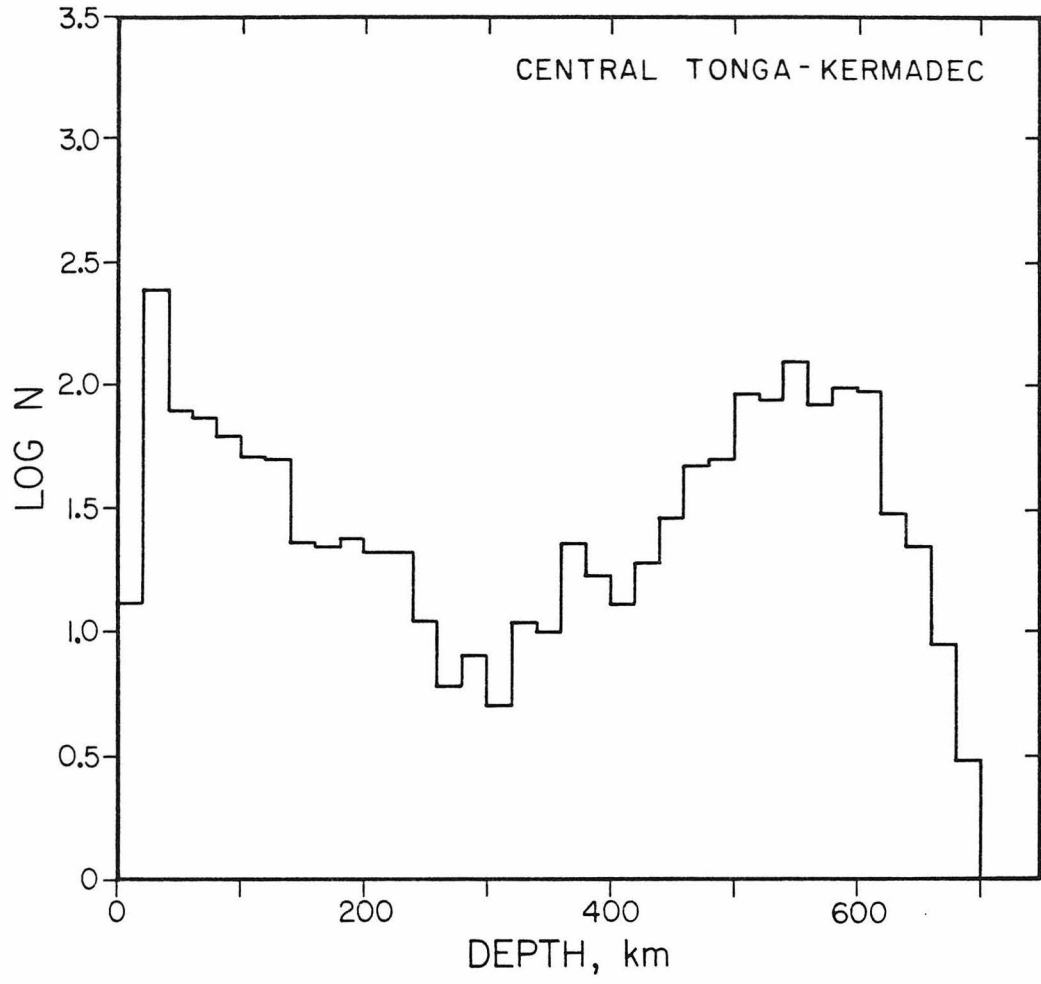


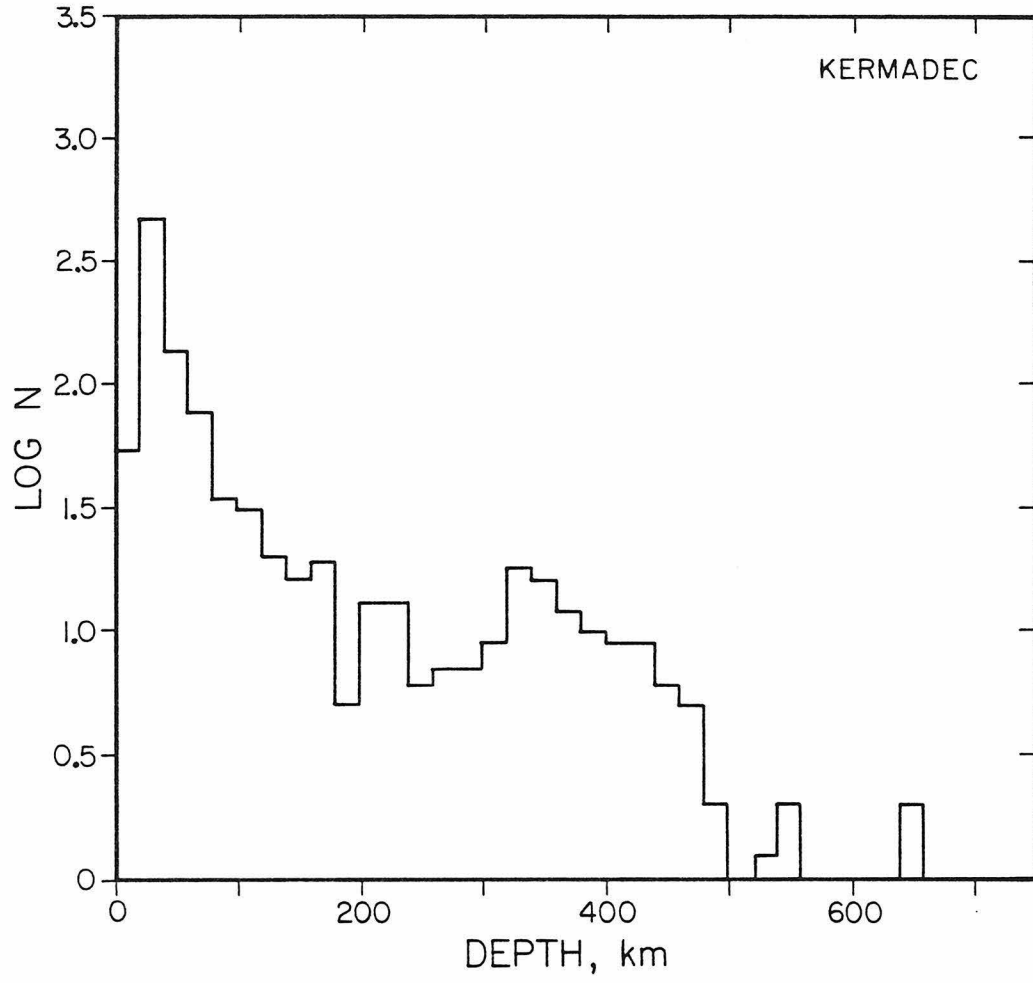


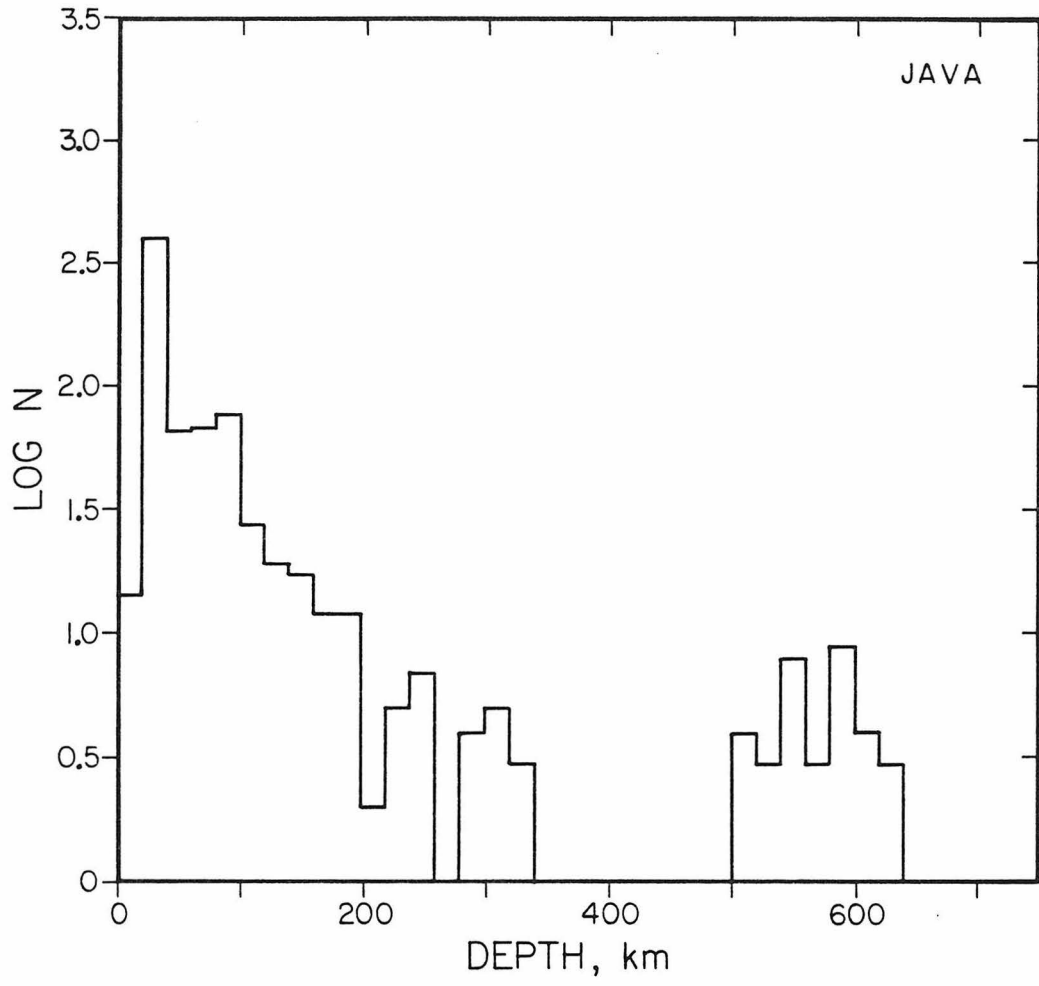


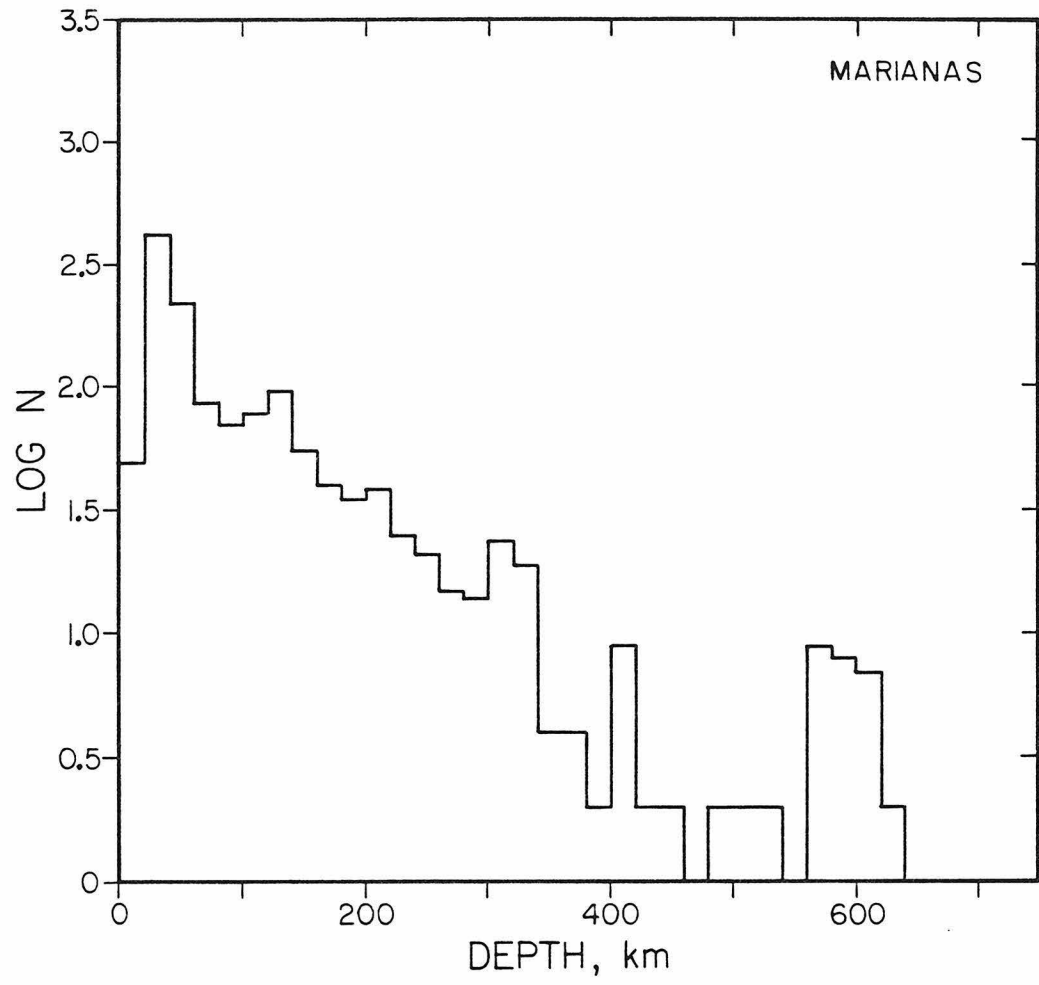


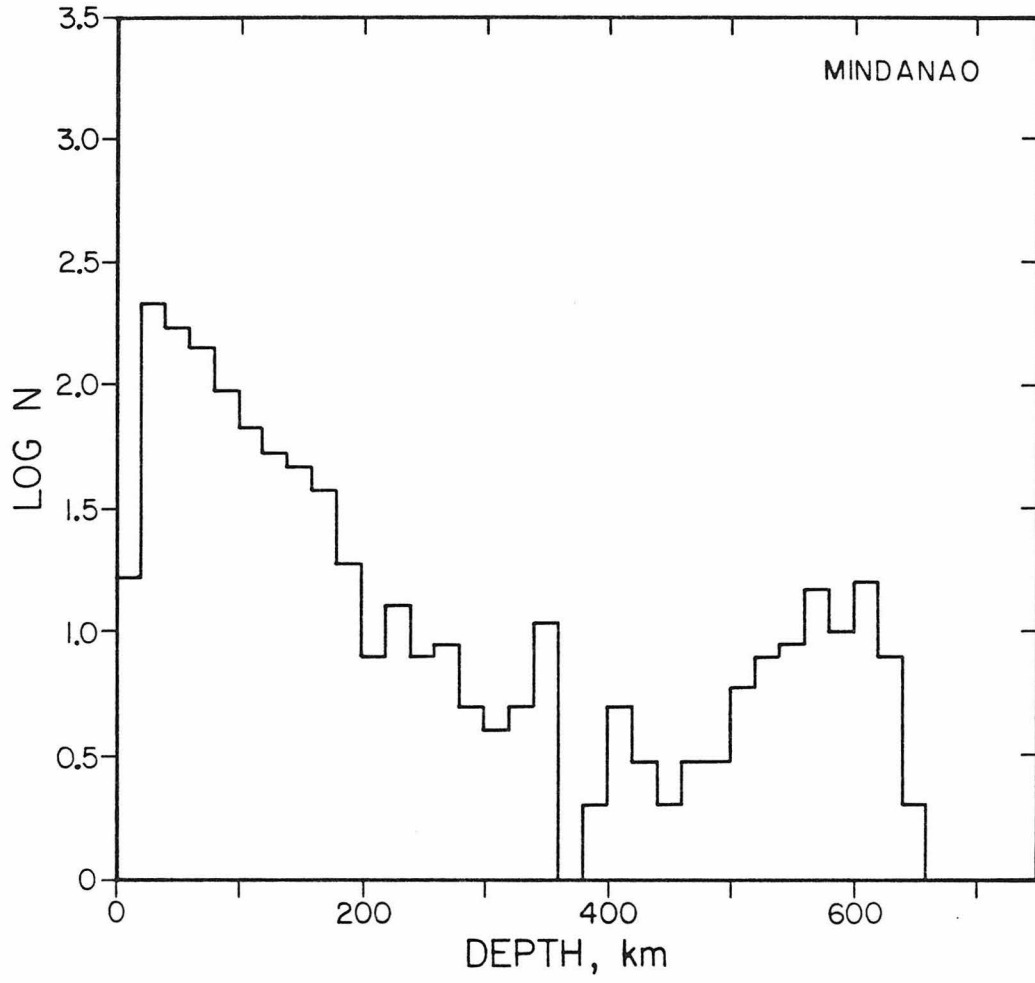


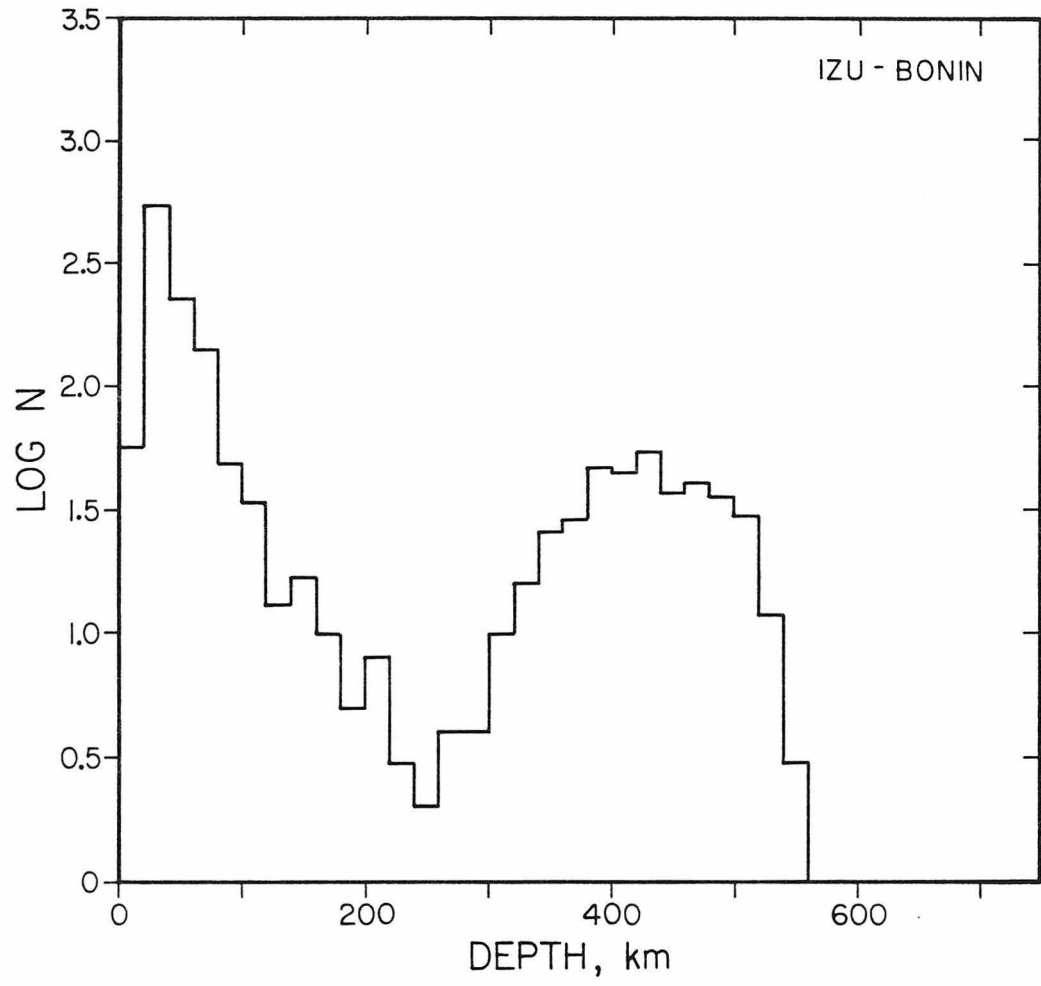


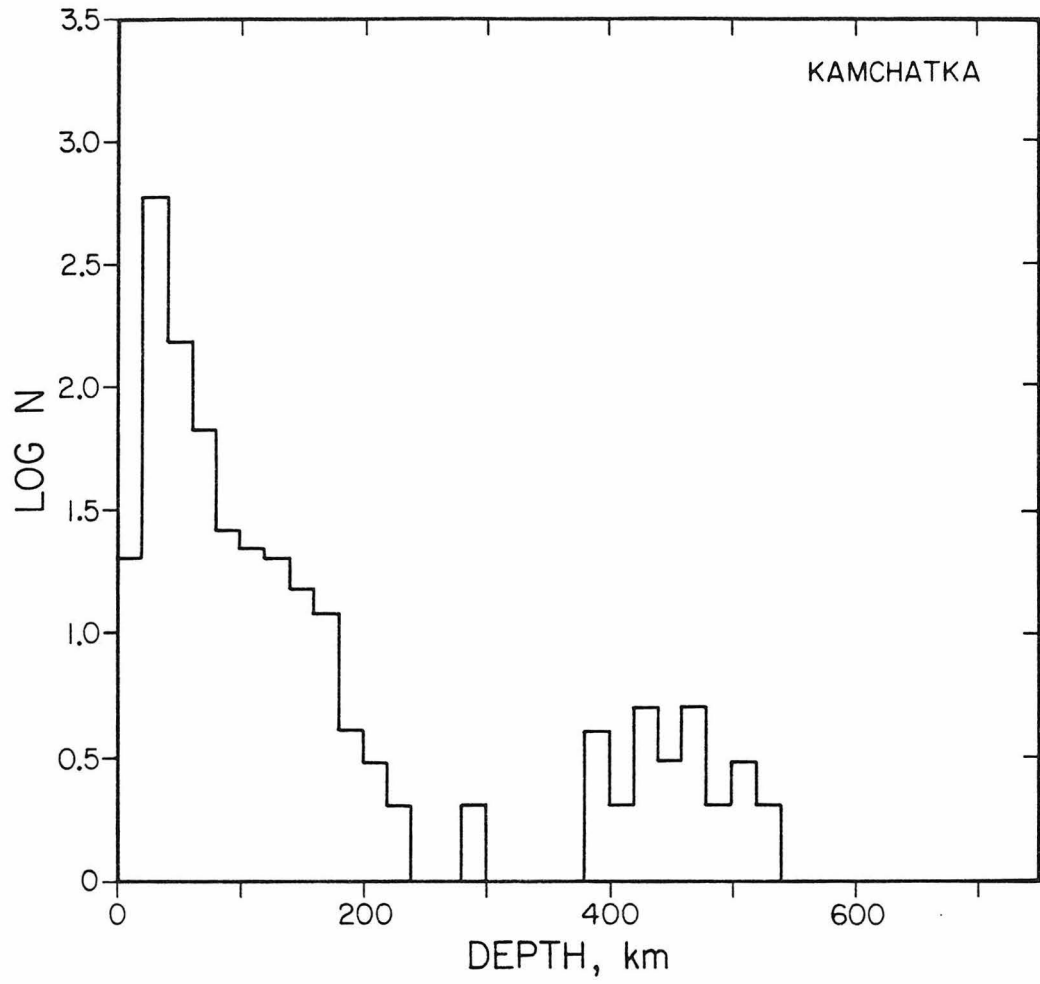


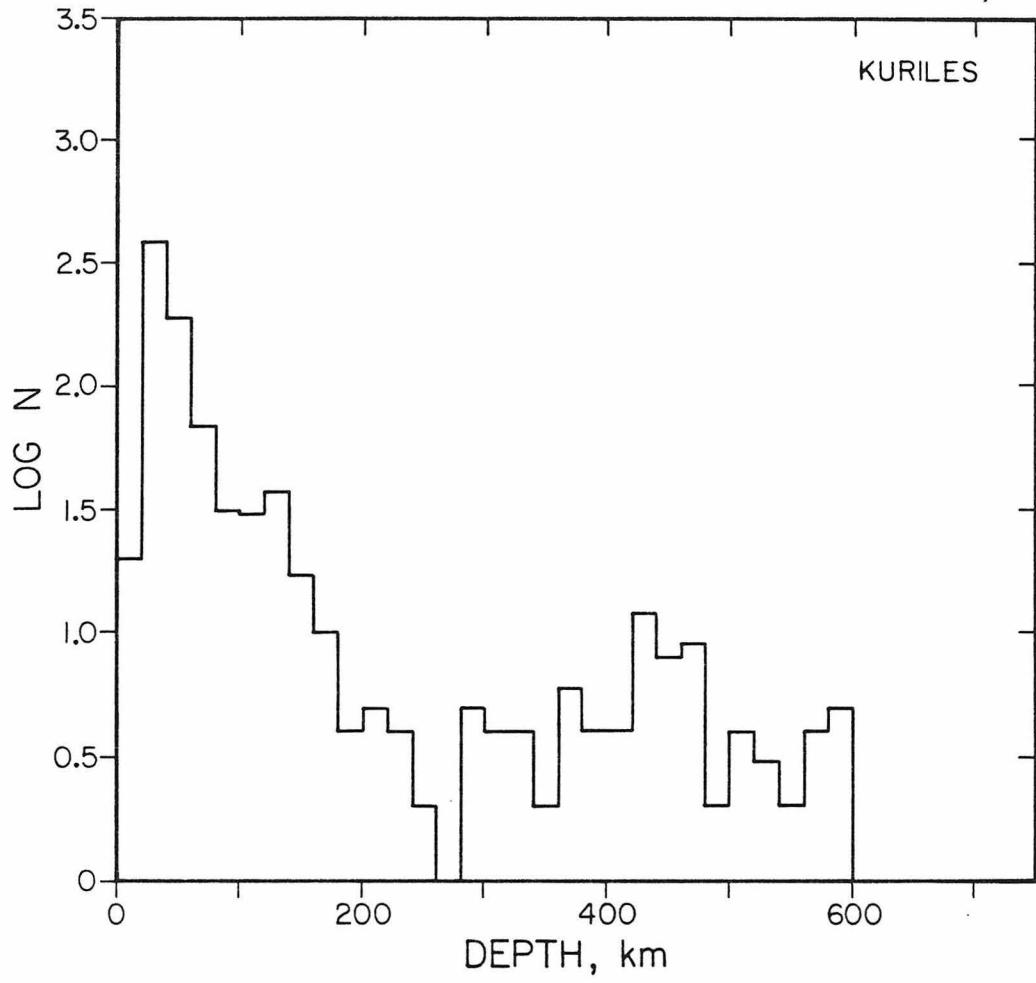


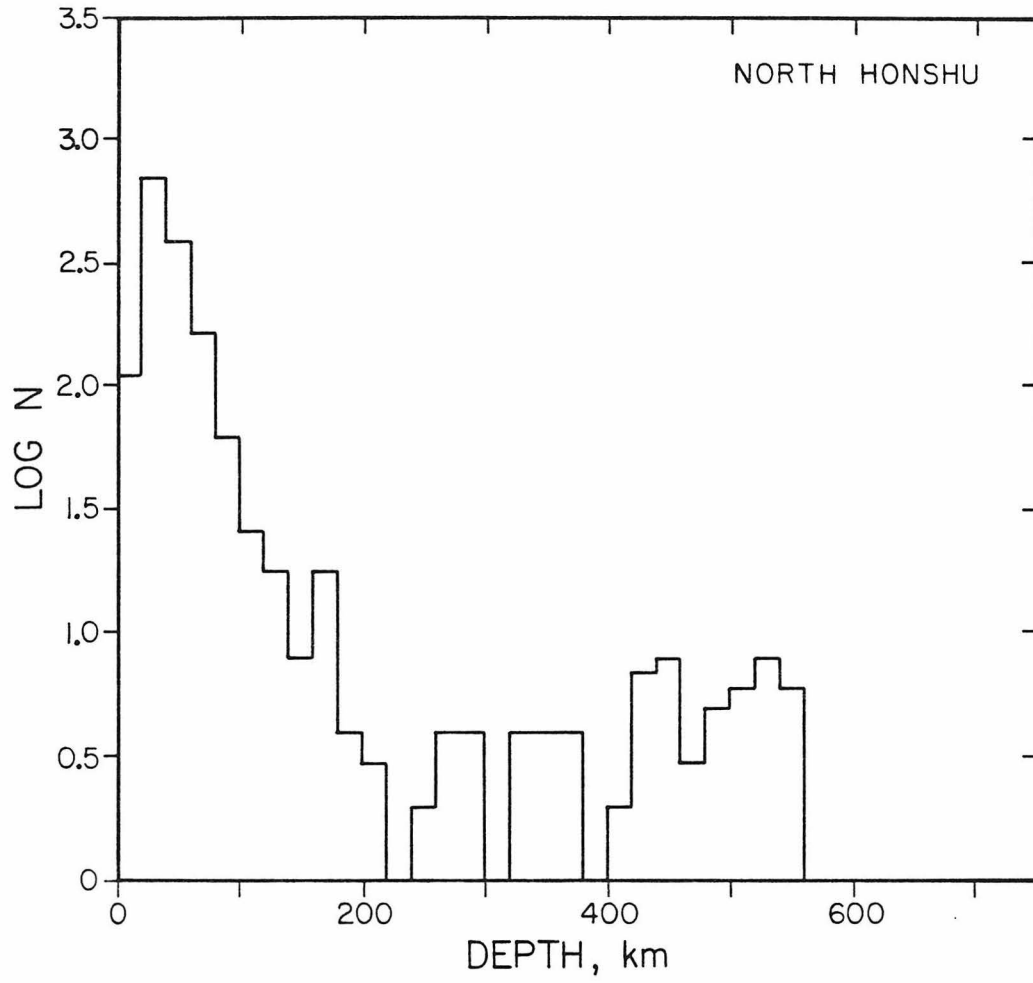








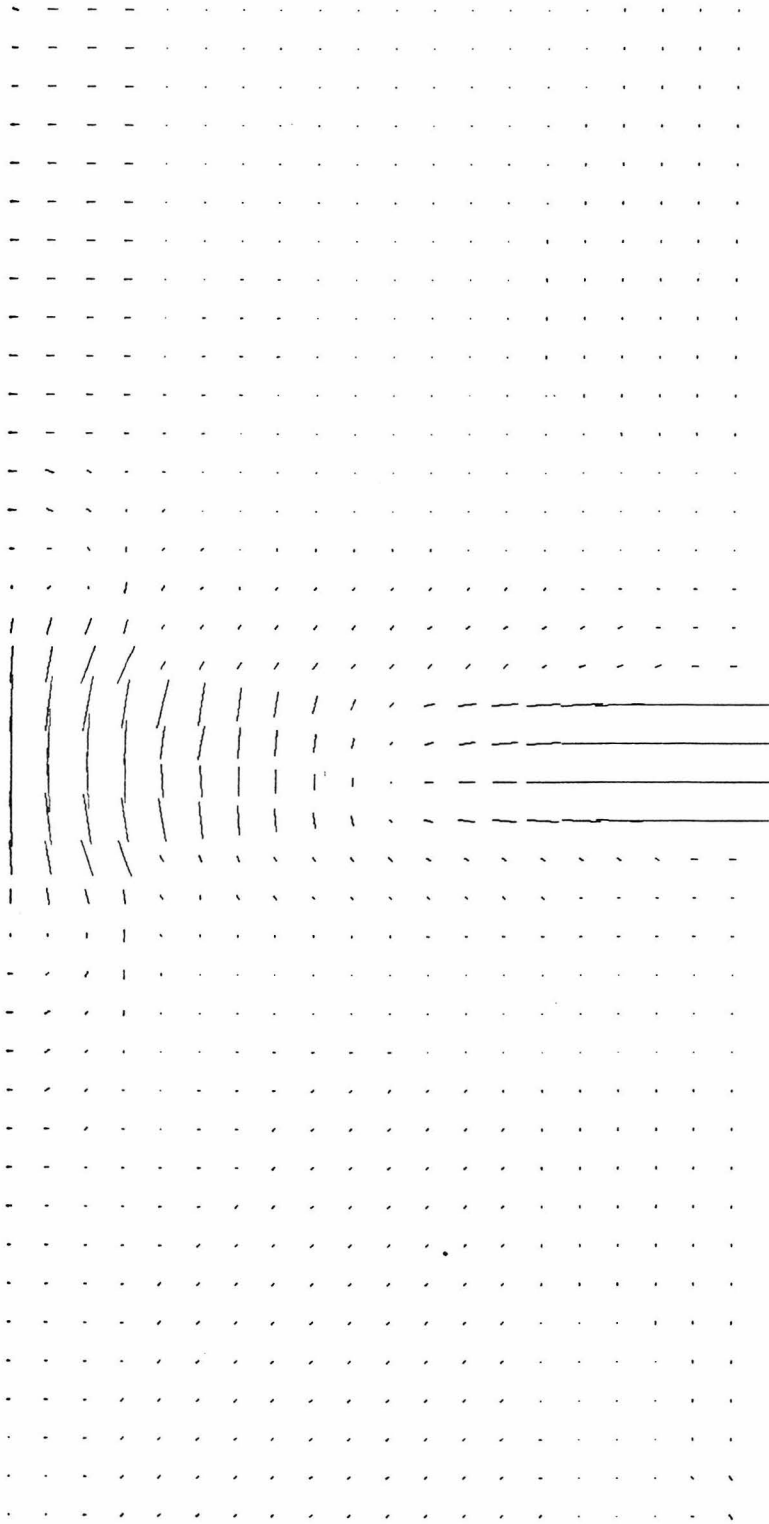
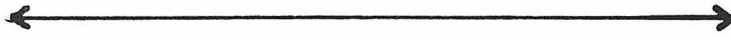




Appendix D: Spatial Stress Plots and Velocity Plots not Included in the Text

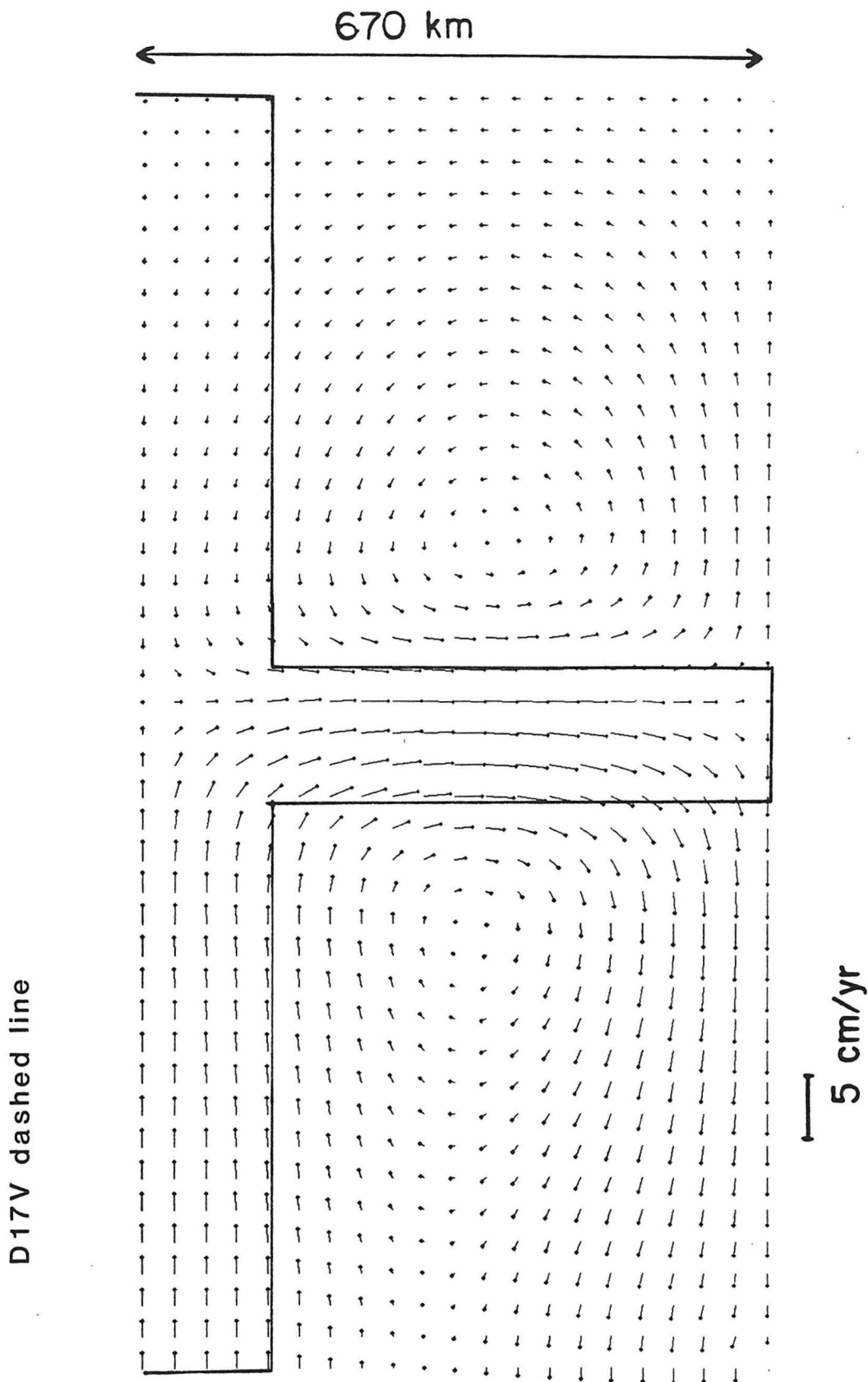
We present here spatial stress plots and flow fields not included in the text, as discussed in Section 3.1.2. Figures are labelled according to the following code: Stress plots are labelled $DnnS$, and velocity plots are labelled $DnnV$. "D" simply indicates Appendix D, S and V respectively indicate that the figure is a stress plot or a velocity plot, and nn is the number of the figure *in the text* to which the particular figure in this appendix corresponds.

670 km

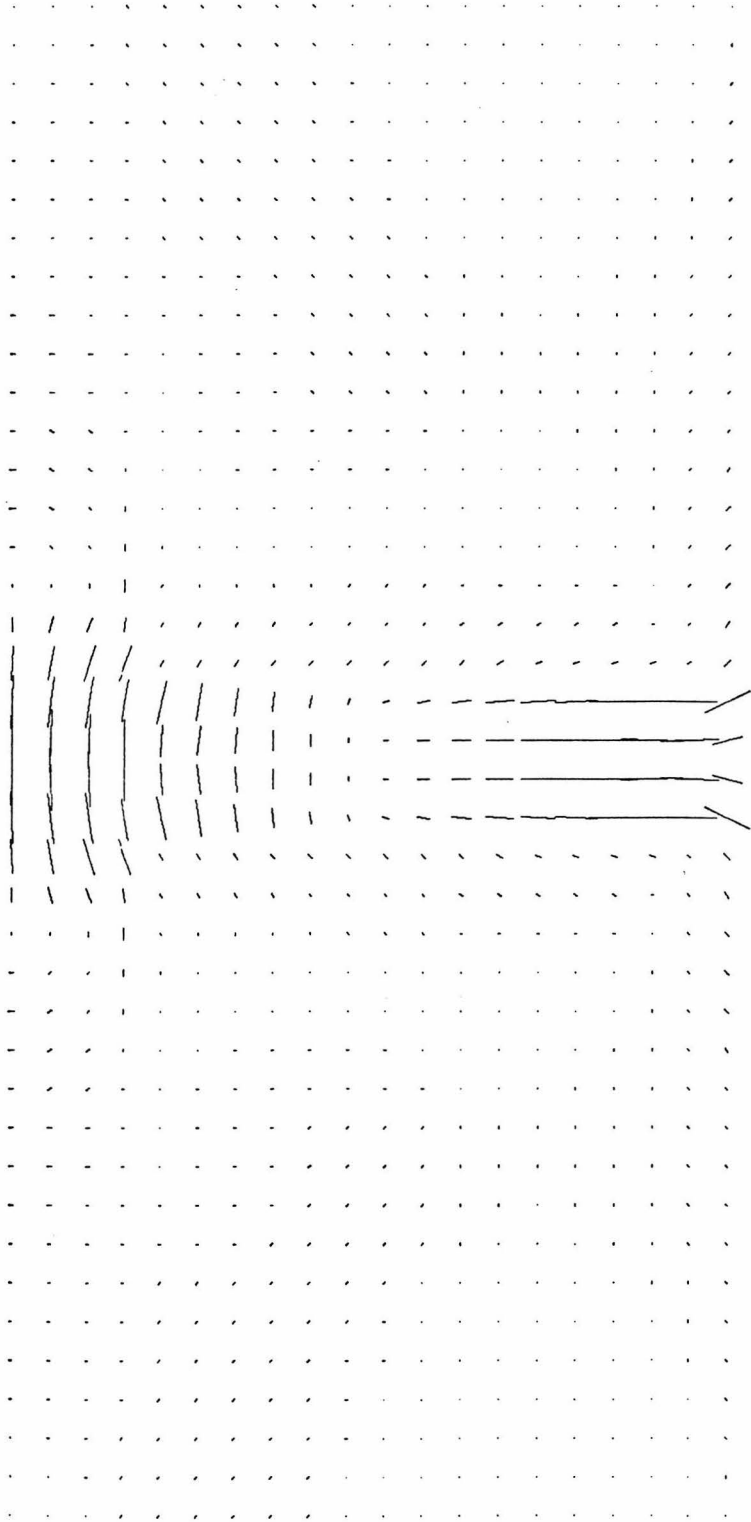
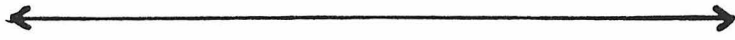


D17S dashed line

1 kbar



670 km

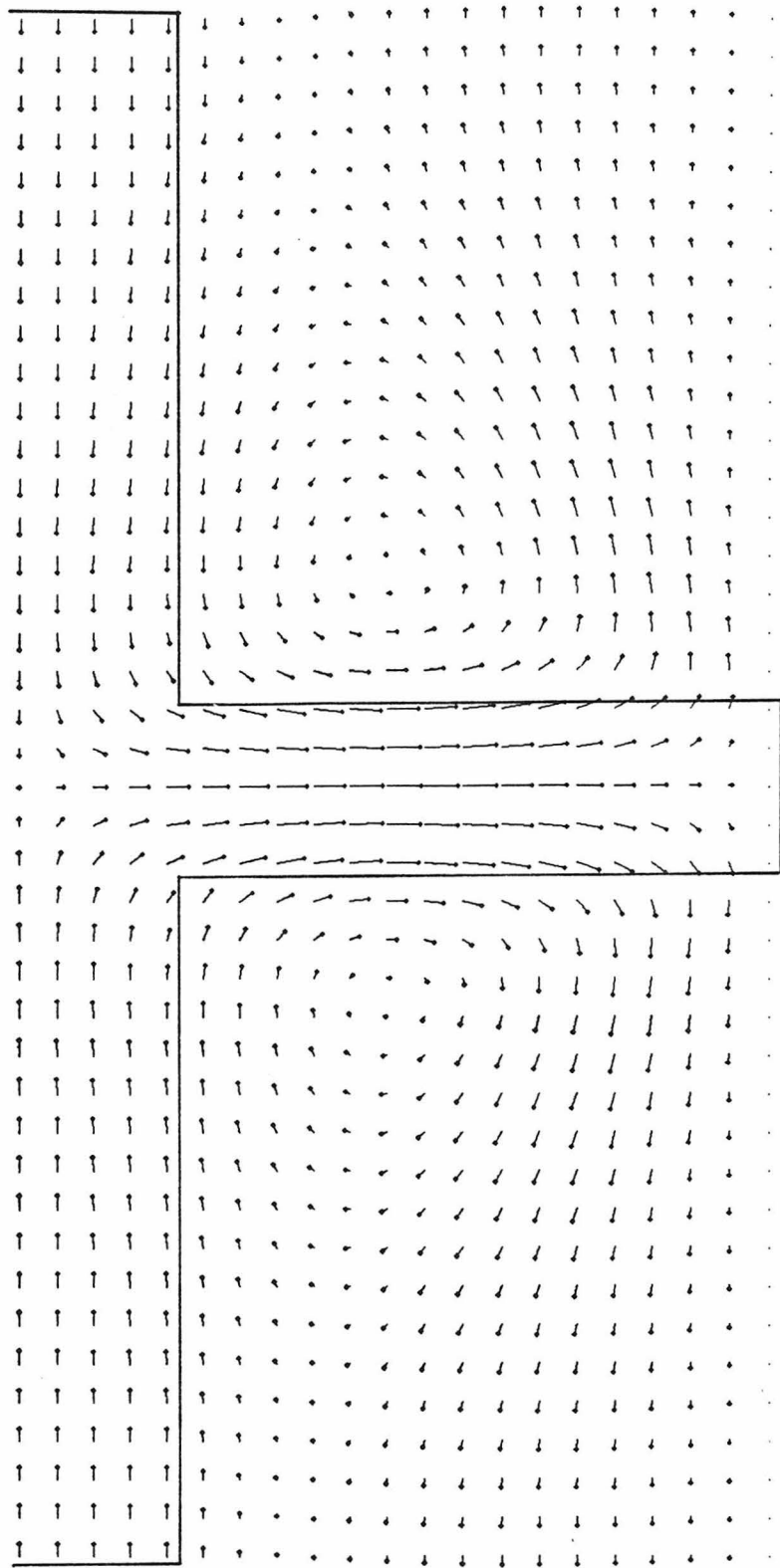


D17S dotted line



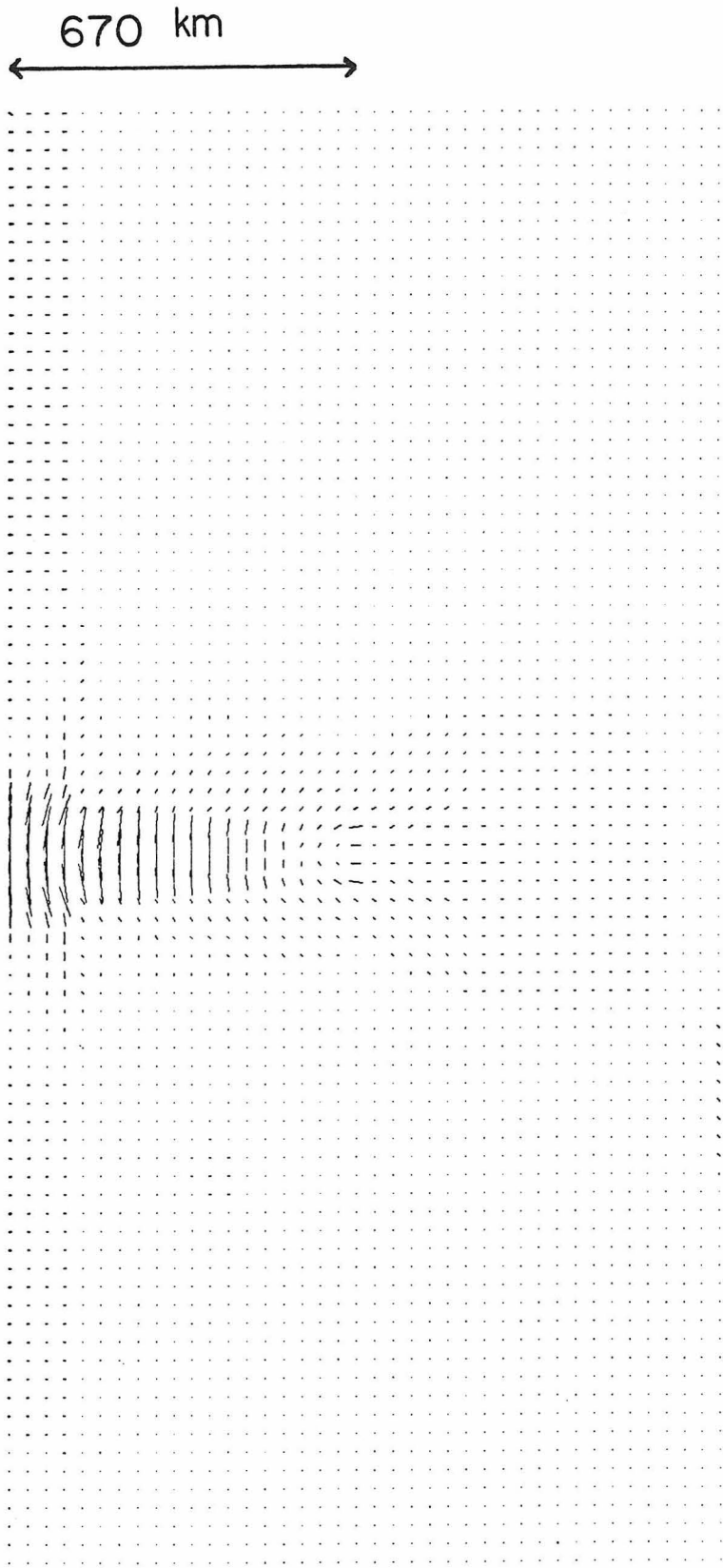
1 kbar

670 km



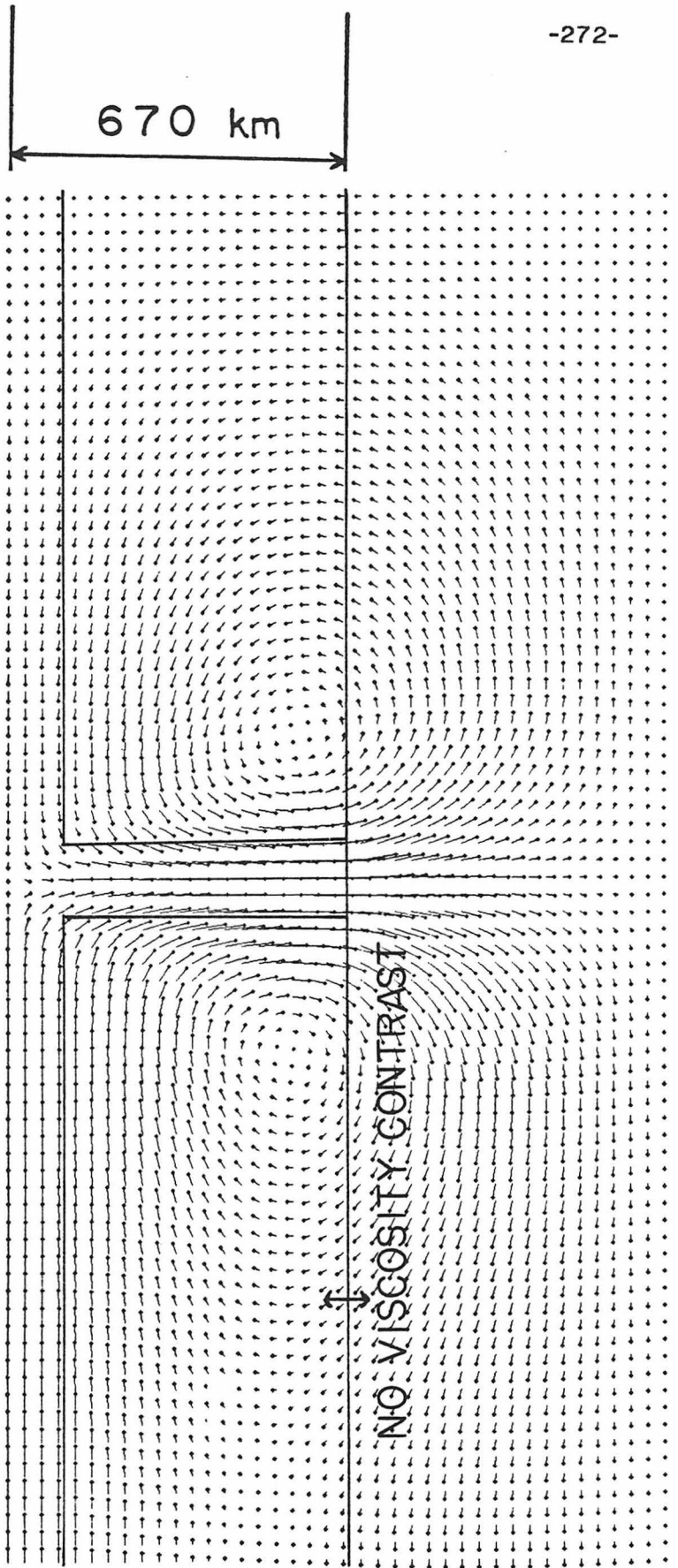
5 cm/yr

D17V dotted line



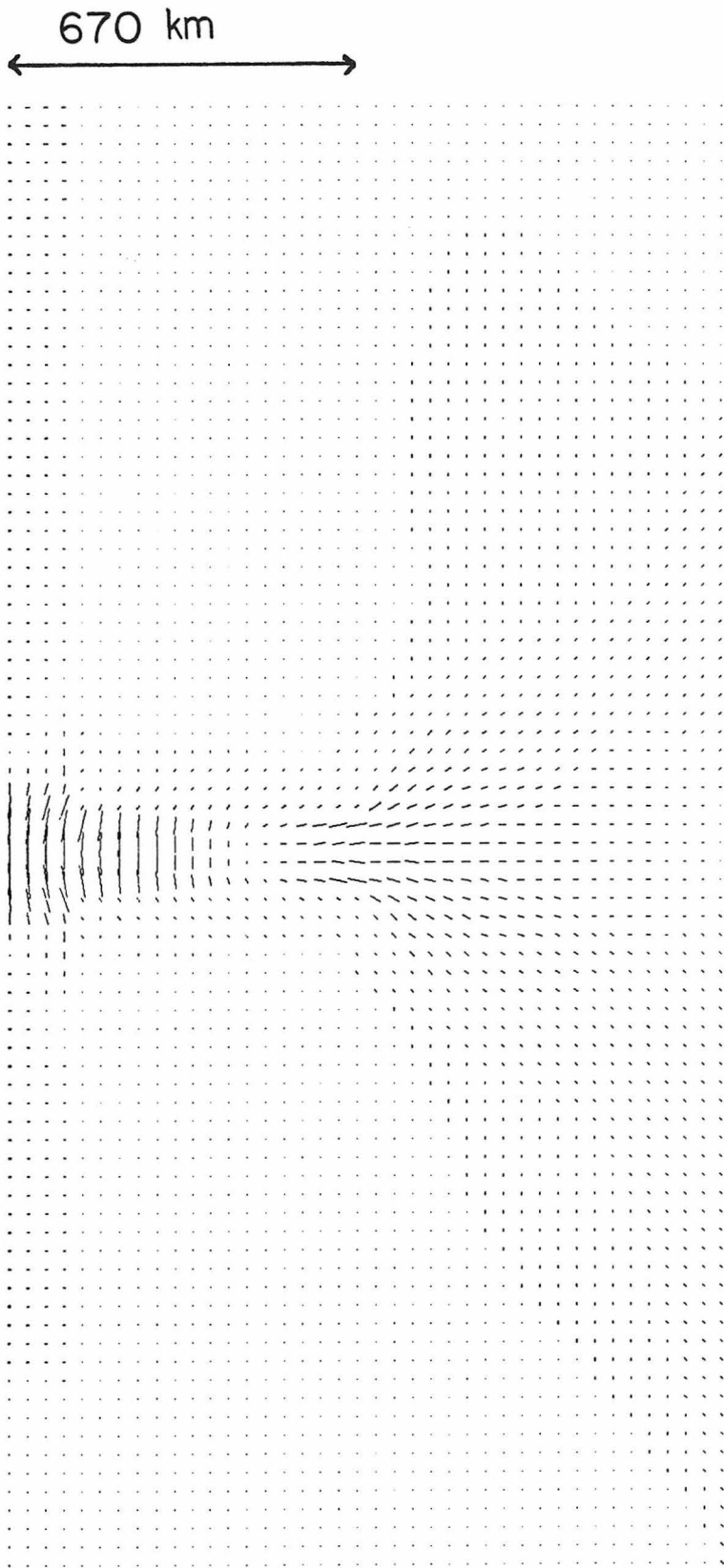
D18S

2 kbar

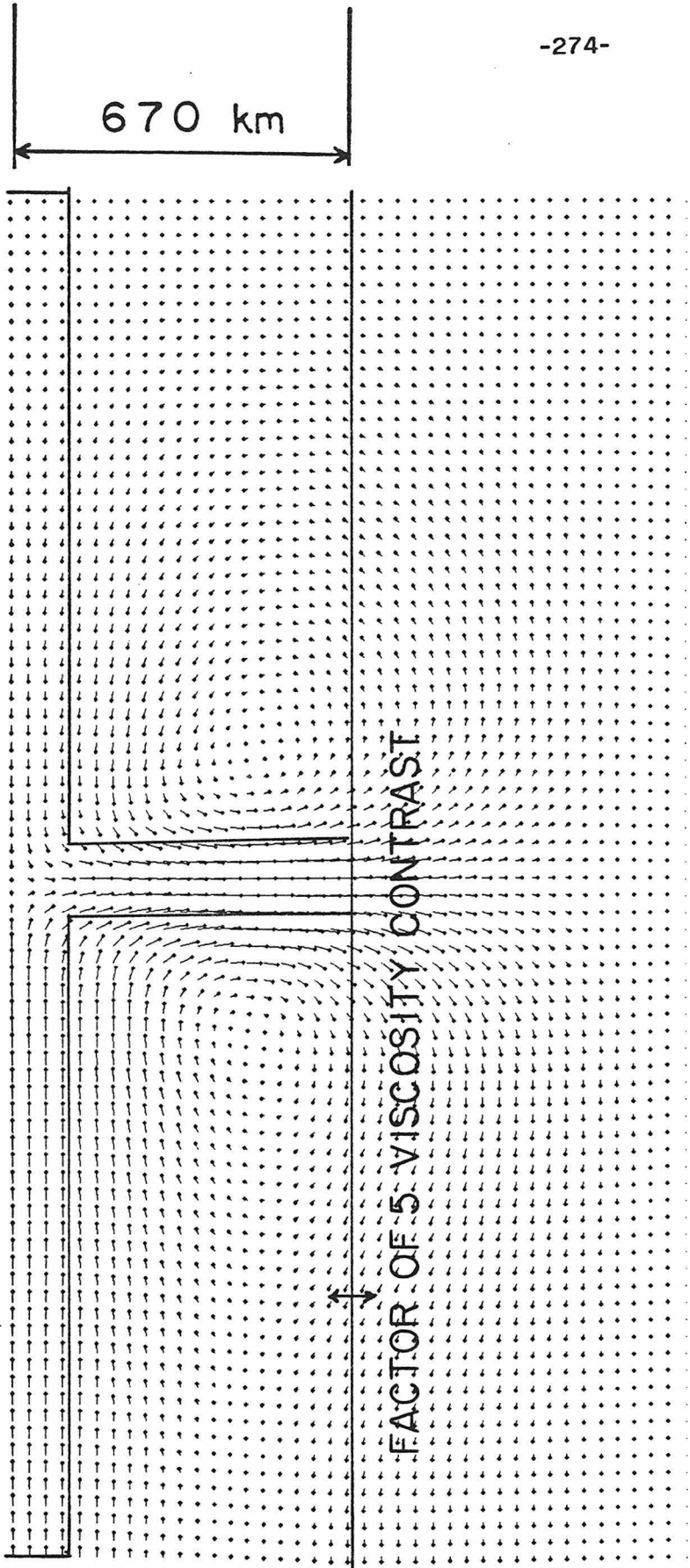


D18V

10 cm/yr



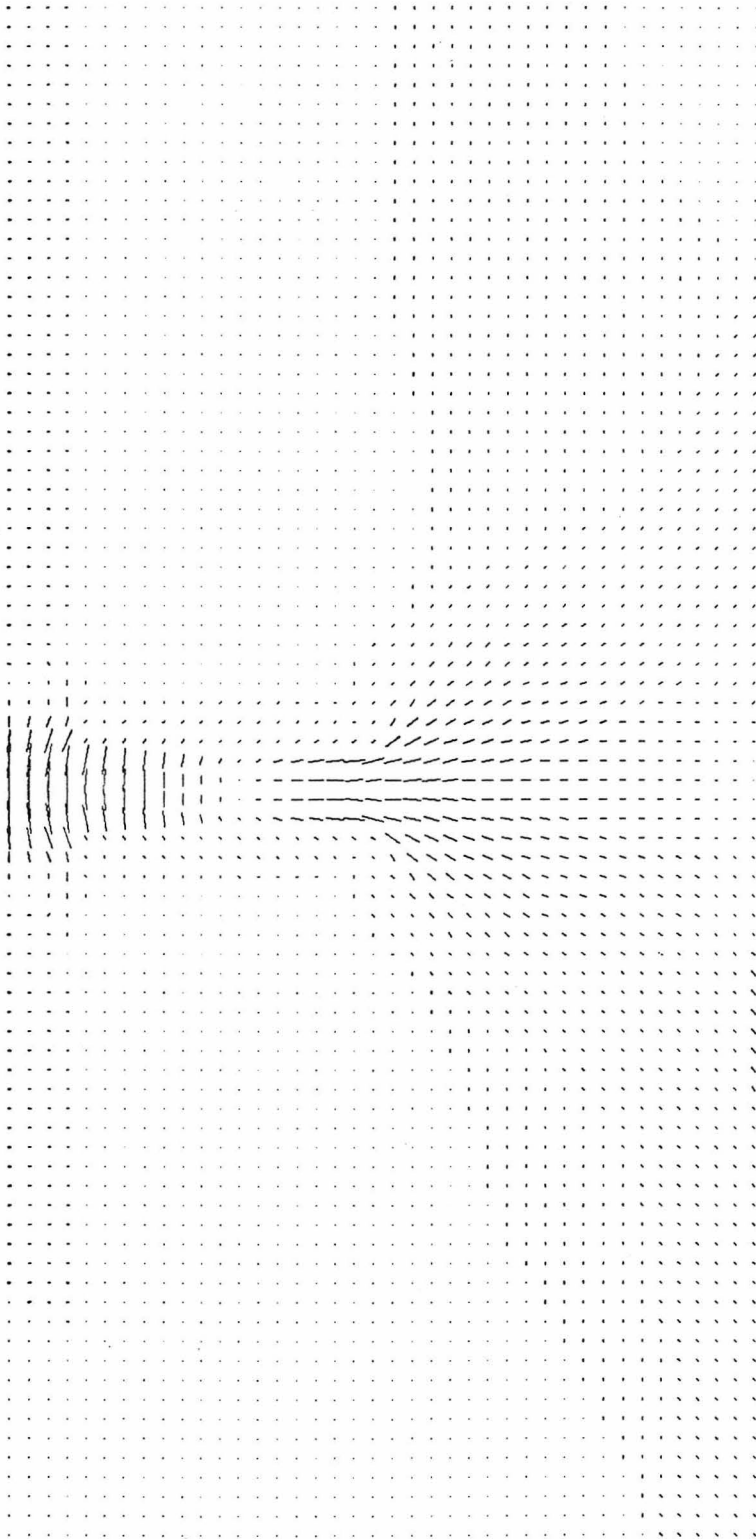
D19S (5)



10 cm/yr

D19V (5)

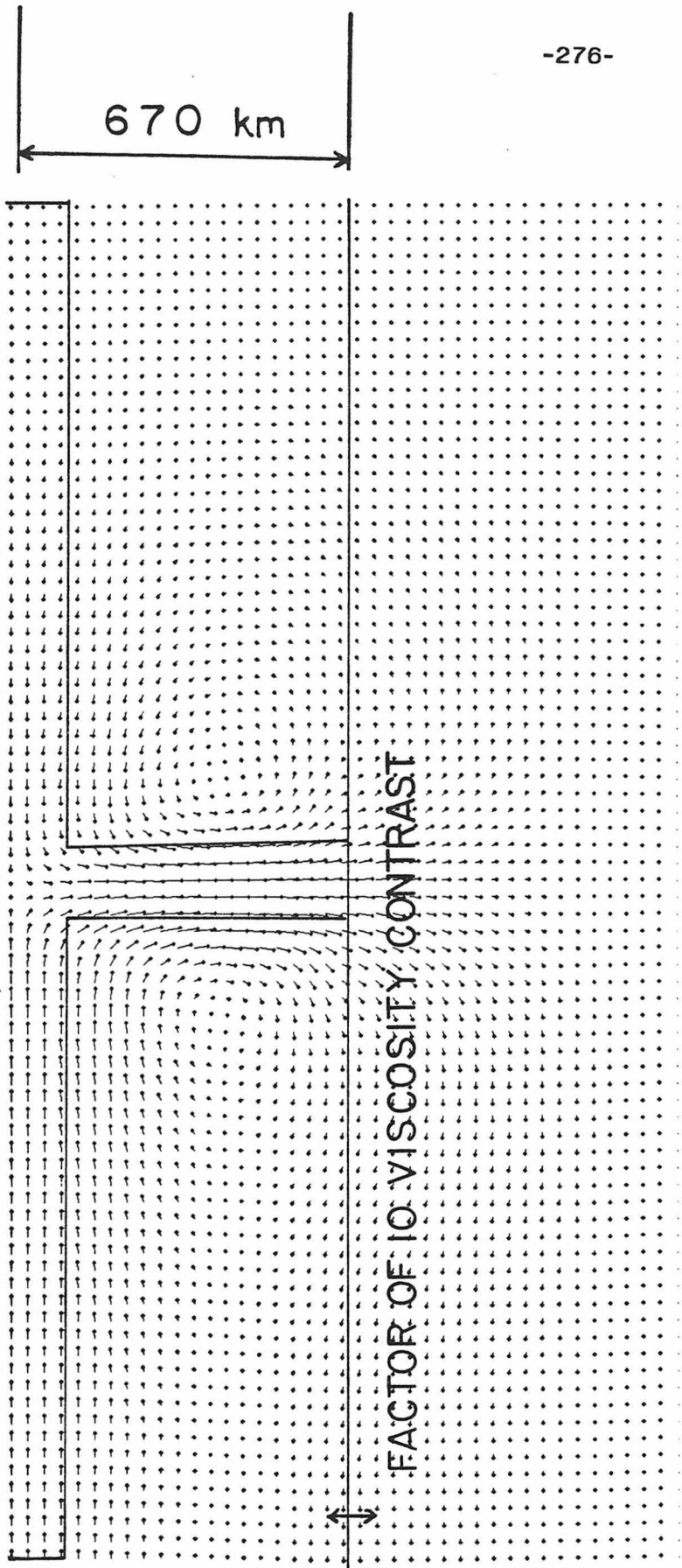
670 km

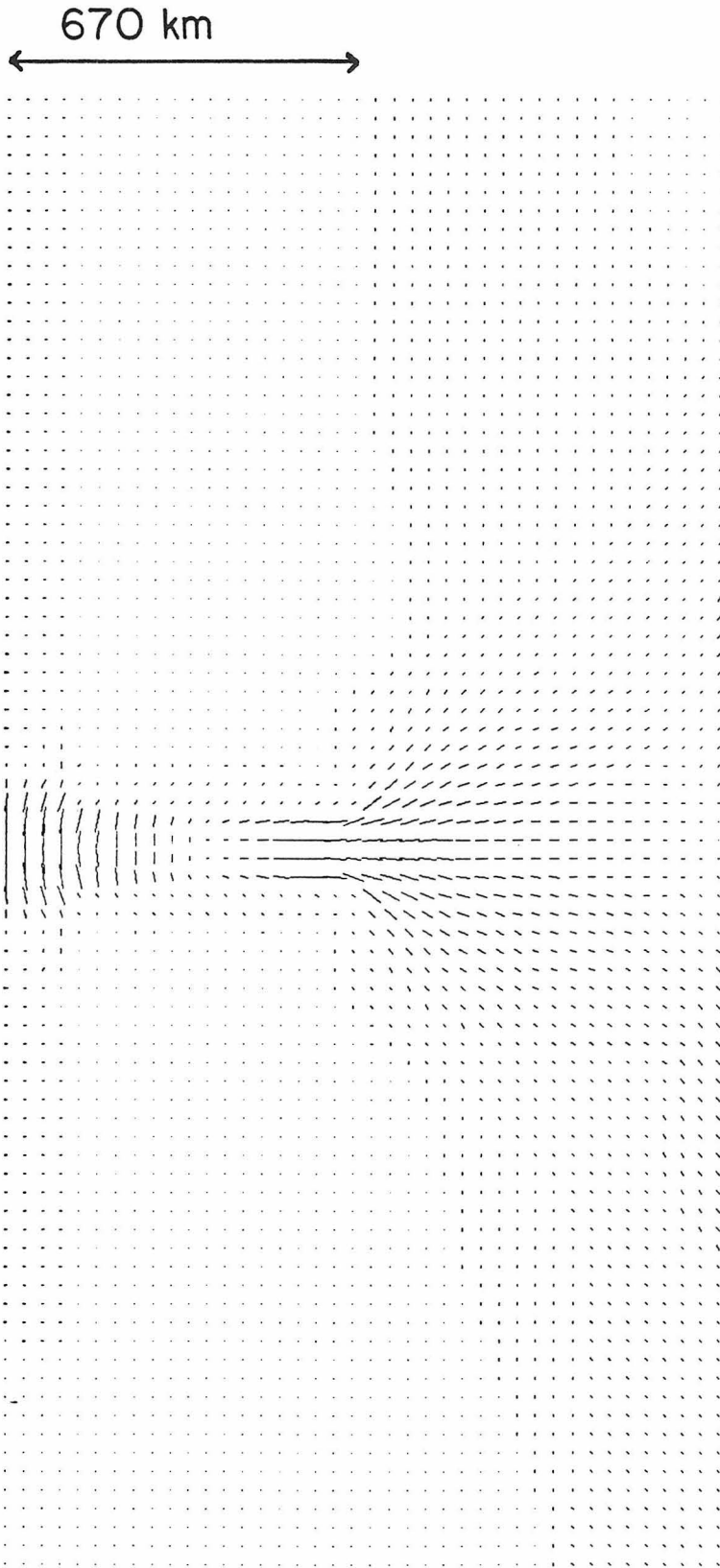


D19S (10)

2 kbar

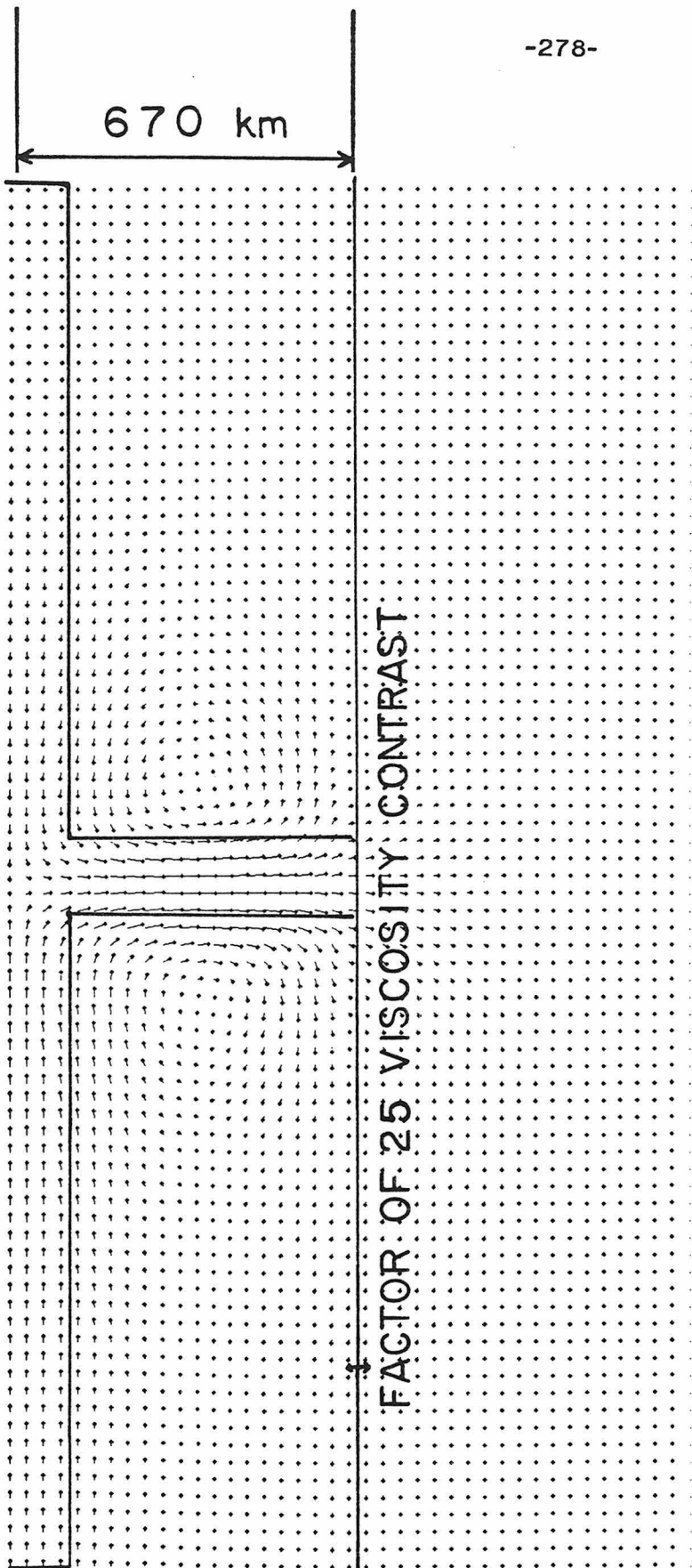






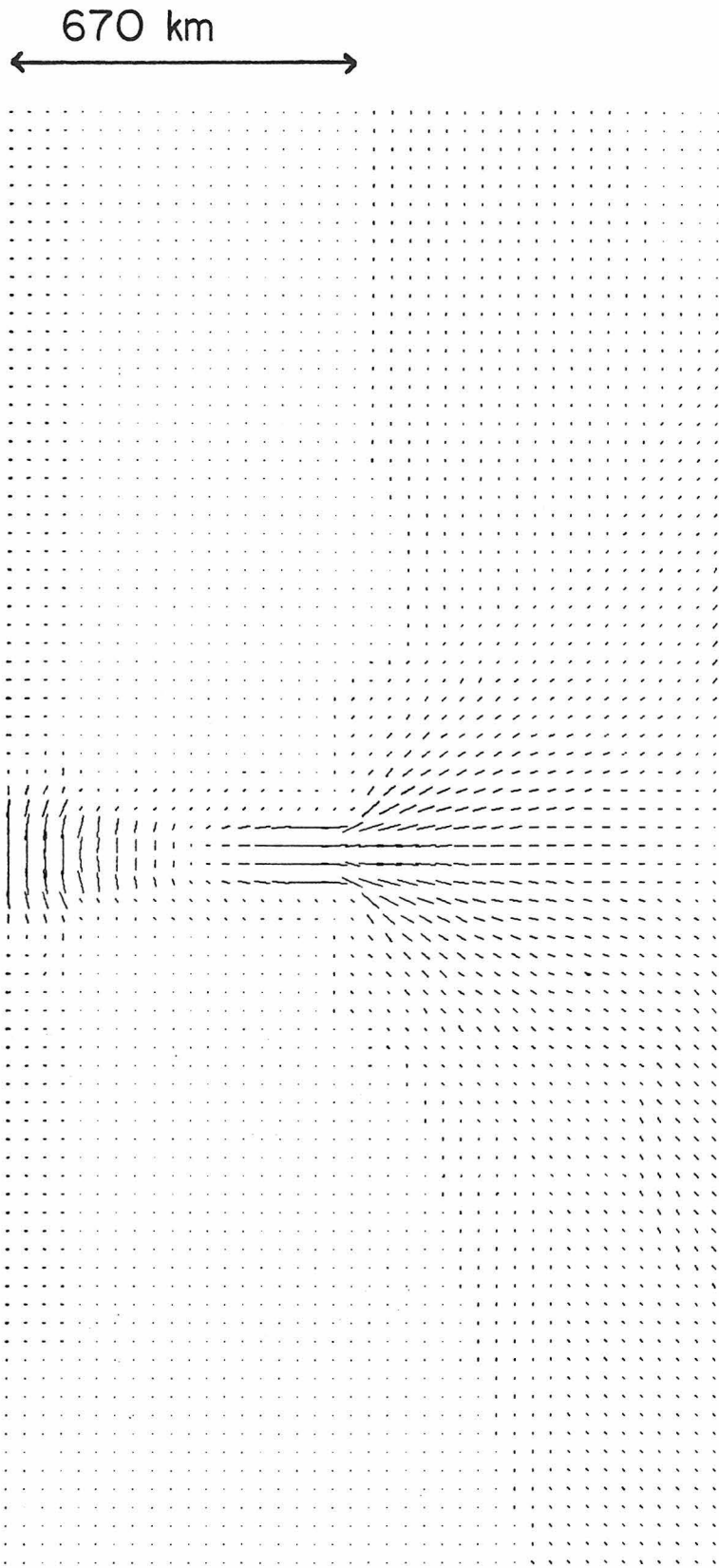
D19S (25)

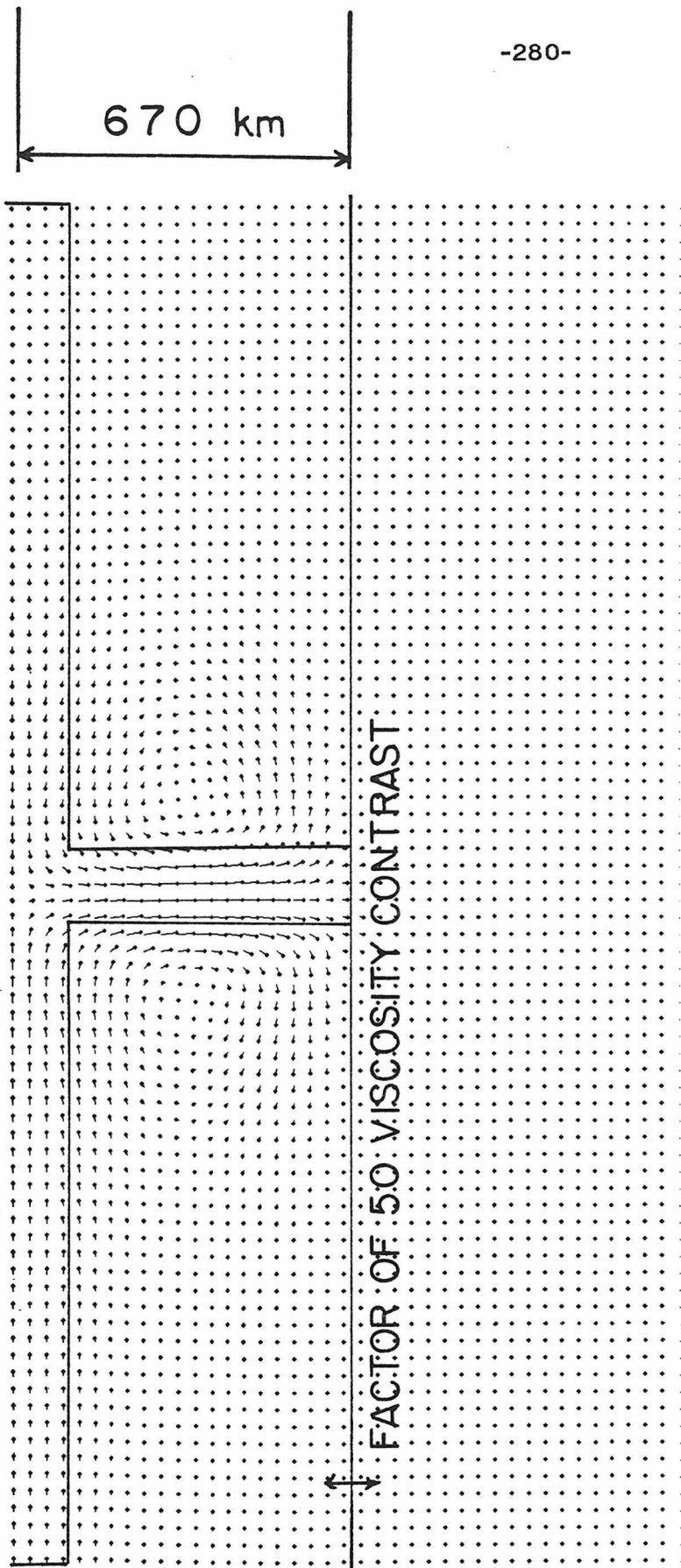
2 kbar



D19V (25)

10 cm/yr

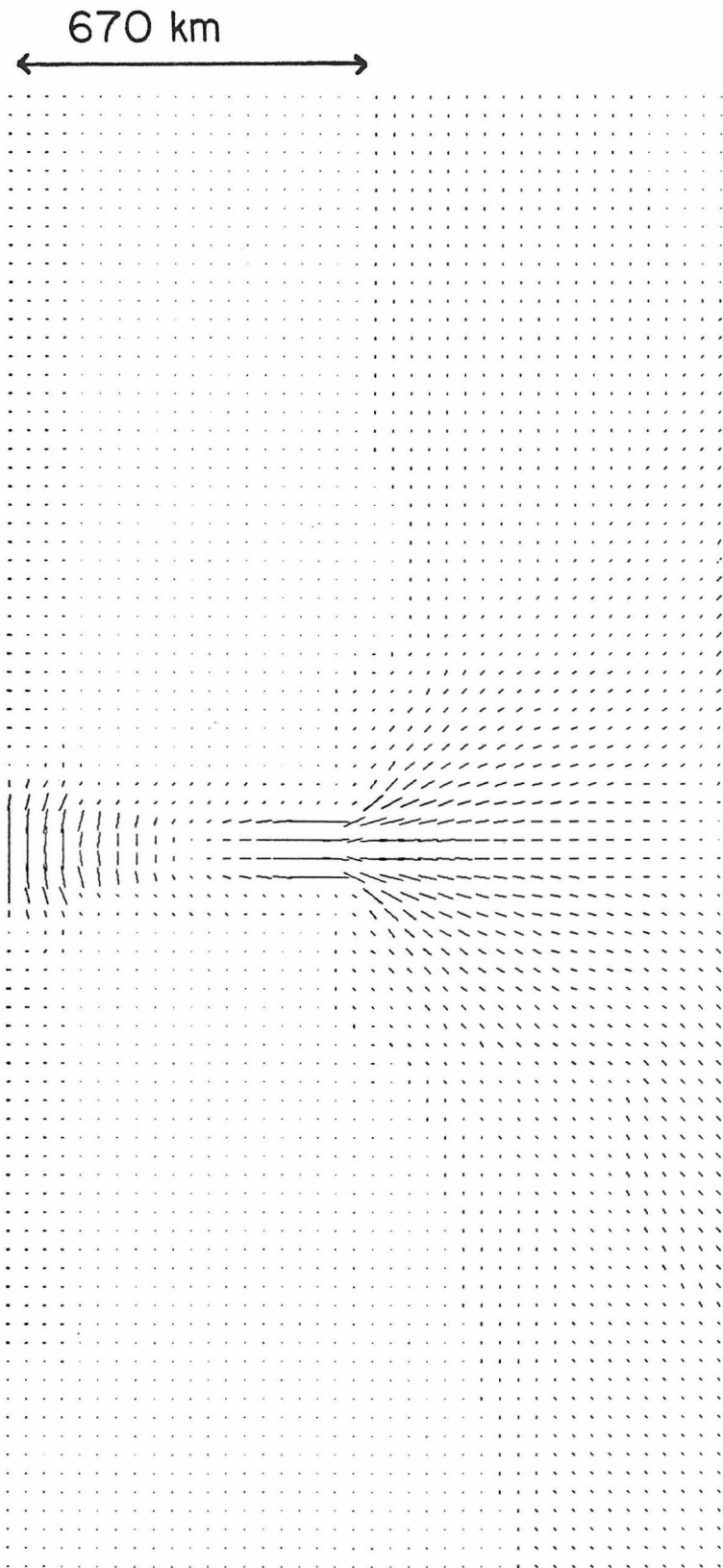


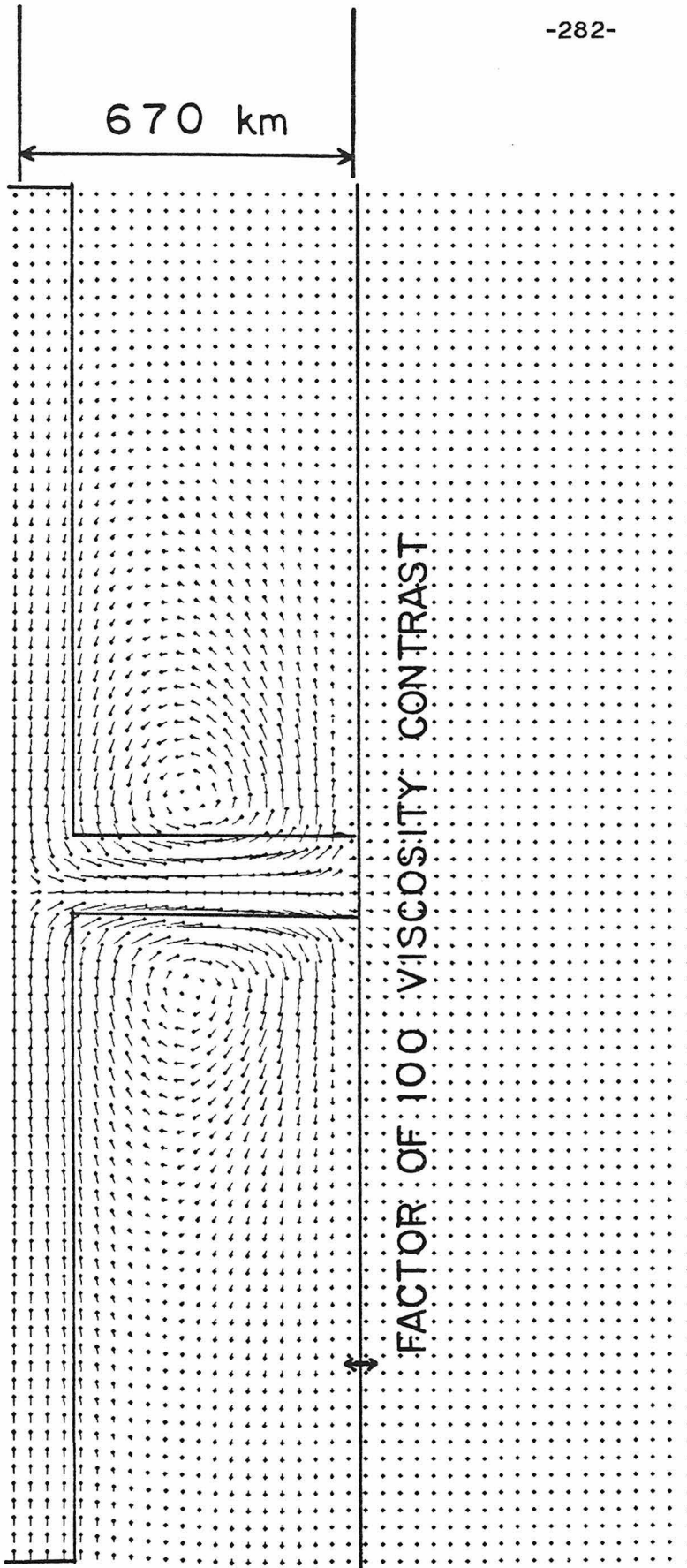


D19V (50)



10 cm/yr

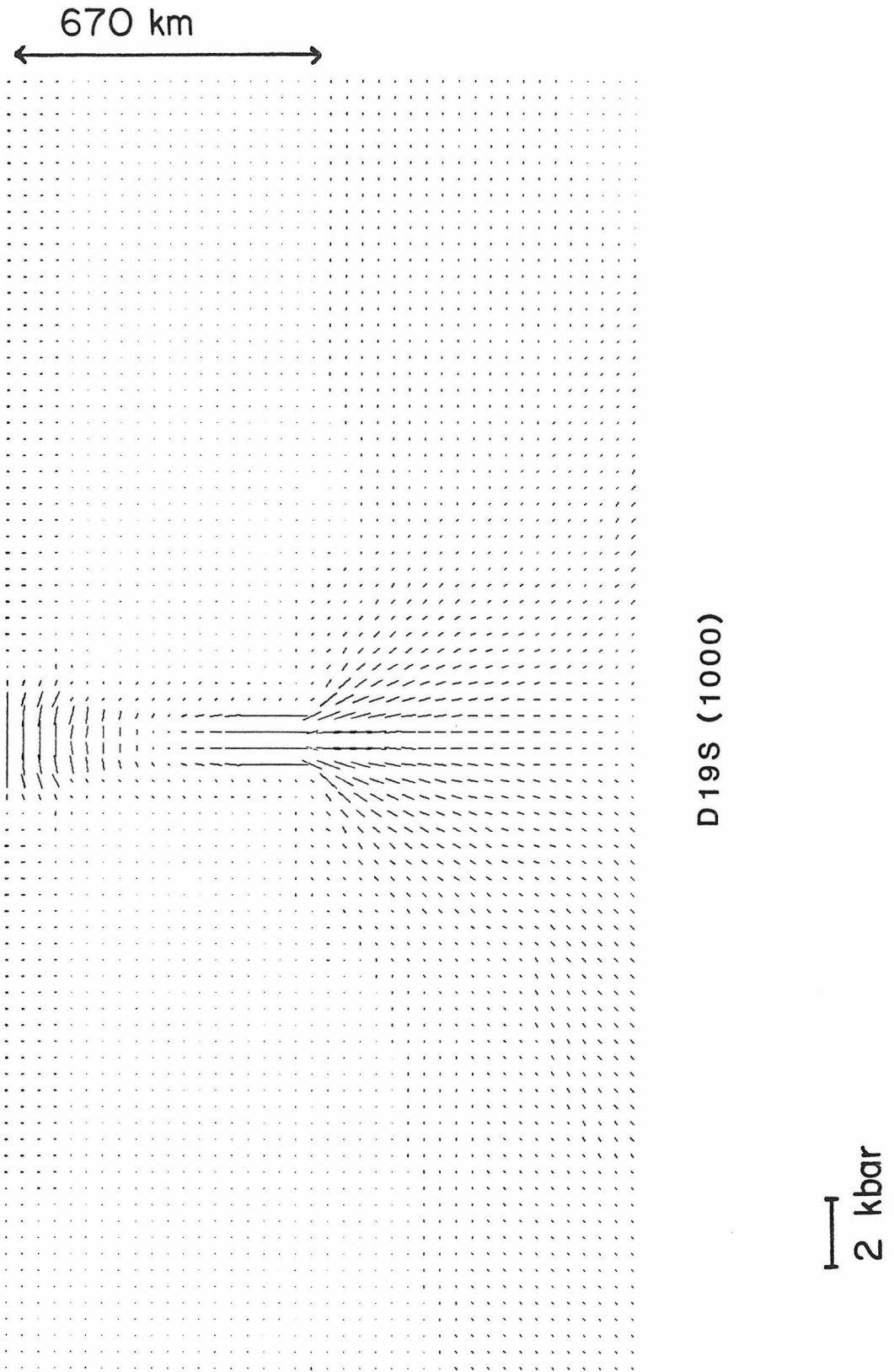


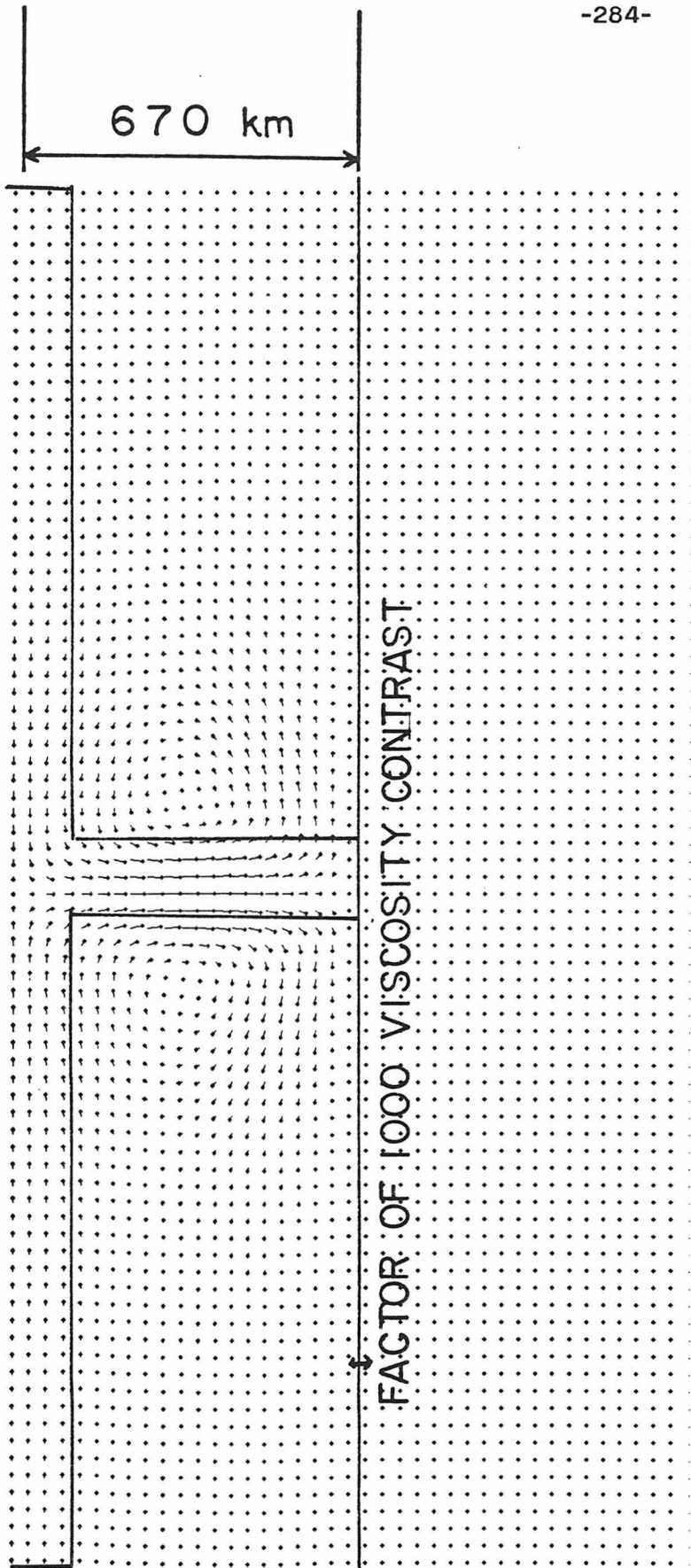


D19V (100)



10 cm/yr



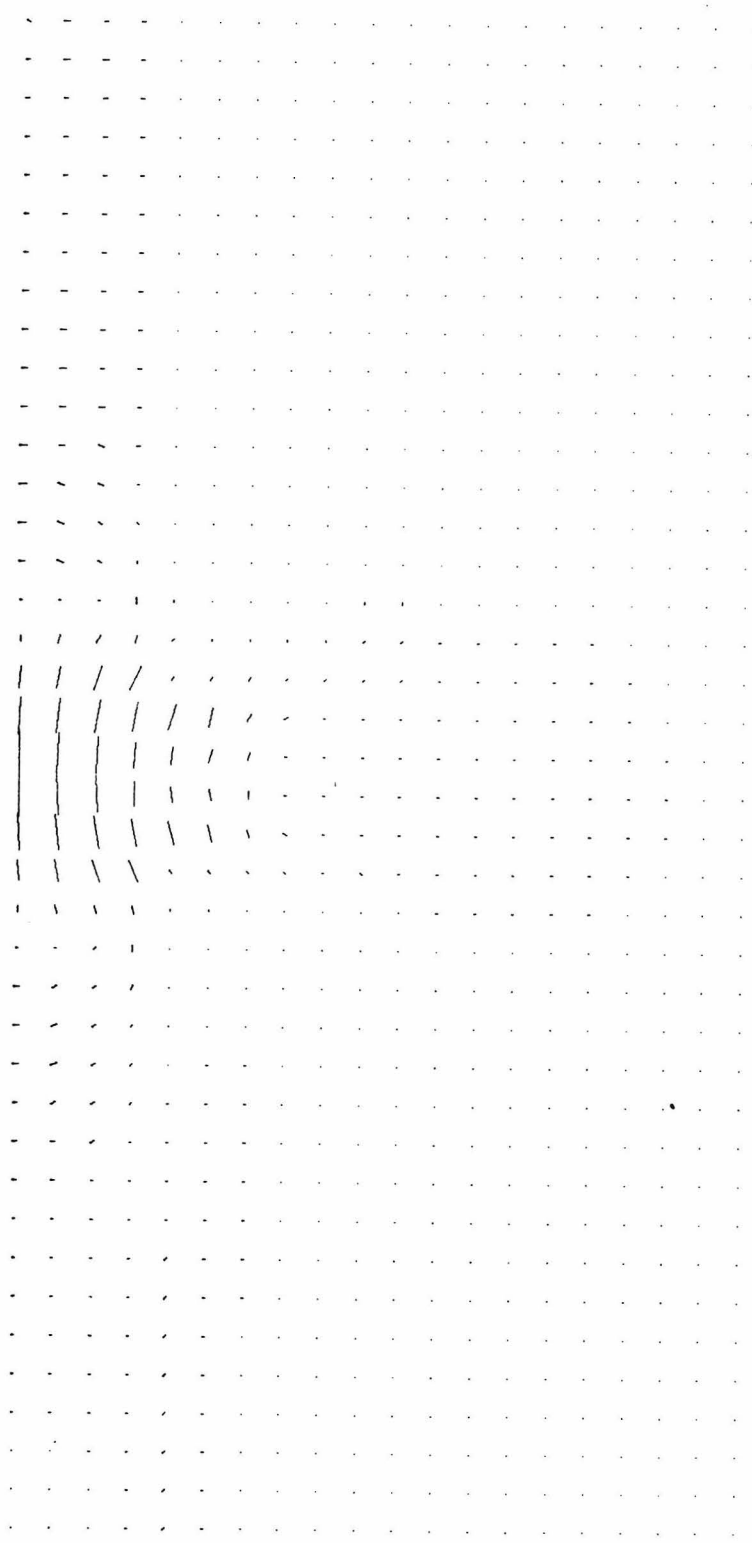


D19V (1000)



10 cm/yr

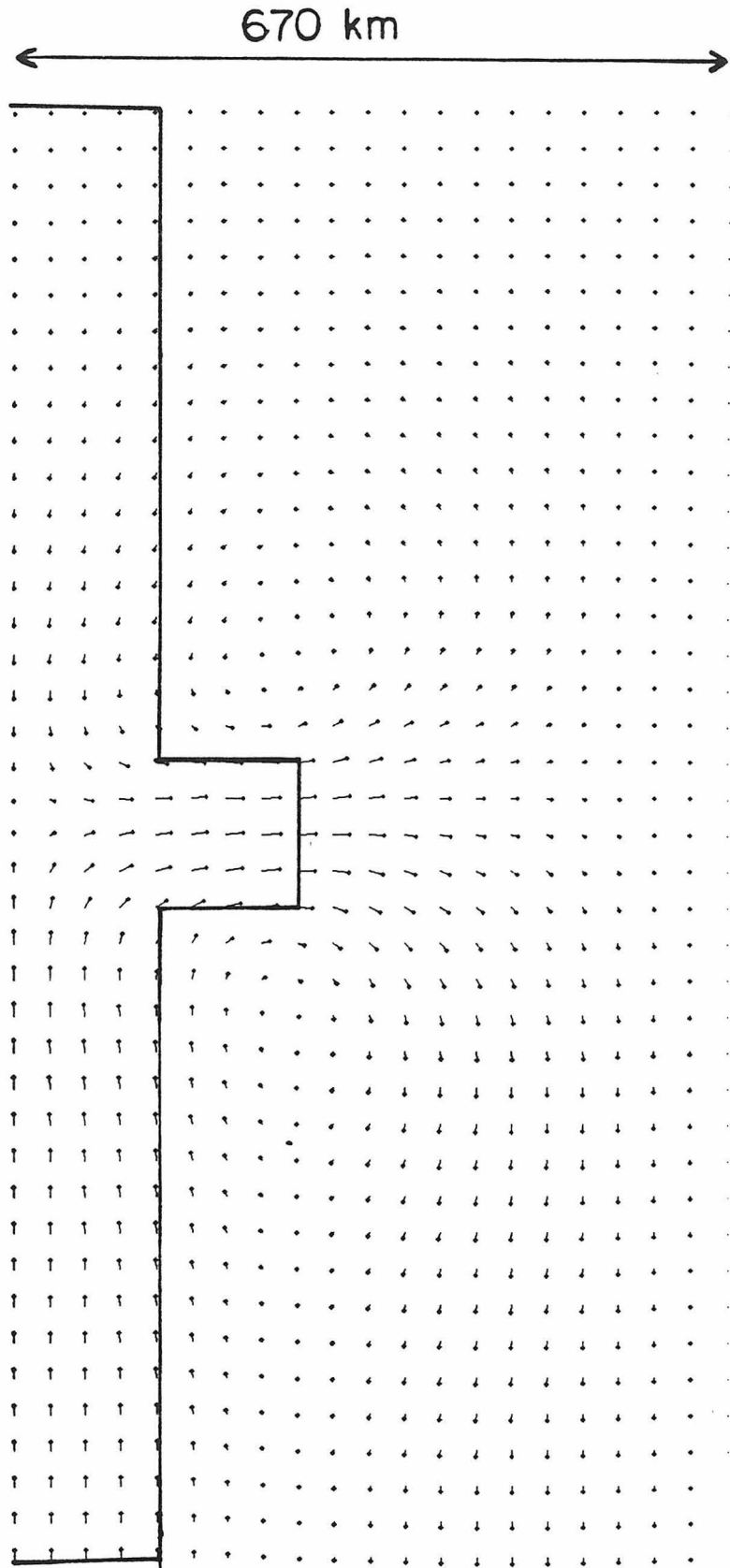
670 km



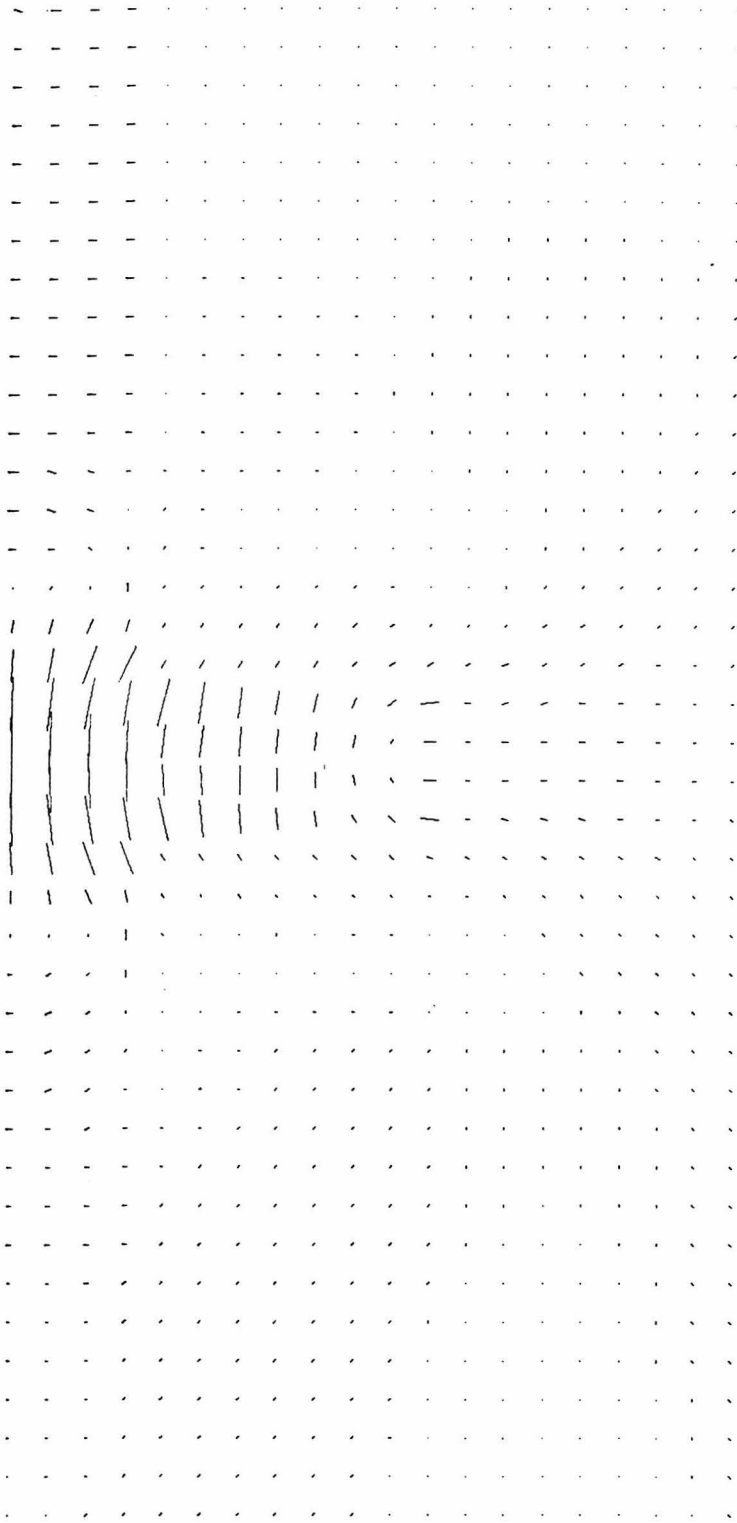
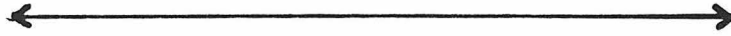
D22aS



1 kbar



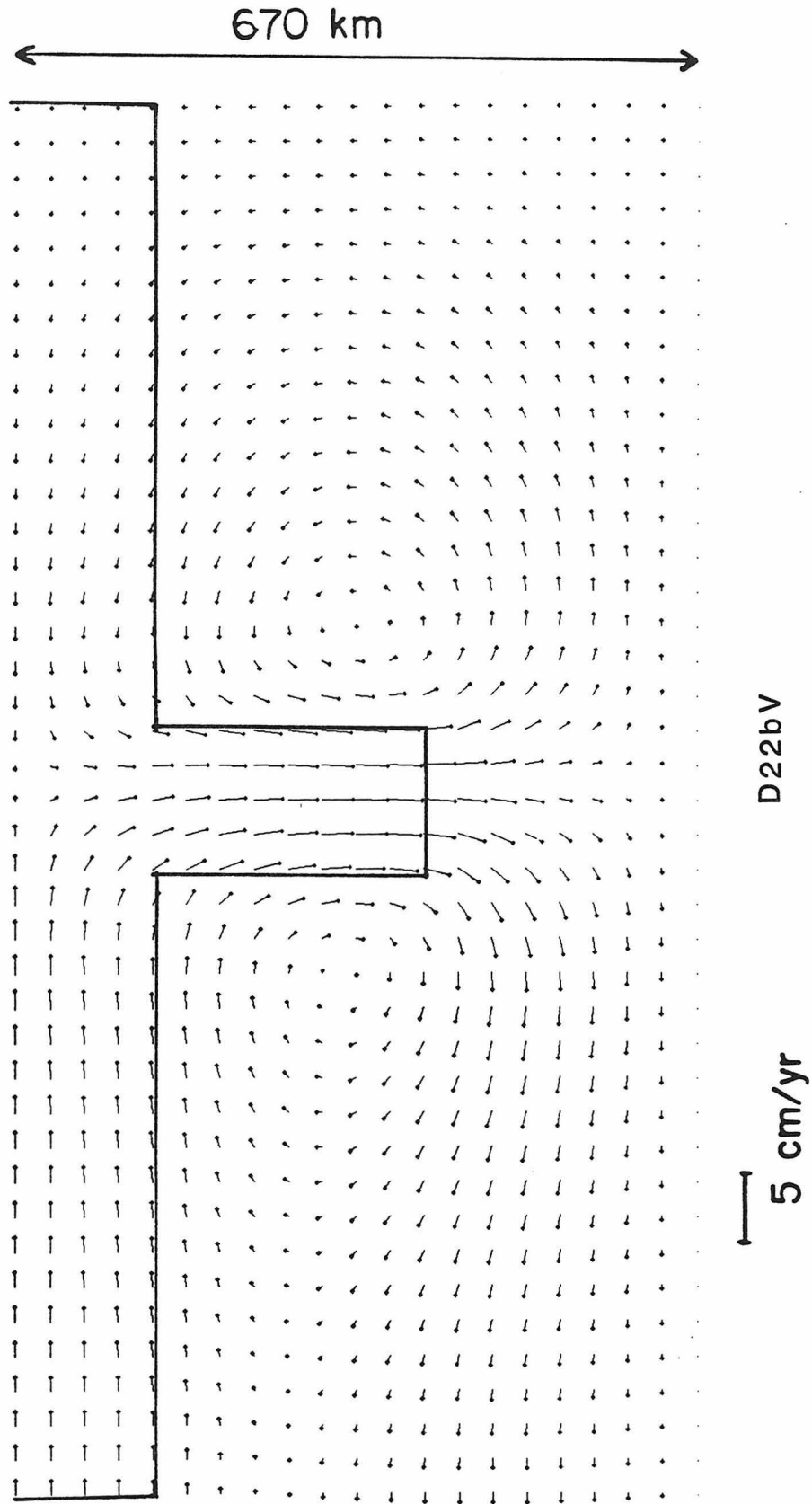
670 km



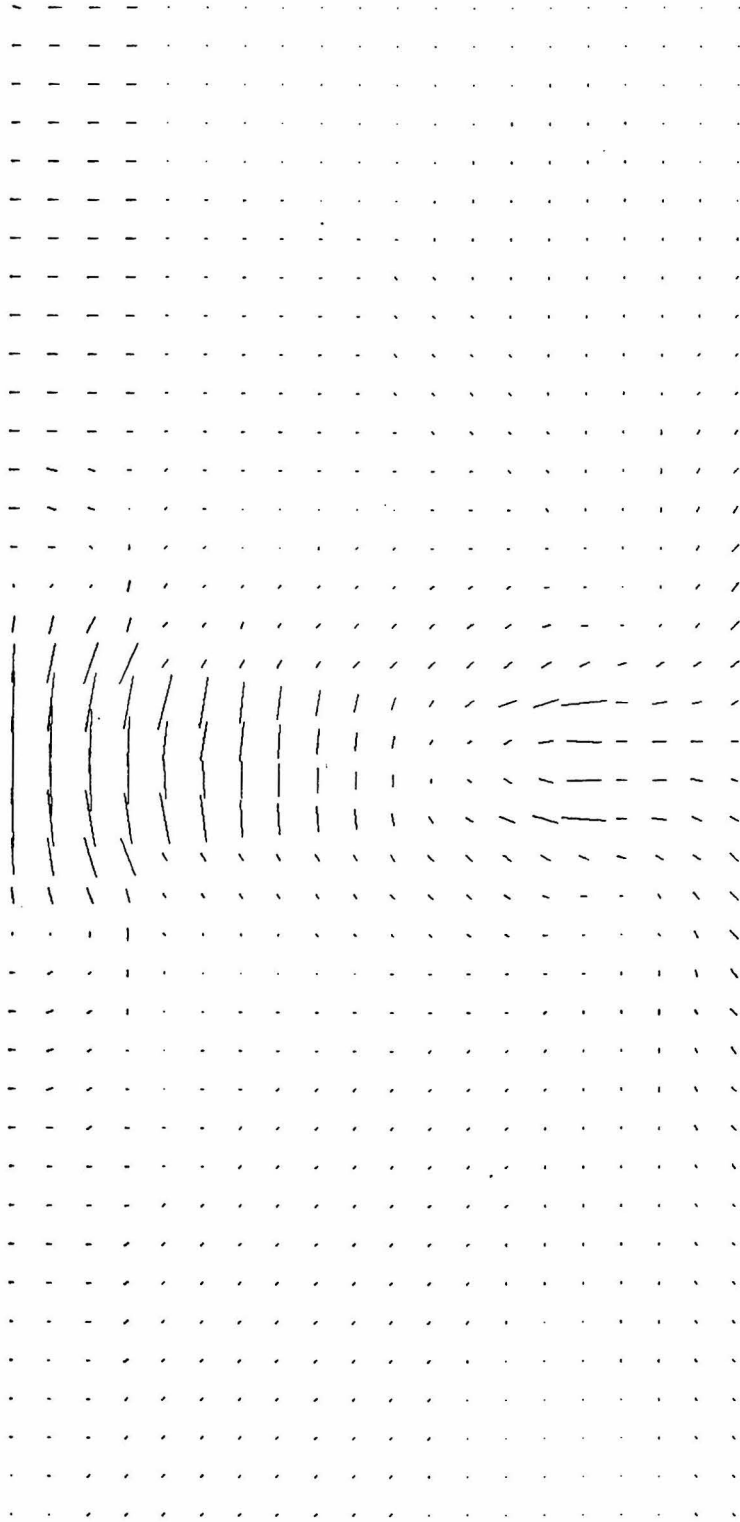
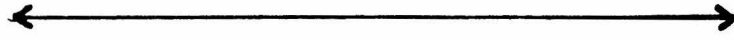
D22bS



1 kbar



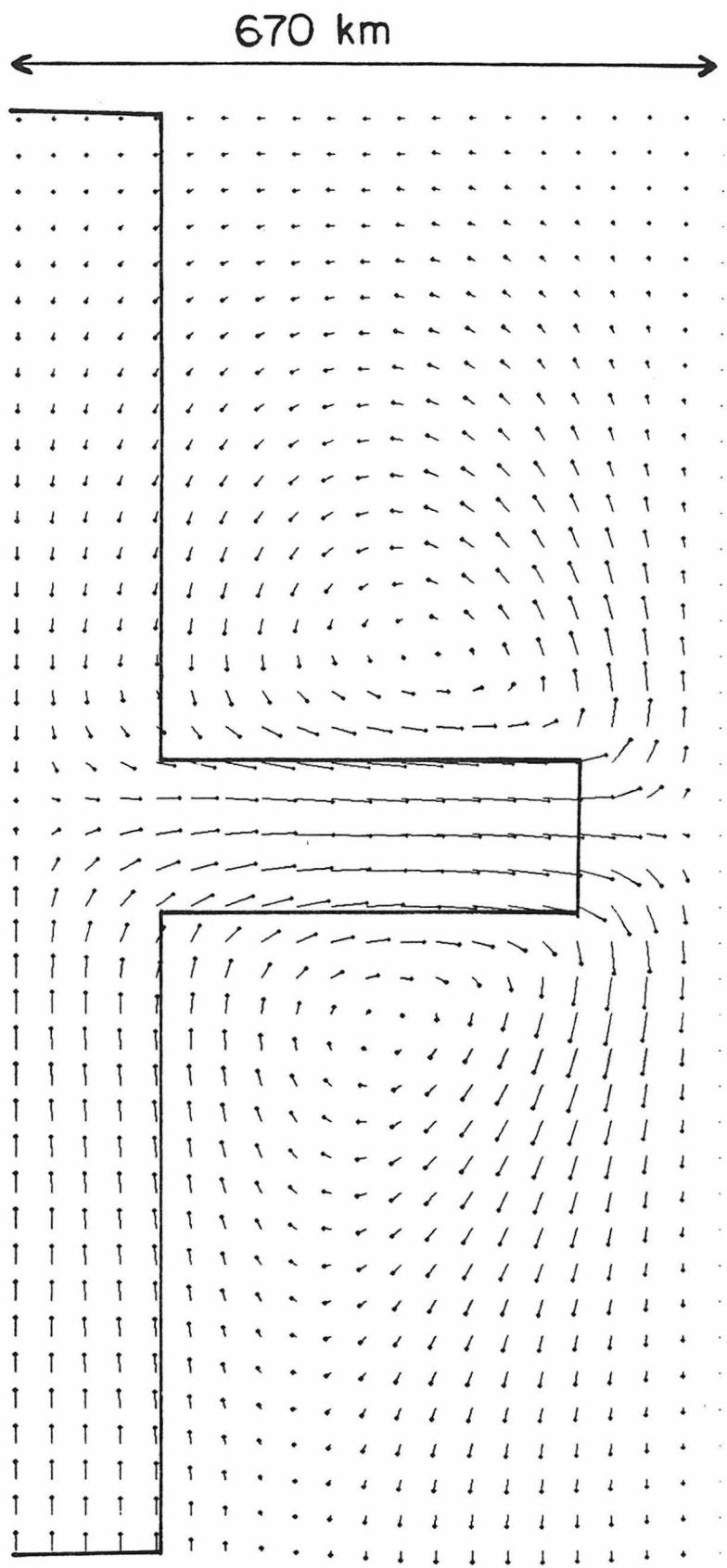
670 km



D22cS



1 kbar

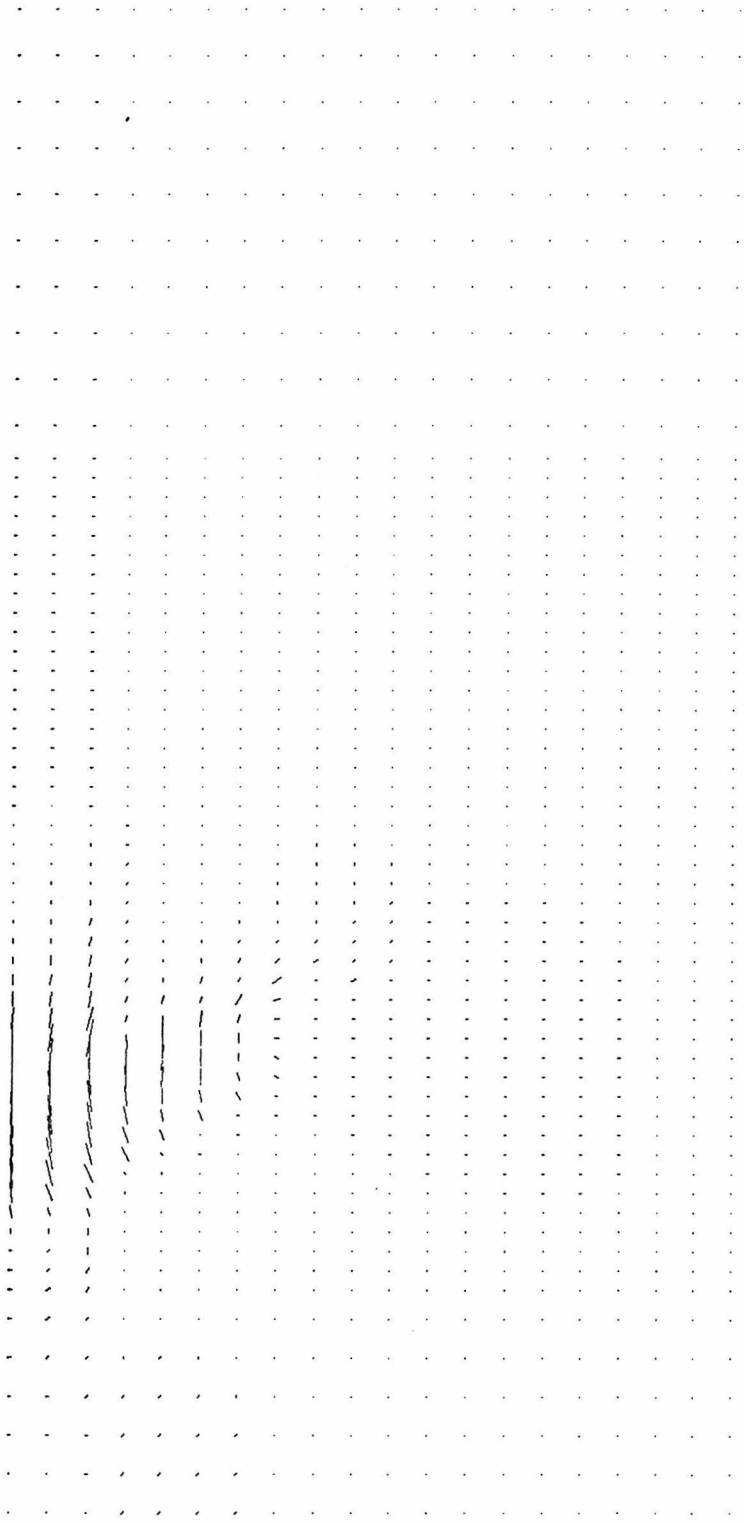
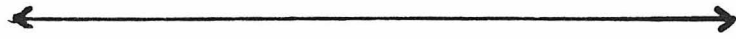


670 km

D22cV

5 cm/yr

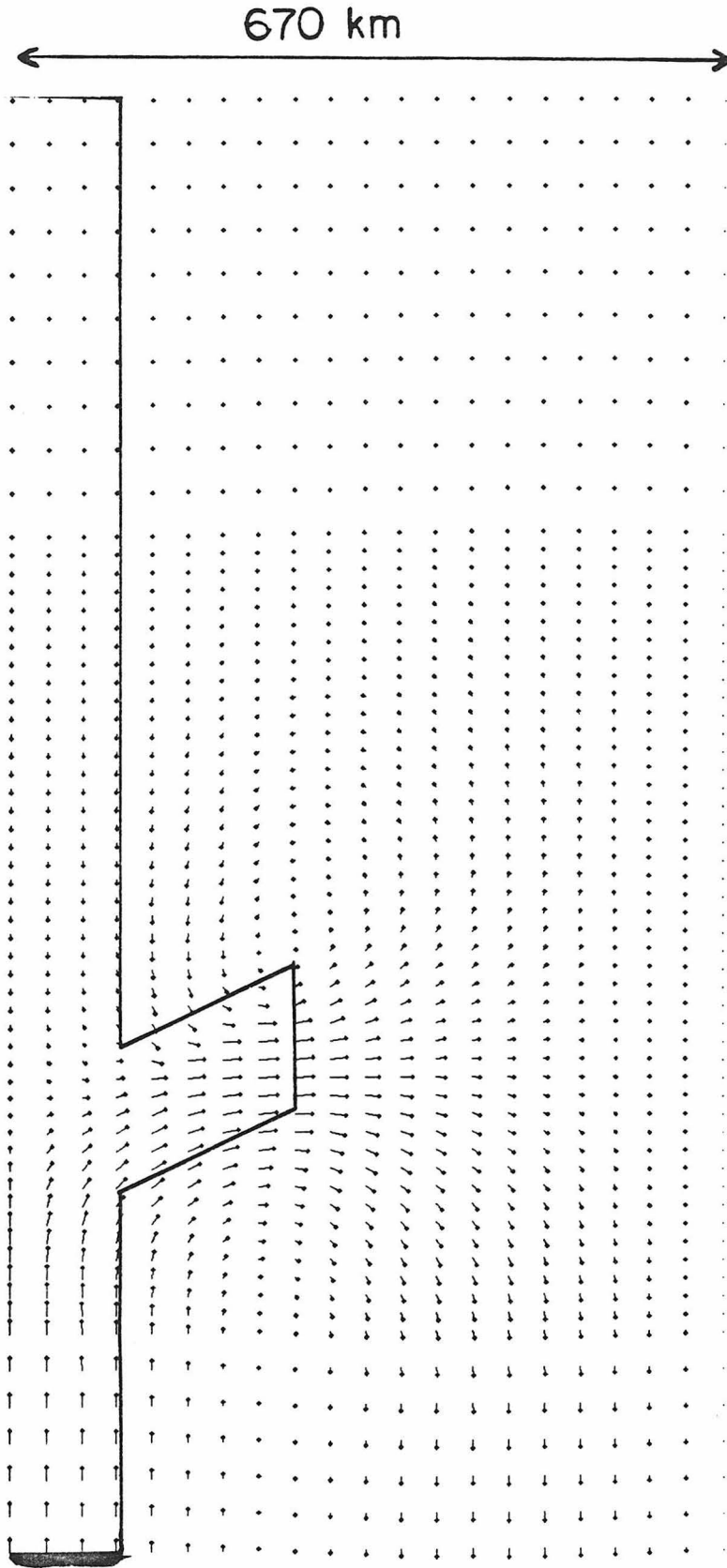
670 km



D23aS

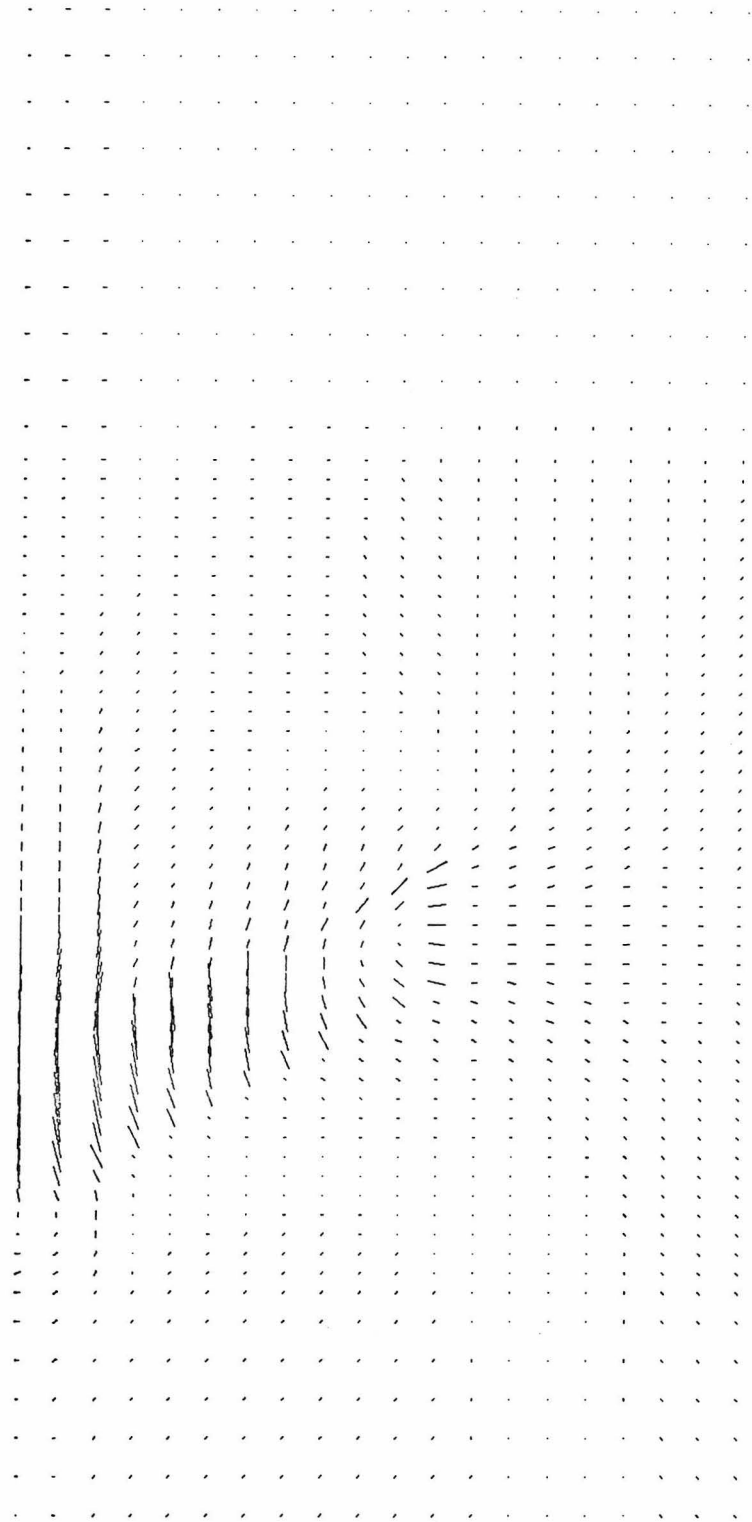


1 kbar



D23aV

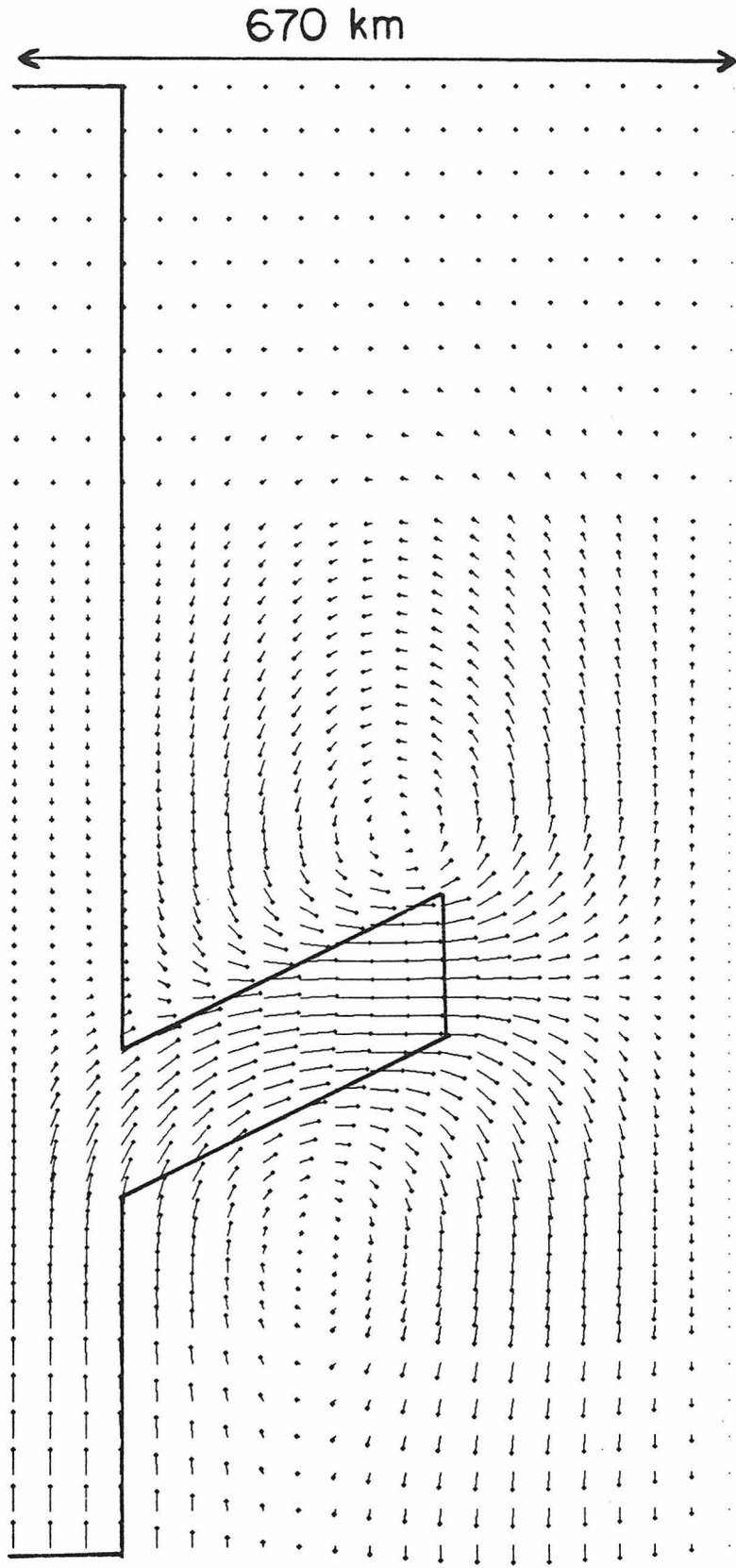
670 km



D23bS

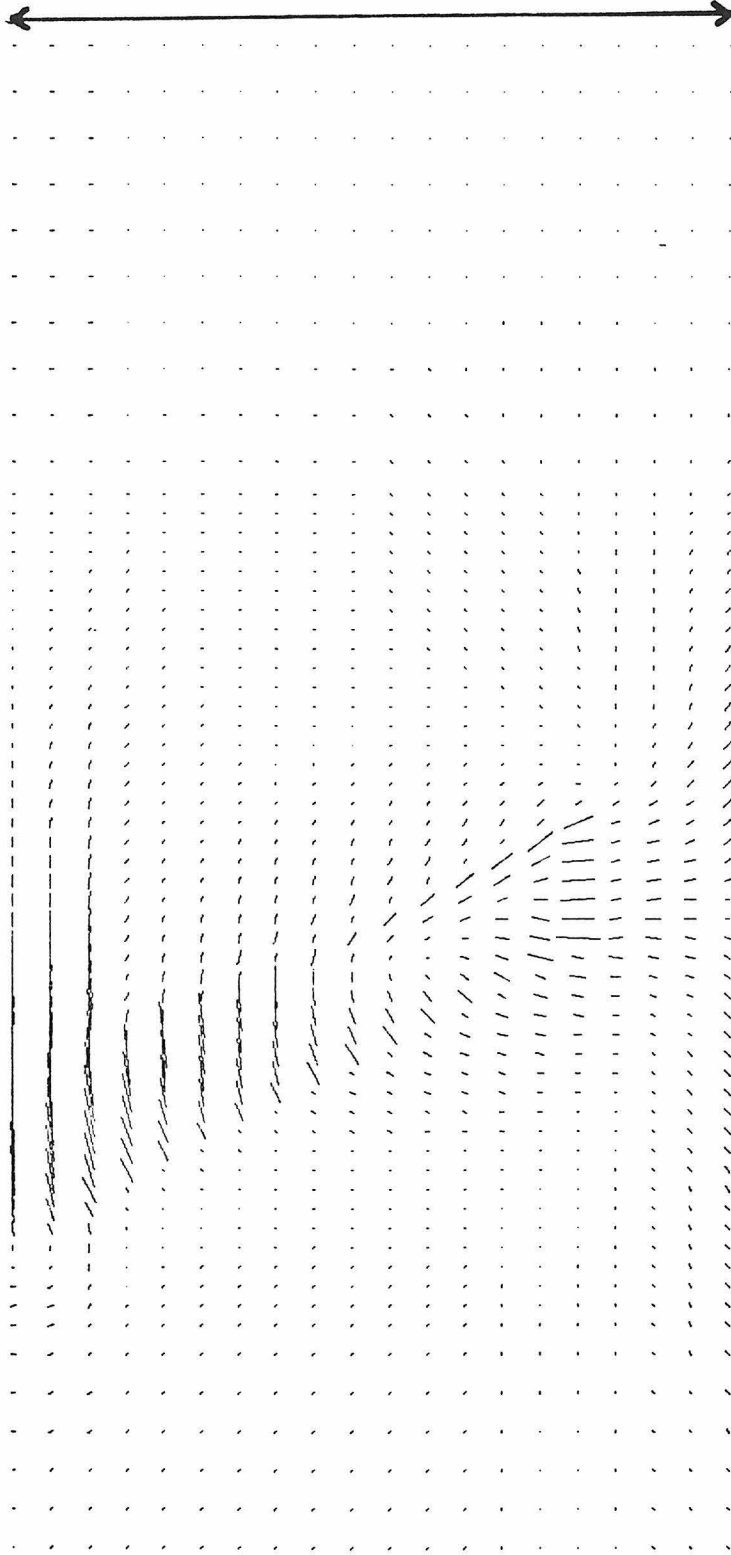


1 kbar



D23b V

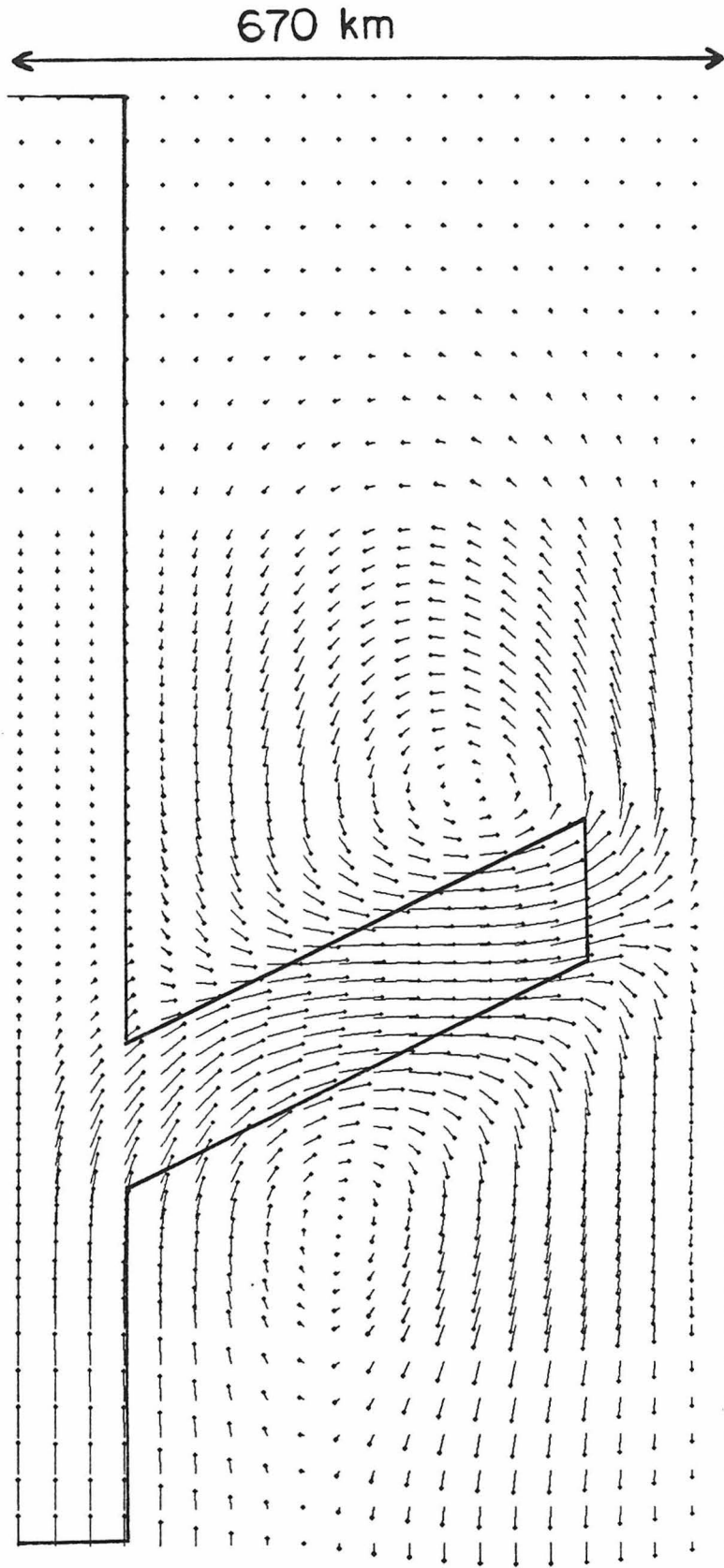
670 km



D23cS

—

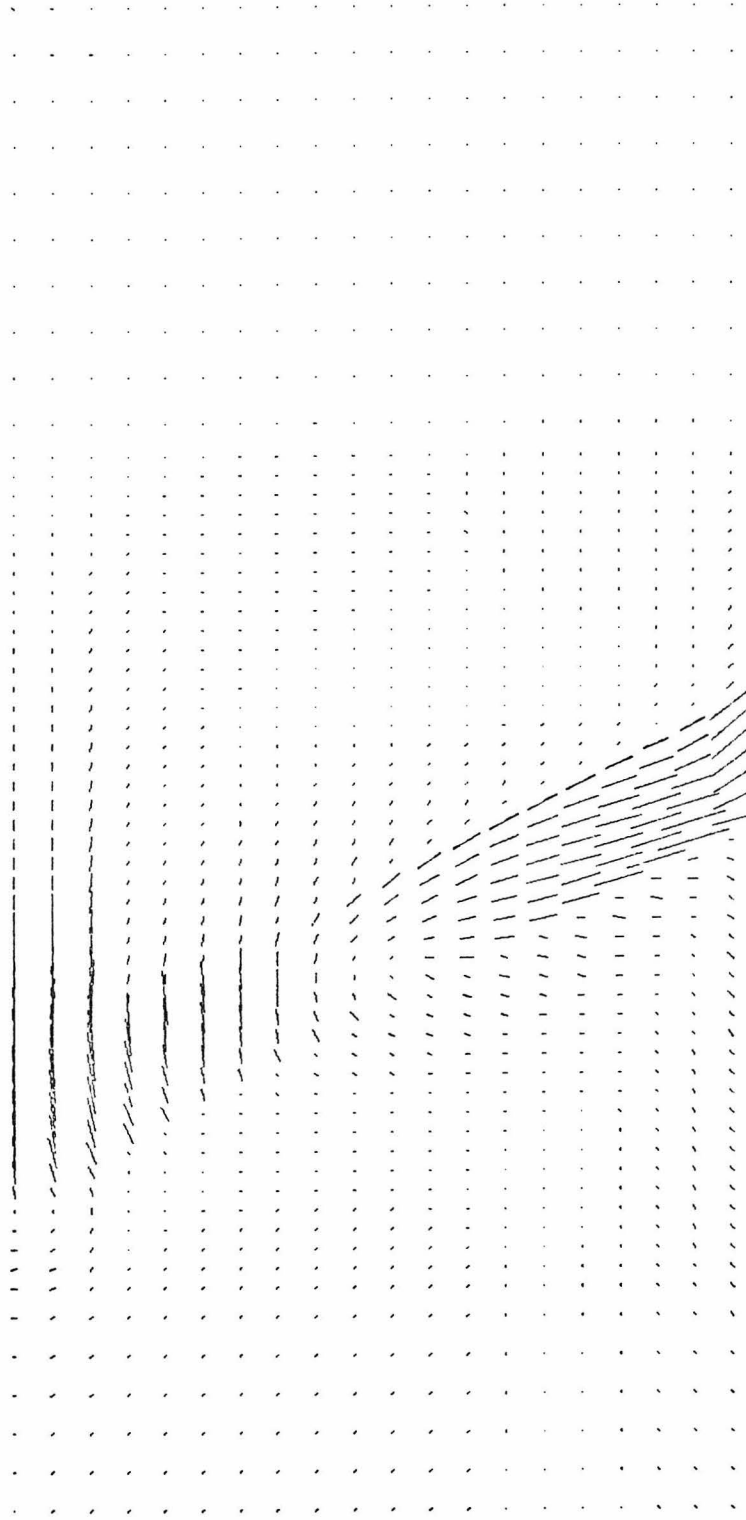
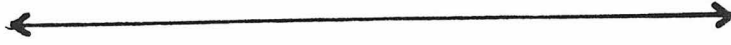
1 kbar



D23cV

5 cm/yr

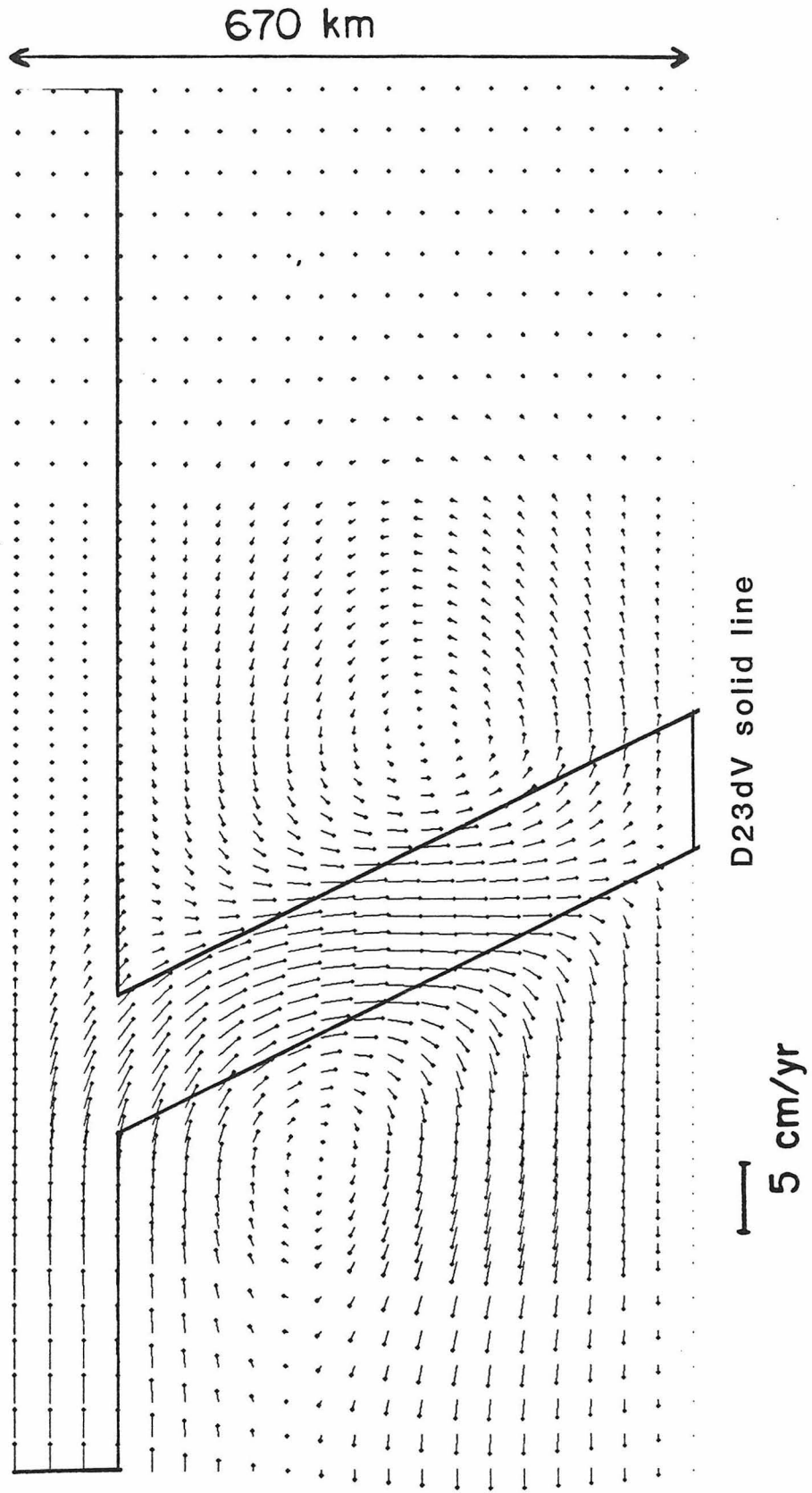
670 km



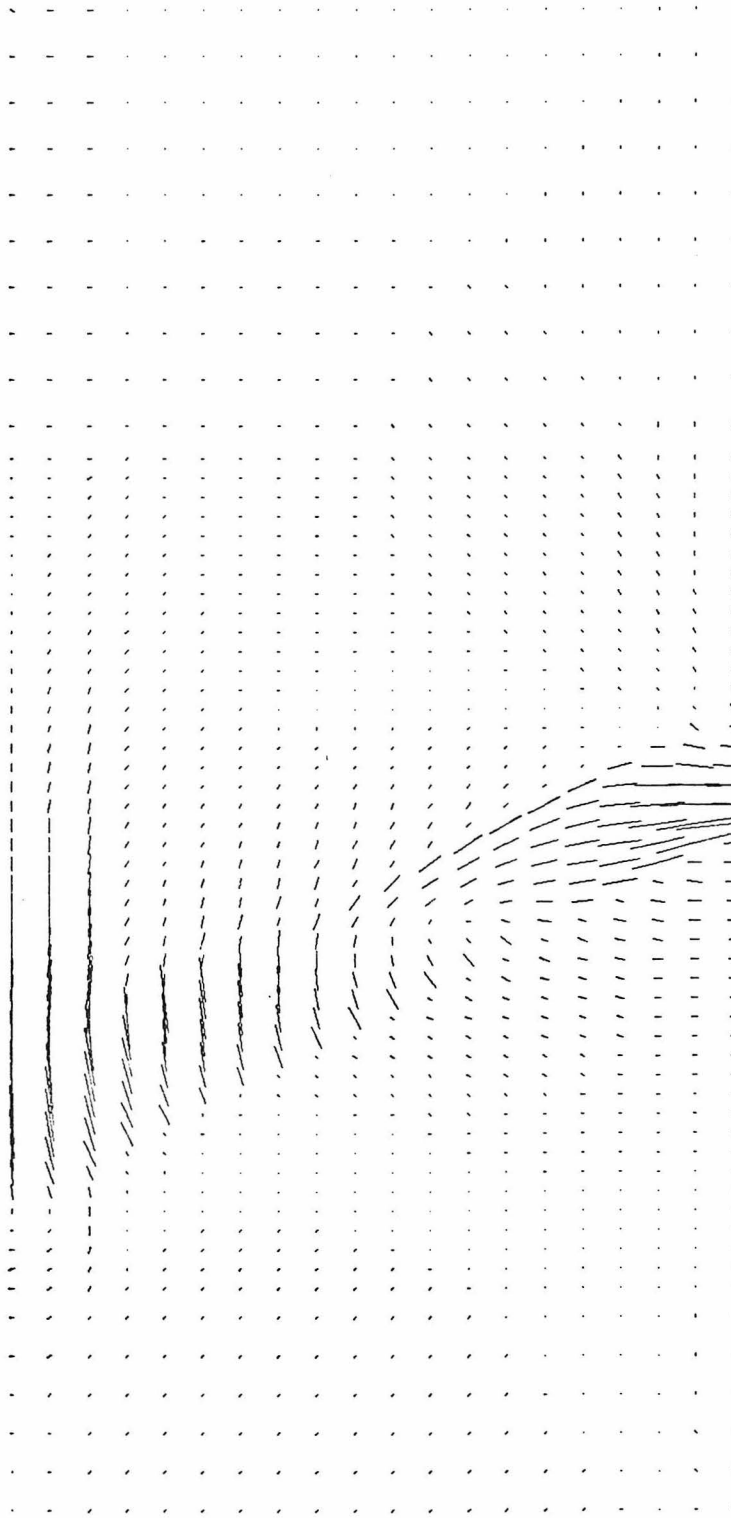
D23dS solid line



1 kbar



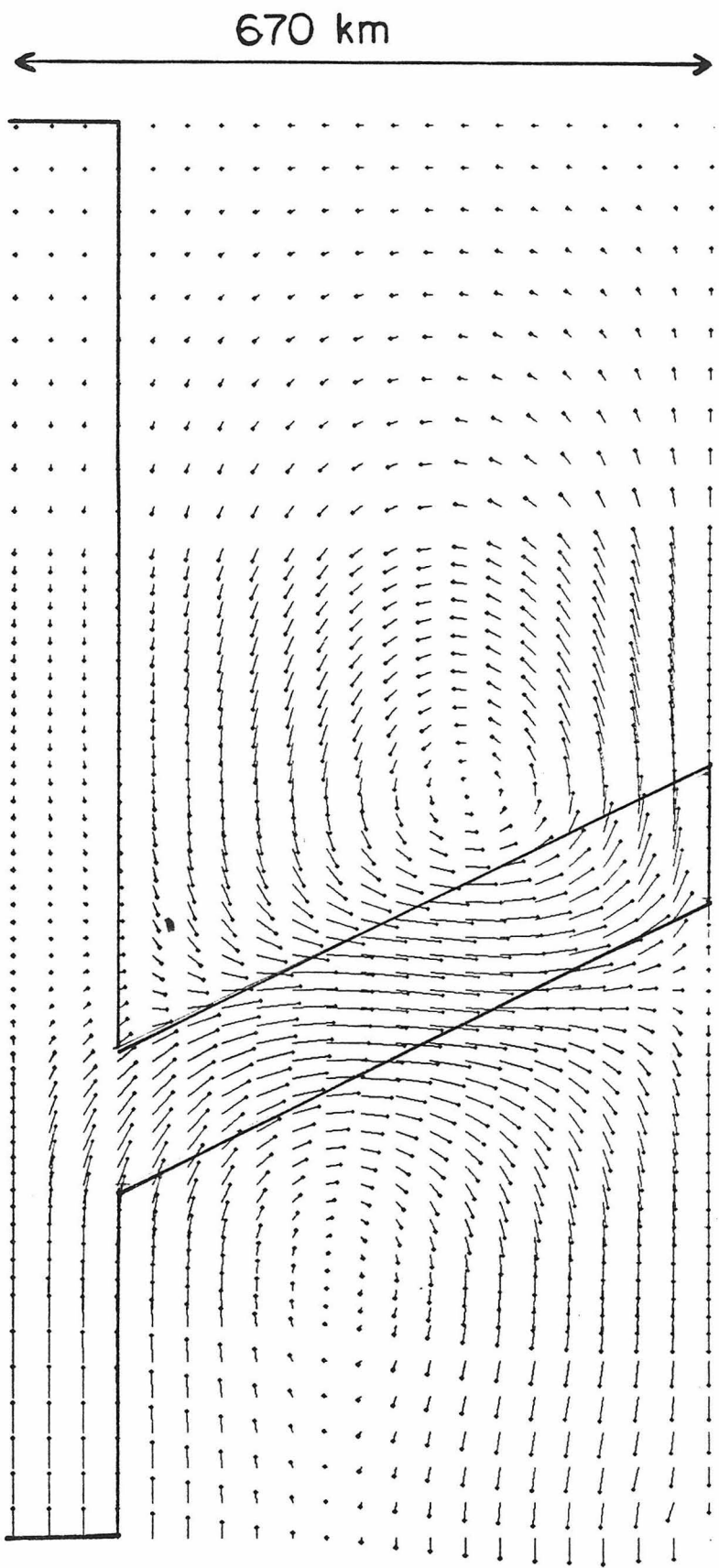
670 km



D23dS dashed line



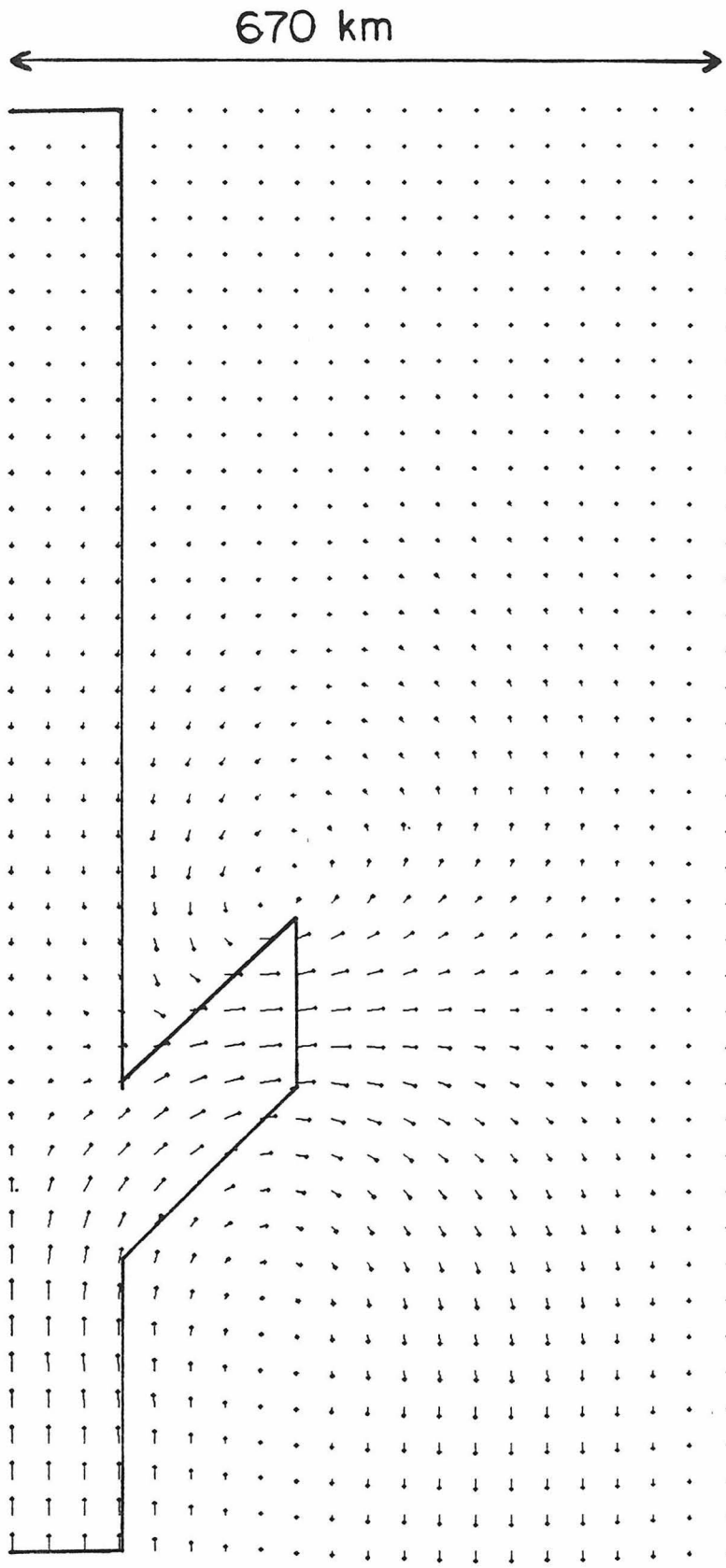
1 kbar



670 km

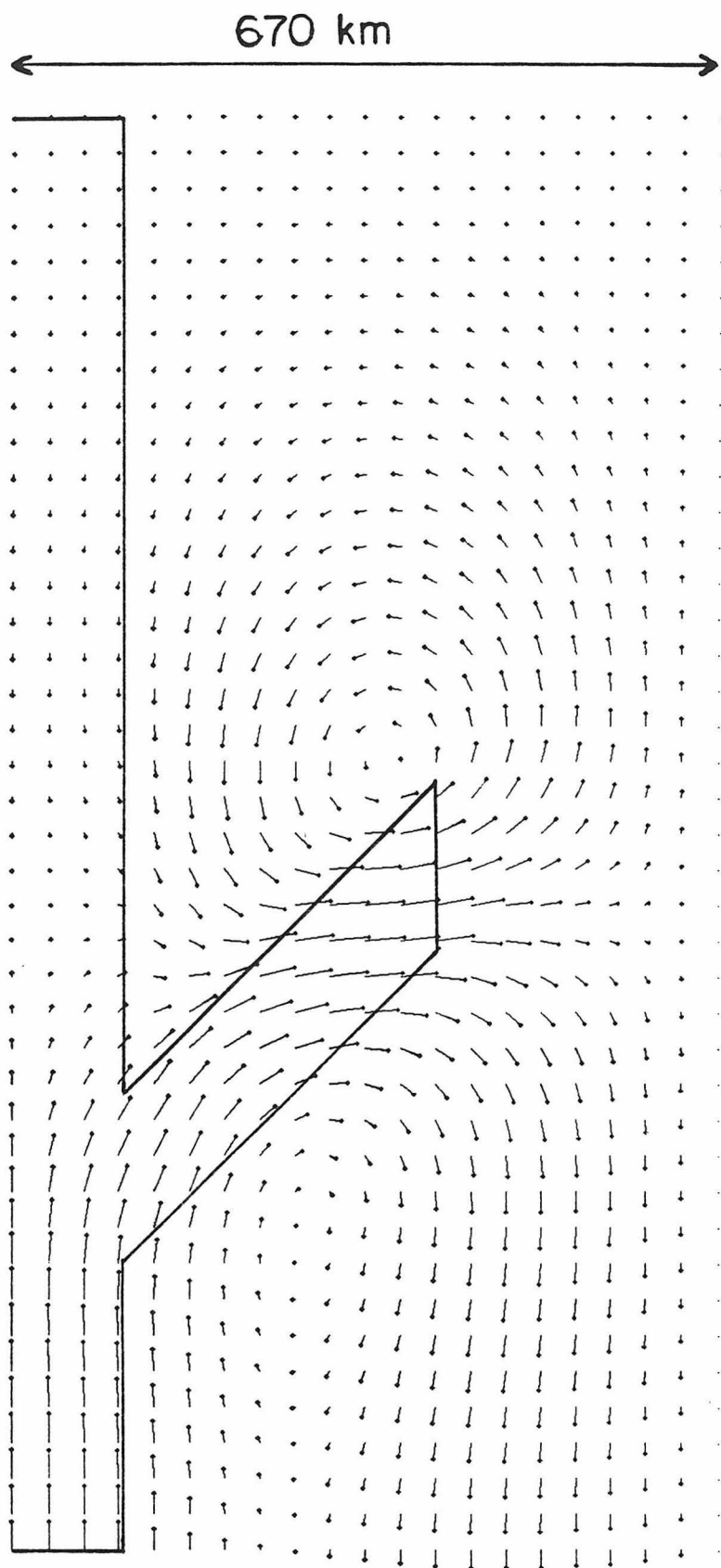
D23dV dashed line

5 cm/yr



D25aV

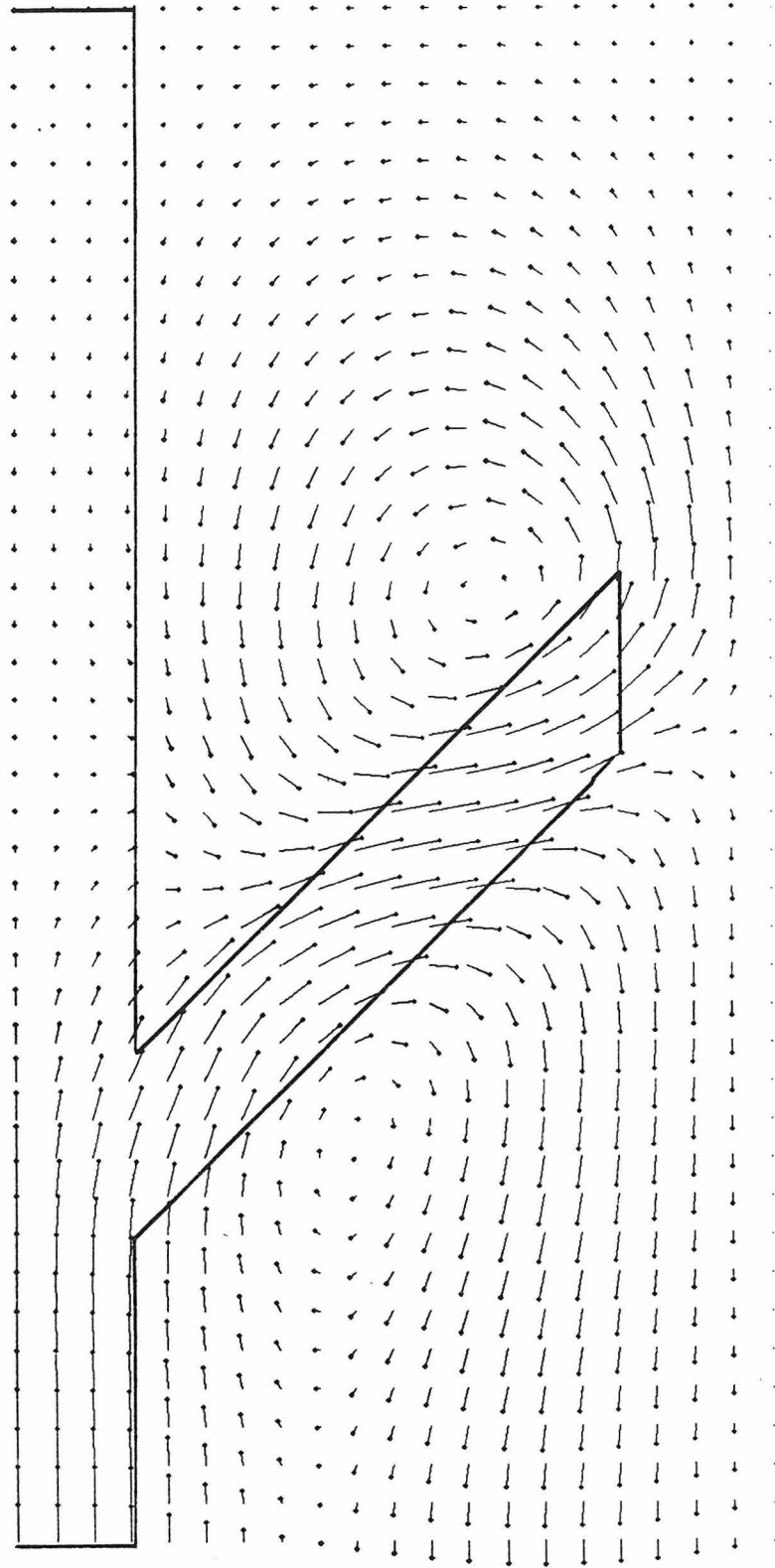
5 cm/yr



D25bV

5 cm/yr

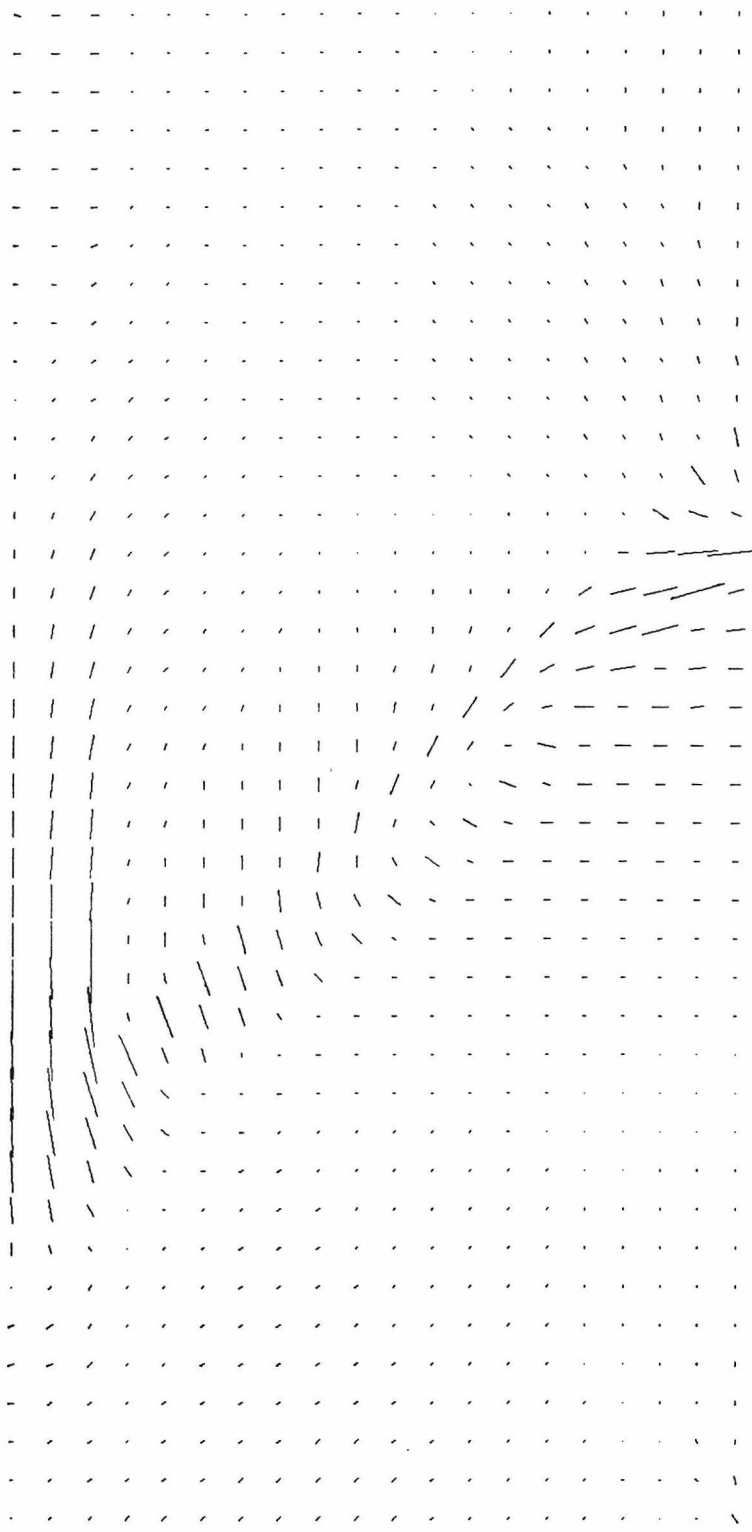
670 km



D25cV

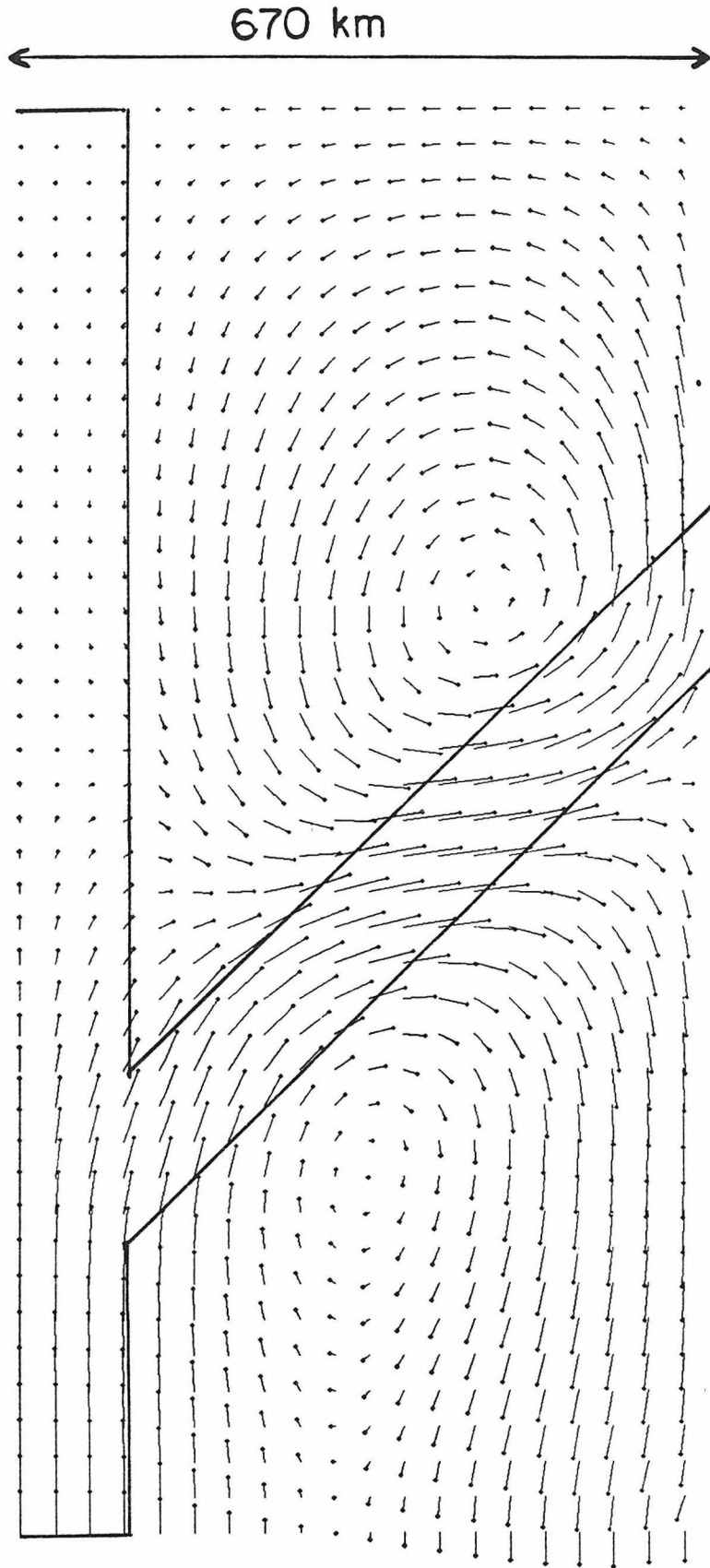
5 cm/yr

670 km



D25dS dashed line

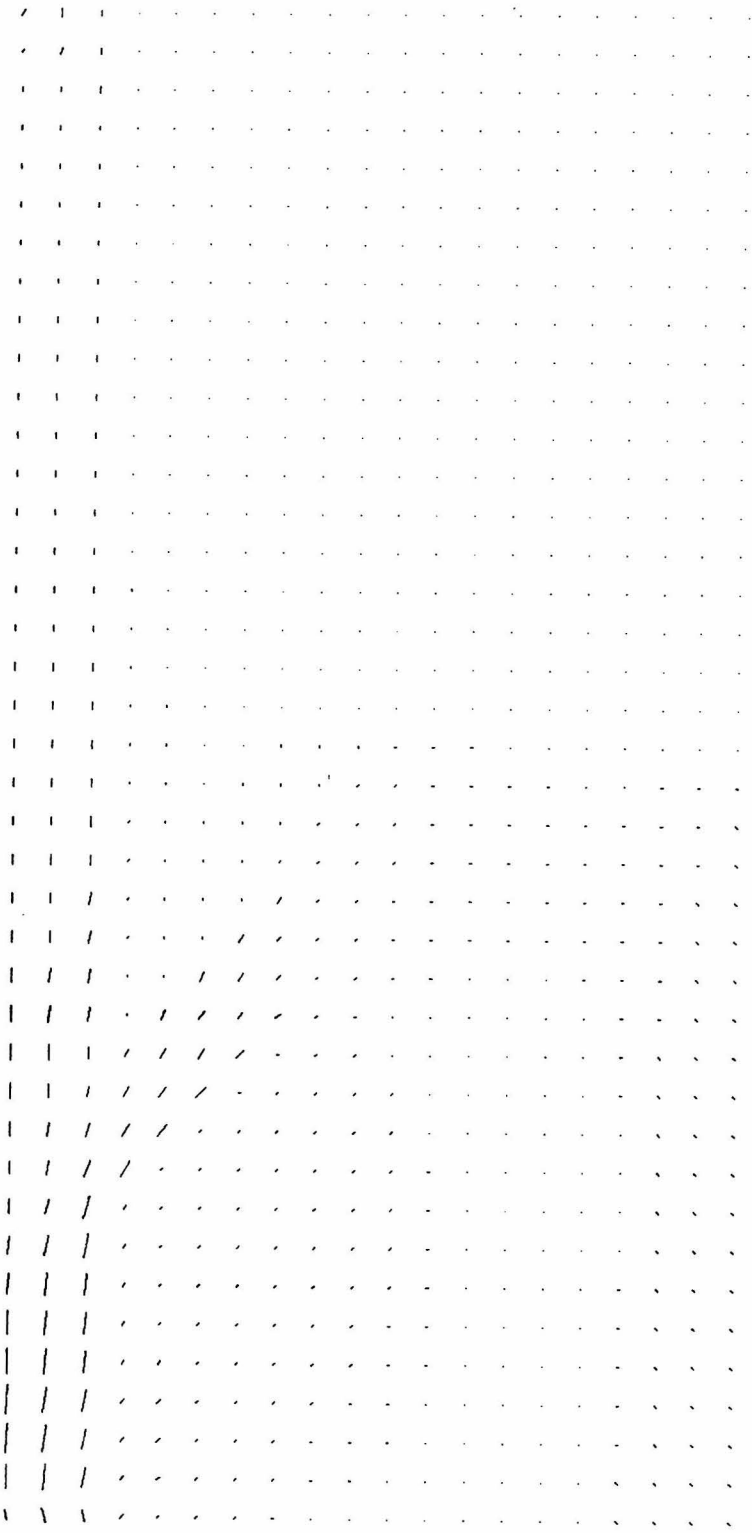
—
| kbar



D25dV dashed line

5 cm/yr

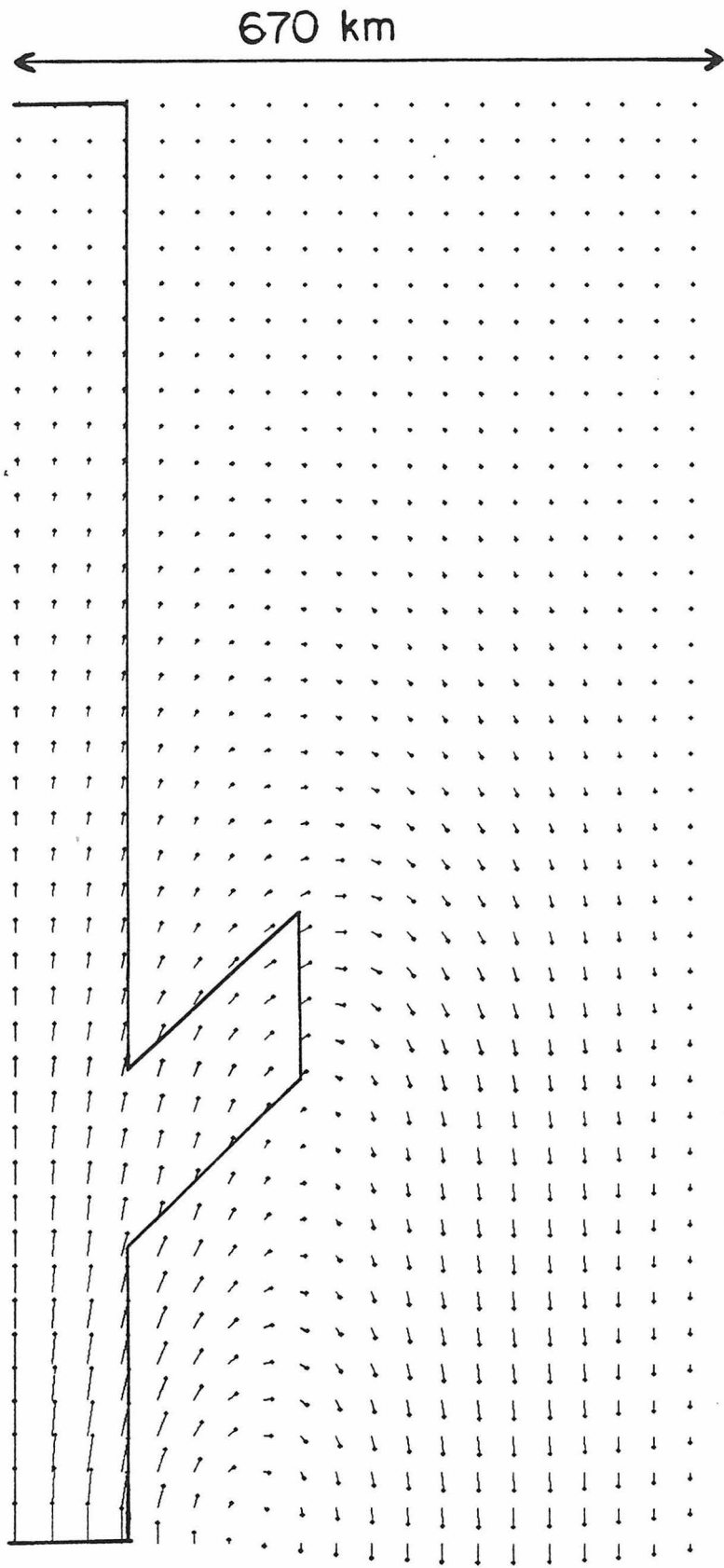
670 km



D26S slab extending to 270 km



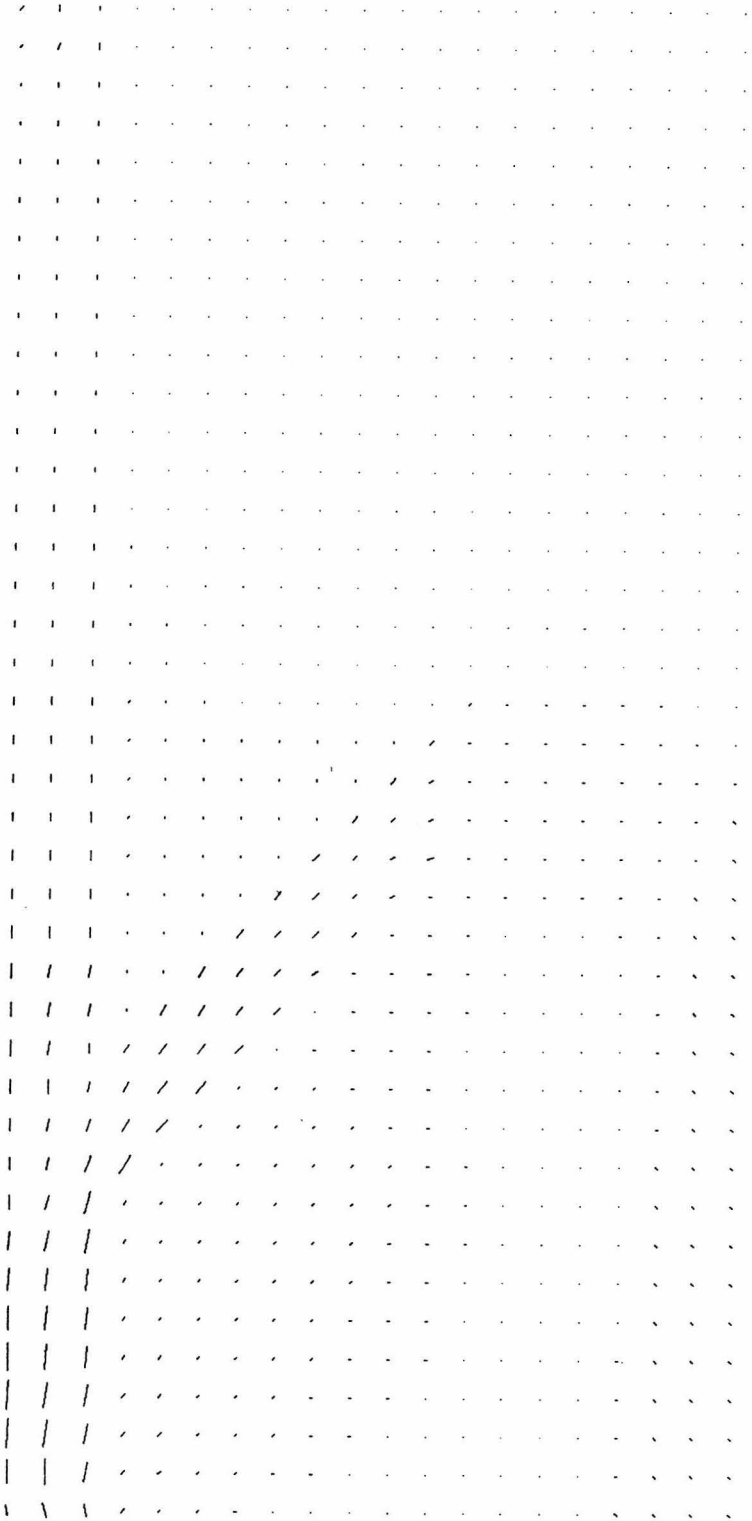
1 kbar



D26V slab extending to 270 km

5 cm/yr

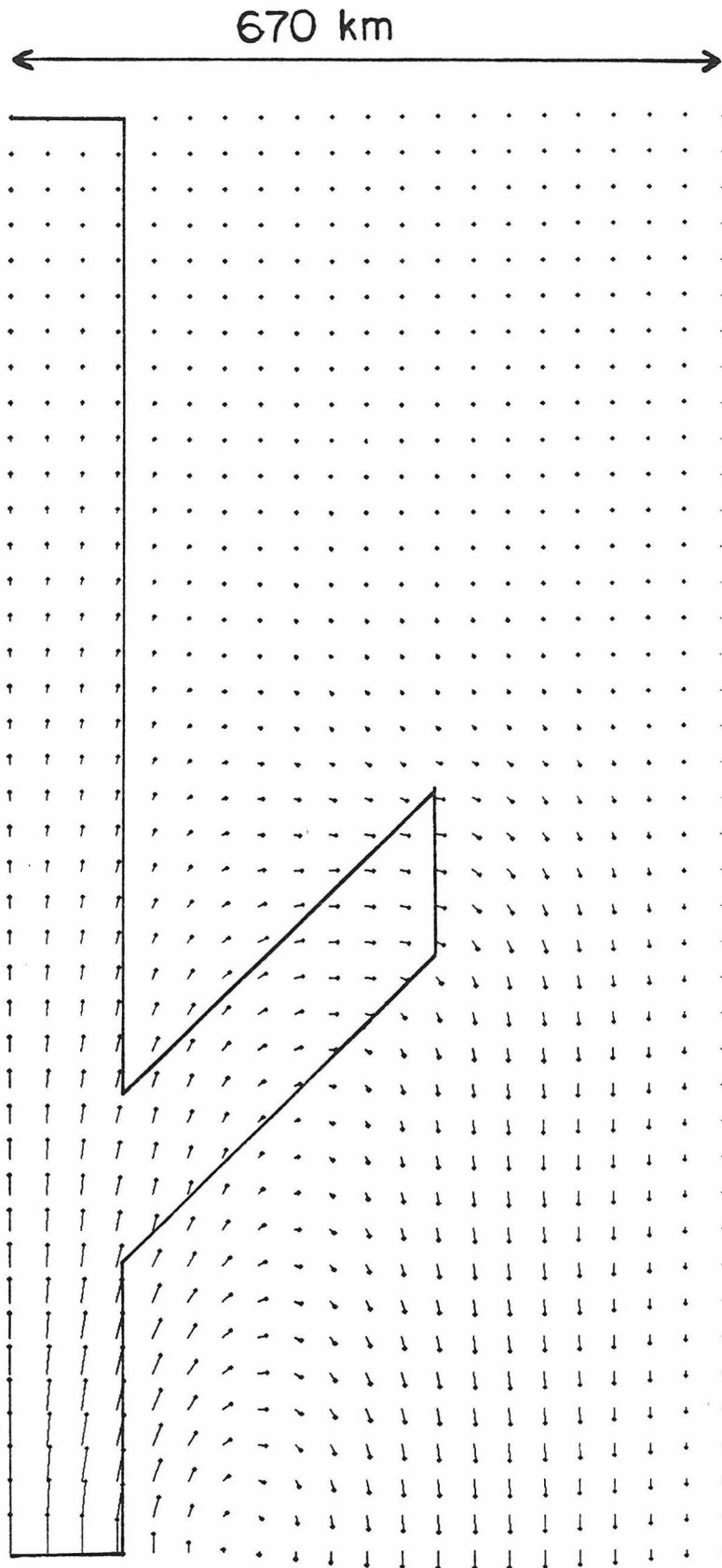
670 km



D26S slab extending to 400 km

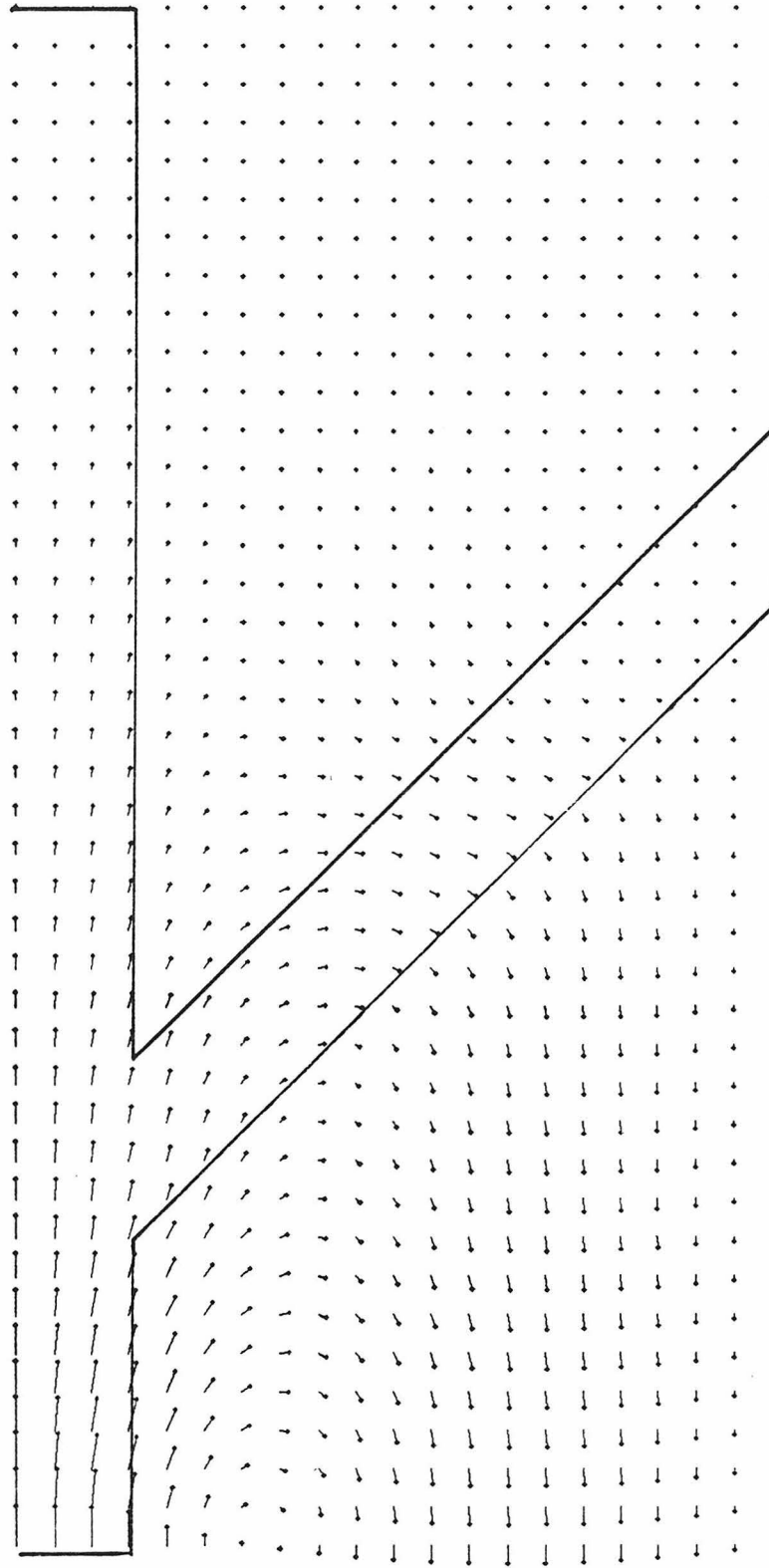


1 kbar



5 cm/yr
D26V slab extending to 400 km

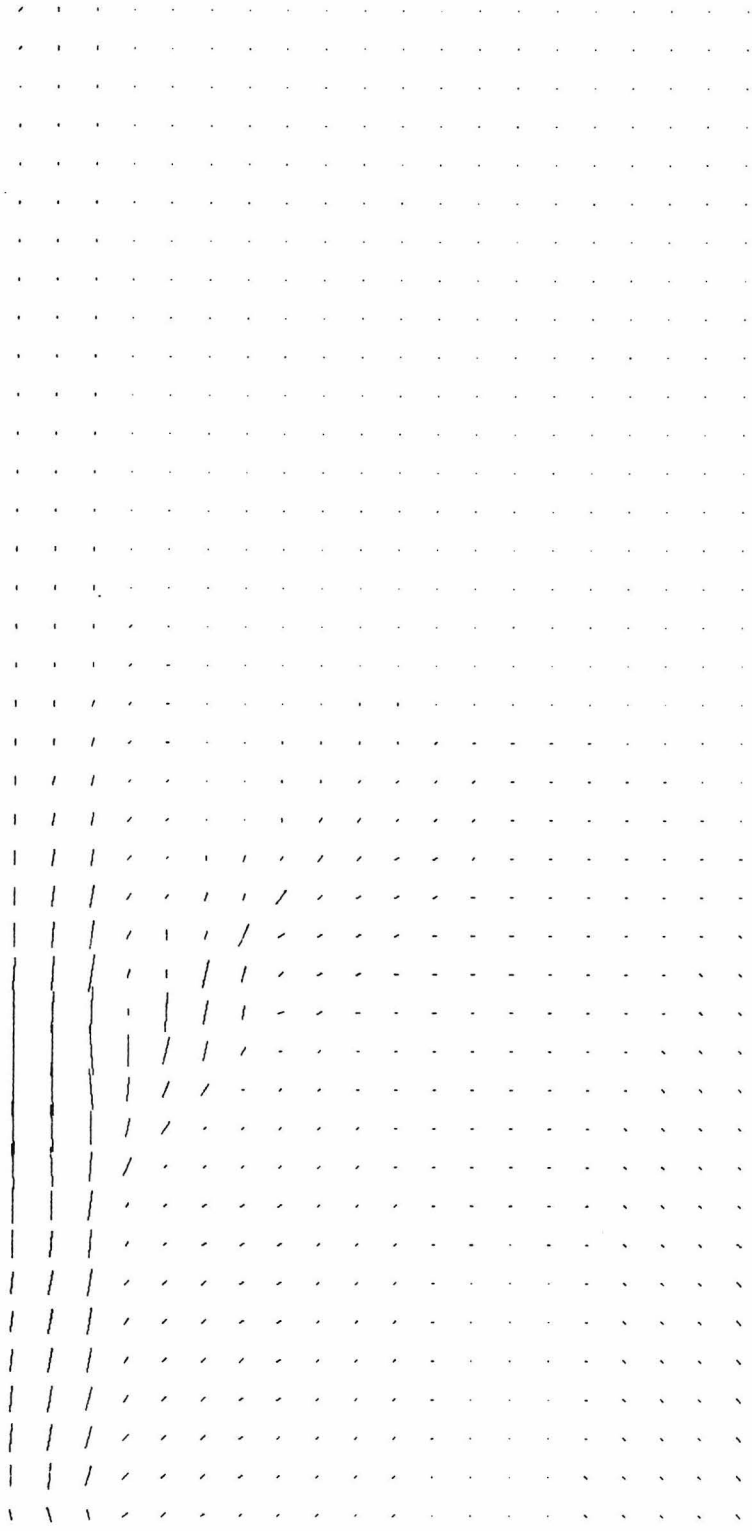
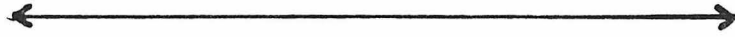
670 km



D26V slab extending to 670 km

5 cm/yr

670 km

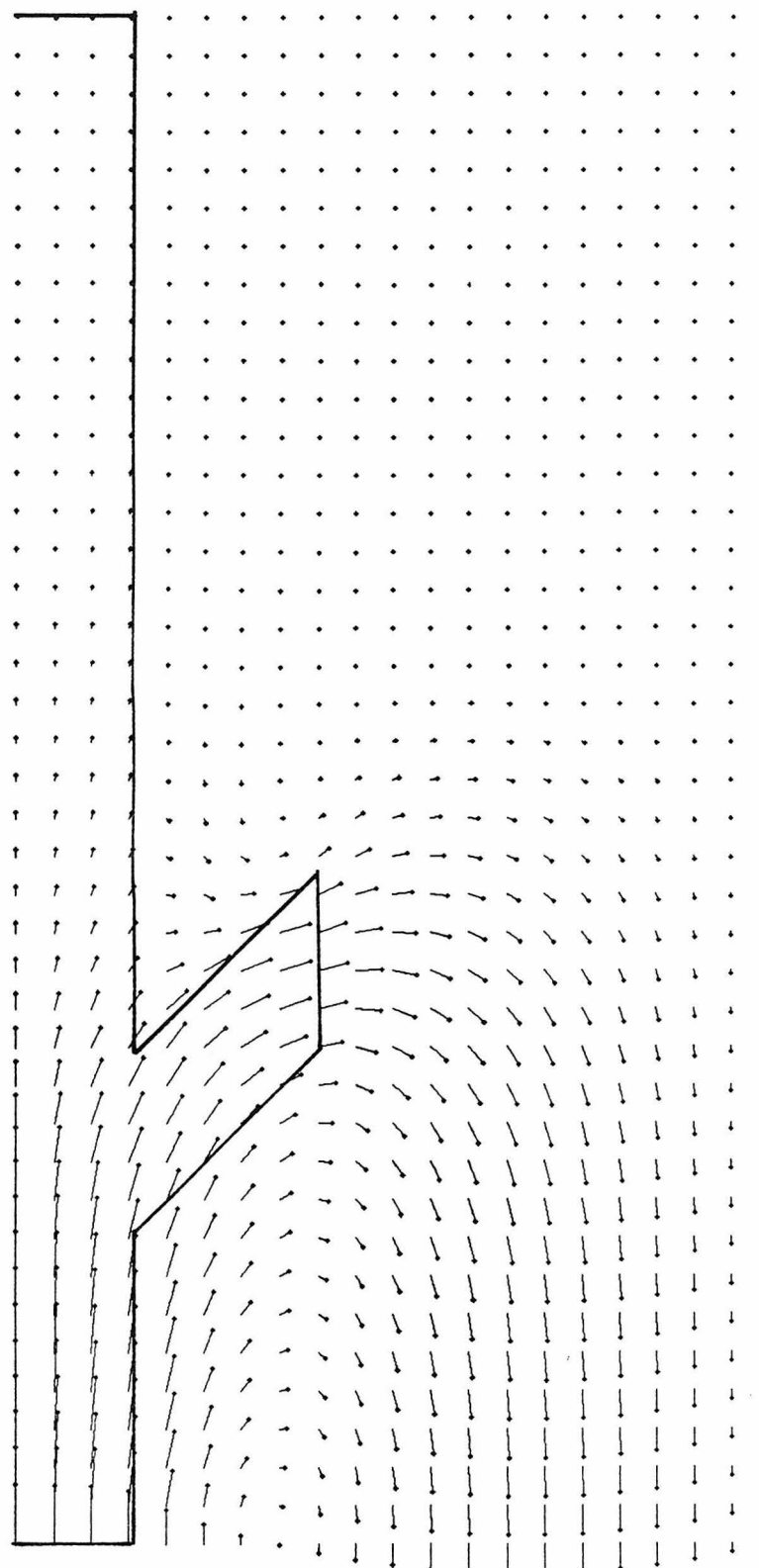


D28S A



1 kbar

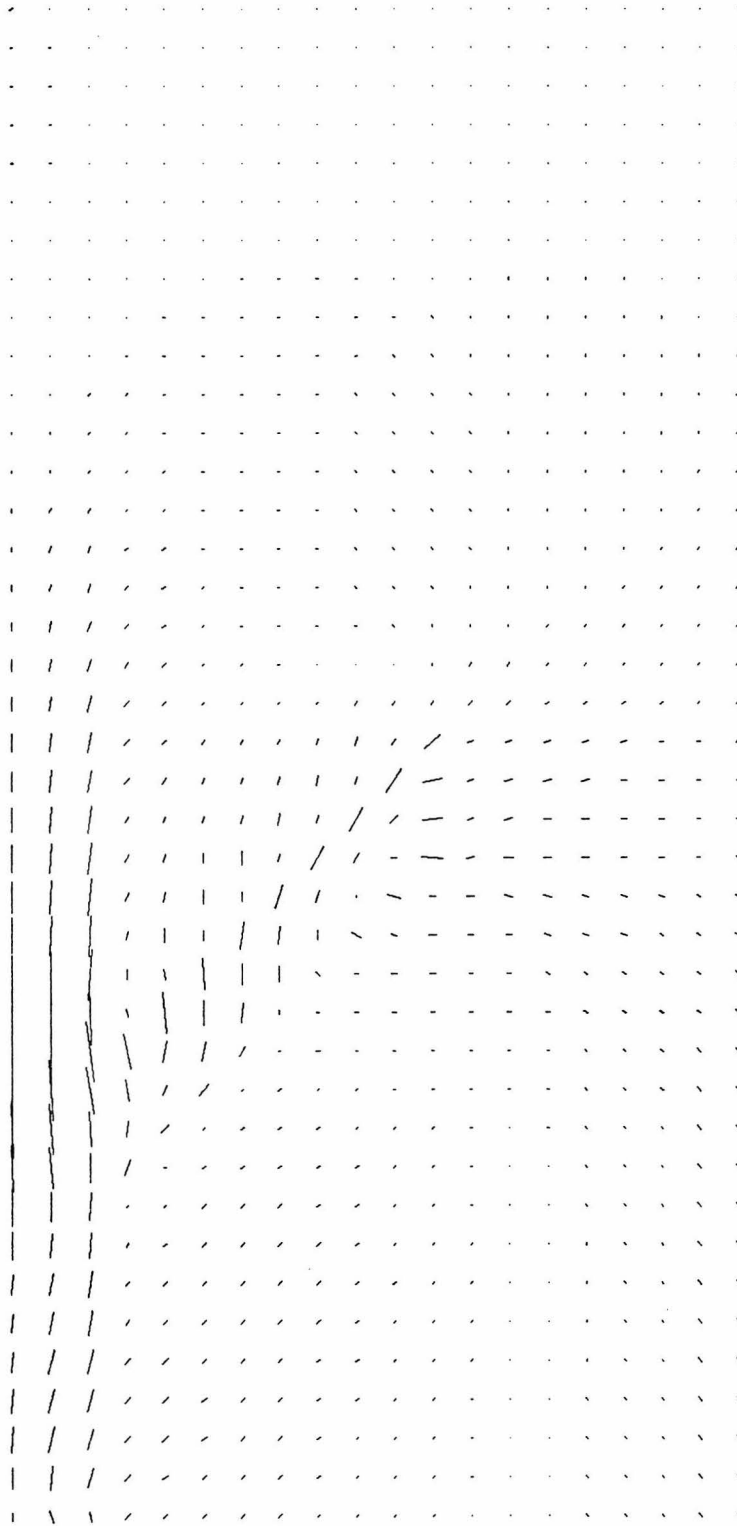
670 km



D28V A

5 cm/yr

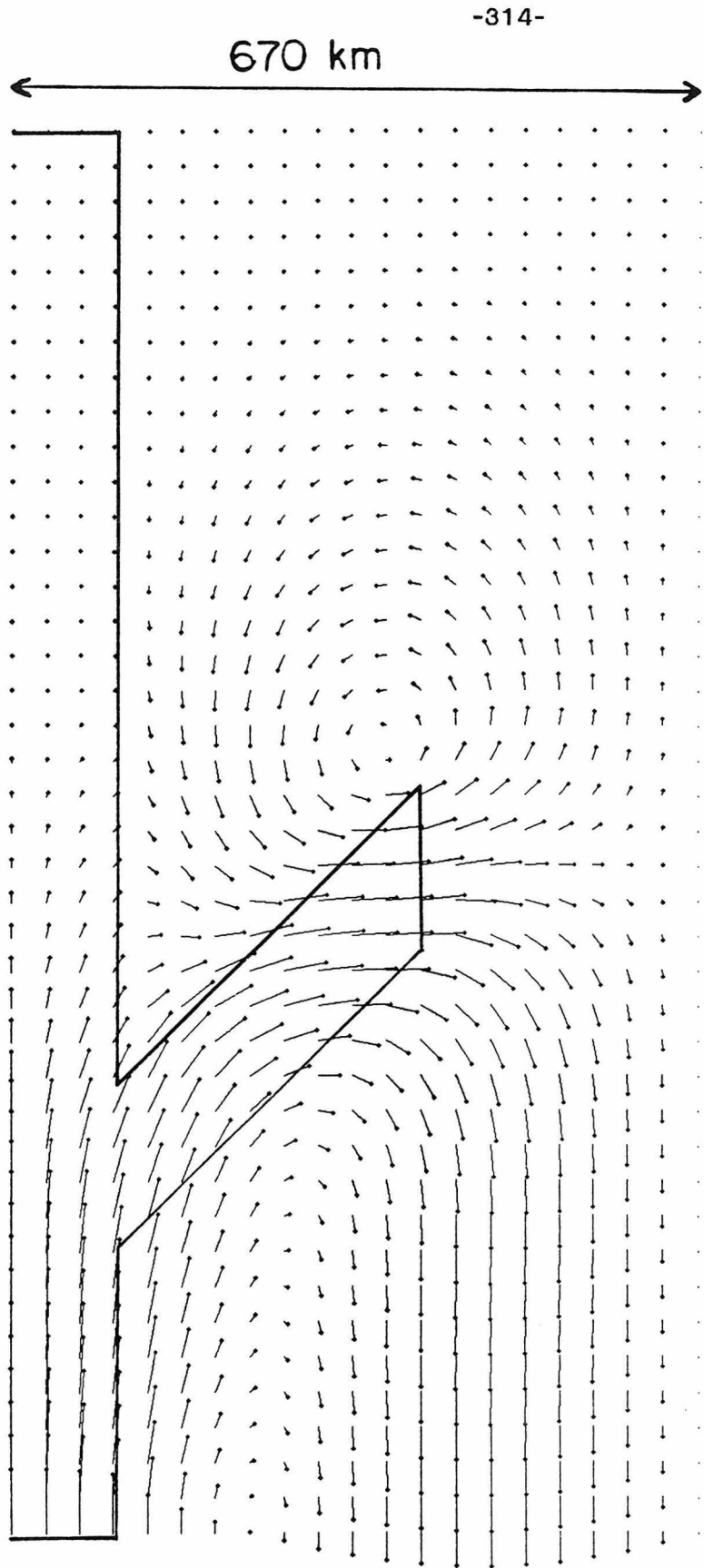
670 km



D28S B



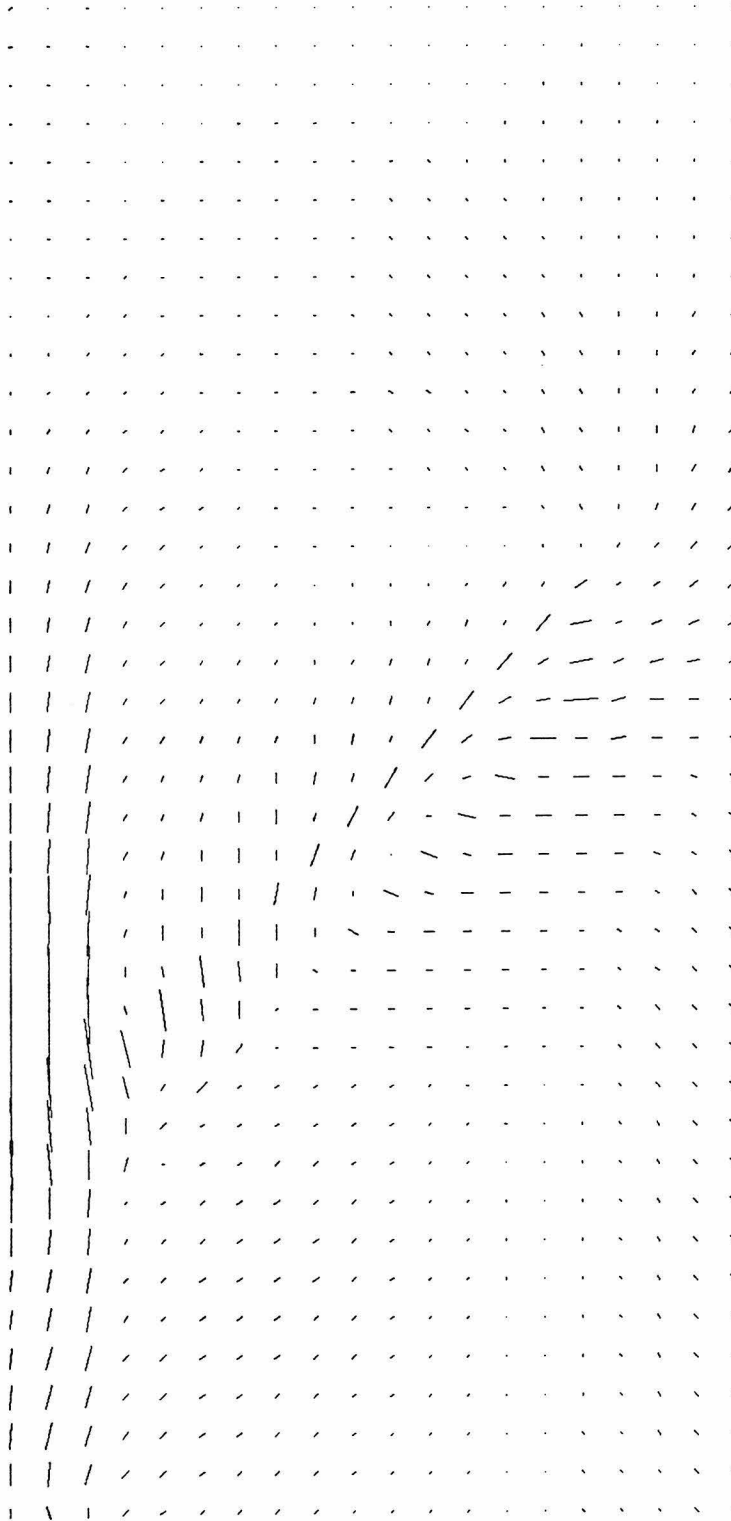
1 kbar



D28V B

5 cm/yr

670 km

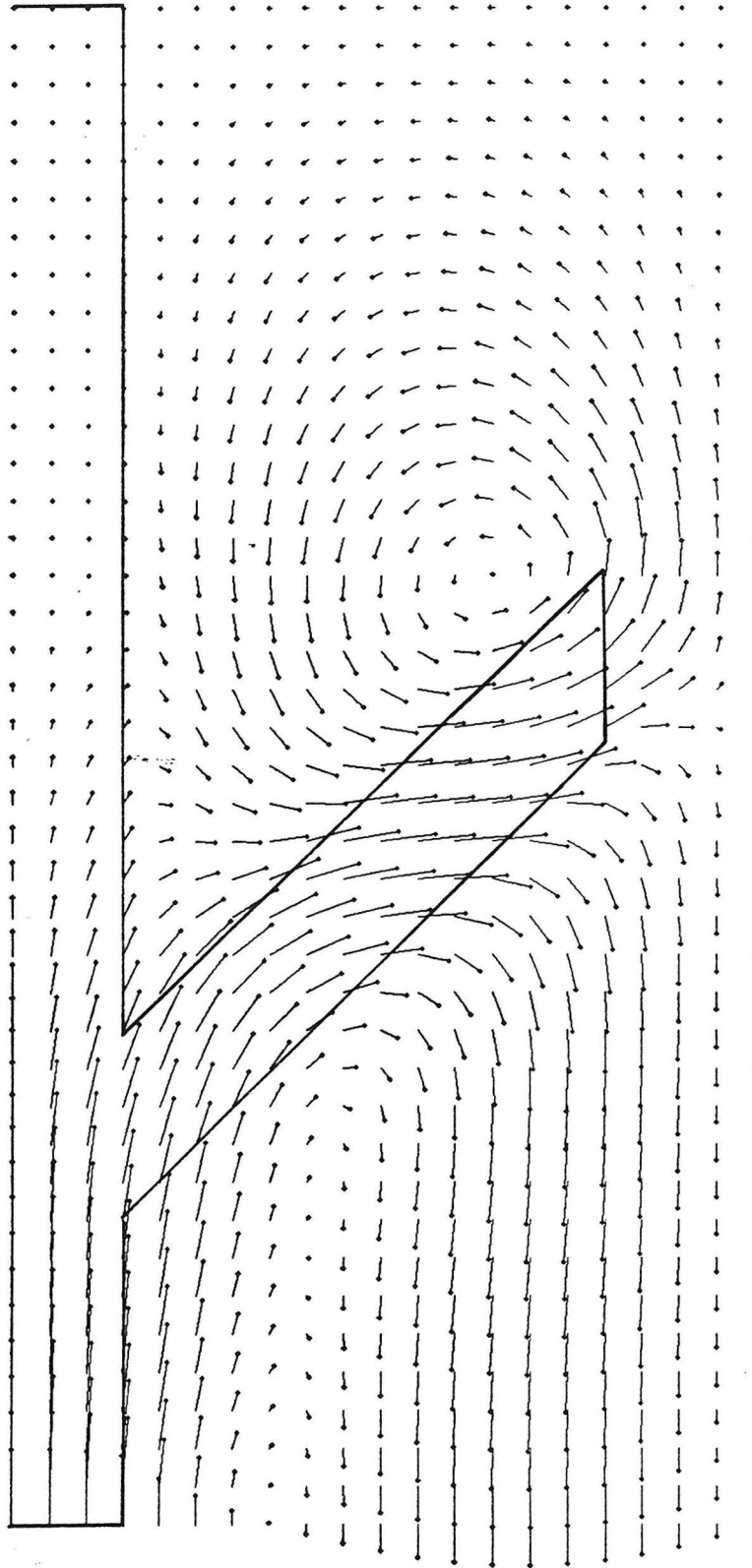


D28S C



1 kbar

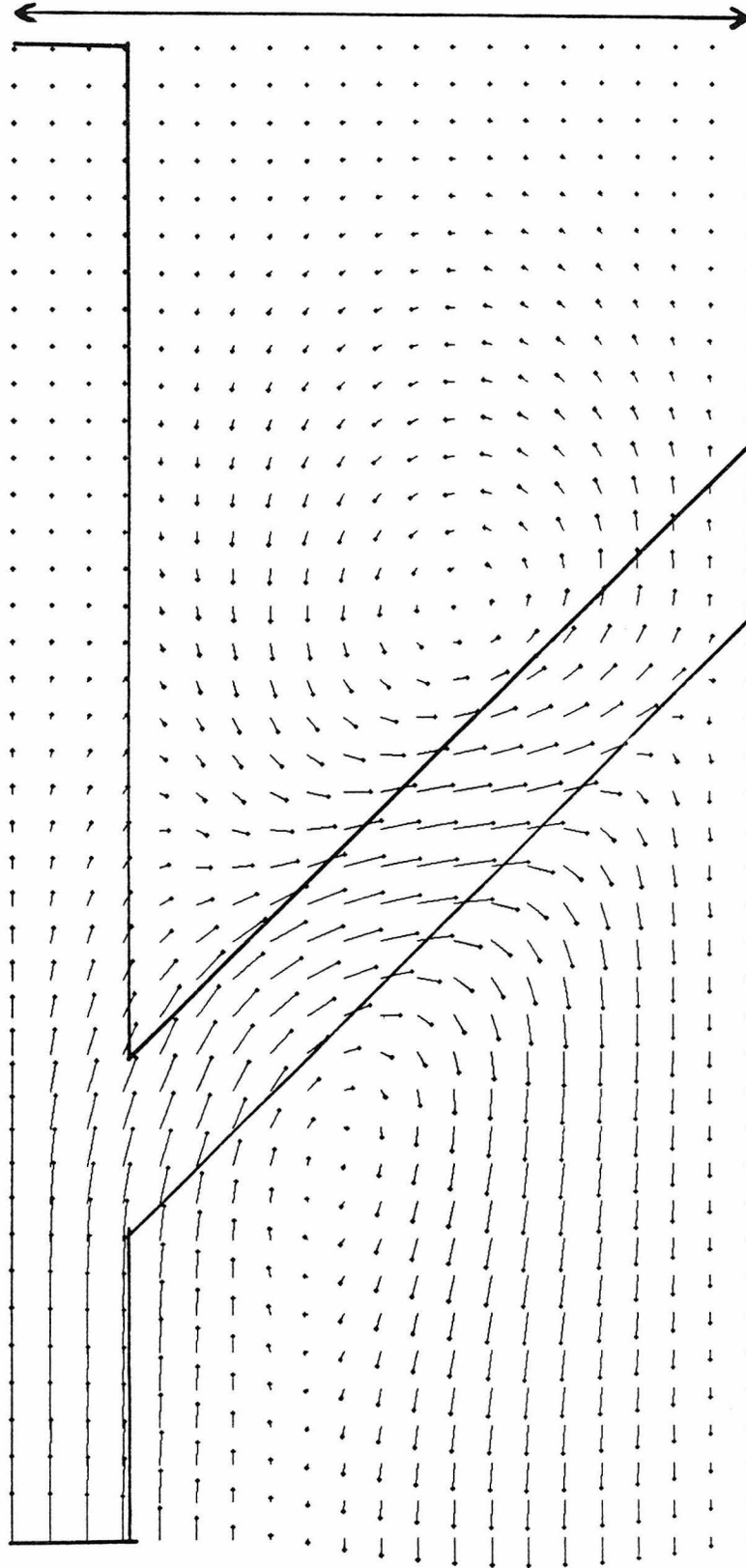
670 km



D28V C

5 cm/yr

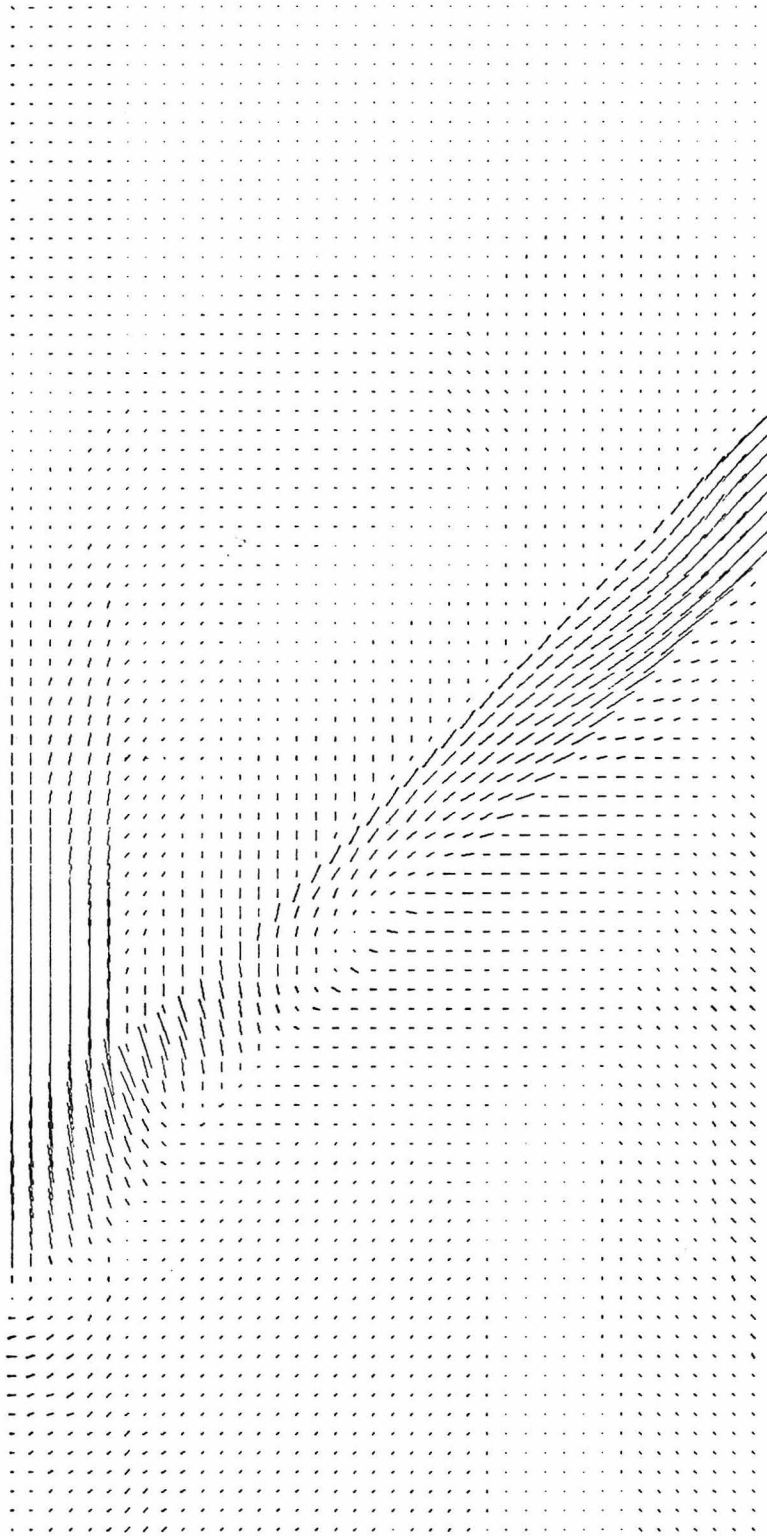
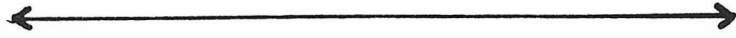
670 km



D28V D

5 cm/yr

670 km

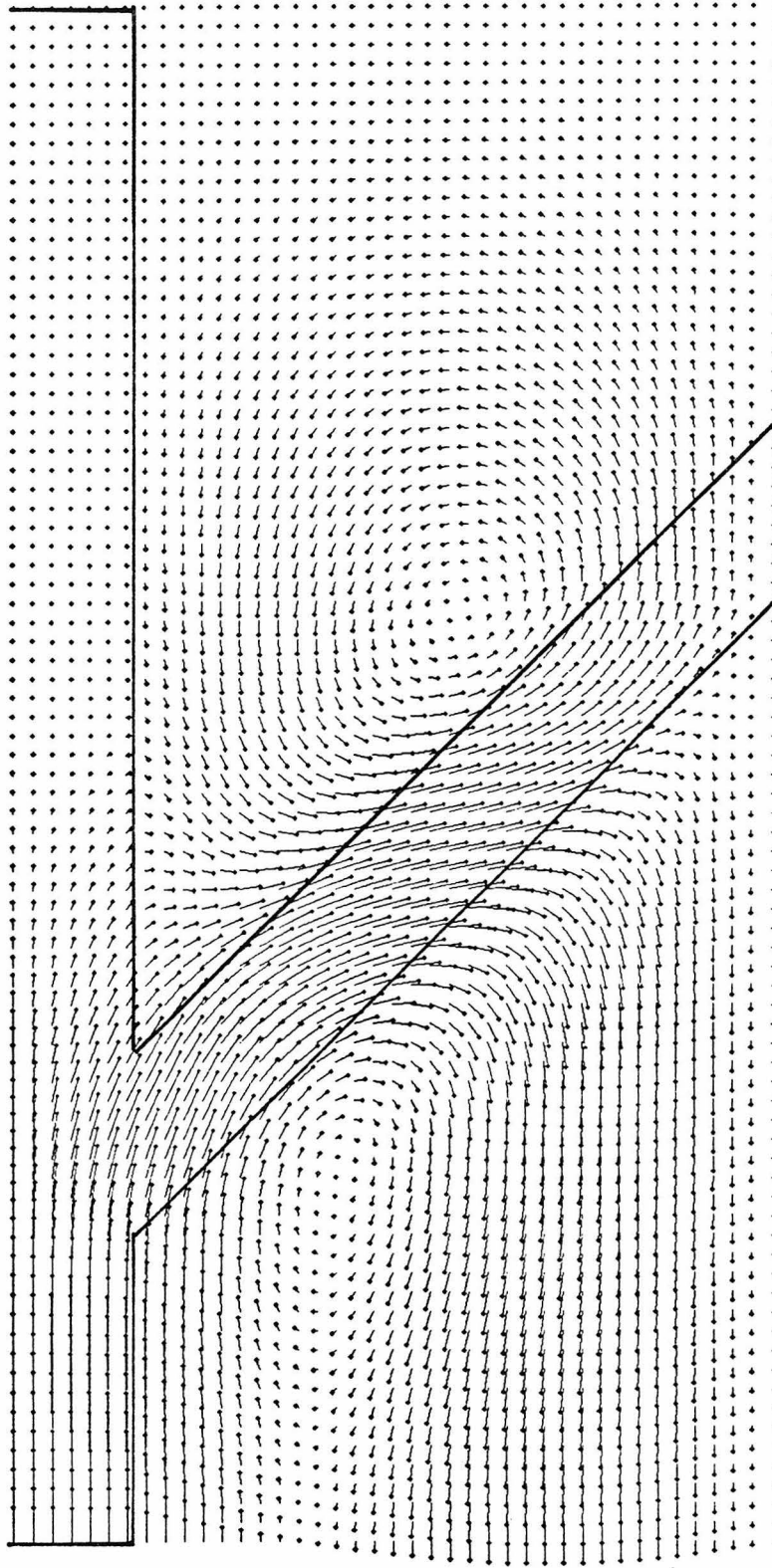


D30S dashed line



1 kbar

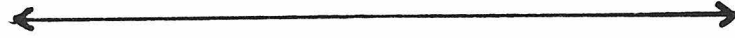
670 km



D30V dashed line

5 cm/yr

670 km

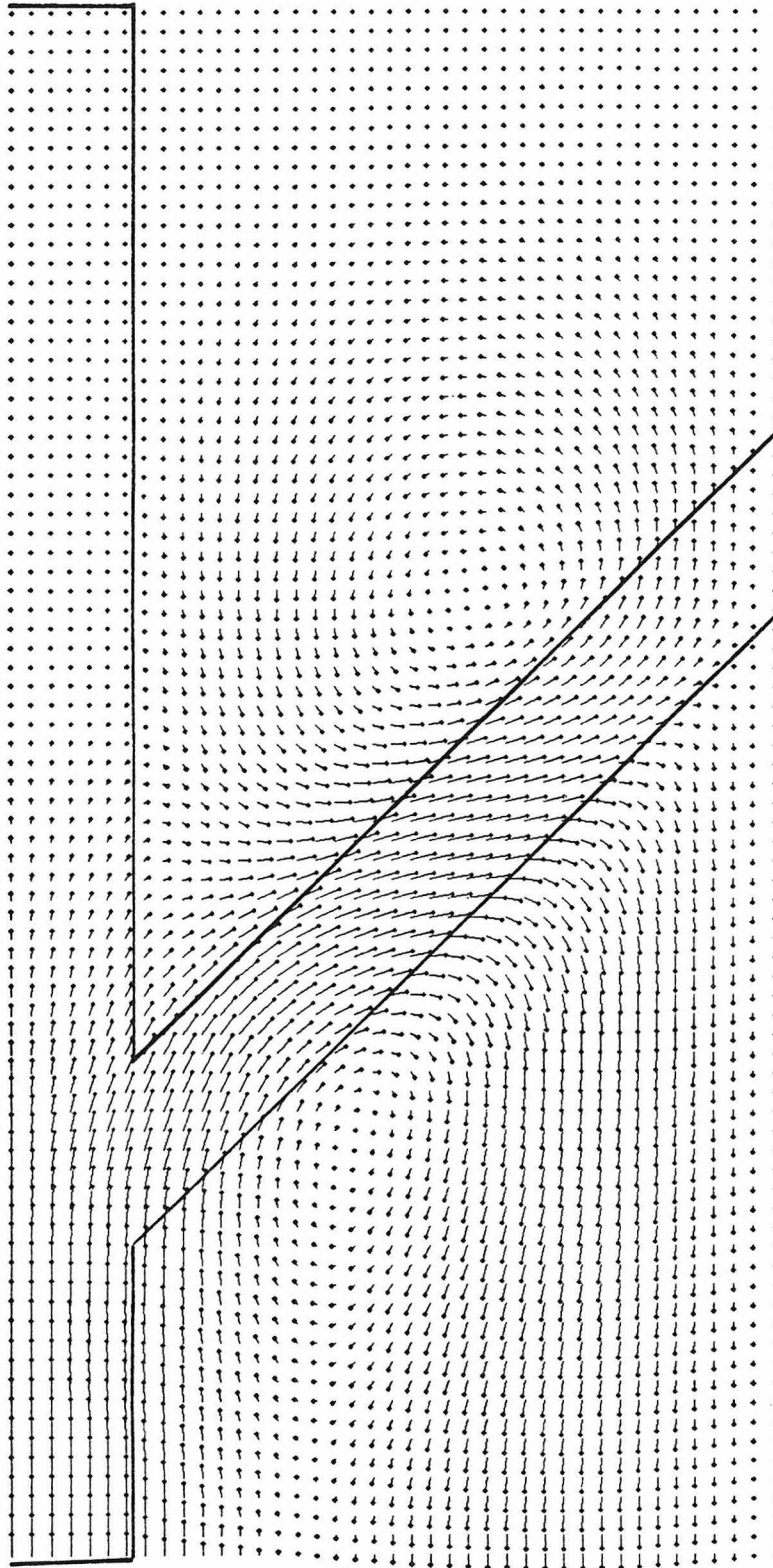


D30S solid line



1 kbar

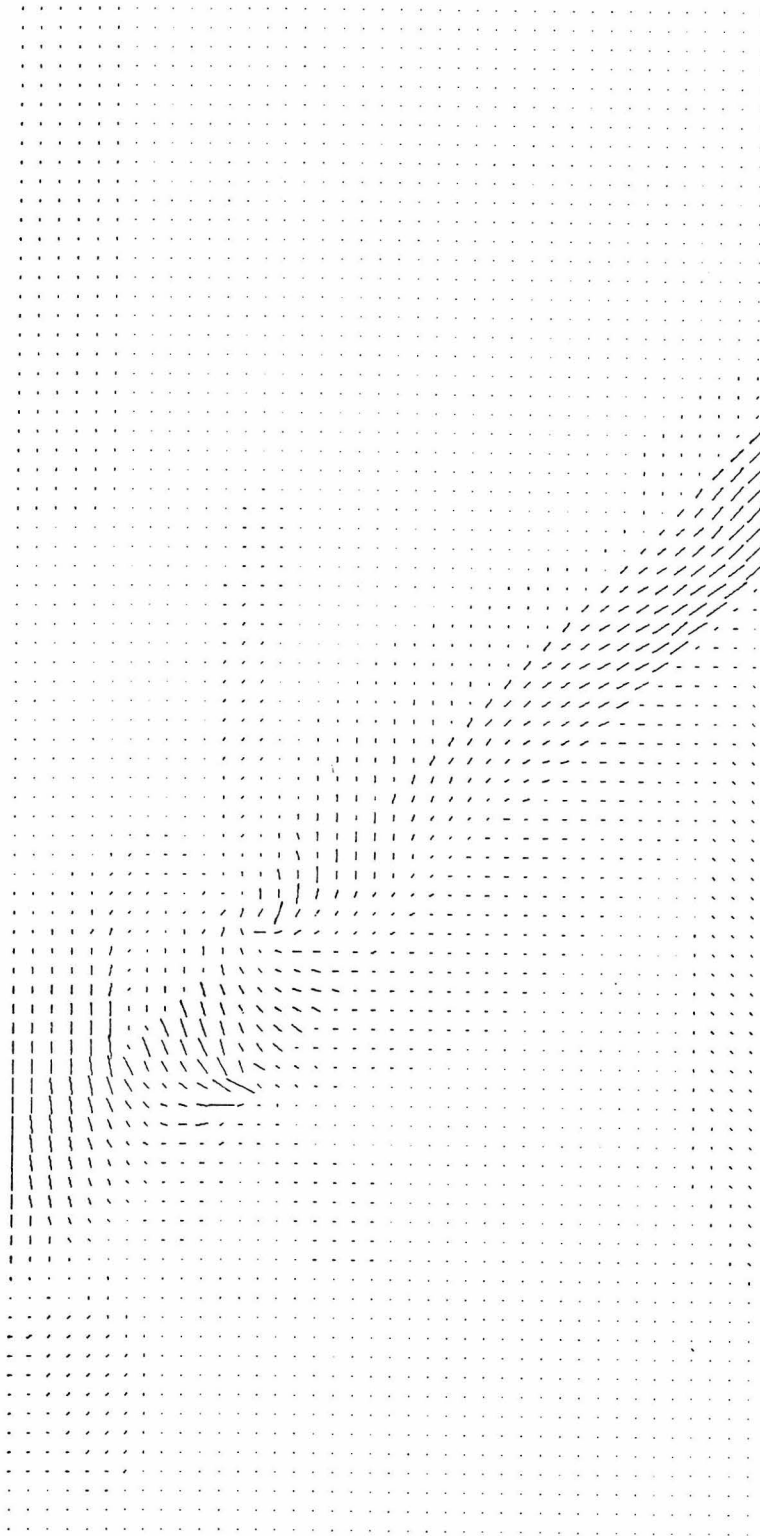
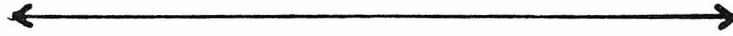
670 km



D30V solid line

5 cm/yr

670 km

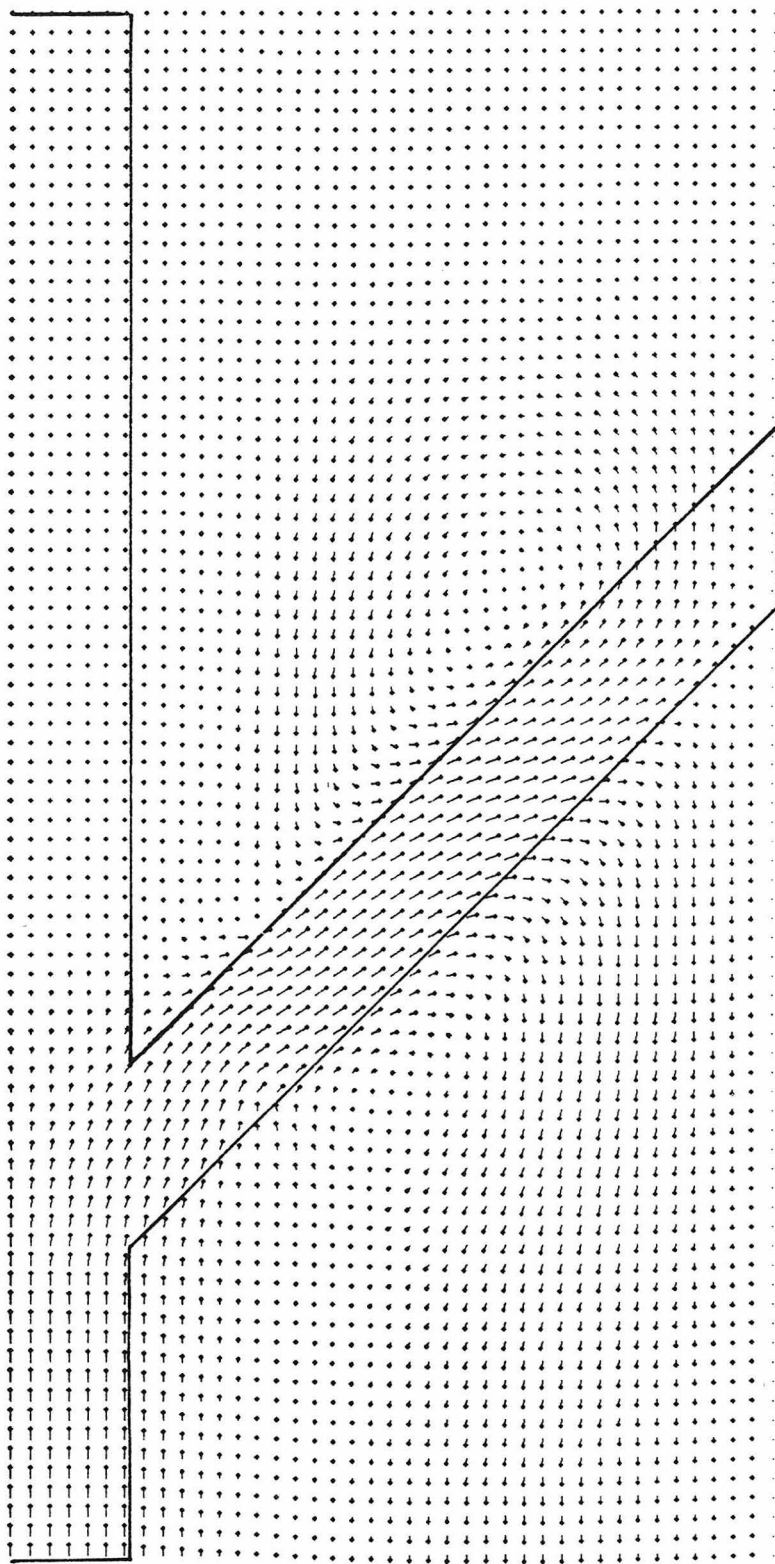


D31S



1 kbar

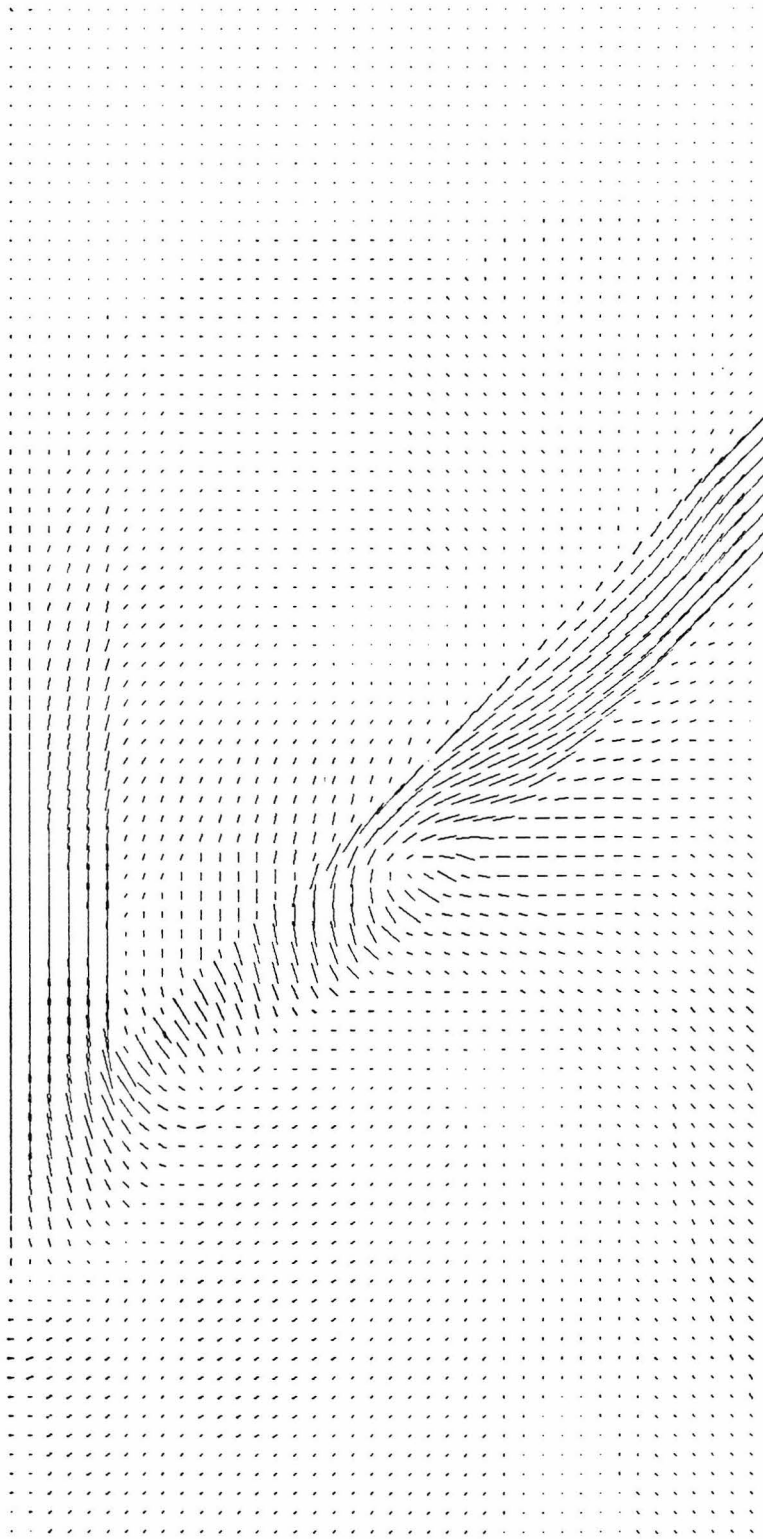
670 km



D31V

5 cm/yr

670 km

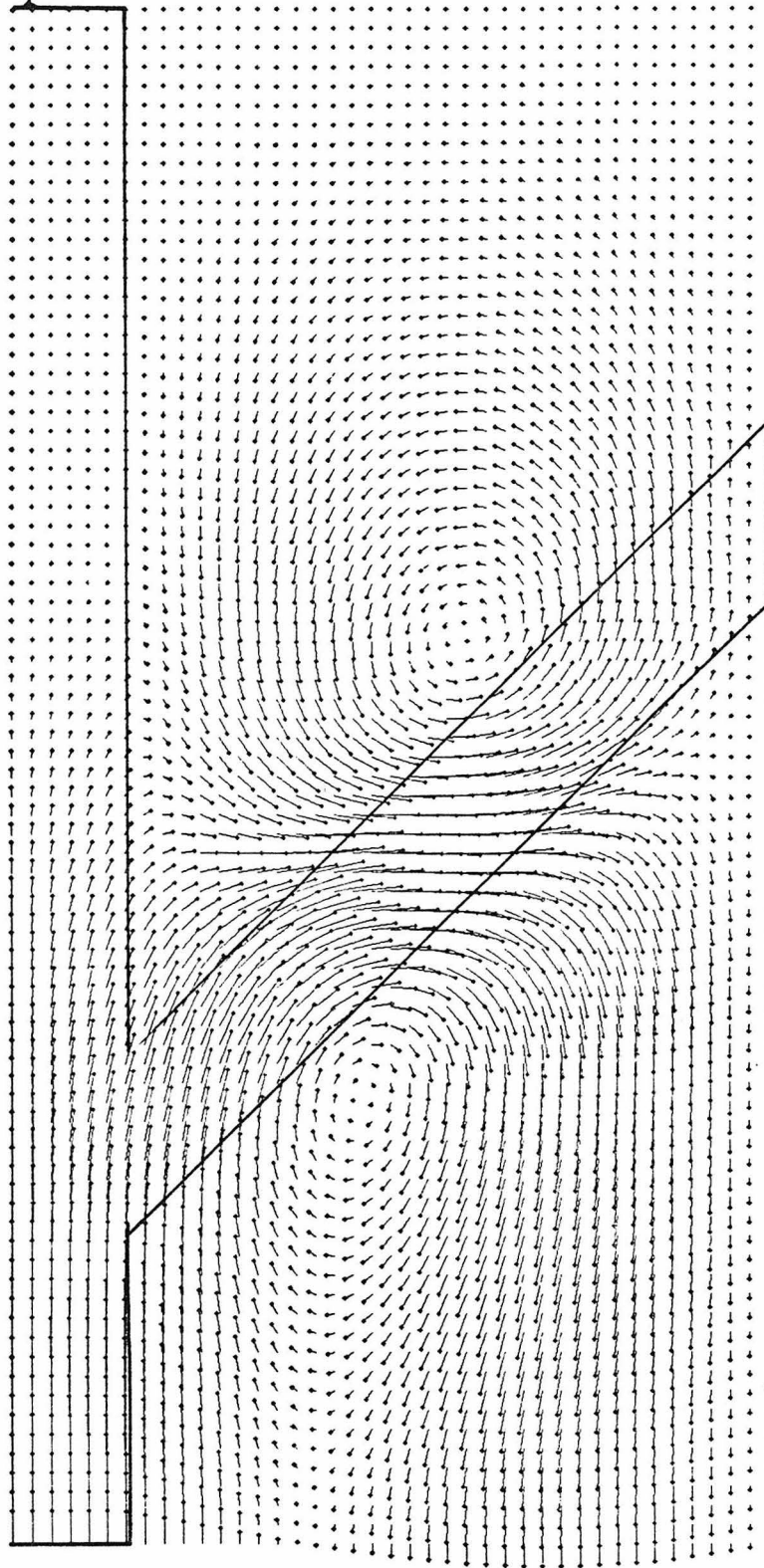
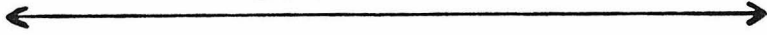


D32S A



1 kbar

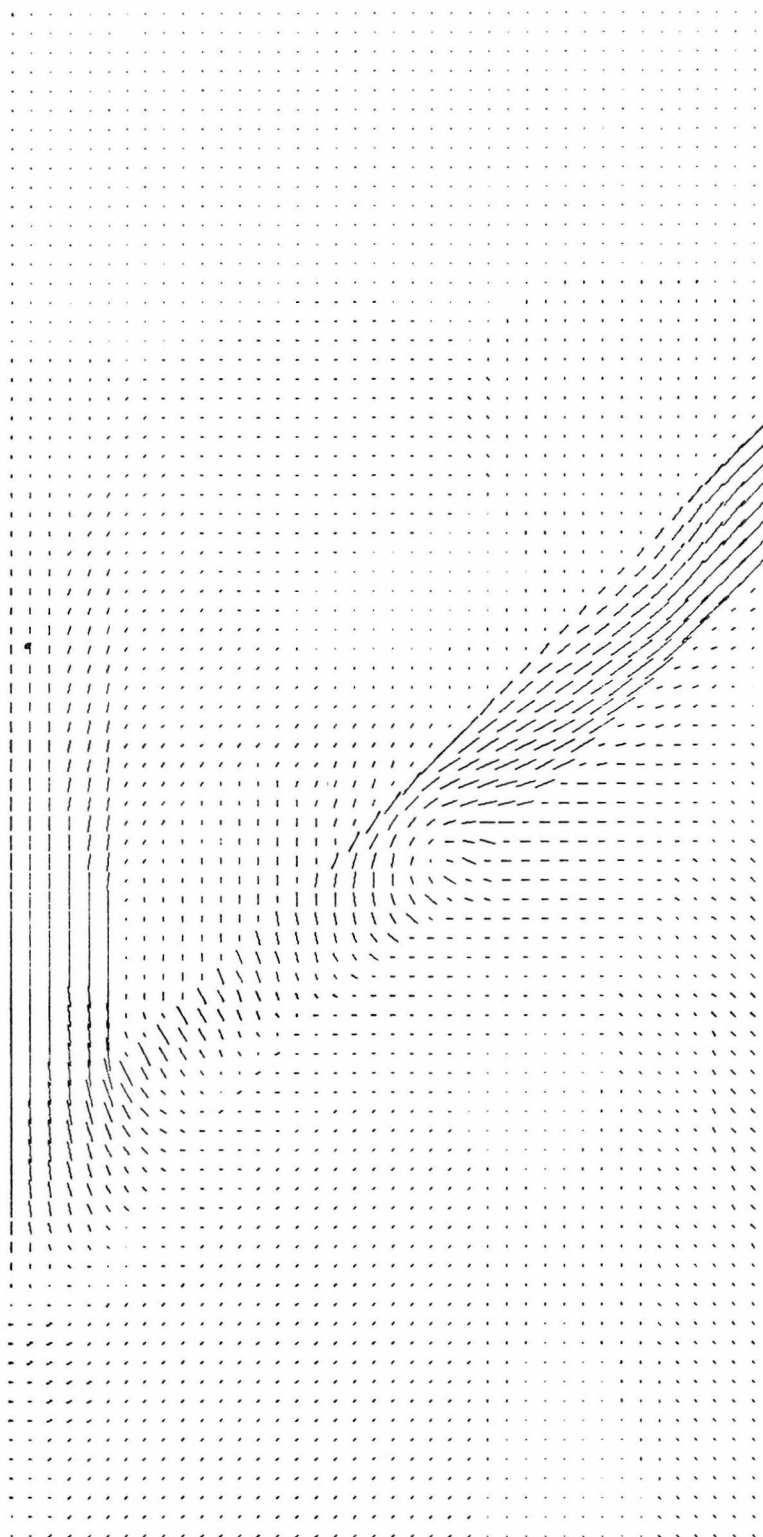
670 km



D32V A

10 cm/yr

670 km

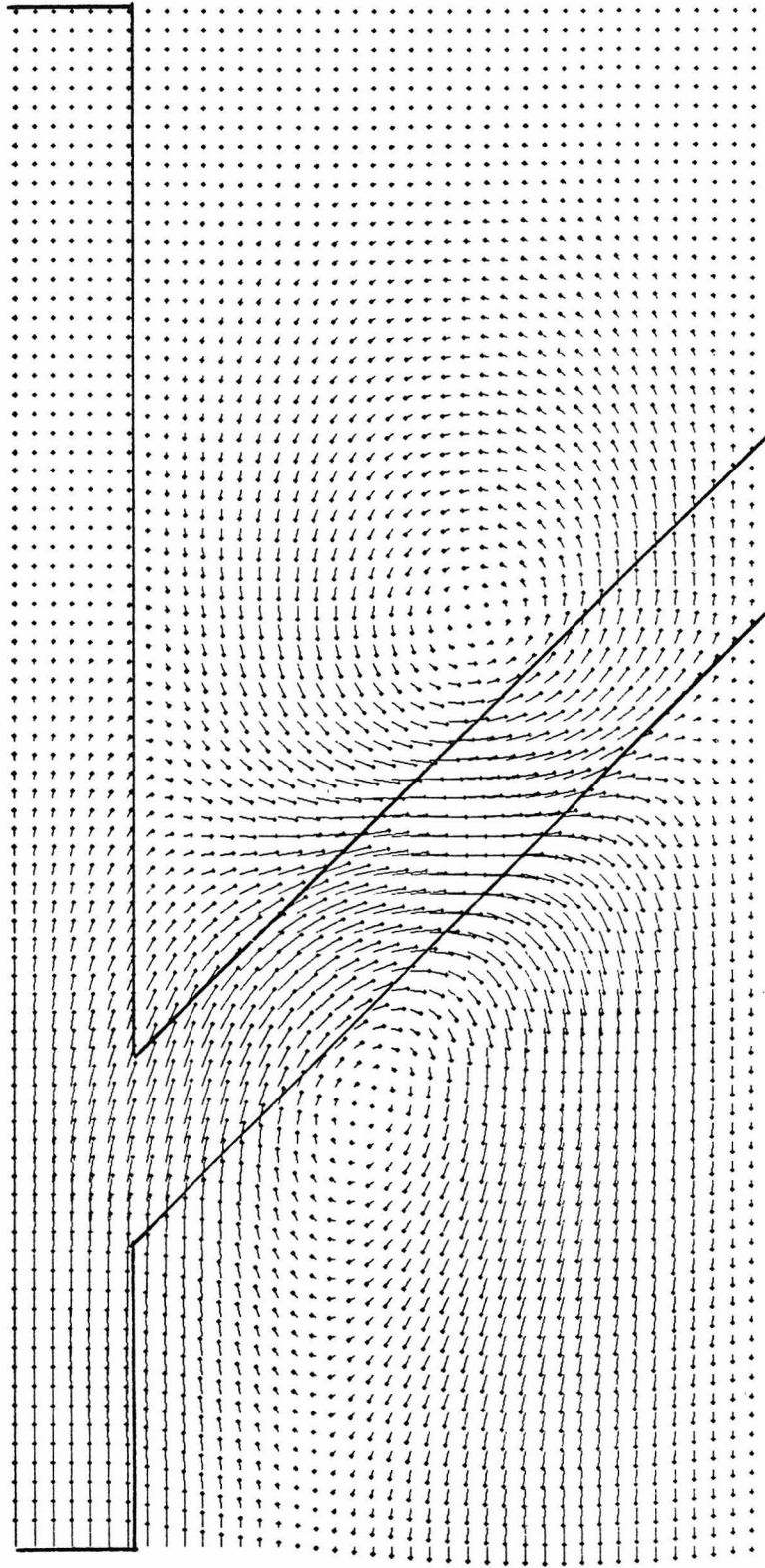


D32S B



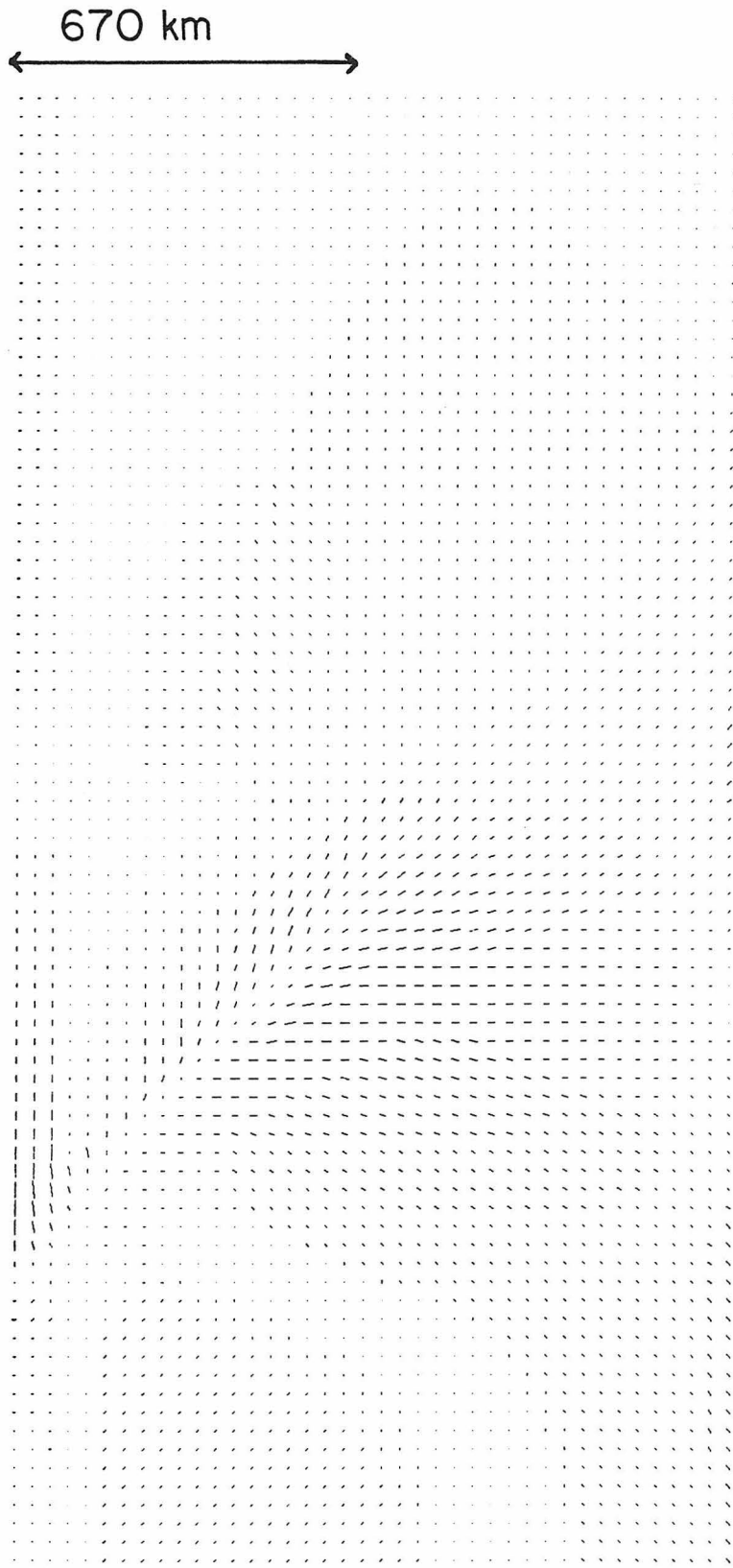
1 kbar

670 km



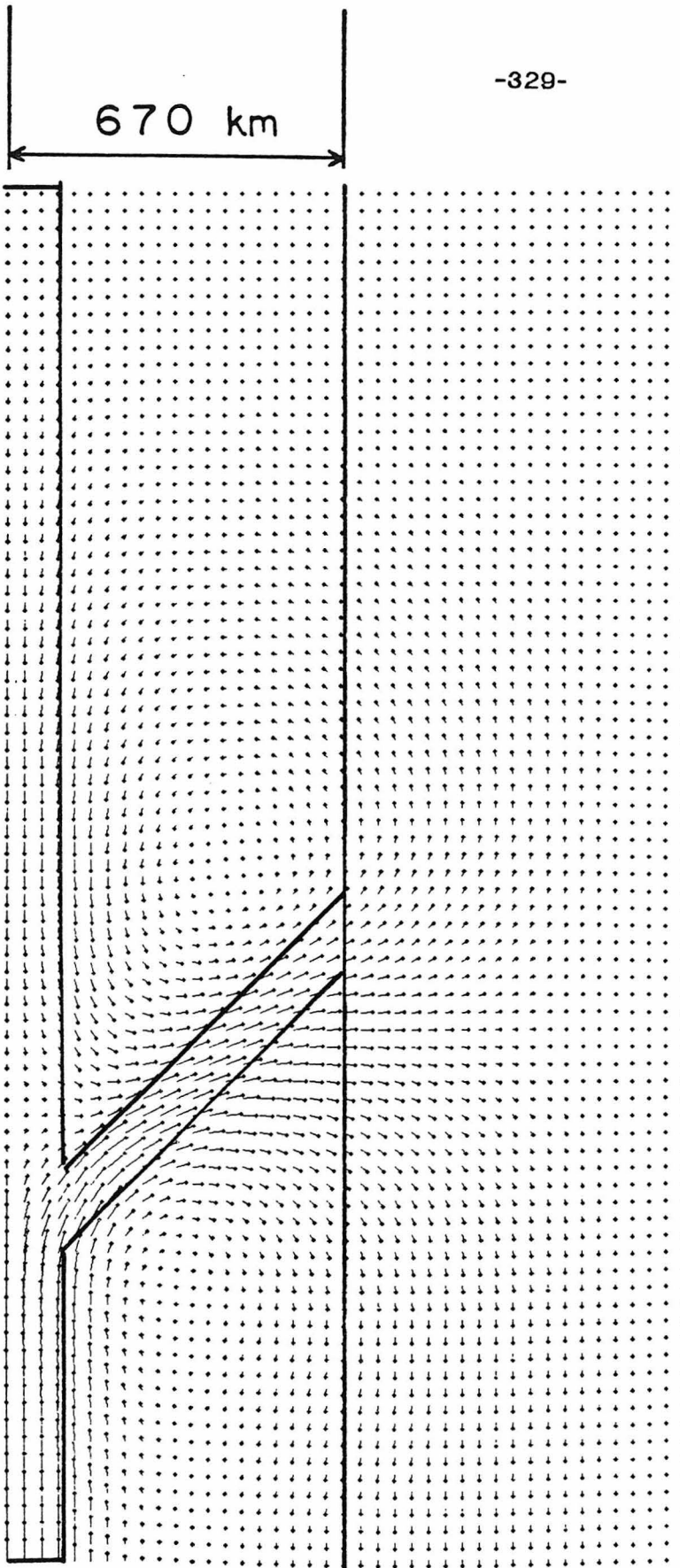
D32V B

10 cm/yr

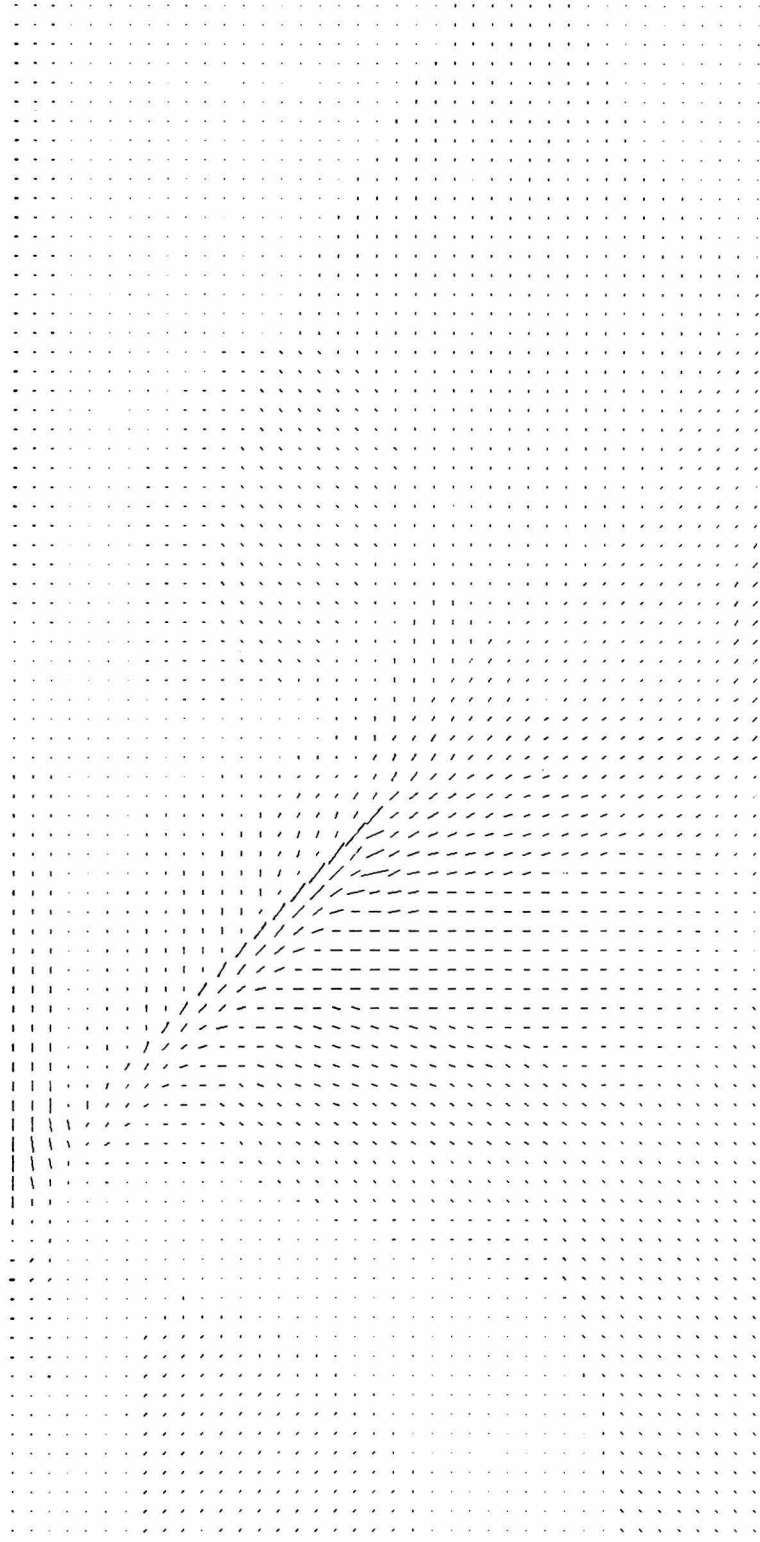


D33S

2 kbar

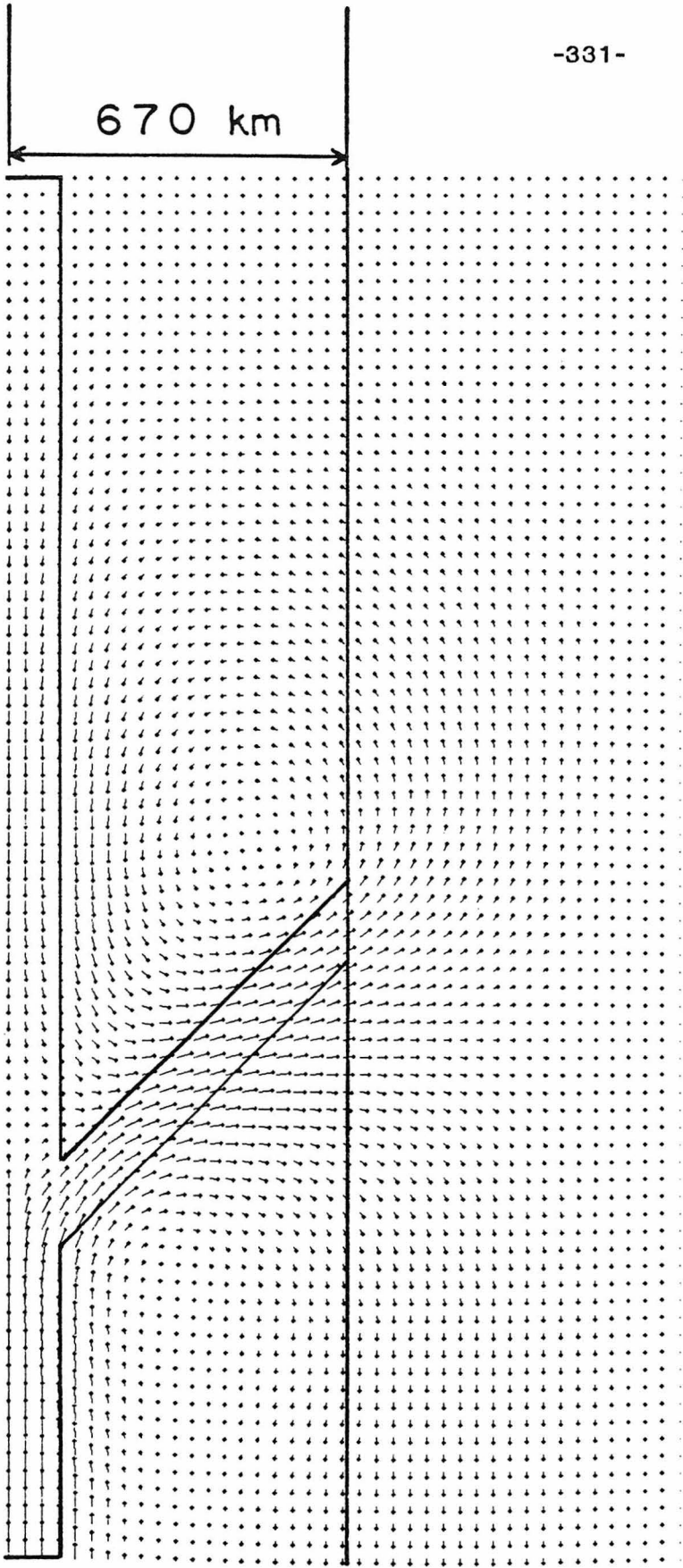


670 km
←—————→



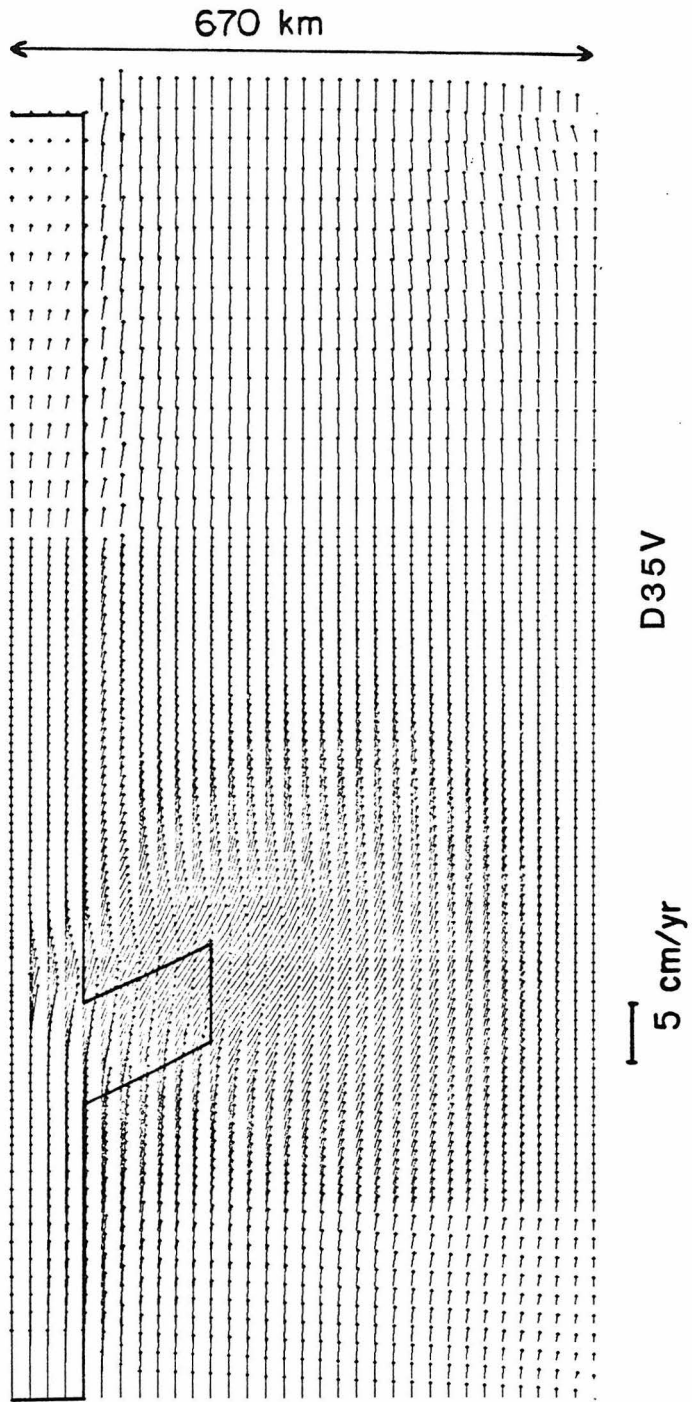
D34S

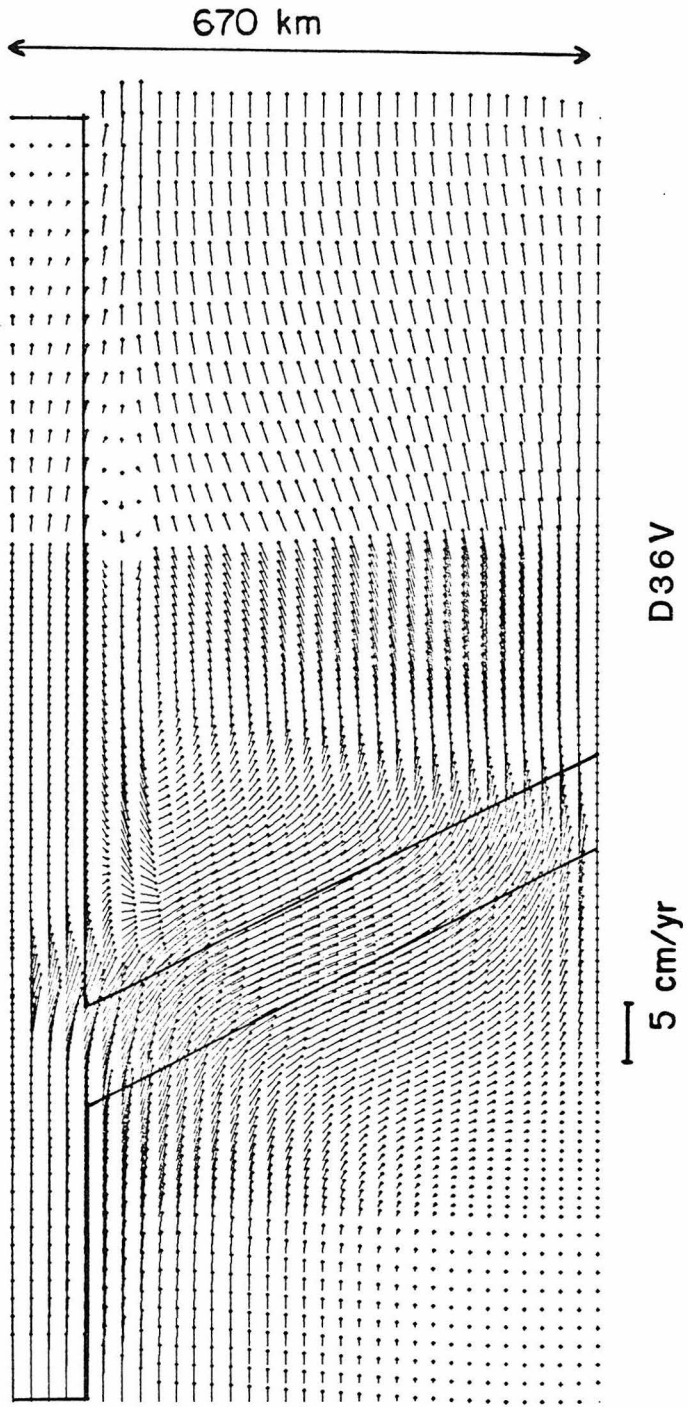
—|—
2 kbar



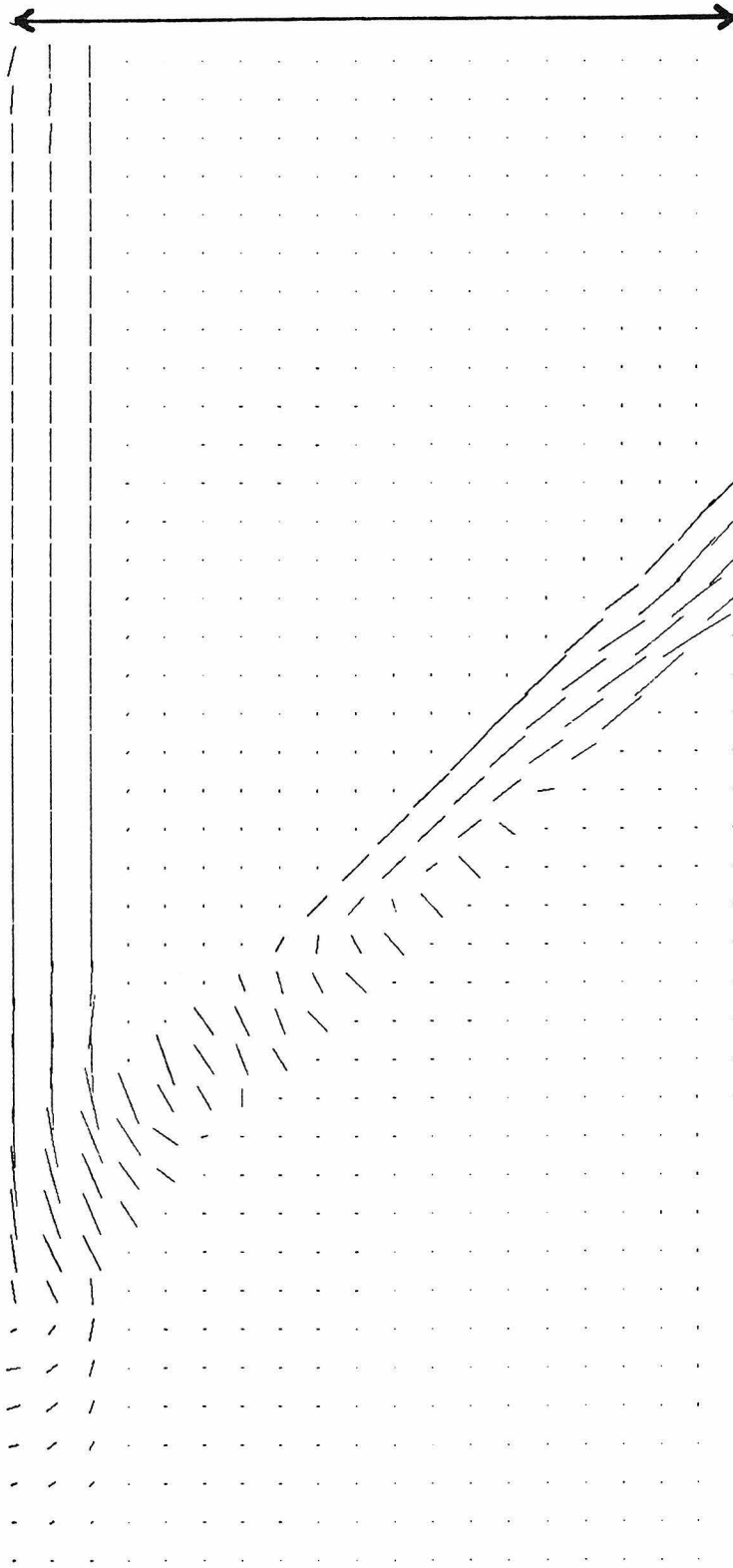
D34V

4 cm/yr





670 km

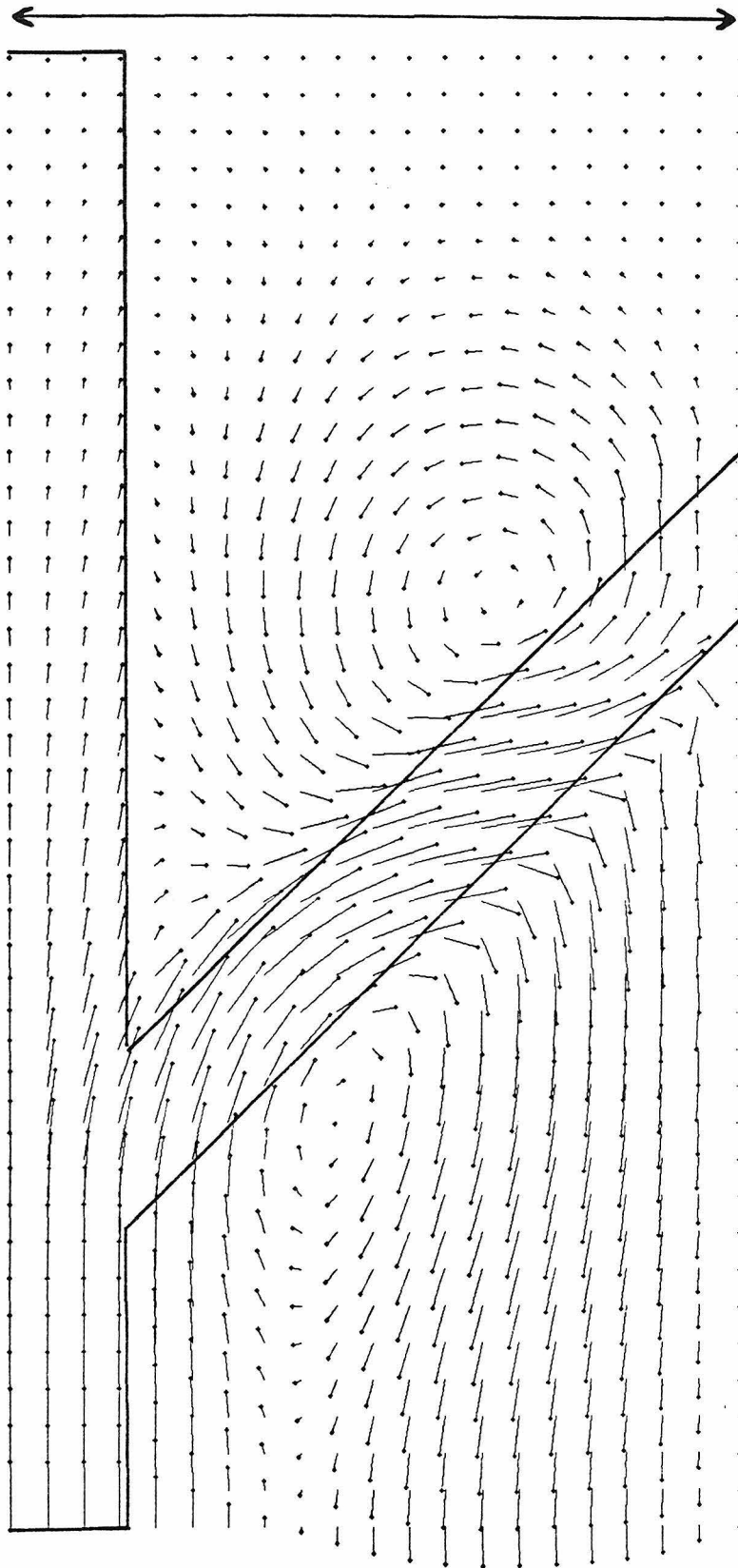


D37S

—

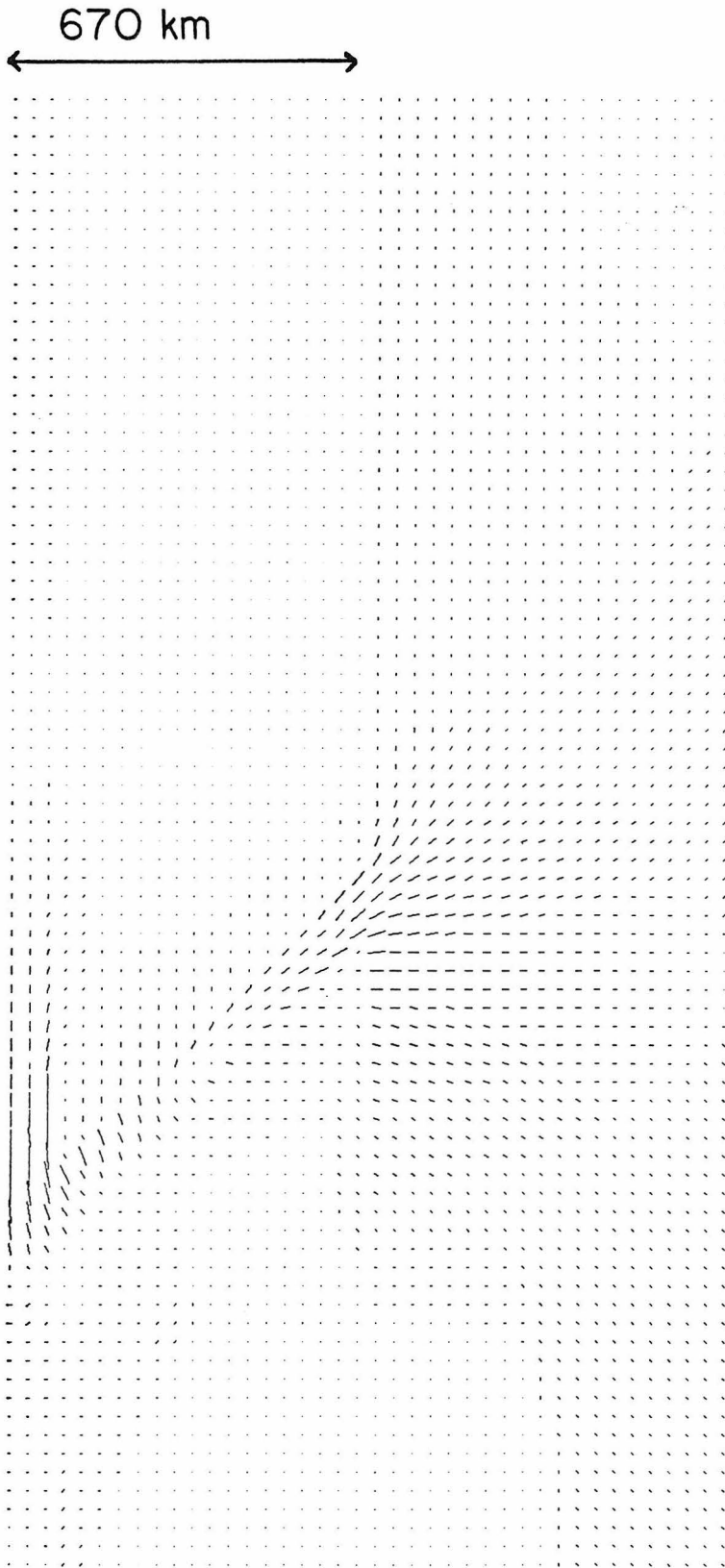
1 kbar

670 km

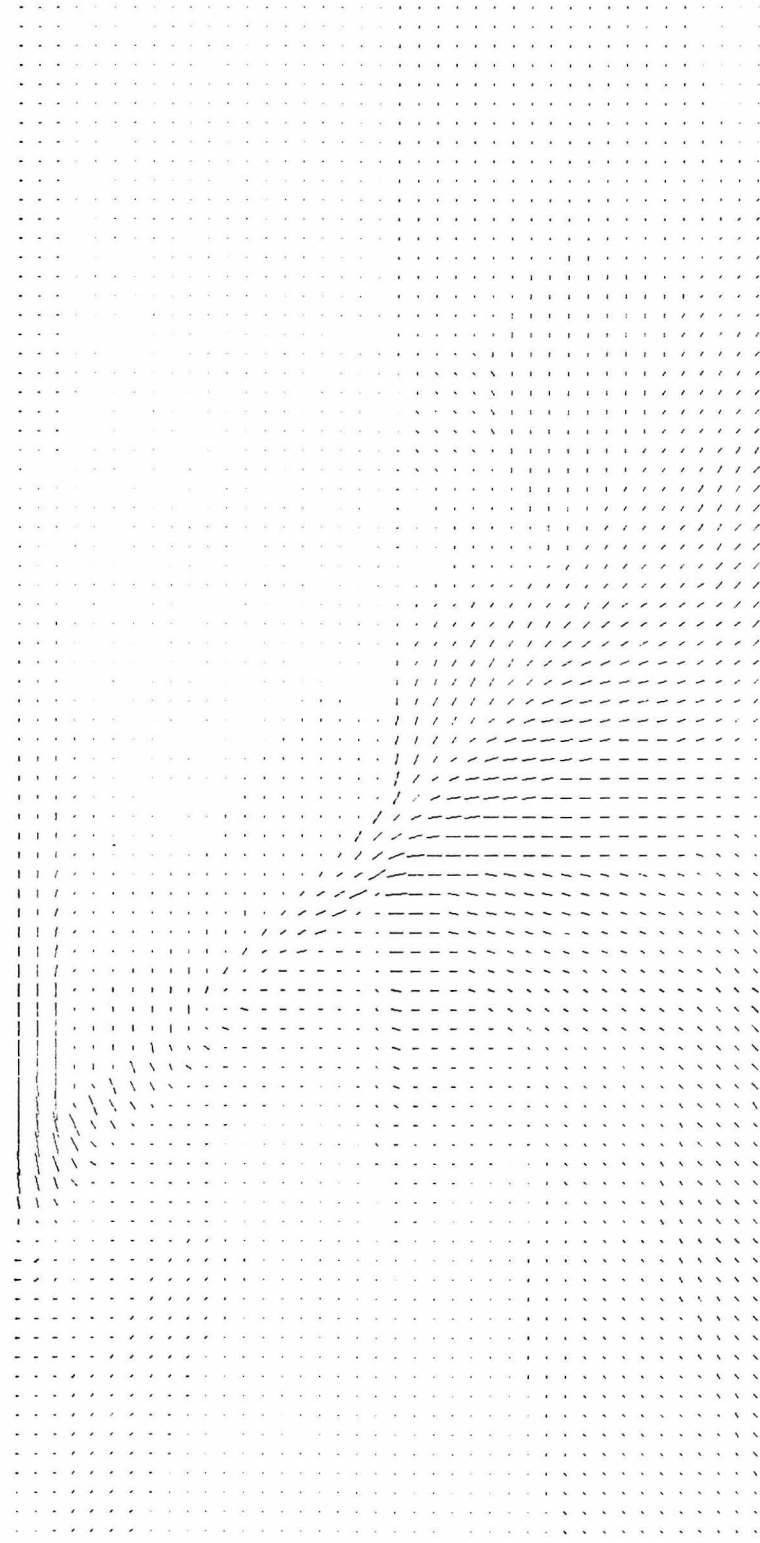
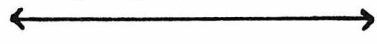


D37V

10 cm/yr



670 km

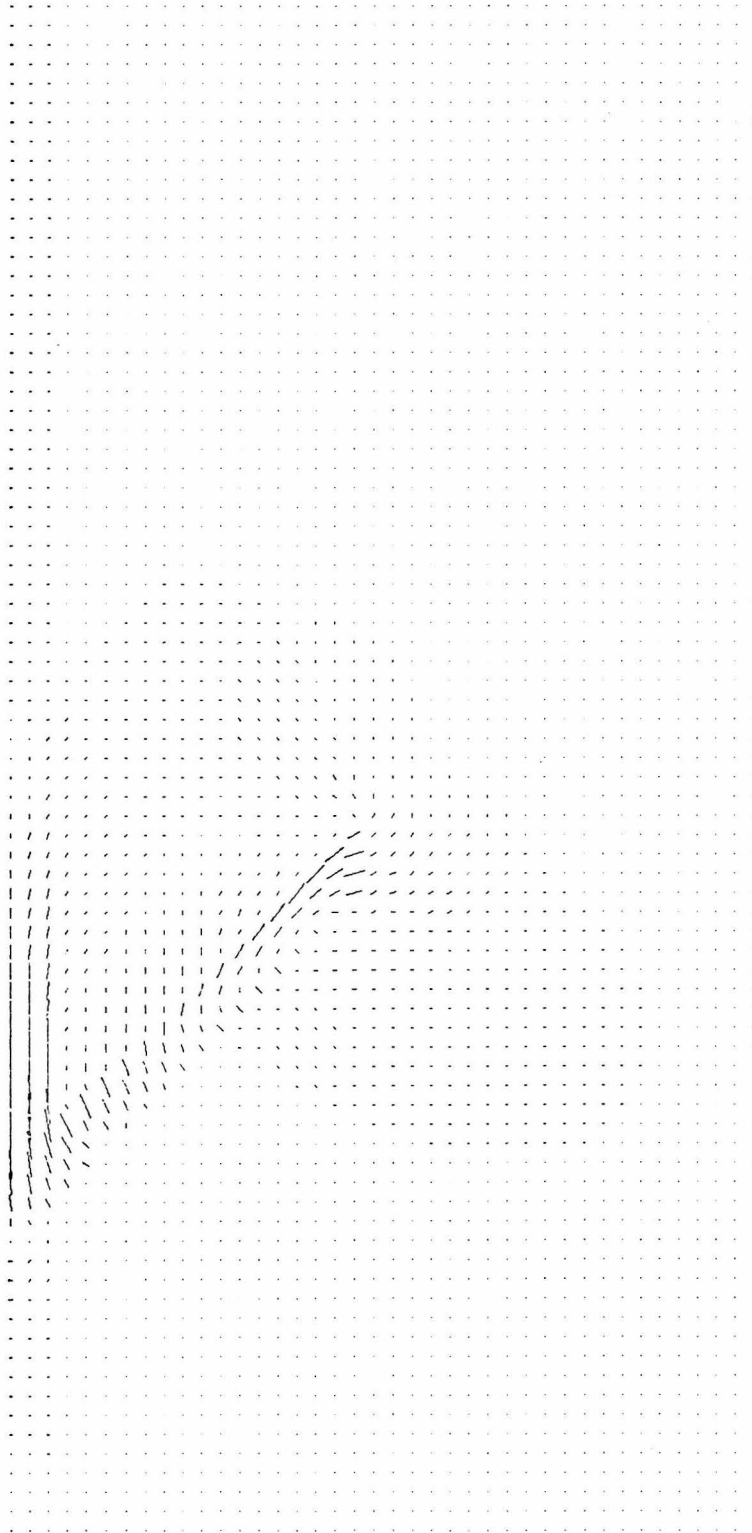


D40bS

2 kbar

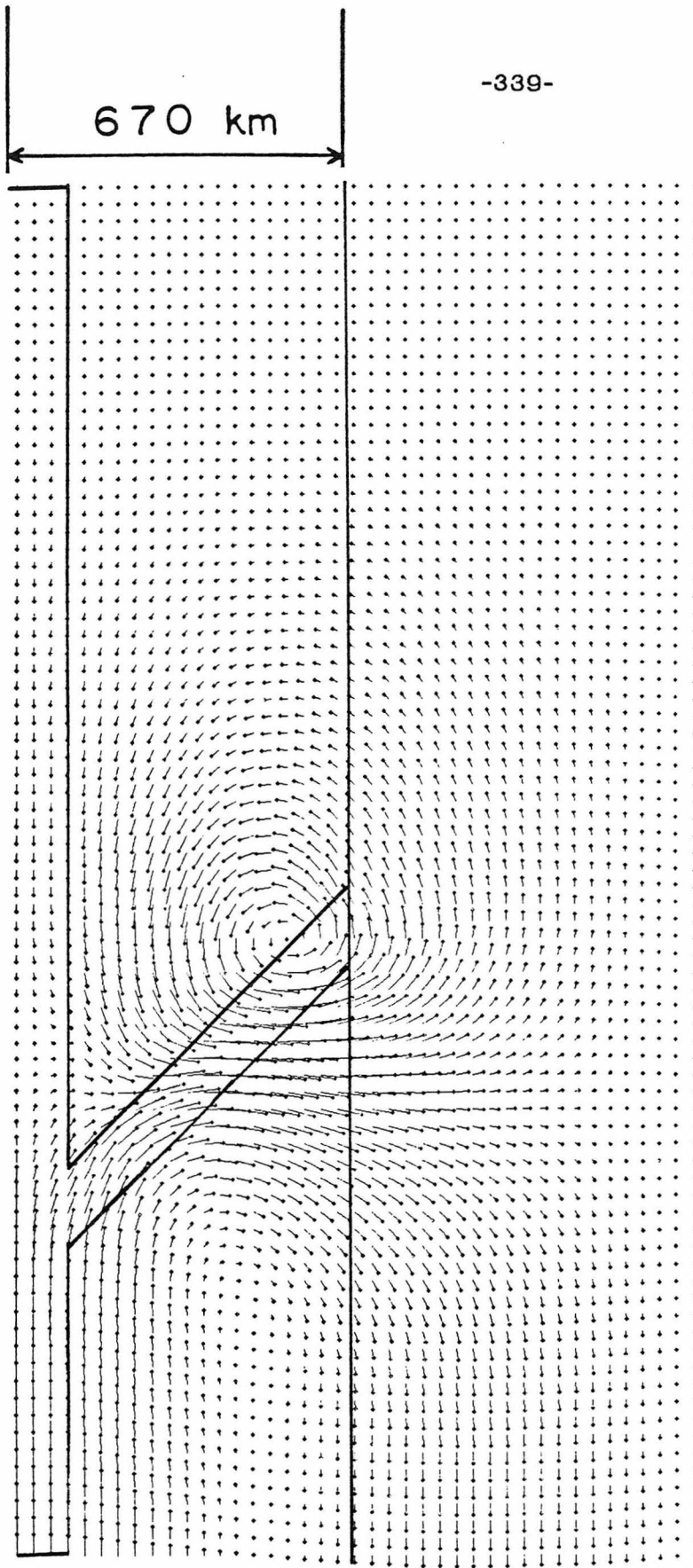


670 km
←————→



D42S

2 kbar



D42V

10 cm/yr